

UNIVERSITY OF BELGRADE
FACULTY OF TECHNOLOGY AND METALLURGY

Hana Elshaflu

**SPECTROSCOPIC AND
ELECTROCHEMICAL
CHARACTERIZATION, QUANTUM
MECHANICAL STUDY AND
BIOLOGICAL ACTIVITY OF 1,3-
SELENAZOL-2-YL-HYDRAZONES, 1,3-
THIAZOLE-2-YL-HYDRAZONES AND
THEIR COMPLEXES WITH COBALT(III)**

Doctoral Dissertation

Belgrade, 2018.

UNIVERZITET U BEOGRADU
TEHNOLOŠKO-METALURŠKI FAKULTET

Hana Elshaflu

**SPEKTROSKOPSKA I
ELEKTROHEMIJSKA
KARAKTERIZACIJA,
KVANTNOMEHANIČKA STUDIJA I
BIOLOŠKA AKTIVNOST 1,3-
SELENAZOL-2-IL-HIDRAZONA, 1,3-
TIAZOL-2-IL-HIDRAZONA I NJIHOVIH
KOMPLEKSA SA KOBALTOM(III)**

Doktorska disertacija

Beograd, 2018.

THESIS ADVISORS:

Dr Aleksandar Marinković, associate professor
University of Belgrade, Faculty of Technology
and Metallurgy

Dr Nenad Filipović, associate professor
University of Belgrade, Faculty of Agriculture

FINAL EXAMINING
COMMITTEE:

Dr Jelena Rogan, associate professor, University
of Belgrade, Faculty of Technology and
Metallurgy

Dr Saša Drmanić, associate professor, University
of Belgrade, Faculty of Technology and
Metallurgy

Dr Miloš Milčić, associate professor, University
of Belgrade, Faculty of Chemistry

Date:

ACKNOWLEDGEMENT

In the name of Allah the beneficent, the Merciful first and above all praise be to Allah the Almighty, who has bestowed upon us His Graces of thinking, searching and learning and His blessing in completing this thesis.

I am most grateful to my thesis advisor, Prof. Aleksandar Marinković for his guidance and support, encouragement and advice throughout time of my dissertation research. I appreciate all contributions of time, ideas, and funding to make my Ph.D. experience productive and stimulating.

I would like to extend my gratitude to the many people who helped to bring this research project to finalization, especially to my family and friends, whose unlimited devotion help me during this period.

I am also deeply thankful to my Co-supervisor Prof. Nenad Filipović and to Prof. Jelena Rogan, Prof. Saša Drmanić and Prof. Miloš Milčić for their support and knowledge in their area of expertise.

I am also very thankful to dr Aleksandra Božić and dr Nevena Prlainović for their kindness and support during my study. This accomplishment would not have been possible without them. Thank you so much.

Spectroscopic and electrochemical characterization, quantum mechanical study and biological activity of 1,3-selenazol-2-yl-hydrazones, 1,3-thiazole-2-yl-hydrazones and their complexes with cobalt(III)

ABSTRACT

In this thesis, series of (1,3-thiazol-2-yl)- and (1,3-selenazol-2-yl)hydrazones and their Cobalt(III) complexes have been synthesized. All the compounds and complexes have been characterized using elemental analysis, UV-Vis, ATR-FTIR, ¹H and ¹³C NMR spectroscopy. The crystal structure of the three newly synthesized compounds (HLS³, 4-Me, 4-OMe) and six Cobalt(III) complex ((1-3)-S and (1-3)-Se) were analyzed using single crystal X-ray diffraction analysis (XRD).

The absorption spectra of the investigated compounds were recorded in twenty three solvents of different polarity. Contributions of appropriate substituent- and solvent-dependent electronic transitions were investigated by the use of linear solvation energy relationships (LSER). The impact of ligand structural changes, as well as isosteric replacement of sulphur with selenium on electrochemical and electronic absorption features of complexes was explored.

Furthermore, to support the experimental data, density functional theory (DFT) calculations were conducted. Theoretical NMR chemical shifts, the relative energies and natural bond orbital (NBO) analysis are calculated within the DFT approach, while the singlet excited state energies and HOMO-LUMO energy gap were calculated with time-dependent density functional theory (TD-DFT). The electrophilic f^- and nucleophilic f^+ Fukui functions are well adapted to describe the electrophile and nucleophile centres in the molecules. It was found that both, substituents and solvents, influence electron density shift, *i.e.* extent of conjugation, and affect intramolecular charge transfer character in the course of excitation.

Additionally, all the compounds and their complexes were tested for biological activities, and they proved as potent antimicrobial, antioxidant and antiproliferative agents, as well as monoamine oxidases (MAO) A/B inhibitors. The results revealed that selenium compounds have a smaller cytotoxicity. Cobalt (III) complex with 2-

hydrazonylthiazoles tested revealed stronger cytotoxic activity on MCF-7 breast cancer cell line, compared to cisplatin.

Keywords: Thiazoles; Cobalt(III) complex; X-ray diffraction; Anticancer activity; Three drug combination study; 1,3-Selenazoles; Solvatochromism; UV-Vis; DFT; Fukui functions; Biological activity.

Scientific field: Organic chemistry

Scientific discipline: Organic chemistry

UDC:

Spektroskopska i elektrohemijška karakterizacija, kvantnomehanička studija i biološka aktivnost 1,3-selenazol-2-il-hidrazona, 1,3-tiazol-2-il-hidrazona i njihovih kompleksa sa kobaltom(III)

IZVOD

U ovoj tezi sintetisane su serije (1,3-tiazol-2-il)- i (1,3-selenazol-2-il)hidrazona i njihovi Co (III) kompleksi. Predmet istraživanja je potpuna strukturna i solvatochromna karakterizacija sintetisanih jedinjenja kombinovanjem eksperimentalnih tehnika i kvantno-hemijskih proračuna. Sva jedinjenja i kompleksi okarakterisani su pomoću elementarne analize, UV-Vis, ATR-FTIR, ^1H i ^{13}C NMR spektroskopije. Kristalna struktura tri novosintetisana jedinjenja (HLS³, 4-Me, 4-OMe) i šest Co(III) kompleksa ((1-3)-S and (1-3)-Se) je određena primenom rendgenskestrukturne analize (RSA) na dobijenim monokristalima.

UV-Vis spektralna svojstva detaljno su ispitana u dvadeset tri rastvarača različite polarnosti, a uticaj specifičnih i nespecifičnih interakcija je procenjen primenom principa LSER analize i to Kamlet-Taft-ovim i Catalán-ovim modelom. Ispitan je i uticaj promene strukture liganda, kao i zamena sumpora selenom u strukturi liganda, na elektrohemijška i elektronska apsorpciona svojstva kompleksa.

U cilju potvrde eksperimentalno dobijenih podataka, izvršena su kvantno-hemijska izračunavanja. Teorijska NMR pomeranja, relativne energije i stabilnost molekula ispitani su pomoću analize prirodnih vezujućih orbitala (NBO), primenom teorije funkcionala gustine (DFT), dok su energije u pobuđenom stanju kao i razlike HOMO-LUMO energija dobijene pomoću vremenski zavisne DFT metode (TD-DFT). Elektrofili f- i nukleofilni f+ Fukui funkcije su dobro prilagođeni da opišu elektrofile i nukleofilne centre u molekulima. Optimizovane geometrije u vakumu izračunate su pomoću B3LYP/6-311++G(d,p) metode. Utvrđeno je da i supstituenti i rastvarači utiču na promenu gustine elektrona, tj. stepen konjugacije, kao i da utiču na intramolekulski prenos naelektrisanja.

Pored toga, svim sintetisanim jedinjenja i kompleksima testirana je biološka aktivnosti, i pokazali su se kao snažnim antimikrobnim, antioksidativnim i antiproliferativnim agensima, kao i inhibitori monoaminog oksidaza (MAO) A/B. Rezultati su pokazali da jedinjenja sa selenom imaju nižu citotoksičnost.

Co (III) kompleks sa 2-hidrazoniltiazolima testiran na ćelijskoj liniji raka dojke MCF-7, pokazao je snažniju citotoksičnu aktivnosti u poređenju sa cisplatinom (CDDP).

Ključne reči: tiazoli; Co (III) kompleks; Rendgenska difrakcija; Antikancer aktivnost; Tri studije o kombinaciji lekova; 1,3-selenazoli; Solvatochromizam; UV-Vis; DFT; Fukui funkcije; Biološka aktivnost.

Naučna oblast: Organska hemija

Naučna disciplina: Organska hemija

UDK:

List of abbreviations

^{13}C NMR – Carbon-13 nuclear magnetic resonance
 ^1H NMR – Proton nuclear magnetic resonance
2CE – 2-Chloroethanol
2ME – 2-Methoxyethanol
2-Pyr – 2-Pyrrolidone
A549 – The Human Lung Cell Line
AAPH – 2,2'-Azobis(2-amidinopropane) dihydrochloride
AcN – Acetonitrile
AOC – Antioxidant Capacity
CDDP – Cisplatin
Chl – Chloroform
CI – Combination Index
CSD – Cambridge Structural Database
CT – Charge Transfer
CV – Cyclic Voltammetry
DCM – Dichloromethane
 D_{CT} – Charge-Transfer Distance
DFT – Density functional Theory
DMEM – Dulbecco's Modified Eagle's medium
DMF – *N,N*-Dimethylformamide
DMSO – Dimethyl sulfoxide
DMSO- d_6 – Deuterated Dimethyl sulfoxide
DNA – Deoxyribonucleic Acid
DPPH – 1,1-diphenyl-2-picrylhydrazyl
 E_{gap} – Energy gap between *HOMO* and *LUMO*
EtAc – Ethyl acetate
EtOH – Ethanol
F – Formamide
FT-IR – Fourier Transform Infrared Spectroscopy
GC – Glassy Carbon
GGA – Generalized-Gradient Approximation
GIAO – Gauge-Independent Atomic Orbital
HBA – Hydrogen-Bonding Acceptor
HBD – Hydrogen-Bond Donor
HBL-100 – The Human Breast Carcinoma Cell Line
HeLa – The Human Cervical Cancer Cells Line
Hex – Hexane
HOMO – Highest Occupied Molecular Orbital
iBuOH – Isobutanol
ICT – Intramolecular Charge Transfer
iPeOH – 3-Methylbutanol

iPrOH – 2-Propanol
LDA –Local Density Approximation)
LMCT – Ligand to Metal Charge Transfer
LSER –Linear Solvation Energy Relationship
LUMO –Lowest Unoccupied Molecular Orbital
MAD – Multiwavelength Anomalous Diffraction
MAO – Monoamine oxidase
MBC –Minimal Bactericidal Concentration
MeOH – Methanol
MIC –Minimal Inhibitory Concentration
MS – Mass Spectroscopy
MS/MSⁿ – Multiple-stage Mass Spectrometry
NBO – Natural Bonding Orbital
NCI – National Cancer Institute
NMP – 1-Methyl-2-pyrrolidone
NMR –Nuclear Magnetic Resonance
OD – Optical Density
ORAC – Oxygen Radical Absorbance Capacity
PBS – Phosphate Saline Buffer
PI – Propidium iodide
Q_{CT} –Amount of Transferred Charge
ROS –Reactive Oxygen Species
RSS – Reactive Sulfur Species
RNS – Reactive Nitrogen Species
SCE – Saturated Calomel Electrode
SRB – Sulforhodamine B
SW1537 – The Human Squamous Lung Cancer Cell Line
T-47D – The Human Breast Cancer Cell Line
TAOC – Total Antioxidant Capacity
TBAP – Tetrabutylammonium Perchlorate
TCA – Trichloroacetic Acid
TD-DFT –Time Dependent - Density Functional Theory
THF –Tetrahydrofuran
THP-1 –Acute Monocytic Leukemia Cells
TMS – Tetramethylsilane
UV-Vis –Ultraviolet–Visible Spectroscopy
WiDr – The Human Colon Carcinoma Cell Line
XRD – X-ray Diffraction

LIST OF FIGURES

Figure 2.1 Azoles: a) 1,2-azole; b) 1,3-azole.....	4
Figure 2.2 1,3-azoles: thiazole and selenazole.	5
Figure 2.3 Delocalization of the 1,3-azoles ring.....	5
Figure 2.4 Thiazole ring in the structures of various natural products.	8
Figure 2.5 Reactivity of thiazole ring.	13
Figure 2.6 2-amino-4-methyl-1,3-selenazole.	13
Figure 2.7 ORTEP presentation of 2-(2-(Pyridin-2-ylmethylene) hydrazinyl) -4-phenyl-1,3-thiazole.	24
Figure 2.8 Energy level diagrams with electronic transitions ⁷²	26
Figure 2.9 The unit cells with corresponding labels of the crystal family (little letter) and Bravais lattice (big letter).	37
Figure 2.10 Graphic view of the <i>Bragg's law</i>	38
Figure 2.11 Electrochemical cell for voltammetry.	42
Figure 2.12 Details for cyclic voltammetry. (a) One cycle of the triangular potential-excitation signal showing the initial potential and the switching potential. (b) The resulting cyclic voltammogram showing the measurement of the peak currents and peak potentials.	43
Figure 4.12 D NOESY spectrum of HLSe ³ in DMSO- <i>d</i> ₆	76
Figure 4.2 (a) Perspective view and labeling of the molecular structure of the ligand HL. Thermal ellipsoids are at the 40% probability level. Selected bond lengths (Å) and angles (°) with SD's in parentheses: N4–C11, 1.342(2); C10–C11, 1.465(2); N3–C10, 1.277(2); N2–N3, 1.3604(19); C1–N2, 1.362(2); N1–C1, 1.300(2); S1–C1, 1.7382(17); S1–C2, 1.7231(19); C2–C3, 1.357(2); C2–S1–C1, 87.88(8); C1–N1–C3, 109.99(13); N1–C1–N2, 123.79(15); N1–C1–S1, 116.05(12); N2–C1–S1, 120.15(12); N3–N2–C1, 116.98(14); C3–C2–S1, 111.26(13); C10–N3–N2, 117.63(14); N3–C10–C11, 119.78(15). (b) Infinite 1-D chains in the crystal structure of HL viewed along the <i>a</i> -axis. (c) 2-D supramolecular layers in the crystal structure of HL viewed along the <i>c</i> -axis.	78
Figure 4.3 Molecular structures of the complexes. Structure of 3-Se is taken as the representative. Atom numbering scheme is given for one ligand. Atoms belonging to other ligand are enumerated in analogous way, with suffix B.	80
Figure 4.4 Crystal packing in the crystal structure of 3-S viewed along the <i>a</i> -axis. H-atoms are omitted for clarity.....	84
Figure 4.5 Orthogonal nature of ligands coordination seen through chelate planes Ω_1A and Ω_1B	85
Figure 4.6 Mean planes through selenazole and phenyl rings in the complex 3-Se	86
Figure 4.7 (a) Query used in the Cambridge Structural Database (CSD) search; (b) Distribution of dihedral angles, 50 angles (colored in red) out of 500 hits are greater than 60°.....	87

Figure 4.8 Mean planes through phenyl ring of ligand A and chelate plane of ligand B.	88
Figure 4.9 UV/Vis spectra of: (A) ligands HLSe(1–3) and HLS(1–3); (B) complexes (1–3)-Se and (1–3)-S.	89
Figure 4.10 Representative cyclic voltammograms of selected substances in DMF + 0.1 M TBAP, GC electrode: (A) HLSe ³ (c = 0.44 mM, v = 0.1 V/s). (B) 3-Se (c = 0.22 mM, v = 0.1 V/s). Full amplitude and cathodic sweep direction. (C) 2-Se (c = 0.42 mM) and HLSe ² (c = 0.46 mM), v = 0.1 V/s. Narrow amplitude, anodic direction. (D) 3-Se (c = 0.22 mM, v = 0.1 V/s). Narrow amplitude and cathodic sweep direction. (E) 2-S (c = 0.40 mM) v = 0.02 and 0.05 V/s. Narrow amplitude and anodic direction. (F) 2-S (c = 0.40 mM, v = 0.05, 0.1 and 0.5 V/s). Full amplitude and anodic direction.	91
Figure 4.11 Time-resolved UV–Vis spectral changes of 3-S in deoxygenated DMF with 0.1 M TBAPF ₆ before (red curve) and after applying the first reduction potential –0.5 V. The arrow indicates the evolution. Blue curve corresponds to the spectrum of the first reduced form. Black curve is the spectrum recorded at equilibrium after applying –1.5 V.	95
Figure 4.12 DFT optimized structures of the ligands in the gas phase.	97
Figure 4.13 DFT optimized structures of Co(III) complexes in the gas phase.	98
Figure 4.14 Graphical representation of calculated HOMO, LUMO and HOMO-LUMO transition of <i>E</i> -1,3-thiazoles and <i>E</i> -1,3-selenazoles in DMF solvent.	100
Figure 4.15 Graphic representation of calculated HOMO, LUMO and HOMO-LUMO transition of Co(III) complexes with <i>E</i> -1,3-thiazoles and <i>E</i> -1,3-selenazoles as ligands, in DMF solvent.	102
Figure 4.16 Concentration-response curves and ED ₅₀ values for 3-S (a) and CDDP (b) on 2-D MCF-7 cell model after 24 h of incubation. Results are presented as percentage of cell death events determined by means of Annexin-V/PI double staining in two independent experiments (open and closed circles) and asymmetric five-parameter sigmoidal curve computed for both replicates in GraphPad Prism software.	109
Figure 4.17 (a) MCF-7 3-D culture changes in growth and morphology induced by the treatment with either 1 or CDDP added in three concentrations over the 8-day incubation period. Images have been acquired every other day, starting from day 0 on the Celigo imaging cytometer using Celigo software. Scale bar: 500 μm. (b) Changes in growth rate of MCF-7 spheroids treated with either 1 or CDDP applied in concentrations of 100 μM (open circle), 10 μM (full square), and 1 μM (open square), and non-treated control (full circle). Growth rate was determined by means of spheroid area established with Celigo software, and afterwards computed for every other day of the 8-day incubation period by dividing the area on the day- <i>n</i> with the area on the day 0. Results are presented as the mean ± SD of two replicates of independent experiments.	110

Figure 4.18 (a) MCF-7 3-D culture changes in growth and morphology induced by the treatment with different combinations of 1, CDDP and paclitaxel. Images have been acquired every other day, starting from day 0 on the Celigo imaging cytometer using Celigo software. Scale bar: 500 μm . (b) Changes in growth rate of MCF-7 spheroids treated with combination of CDDP and paclitaxel (open triangle), combination of 1 and paclitaxel (open circle), combination of 1 and CDDP (open square), combination of 1 with CDDP and paclitaxel (closed square), and non-treated control (full circle). Growth rate was determined by means of spheroid area established with Celigo software, and afterwards computed for days 4 and 8 by dividing the area on the day-n with the area on the day 0. Results are presented as the mean \pm SD of two replicates of independent experiments. (c) Type of interactions between drugs in combination treatments expressed by means of Combination index (CI), where $\text{CI} < 0.9$ indicates on synergistic, $0.9 < \text{CI} < 1.1$ indicates on additive, and $\text{CI} > 1.1$ indicates on antagonistic type of interaction. Results are presented as the mean \pm SD of two replicates of independent experiments..... **112**

Figure 4.19 ORTEP drawings of the molecular structures of compounds 4-Me (A) and 4-OMe (B) with labeling of non-H atoms. Displacement ellipsoids are shown at the 50% probability level and H atoms are drawn as spheres of arbitrary radii..... **116**

Figure 4.20 Crystal packing diagrams of compound 4-Me (A) and 4-OMe (B)..... **116**

Figure 4.21 Structural superposition of 4-Me (yellow) and 4-OMe (red)..... **118**

Figure 4.22 Cyclic voltammograms of compounds 1 and 2 (A) and 3 and 4 (B). **120**

Figure 4.23 Full MS/MS spectra of 1-Me (top) and 1-OMe (bottom) **121**

Figure 4.24 Full MS/MS spectra of 2-Me (top) and 2-OMe (bottom). **122**

Figure 4.25 Common fragmentation paths of compound 1..... **122**

Figure 4.26 Common fragmentation paths of 1-OMe. **123**

Figure 4.27 Common fragmentation paths of 1-Me. **124**

Figure 4.28 Common fragmentation paths of 2, 3 and 4. **126**

Figure 4.29 Common fragmentation paths of 2-OMe, 3-OMe and 4-OMe. **127**

Figure 4.30 Common fragmentation paths of 2-Me, 3-Me and 4-Me. **129**

Figure 4.31 Common fragmentation pathway of 1, 1-OMe and 1-Me..... **130**

Figure 4.32 Common fragmentation paths of 2, 3 and 4. **131**

Figure 4.33 Common fragmentation paths of 2-OMe, 3-OMe and 4-OMe. **132**

Figure 4.34 Common fragmentation paths of 2-Me, 3-Me and 4-Me. **133**

Figure 4.35 Absorption spectra of benzylidene-based (1,3-selenazol-2-yl)hydrazones in (A) DMSO and (B) EtOH..... **135**

Figure 4.36 Molecular orbital plots and energy levels of the HOMO, the LUMO and HOMO-LUMO transitions of the benzylidene-based (1,3-selenazol-2-yl)hydrazones in DMSO. **144**

Figure 7.1 ^1H NMR spectrum of HLSe¹ in DMSO-*d*₆..... **182**

Figure 7.2 ^{13}C NMR spectrum of HLSe¹ in DMSO-*d*₆ **182**

Figure 7.3 2D COSY spectrum of HLSe¹ in DMSO-*d*₆ **183**

Figure 7.4	2D HMBC spectrum of HLSe ¹ in DMSO- <i>d</i> ₆	183
Figure 7.5	2D HSQC spectrum of HLSe ¹ in DMSO- <i>d</i> ₆	184
Figure 7.6	¹ H NMR spectrum of HLSe ² in DMSO- <i>d</i> ₆	184
Figure 7.7	¹³ C NMR spectrum of HLSe ² in DMSO- <i>d</i> ₆	185
Figure 7.8	2D COSY spectrum of HLSe ² in DMSO- <i>d</i> ₆	185
Figure 7.9	2D HMBC spectrum of HLSe ² in DMSO- <i>d</i> ₆	186
Figure 7.10	2D HSQC spectrum of HLSe ² in DMSO- <i>d</i> ₆	186
Figure 7.11	¹ H NMR spectrum of HLSe ³ in DMSO- <i>d</i> ₆	187
Figure 7.12	¹³ C NMR spectrum of HLSe ³ in DMSO- <i>d</i> ₆	187
Figure 7.13	2D COSY spectrum of HLSe ³ in DMSO- <i>d</i> ₆	188
Figure 7.14	2D HMBC spectrum of HLSe ³ in DMSO- <i>d</i> ₆	188
Figure 7.15	2D HSQC spectrum of HLSe ³ in DMSO- <i>d</i> ₆	189
Figure 7.16	¹ H NMR spectrum of HLS ¹ in DMSO- <i>d</i> ₆	189
Figure 7.17	¹³ C NMR spectrum of HLS ¹ in DMSO- <i>d</i> ₆	190
Figure 7.18	2D COSY spectrum of HLS ¹ in DMSO- <i>d</i> ₆	190
Figure 7.19	2D HMBC spectrum of HLS ¹ in DMSO- <i>d</i> ₆	191
Figure 7.20	¹ H NMR spectrum of HLS ² in DMSO- <i>d</i> ₆	191
Figure 7.21	¹³ C NMR spectrum of HLS ² in DMSO- <i>d</i> ₆	192
Figure 7.22	2D COSY spectrum of HLS ² in DMSO- <i>d</i> ₆	192
Figure 7.23	2D HMBC spectrum of HLS ² in DMSO- <i>d</i> ₆	193
Figure 7.24	2D HSQC spectrum of HLS ² in DMSO- <i>d</i> ₆	193
Figure 7.25	¹ H NMR spectrum of HLS ³ in DMSO- <i>d</i> ₆	194
Figure 7.26	¹³ C NMR spectrum of HLS ² in DMSO- <i>d</i> ₆	194
Figure 7.27	¹ H NMR spectrum of 1-Se in DMSO- <i>d</i> ₆	195
Figure 7.28	¹³ C NMR spectrum of 1-Se in DMSO- <i>d</i> ₆	195
Figure 7.29	¹ H NMR spectrum of 2-Se in DMSO- <i>d</i> ₆	196
Figure 7.30	¹³ C NMR spectrum of 2-Se in DMSO- <i>d</i> ₆	196
Figure 7.31	¹ H NMR spectrum of 3-Se in DMSO- <i>d</i> ₆	197
Figure 7.32	¹³ C NMR spectrum of 3-Se in DMSO- <i>d</i> ₆	197
Figure 7.33	¹ H NMR spectrum of 1-Sin DMSO- <i>d</i> ₆	198
Figure 7.34	¹³ C NMR spectrum of 1-Sin DMSO- <i>d</i> ₆	198
Figure 7.35	¹ H NMR spectrum of 2-Sin DMSO- <i>d</i> ₆	199
Figure 7.36	¹³ C NMR spectrum of 2-Sin DMSO- <i>d</i> ₆	199
Figure 7.37	¹ H NMR spectrum of 3-Sin DMSO- <i>d</i> ₆	200
Figure 7.38	¹³ C NMR spectrum of 3-Sin DMSO- <i>d</i> ₆	200
Figure 7.39	¹ H NMR spectrum of 1 in DMSO- <i>d</i> ₆	201
Figure 7.40	¹³ C NMR spectrum of 1 in DMSO- <i>d</i> ₆	201
Figure 7.41	COSY spectrum of 1 in DMSO- <i>d</i> ₆	202
Figure 7.42	NOESY spectrum of 1 in DMSO- <i>d</i> ₆	202
Figure 7.43	¹ H- ¹³ C HSQC NMR spectrum of 1 in DMSO- <i>d</i> ₆	203
Figure 7.44	¹ H- ¹³ C HMBC NMR spectrum of 1 in DMSO- <i>d</i> ₆	203
Figure 7.45	¹ H NMR spectrum of 1-OMe in DMSO- <i>d</i> ₆	204

Figure 7.46	^{13}C NMR spectrum of 1-OMe in DMSO- d_6	204
Figure 7.47	^1H NMR spectrum of 1-Me in DMSO- d_6	205
Figure 7.48	^{13}C NMR spectrum of 1-Me in DMSO- d_6	205
Figure 7.49	^1H NMR spectrum of 2 in DMSO- d_6	206
Figure 7.50	^{13}C NMR spectrum of 2 in DMSO- d_6	206
Figure 7.51	^1H NMR spectrum of 2-OMe in DMSO- d_6	207
Figure 7.52	^{13}C NMR spectrum of 2-OMe in DMSO- d_6	207
Figure 7.53	COSY spectrum of 2-OMe in DMSO- d_6	208
Figure 7.54	NOESY spectrum of 2-OMe in DMSO- d_6	208
Figure 7.55	^1H - ^{13}C HSQC NMR spectrum of 2-OMe in DMSO- d_6	209
Figure 7.56	^1H - ^{13}C HMBC NMR spectrum of 2-OMe in DMSO- d_6	209
Figure 7.57	^1H NMR spectrum of 2-Me in DMSO- d_6	210
Figure 7.58	^{13}C NMR spectrum of 2-Me in DMSO- d_6	210
Figure 7.59	^1H NMR spectrum of 3 in DMSO- d_6	211
Figure 7.60	^{13}C NMR spectrum of 3 in DMSO- d_6	211
Figure 7.61	^1H NMR spectrum of 3-OMe in DMSO- d_6	212
Figure 7.62	^{13}C NMR spectrum of 3-OMe in DMSO- d_6	212
Figure 7.63	^1H NMR spectrum of 3-Me in DMSO- d_6	213
Figure 7.64	^{13}C NMR spectrum of 3-Me in DMSO- d_6	213
Figure 7.65	COSY spectrum of 3-Me in DMSO- d_6	214
Figure 7.66	NOESY spectrum of 3-Me in DMSO- d_6	214
Figure 7.67	^1H - ^{13}C HSQC NMR spectrum of 3-Me in DMSO- d_6	215
Figure 7.68	^1H - ^{13}C HMBC NMR spectrum of 3-Me in DMSO- d_6	215
Figure 7.69	^1H NMR spectrum of 4 in DMSO- d_6	216
Figure 7.70	^{13}C NMR spectrum of 4 in DMSO- d_6	216
Figure 7.71	COSY spectrum of 4 in DMSO- d_6	217
Figure 7.72	NOESY spectrum of 4 in DMSO- d_6	217
Figure 7.73	^1H - ^{13}C HSQC NMR spectrum of 4 in DMSO- d_6	218
Figure 7.74	^1H - ^{13}C HMBC NMR spectrum of 4 in DMSO- d_6	218
Figure 7.75	^1H NMR spectrum of 4-OMe in DMSO- d_6	219
Figure 7.76	^{13}C NMR spectrum of 4-OMe in DMSO- d_6	219
Figure 7.77	^1H NMR spectrum of 4-Me in DMSO- d_6	220
Figure 7.78	^{13}C NMR spectrum of 4-Me in DMSO- d_6	220
Figure 7.79	Molecular orbital plots and energy levels of the HOMO, the LUMO and HOMO-LUMO transition of the benzyldene-based (1,3-selenazol-2-yl)hydrazones in EtOH.	221
Figure 7.80	Molecular orbital plots and energy levels of the HOMO, the LUMO and HOMO-LUMO transition of the benzyldene-based (1,3-selenazol-2-yl)hydrazones in THF.	222

LIST OF TABLES

Table 2.1 Summary of sample methods used in DFT.....	33
Table 2.2 Classification of crystals according to the length of the crystallographic axes and the angular size between them with given minimal number of elements of symmetry	35
Table 4.1 Data collection and refinement parameters for the crystal structures of the HLS ³	77
Table 4.2 Crystal packing parameters in the crystal structures of HLS ³	79
Table 4.3 Crystallographic details HLSe ¹⁻³	81
Table 4.4 Crystallographic details HLS ¹⁻³	82
Table 4.5 Crystal packing parameters in the crystal structures 3-S.....	84
Table 4.6 Selected bond lengths (Å) for the complexes.	86
Table 4.7 Electronic absorption properties and HOMO–LUMO energy gaps of HLSe ¹⁻³ and HLS ¹⁻³	89
Table 4.8 Electronic absorption properties and DFT calculation and assignment of λ_{\max} (in nm) in DMF for (1–3)-S and (1–3)-Se.....	90
Table 4.9 Voltammetric characteristics of the ligands at $v = 0.10$ V/s.....	92
Table 4.10 Values of k^0 for the processes I_R and II_R in solutions of complexes calculated according to reference. ³⁴	93
Table 4.11 Voltammetric characteristics of the complexes. *	94
Table 4.12 Calculated the relative energy ΔE (kcal/mol) of <i>E</i> -1,3-thiazoles and <i>E</i> -1,3-selenazoles.	97
Table 4.13 Electrochemical properties and energies of HOMO orbitals of (1–3)-S and (1–3)-Se.	104
Table 4.14 Antibacterial activity of investigated compounds tested by the disc-diffusion method.	104
Table 4.15 Antifungal activity of investigated compounds tested by the disc-diffusion method (inhibition zone size including disc/mm)	105
Table 4.16 LC ₅₀ values of the <i>A. salina</i> cytotoxic activity and IC ₅₀ of the DPPH free-radical scavenging activity of investigated compounds	106
Table 4.17 LC ₅₀ values of the <i>A. salina</i> cytotoxic activity and IC ₅₀ of the DPPH free-radical scavenging activity of investigated compounds	107
Table 4.18 Crystallographic data of 4-Me and 4-OMe.....	115
Table 4.19 Selected experimentally obtained (XRD) and calculated (DFT) bond lengths (Å) and angles (°) for 4-Me and 4-OMe.....	117
Table 4.20 Angles between the selenazole ring least square plane and phenyl rings least square planes.....	118
Table 4.21 Voltammetric characteristics of the the benzylidene-based (1,3-selenazol-2-yl)hydrazones ^a	119
Table 4.22 Absorption maxima shifts, ν_{\max} (10^{-3} cm ⁻¹), of investigated (1,3-selenazol-2-yl)hydrazones in selected solvents	137

Table 4.23 Results of LSER correlations for investigated benzylidene-based (1,3-selenazol-2-yl)hydrazones obtained by the use of the Kamlet–Taft eq (3.4).....	138
Table 4.24 Correlation results of investigated benzylidene-based (1,3-selenazol-2-yl)hydrazones according to Catalán eq. (3.5).....	140
Table 4.25 The experimental (λ_{abs}) and calculated absorption maxima (λ^*), obtained by the use of TD/DFT method, of (1,3-selenazol-2-yl)hydrazones in DMSO, EtOH and THF.....	142
Table 4.26 Calculated energies of the HOMO and LUMO orbitals and energy gap (in eV) for <i>E</i> -(1,3-selenazol-2-yl)hydrazones in DMSO, EtOH and THF, obtained by TD/DFT.	143
Table 4.27 Selected highest values of the condensed Fukui functions (f^+ and f^-) for unsubstituted (1,3-selenazol-2-yl)hydrazones, considering DFT/DMSO/NBO charges according to eqs. (3.2) and (3.3).....	146
Table 4.28 Selected highest values of the condensed Fukui functions (f^+ and f^-) for the nitro substituted (1,3-selenazol-2-yl)hydrazones, considering DFT/DMSO/NBO charges according to eqs. (3.2) and (3.3).....	147
Table 4.29 Antibacterial activity of investigated benzylidene-based (1,3-selenazol-2-yl)hydrazones tested by the disc-diffusion method.	148
Table 4.30 Antifungal activities of benzylidene-based (1,3-selenazol-2-yl)hydrazones	149
Table 4.31 Antioxidant capacity of investigated benzylidene-based (1,3-selenazol-2-yl)hydrazones and the standard.	150
Table 4.32 Antiproliferative activities of benzylidene-based (1,3-selenazol-2-yl)hydrazones.	152
Table 4.33 Monoamine oxidase (MAO) A/B inhibition capacities of benzylidene-based (1,3-selenazol-2-yl)hydrazones.	153
Table 7.1 Solvent parameters used in Kamlet–Taft equation ^{172,173}	167
Table 7.2 Solvent parameters ²² used in Catalán equation ^a	168
Table 7.3 Selected dihedral angles (°) for complexes.	168
Table 7.4 Elements of DFT optimized geometries of <i>E</i> - and <i>Z</i> -isomers of ligands compared with available crystal structure data.....	169
Table 7.5 Comparison of average values of the theoretically calculated Co–N bond lengths (in Å) and N–Co–N angles (in °) obtained for the complex 1-S, using two DFT functionals with several basis sets and experimental measured values.	170
Table 7.6 Comparison of average values of the experimental and theoretical calculated Co–N bond lengths (in Å) and N–Co–N angles (in °) obtained for the (1–3)-Se and (1–3)-S complexes.....	170
Table 7.7 Average values of experimental and calculated chemical shifts (δ in ppm), coupling constants (J in Hz) and assignments of the signals in ¹ H and ¹³ C NMR spectra of (1–3)-Se and (1–3)-S complexes	171

Table 7.8 TD-DFT/B3LYP calculated electronic transitions (absorption maxima λ_{max} in cm^{-1} and nm), oscillator strengths (f) and major MO contributors in percent of <i>E</i> -1,3-thiazoles and <i>E</i> -1,3-selenazoles in DMF solvent.	174
Table 7.9 TD-DFT/B3LYP calculated electronic transitions (absorption maxima λ_{max} in cm^{-1} and nm), oscillator strengths (f) and major MO contributors in percent of Co(III) complexes with <i>E</i> -1,3-thiazoles and <i>E</i> -1,3-selenazoles in DMF solvent.	177
Table 7.10 Selected highest values of the condensed Fukui functions (f^+ and f^-) for the ligands, considering DFT / DMF / NBO charges according to equations (1 and 2).	180
Table 7.11 Calculated absorption maxima (λ^* , nm), oscillator strengths (f) and composition of bands of benzyldene-based (1,3-selenazol-2-yl)hydrazones in DMSO, EtOH and THF obtained by the use of TD/DFT method.....	181

CONTENTS

ABSTRACT	I
LIST OF FIGURES	VII
LIST OF TABLES	XII
1 INTRODUCTION	1
2 THEORETICAL PARTS	4
2.1 Structure and classification of 1,3-selenazol-2-yl-hydrazones, 1,3-thiazole-2-yl-hydrazones.....	4
2.1.1 Azoles.....	4
2.1.2 1,3-Thiazoles	8
2.1.3 1,3-selenazoles	13
2.1.4 (1,3-thiazol-2-yl)hydrazones and (1,3-selenazol-2-yl)hydrazones	17
2.2 Linear solvation energy relationship (LSER)	25
2.2.1 Solvatochromism of organic molecules	25
2.2.2 Solvent effect - multi-parameter approach	26
2.3 Density Functional Theory (DFT)	29
2.3.1 Fundamental aspects of DFT.....	29
2.3.2 Methods in DFT	31
2.3.3 Application of DFT	33
2.4 Introduction to X-ray crystallography ⁸⁹	34
2.5 Electrochemistry in analysis of organic compounds	40
2.5.1 Voltammetry.....	41
2.5.2 Cyclic voltammetry	42
2.5.3 Electrochemistry of hydrazones	44
2.6 Biological activity.....	45
2.6.1 Antimicrobial activity.....	46
2.6.2 Antioxidant activity.....	47
2.6.3 Anticancer activity	48
3 EXPERIMENTAL PART	51

3.1	Synthesis 1,3-seleno(thi)azoles-2-yl-hydrazones.....	51
3.1.1	General procedure for synthesis first series HL(Se/S) ¹⁻³	51
3.1.2	General procedure for synthesis complexes with HL(Se/S) ¹⁻³	52
3.1.3	General procedure for synthesis second series.....	52
3.2	Characterization of synthesized compounds and complexes.....	53
3.3	X-ray crystallography.....	64
3.4	Cyclic voltammetry and spectroelectrochemistry.....	65
3.5	MS/MS ⁿ study.....	65
3.6	Computational methodology.....	66
3.7	Multi parameter correlation analysis.....	67
3.8	Biological experiments.....	68
3.8.1	Antimicrobial activity.....	68
3.8.2	Antioxidant activity.....	69
3.8.3	Anticancer activity.....	70
3.8.4	Monoamine oxidase A/B inhibition.....	74
4	RESULTS AND DISCUSSION.....	75
4.1	Pyridine-2-carboxaldehyde-based (1,3-selenazol-2-yl)hydrazones.....	75
4.1.1	Synthesis and structural characterization of first series HL(Se/S) ¹⁻³	75
4.1.2	Synthesis and structural characterization complexes with HL(Se/S) ¹⁻³	79
4.1.3	The absorption spectra of HL(Se/S) ¹⁻³ and their Co(III) complexes.....	88
4.1.4	Voltammetric and spectroelectrochemical studies.....	90
4.1.5	DFT calculations.....	96
4.1.6	Biological activity.....	104
4.2	Nitro (<i>o</i> , <i>p</i> and <i>m</i>) benzaldehyde-based (1,3-selenazol-2-yl)hydrazones.....	113
4.2.1	Synthesis and characterization of second series 1-4 (OMe, Me).....	113
4.2.2	Analysis of crystal structures.....	114
4.2.3	Cyclic voltammetry (CV).....	119
4.2.4	MS/MS ⁿ analysis.....	121
4.2.5	Solvatochromism.....	134

4.2.6	DFT and TD-DFT calculations	142
4.2.7	Biological activity	148
5	CONCLUSIONS	154
6	REFERENCES	158
7	APPENDIX	167

1 INTRODUCTION

Sulfur and selenium heterocycles represent an impressive class of compounds because of both, outstanding chemical properties and pharmaceutical applications. 1,3-Thiazole ring system is a building block found in major natural and synthetic biologically active compounds.¹ Thiazoles are easily metabolized by known biochemical reactions, and are non-carcinogenic in nature. Their diverse biological activity is widely known.²⁻⁷ Selenazole is the selenium analogue of thiazole. Selenium, the essential trace element, is controversial regarding its biological activity. In 1930s it was marked as toxic, but twenty years later it has been shown that Se prevented pathologies in vitamin E-deficient animals. After selenium was recognized as essential element to mammals, awareness about selenium toxicity changed in great extent and nowadays it is considered as micronutrient used in disease prevention and treatment by selenium supplementation.⁸

Developing of synthetic organosulfur and organoselenium compounds, as well as their metal complexes, has been subject of research in the field of modern medicinal chemistry. The potential of synthetic sulfur and selenium compounds in medicinal chemistry include antioxidant, antitumor, antiviral, antimicrobial, anti-infective, anti-inflammatory, antiparasitic, antidiabetic, antimalarial, neuroprotective, antihypersensitive and cardiogenic agents as well as enzyme inhibitors and immunomodulators.⁴³⁻⁴⁵ 1,3-Thiazole and 1,3-selenazole rings are well recognized pharmacophores. Thiazole ring is a constituent of many drugs such as thiazofurin (antineoplastic agents), ritonavir (anti-HIV drug), ravuconazole (antifungal agent), nitazoxanide (antiparasitic agent), fanetizole (anti-inflammatory agent), and nizatidine (antiulcer agent).⁹ Also, a number of recent studies have indicated that 1,3-selenazole derivatives inhibit the synthesis of nitric acid,¹⁰ and they are antagonists for histamine H₂ receptors.¹¹ 1,3-Selenozoles also display anticancer,¹²⁻¹⁴ antimicrobial,¹⁵⁻¹⁹ and xanthine oxidase inhibitory activities.²⁰

Regarding the fact that biological activity is influenced by the structural and molecular properties, particularly electronic, future prospects for designing and development of new molecules with potential targeted biological activity can be based on the information obtained from experimental and theoretical data. In the present dissertation we synthesized and characterized two series of (1,3-thiazol-2-yl)- and (1,3-

selenazol-2-yl)hydrazones by Hantzsch's reaction between the corresponding thio(seleno)semicarbazone and 2-bromoacetophenone or its *p*-methyl and *p*-methoxy derivatives. Such compounds differ in each other by the nature of heteroatom of the azole ring (S or Se), by the type of the group (pyridine or *o*-/*m*-/*p*-nitrobenzyl) attached to the azometine carbon or by the nature of the phenyl substituent connected to the thio(seleno)azole ring. In addition, within the first series of investigated compounds Co(III) complexes have been synthesized, with the emphasis that the selenium ligands, as well as their complexes are synthesized for the first time. All the compounds and complexes have been characterized using elemental analysis, UV-Vis, ATR-FTIR, ¹H and ¹³C NMR spectroscopy.

As the compounds synthesized in this work belong to the class of Schiff bases, and carry imine (–C=N–) functional group it was of interest to investigate electrochemical behavior. The knowledge of the redox properties of hydrazone compounds is important for better understanding of their behavior in chemical and biological processes. Voltammetric techniques, especially cyclic voltammetry, is favourable and was successfully applied to synthesized (1,3-thiazol-2-yl)- and (1,3-selenazol-2-yl)hydrazones.

To obtain comprehensive insight about solid-state structure, stability of molecules and investigate the impact of the polarity of the medium, hydrogen bonding and electronic substituent effects on their solvatochromism, a single crystal X-ray diffraction analysis (XRD), mass spectrometry (MS) as well as spectral and computational solvatochromic study of this class of compounds has been performed for the first time. The computational studies include density functional theory (DFT) geometry optimization and time-dependent density functional theory calculations (TD-DFT) of absorption spectra, electronic transitions and evaluation of intramolecular charge transfer (ICT) in the course of transition. Contributions of appropriate substituent- and solvent-dependent electronic transitions were investigated by the use of linear solvation energy relationships (LSER). The effects of non-specific solvent effects, dipolarity and polarizability, and specific, solvent–solute hydrogen bonding interactions, were evaluated by means of the LSER principles using Kamlet-Taft²¹ and Catalán model.²²

In order to investigate the effect of the structure on the activity, a systematic testing of the antimicrobial and antioxidant activity of the synthesized compounds and complexes has been conducted. Antimicrobial activity was examined against four Gram-negative, four Gram-positive bacteria and three fungi strains. Antioxidant activity was evaluated in term of their abilities to scavenge stable free radical, two physiologically relevant reactive oxygen species (ROS) and their reducing antioxidant power for ferric and molybdenum(VI) ions. Results showed that selenium based compounds possess more potent antimicrobial activity, lower toxicity and superior free-radical scavenging activity in comparison to the sulphur analogues.

Also, the first study of anticancer property of Cobalt (III) complex of pyridine based 1,3-thiazole was conducted in this dissertation. The complex has been tested on human breast cancer MCF-7 cell line. Investigation has been performed on standard monolayer two-dimensional (2-D) cell culture model, and on three-dimensional (3-D) spheroid model. To the best of our knowledge this is the first three-drug combination study carried out on a 3-D cell culture up to date.

Finally, benzylidene based 1,3-selenazoles – II series, has been tested on a panel of six human solid tumor cell lines: A549, HBL-100, HeLa, SW1573, T-47D and WiDr, and as selective monoamine oxidases (MAO) A/B inhibitors. The results have shown that some of the synthesized compounds are very powerful candidates for further testing as potential anti-cancer drugs.

2 THEORETICAL PARTS

More than seventy percent of drugs used today are heterocyclic compounds. They are widely distributed in nature and heterocyclic compounds isolated from natural sources act as lead compounds for the development of new molecules of biological interest. In addition, most heterocyclic drugs are synthesized easily, therefore, synthesis and characterization of new molecular entities incorporating heterocyclic structures is of high significance.²³

2.1 Structure and classification of 1,3-selenazol-2-yl-hydrazones, 1,3-thiazole-2-yl-hydrazones

2.1.1 Azoles

Heterocyclic chemistry includes a large class of compounds, and *azoles* being one among them. Azoles are five-membered heterocyclic compounds containing nitrogen atom and at least one other non-carbon atom of either nitrogen, sulphur, or oxygen.²³ There are two classes of these types of compounds with the two heteroatoms: 1,2- and 1,3-azoles (Figure 2.1). These compounds have many features of heterocycles containing five atoms: furan, thiophene, pyrrole and selenazole, but, as expected, their chemical behavior is further influenced by the other heteroatom inside the ring²⁴. Considering this paper analyzes 1,3-thi-(selen)-azoles, the following text will include overview of the properties, synthesis and application of these types of compounds.

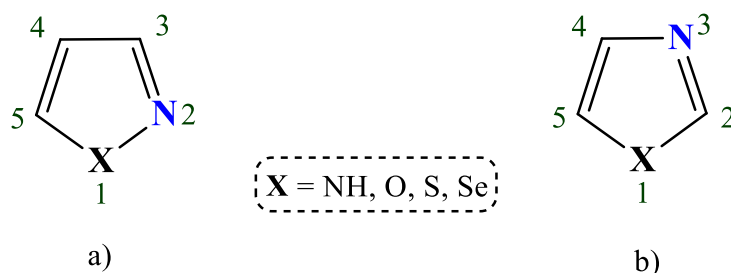


Figure 2.1 Azoles: a) 1,2-azole; b) 1,3-azole.

2.1.1.1 Properties of 1,3-azoles

Thiazole and selenazole belong to class of 1,3-azoles (Figure 2.2). The structure resembles on the 5-membered heterocycles with one hetero atom. 1,3-azoles contain a

nitrogen (position **3**) in an environment analogous to that in pyridine, that is, an imine nitrogen with a lone pair of electrons in an sp^2 orbital in the plane of the ring and not involved in the aromatic sextet (Figure 2.3).²⁵

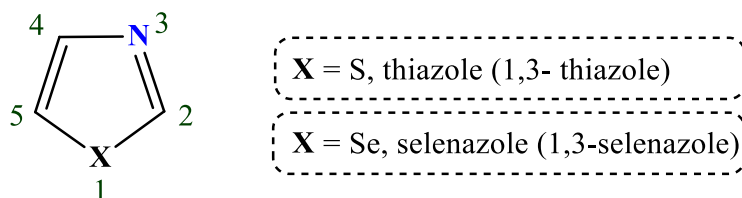


Figure 2.2 1,3-azoles: thiazole and selenazole.

A lone pair of electrons in a position **1**, (in structure of furan, pyrrole, thiophene or selenophene) is placed inside p orbital and forms an integral part of an electronic sextet ring having aromatic character. Consequently, the nitrogen in the position **3** can easily react with a proton or an electrophile (Scheme 2.1)

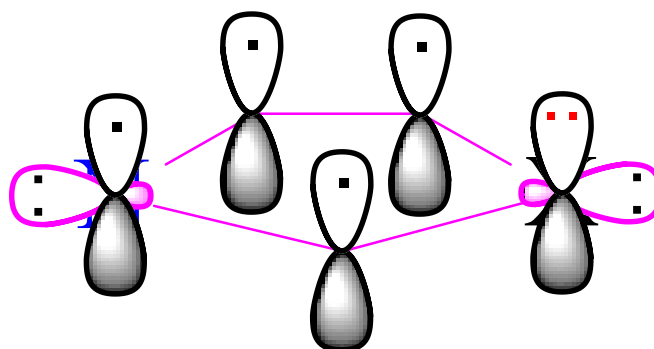
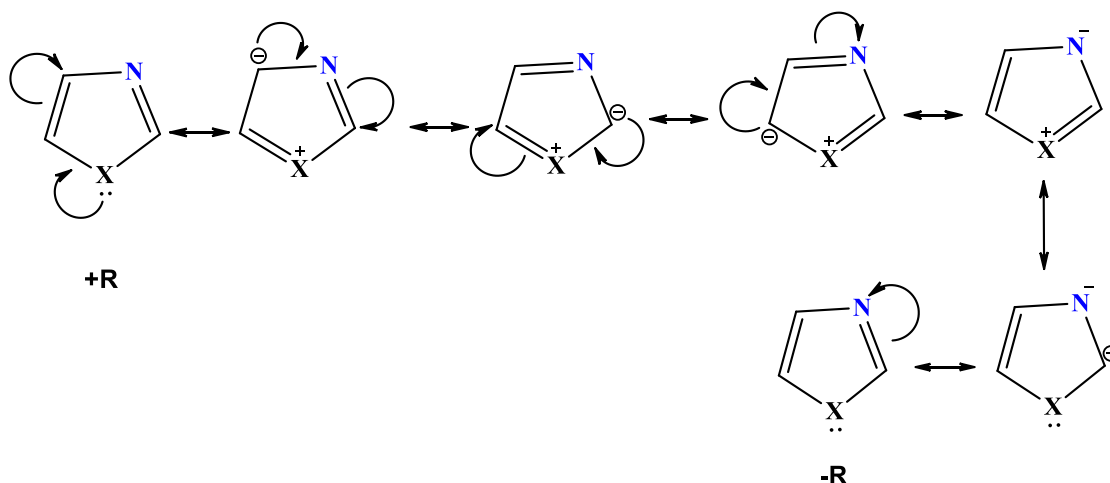


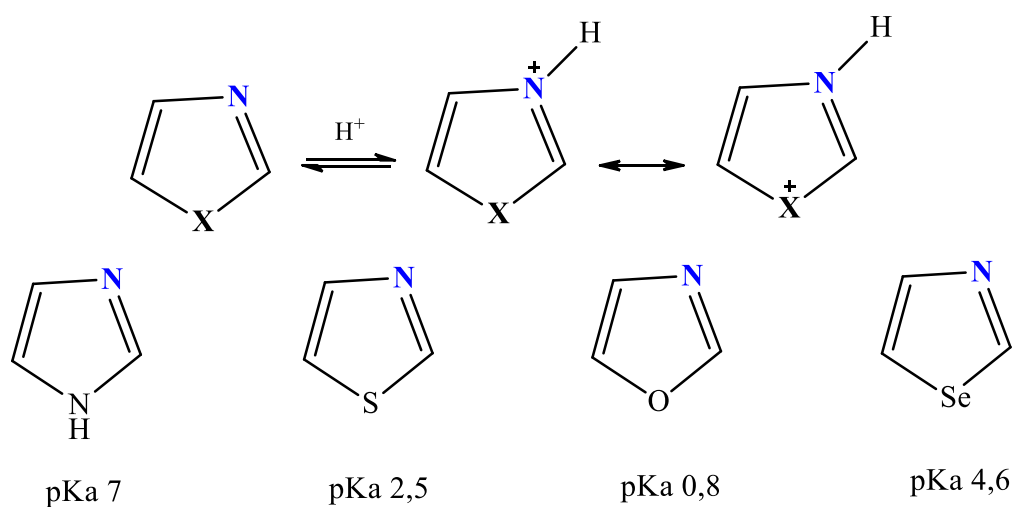
Figure 2.3 Delocalization of the 1,3-azoles ring.

This heteroatom also affects the reactivity of the ring due to resonance and inductive effects ($-R$ and $-I$) and has an important role in defining the acid-base properties of these classes of compounds. Compared with the pyrrole, an additional heteroatom causes an increase in acidity N-H bonds and the same effect has each subsequent heteroatom which replaces the C-H group. It is obvious that heteroatom contribute to a higher polarization of N-H bond and also an improved stabilization of the resulting anion²⁴.



Scheme 2.1 Delocalization electrons in the 1,3-azoles ring.

The base properties of a 1,3-azoles are derived from a nitrogen in the position **3**. A cation formed by protonation is stabilized with delocalized electrons of heteroatom in the position **1**. The heteroatom substantially influences the basic properties of the final compound (Scheme 2.2).

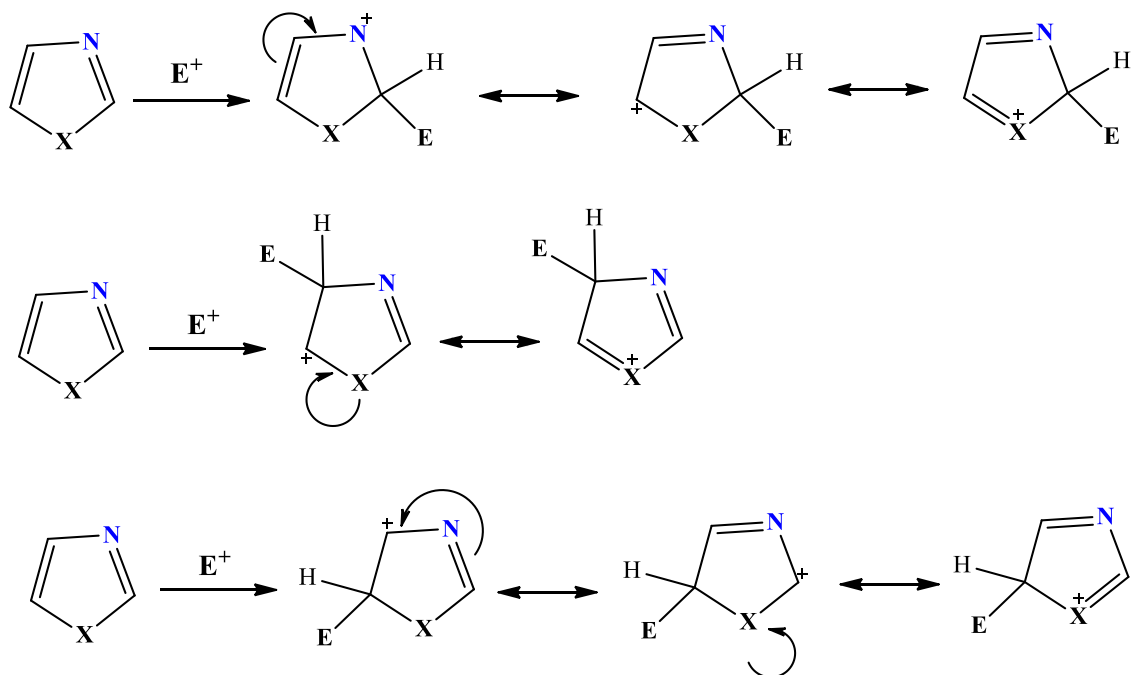


Scheme 2.2 Acidity constant: imadizole, thiazole, oxazole, and selenazole.

2.1.1.2 Reactivity of 1,3-azoles

Electrophilic aromatic substitution

1,3-Azoles are generally less reactive in the electrophilic aromatic substitution reactions than corresponding analogs with a single heteroatom. The contribution of an additional *N*-atom (**-R**, **-I** effect) makes the ring an electron-deficient and therefore less reactive. The process of electrophilic substitution of these compounds can be explained by considering the stability of the intermediate σ -complex (Scheme 2.3)

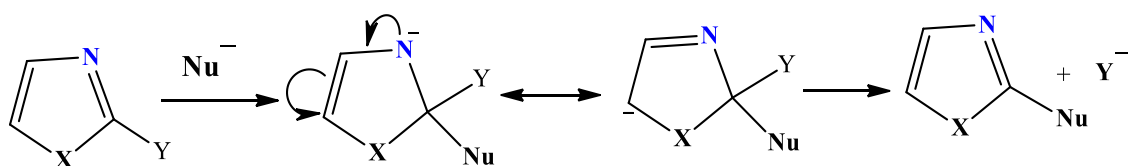


Scheme 2.3 Electrophilic aromatic substitution.

The most reactive position in a 1,3-azoles is C-5, because an intermediate that leads to final product of substitution is stabilized by resonant structures in which the positive charge is not located on the nitrogen atom in the 3-position.

Nucleophilic aromatic substitution

The nucleophilic substitutions of H atoms in 1,3-azoles are not characteristic reactions for this class of compounds. If they occur, the substitution takes place at the C-2 atom. On the other hand, the halogen derivatives of 1,3-azoles, and in particular 2-halo-1,3-azoles, participate in this type of reactions. Increased reactivity of 2-halo azoles is a consequence of the N-3 atom. Nitrogen of the pyridine type contributes to the higher electron-deficiency of the C-2 carbon and better stability of the intermediate (Scheme 2.4). Of particular importance is the structure in which the N-3 is the carrier of the negative charge.



Scheme 2.4 Nucleophilic aromatic substitution of 2-haloazoles.

2.1.2 1,3-Thiazoles

2.1.2.1 Properties and applications

Thiazoles and their derivatives have been known since the 19th century. Wallach presented synthesis of some thiazoles in the 1870. One of the first synthesized thiazole is 5-aminothiazole-2-formamide²⁶. Detailed studies of thiazole and its derivatives were initiated by Hantzsch's group in the 1887. So far, many studies in chemistry of thiazoles have been conducted: investigation of physical properties, synthetic methods, reaction mechanisms and industrial applications. 1,3-Thiazole (Scheme 2.2) is an aromatic compound, with weak basic properties ($pK_a = 2.5$). N-3 atom is the carrier of basic features, but presents of substituents can significantly affect those features. Electron-acceptor group on the ring contribute to the reduction of basic properties of thiazole derivatives, while the electron-donor substituents have the opposite effect. Aromatic character of thiazoles is attributed to delocalisation of one pair of electrons on the sulfur atom, thereby completing the required 6π electrons, in accordance with Huckel's rule.

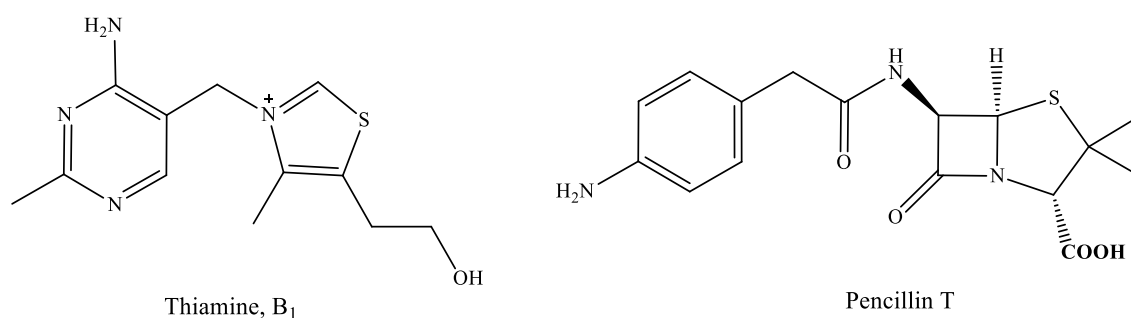
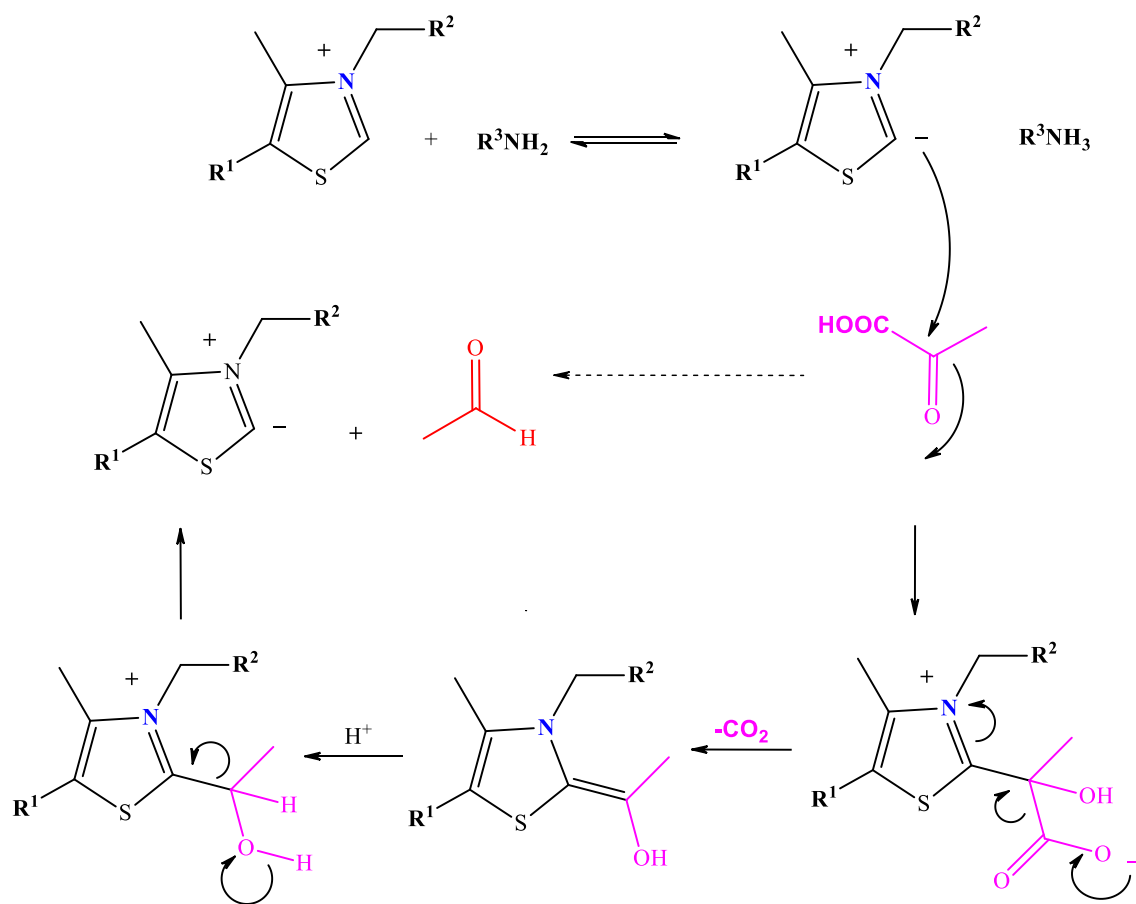


Figure 2.4 Thiazole ring in the structures of various natural products.

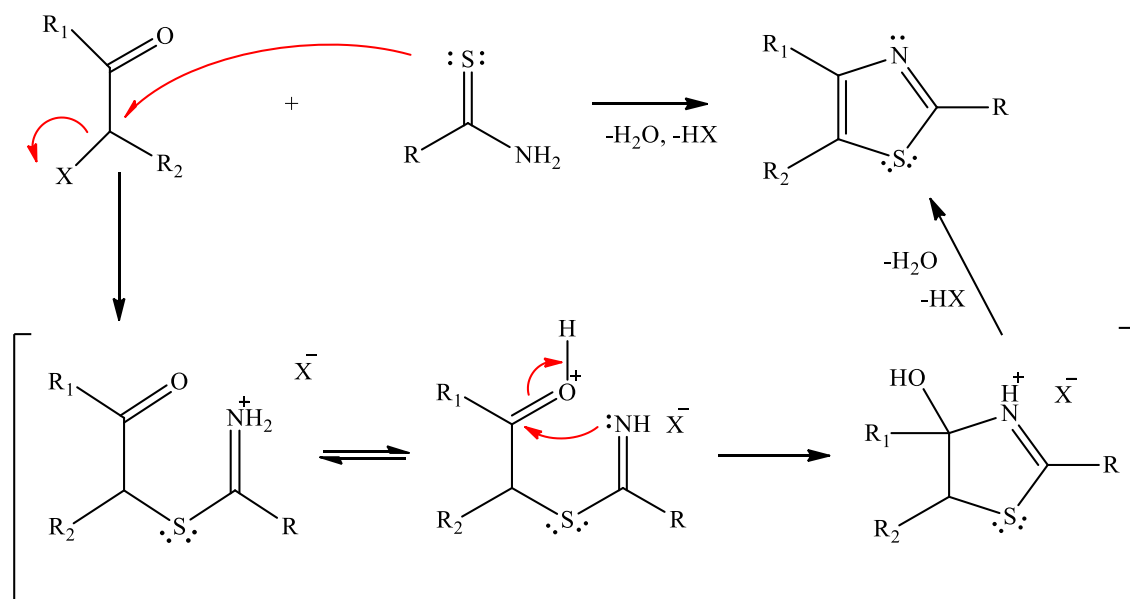
Thiazole ring is the structural component of various natural products (Figure 2.4), including vitamin B1 (thiamine). In a reduced form, this ring became part of penicillin derivatives. Vitamin B1 in the phosphorylated form is a coenzyme of the pyruvate decarboxylase, an enzyme which catalyses the decarboxylation of pyruvic acid to acetaldehyde²⁷. That biochemical process is based on the properties of C2-H bond of thiazolium compounds. Interruption of the bond causes formation of an anion, which as nucleophile participates in the decarboxylation of pyruvic acid (Scheme 2.5).



Scheme 2.5 Decarboxylation of pyruvic acid.

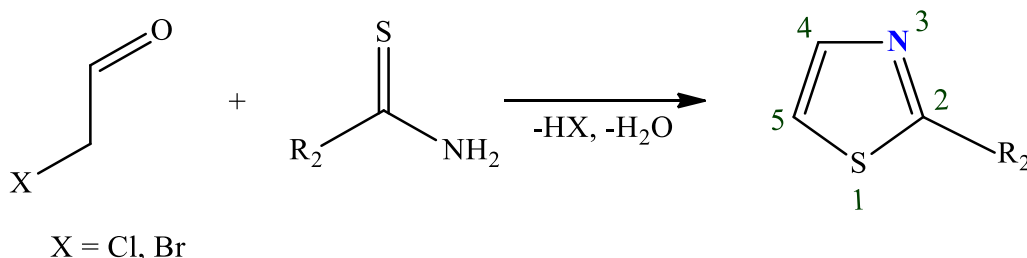
2.1.2.2 Synthesis 1,3-thiazoles

Classical methods for the synthesis of thiazoles is the Hantzsch's reaction in which the α -halocarbonyl compound (or the corresponding α -haloacetate compound) are condensed with a primary thioamides (thiourea in order to obtain the corresponding 2-amino thiazole derivatives)²⁸. The reaction is initiated by nucleophilic attack of the sulfur atom to a carbon atom which is bonded to a halogen. Acyclic intermediate (isolated only in a few cases) α -S-alkyliminium salt, upon proton transfer, starts acid catalyzed cyclization reaction with elimination of water molecules (Scheme 2.6).



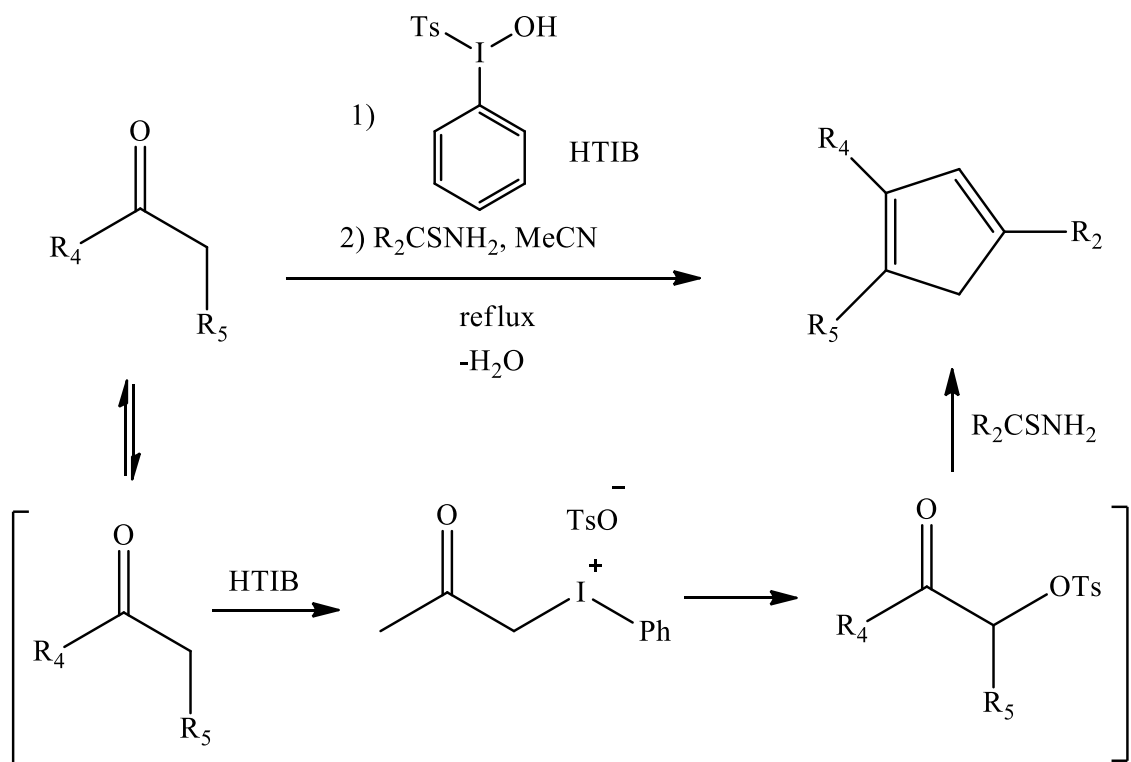
Scheme 2.6 The mechanism of Hantzsch's reaction.

This reaction is typically carried out without obstructions and the yields, in a case of simple thiazoles are satisfying. The selection of the substituted α -halocarbonyl compounds determines the substituents in the positions **4** and **5**. Consequently, the choice of a substituted thioamide (thioamino) determines the substituents in the **2**-position (Scheme 2.7).

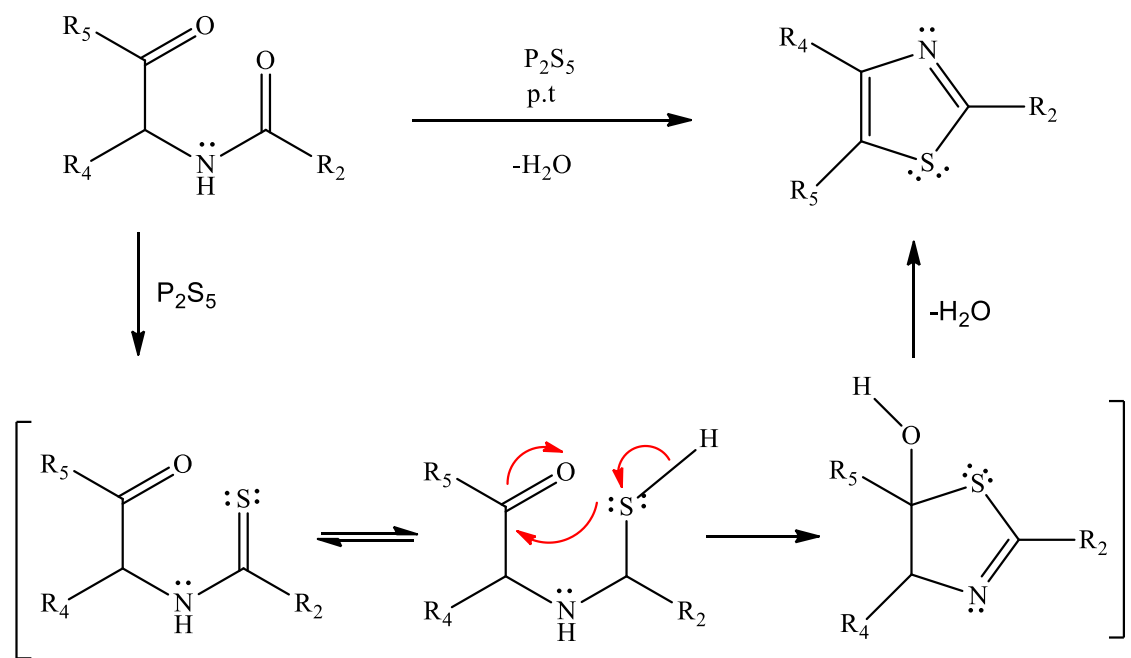


Scheme 2.7 Simplified mechanism of Hantzsch's reaction.

Modification of Hantzsch reaction conditions consistimplies the use of tosyl ketones instead of α -halocarbonyl compound²⁸. The advantage of this modified reaction is the avoidance of toxic and lachrymatory α -halocarbonyl compounds. The method involves the reaction of a ketone with hypervalent iodine reagent HTIB hydroxy (tosyloxy) iodo benzene, which gives the α -tosyl ketones from the intermediate structure of the α - λ^3 iodonil-ketone (Scheme 2.8).



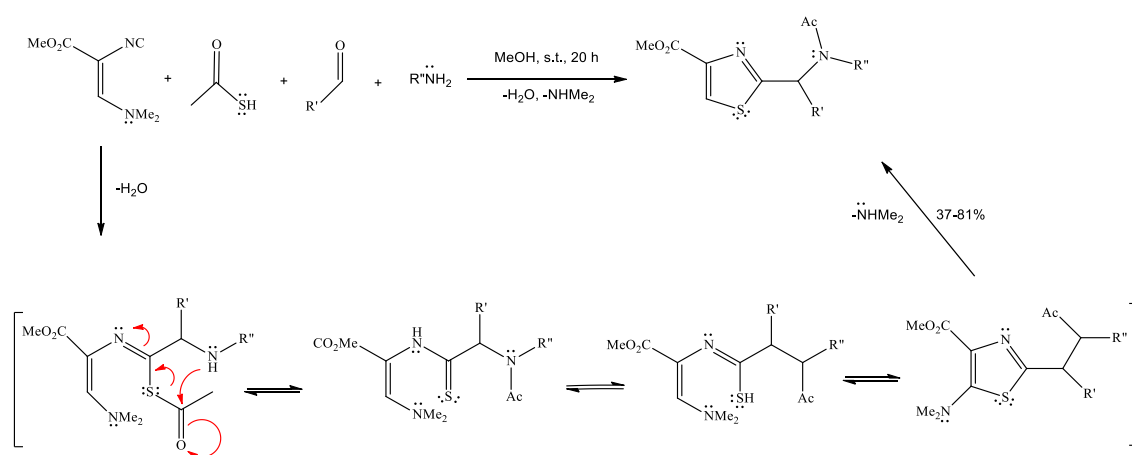
Scheme 2.8 Modified Hantzsch's reaction with α -tosyl ketones instead of halocarbonyl compound.



Scheme 2.9 Gabriel's synthesis.

It is important to mention that α - λ^3 iodonil-ketones, obtained *in situ*, can also be subjected to a cyclization reaction with thioamides, thereby avoiding the isolation of α -tosyl ketone²⁹. Another important method of isolating thiazole comprises treating of α -acylamino ketone with phosphorus pentasulfide as a Lewisson reagent (Gabriel's synthesis, Scheme 2.9).

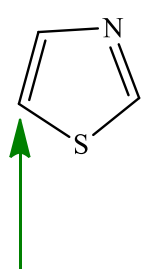
There is also the synthesis of the 2,4-substituted thiazole, which combines isocyanide with other three components, so-called four component synthesis (Scheme 2.10). Substituent at the C-4 atom is the carbomethoxy group³⁰.



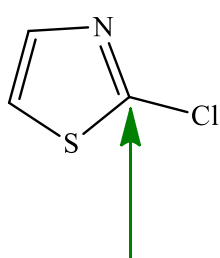
Scheme 2.10 Four component synthesis of 1,3-thiazoles.

2.1.2.3 Reactivity of 1,3-thiazoles

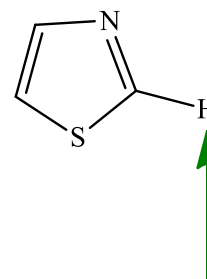
The thiazole is not particularly reactive in electrophilic aromatic substitution reactions, except in cases where the ring is activated by electron-donor substituents. As expected, in the reactions of sulfonylation and nitration the major products are the results of the substitution at C-5 atom, but in those reactions often appears C-4-substituted product (Figure 2.5). In the strong acid conditions thiazolium cation participate in the reaction. The C-2 position in the nucleophilic substitution reactions is more reactive than the positions C-4 and C-5. Reactivity further increases when thiazolium salt participates in the substitution reaction, or in the presence of electron-acceptor substituents, which cause the ring to be electron-deficient (Figure 2.5).



Electrophilic substitution



Nucleophilic substitution



Reacts with strong bases

Figure 2.5 Reactivity of thiazole ring.

2.1.3 1,3-selenazoles

2.1.3.1 Properties and applications

The first selenazoles were described in 1889, when Hantzsch's student, Hoffman performed the condensation of selenourea with chloroacetone and obtained 2-amino-4-methyl-1,3-selenazole (Figure 2.6). Selenazoles are extensively studied and they shown to have a biological activity. 1,3-Selenoazoles are pharmacologically important because of their antibacterial and anticancer activity, and 2-amino-1,3-selenazole proved to be an excellent scavenger of superoxide anion³¹.

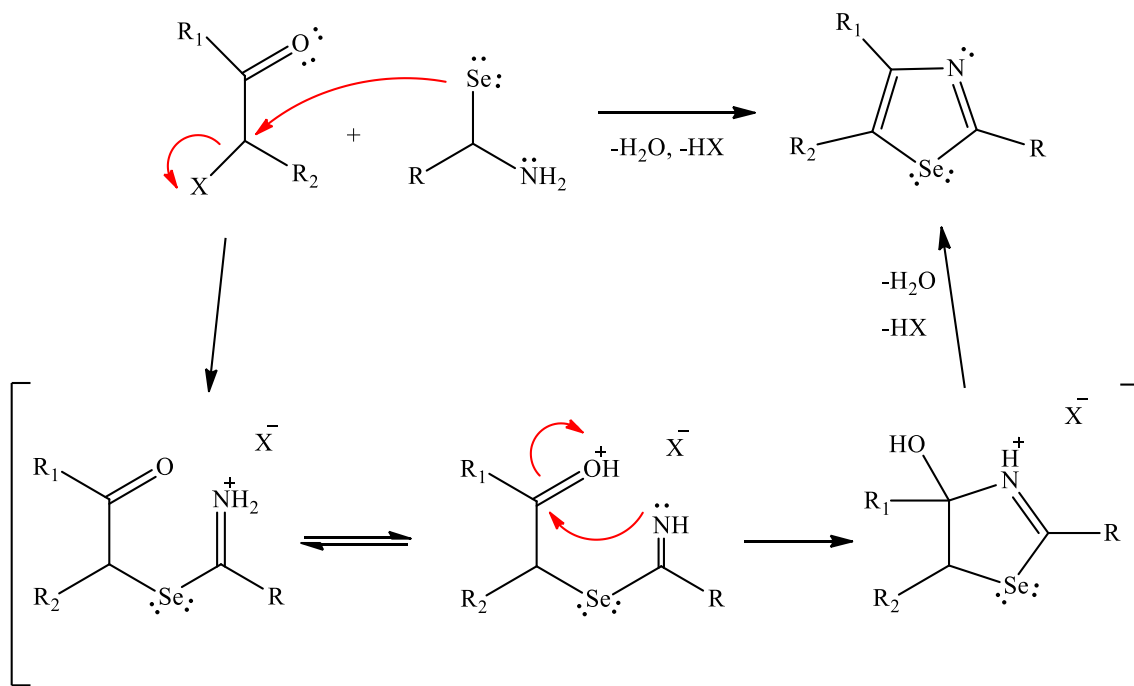


Figure 2.6 2-amino-4-methyl-1,3-selenazole.

2.1.3.2 Synthesis of 1,3-selenazoles

The selenazoles are formed by cyclization of the primary selenoamides with α -halocarbonyl compounds. This procedure provides possibiliti to produce a wide range of selenazoles by using appropriate reactants (Scheme 2.11). The choice of the substituted selen-carboxyl amides determines positions **2** and **3** in the ring, while the choice of α -halocarbonyl component in the same way determines the substituent at the positions **4** and **5** (Figure 2.2). Attempts to obtain unsubstituted selenazole by reduction of the 2-aminoselenoazole have proved to be unsuccessful. In contrast, unsubstituted selenazole is successfully obtained by condensation of α -selenoformamides with chloroacetone and

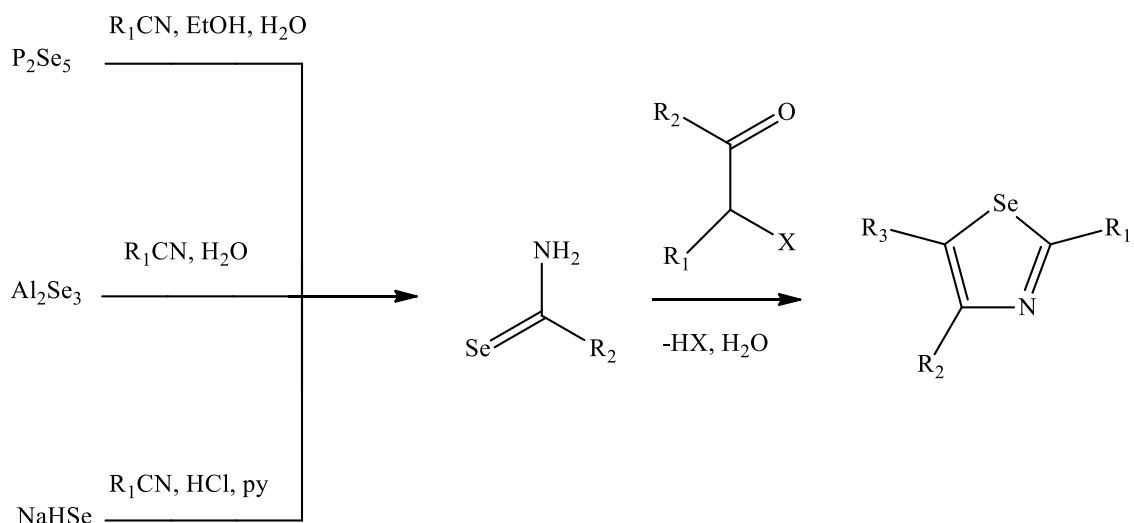
resulting yield was 34%. Structure of unsubstituted selenazoles was confirmed by mass spectrometry. Unsubstituted selenazol decomposes under light and during the degradation releases selenium. Alkyl and aryl components lead to stabilization of selenazole ring.³²



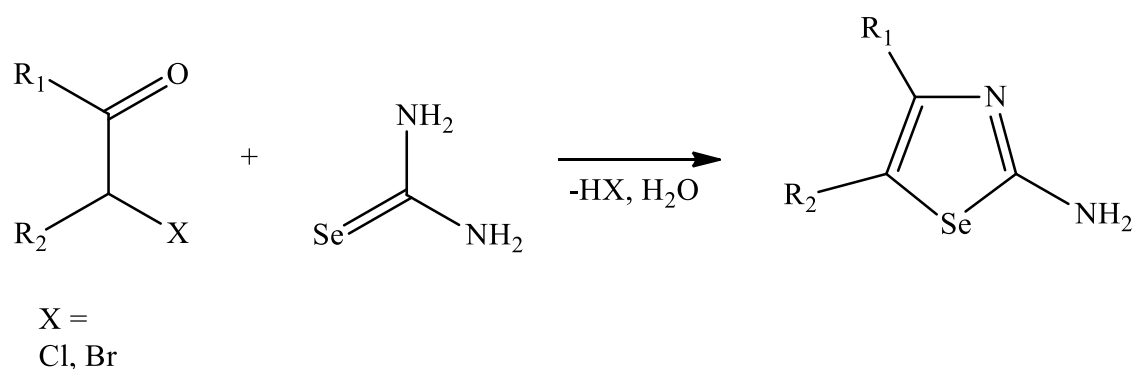
Scheme 2.11 Mechanism of Hantzsch's reaction for synthesis of 1,3-selenazoles.

One of the synthetic routes of primary selenoamides is introduction of selenium using a hydrogen source which is derived from selenide and reacts with nitrile. Accordingly, selenoamides can be prepared by reaction of nitrile and aluminum selenide³³. Convenient procedure is also the reaction mixture of P₂Se₅ and a nitrile in the presence of ethanol and water. Formamide can be converted into selenoformamide with P₂Se₅³⁴. Also, the mixture of the nitrile and pyridine reacts with sodium hydrogen selenide in the presence of hydrochloric acid to obtain alkyl and aryl selenoamides³⁵ (Scheme 2.12).

Utilization of selenourea in Hantzsch's reaction provides as a product 2-amino selenazoles (Scheme 2.13). Analogously, the cyclocondensation of selenourea with ketone and iodine gives selenazole³⁶

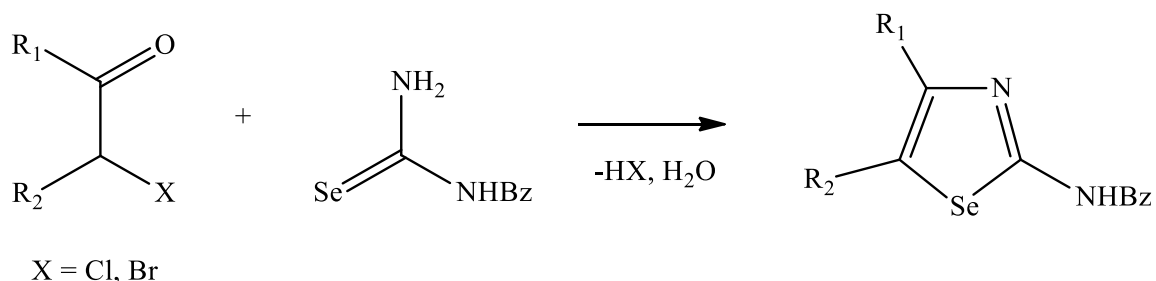


Scheme 2.12 Synthesis and Cyclocondensation of Selenocarboxamides.



Scheme 2.13 Synthesis of 2-amino selenazole.

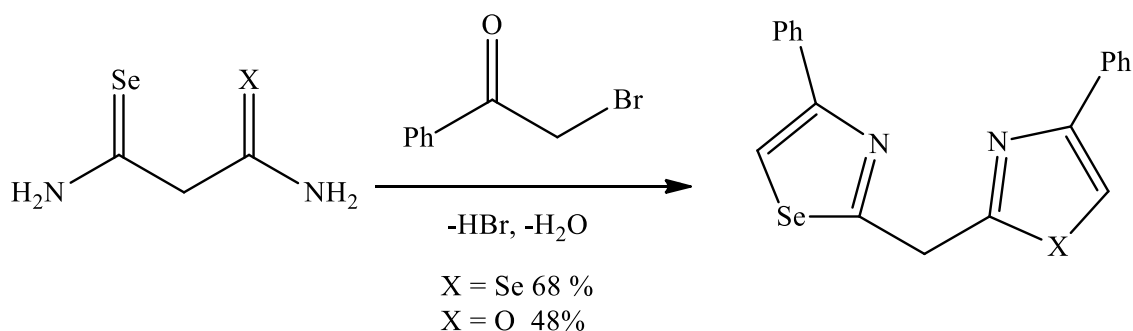
The reaction of N-benzoylselenourea and α -halocarbonyl compounds results in 2-substituted benzylamino selenazoles (Scheme 2.14)³⁷



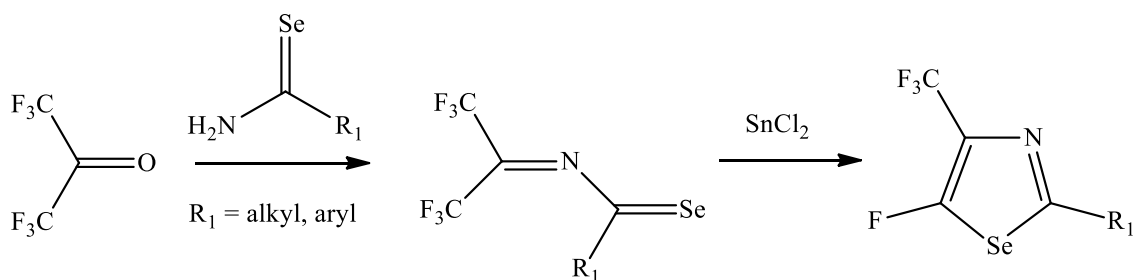
Scheme 2.14 Synthesis of substituted 2-benzylamino selenazoles.

This procedure can be used in order to obtain other acyl (aryl) – selenourea products. Hydrolysis of the substituted 2-benzoylamido selenazoles in the presence of sulfuric or phosphoric acid produces 2-amino selenazole, which are identical to those

obtained by direct synthesis from selenourea. The reaction diselenomalonamide and monoselenomalonamide with phenylacetyl bromide produces bis(4-phenyl selenazole-2-yl)methane (Scheme 2.15). The starting reactant is obtained by reaction of cyanoacetamide or malonodinitrile with hydrogen selenide.^{32,37} 5-Fluoro-4-(trifluoromethyl) selenazole is obtained by reacting hexafluoroacetone with primary selenoamides³⁸ (Scheme 2.16).

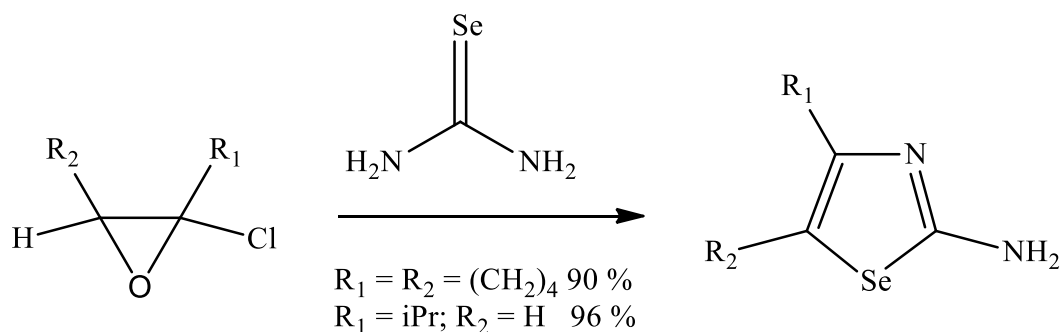


Scheme 2.15 Synthesis of bis(4-phenyl selenazole-2-yl)methane.



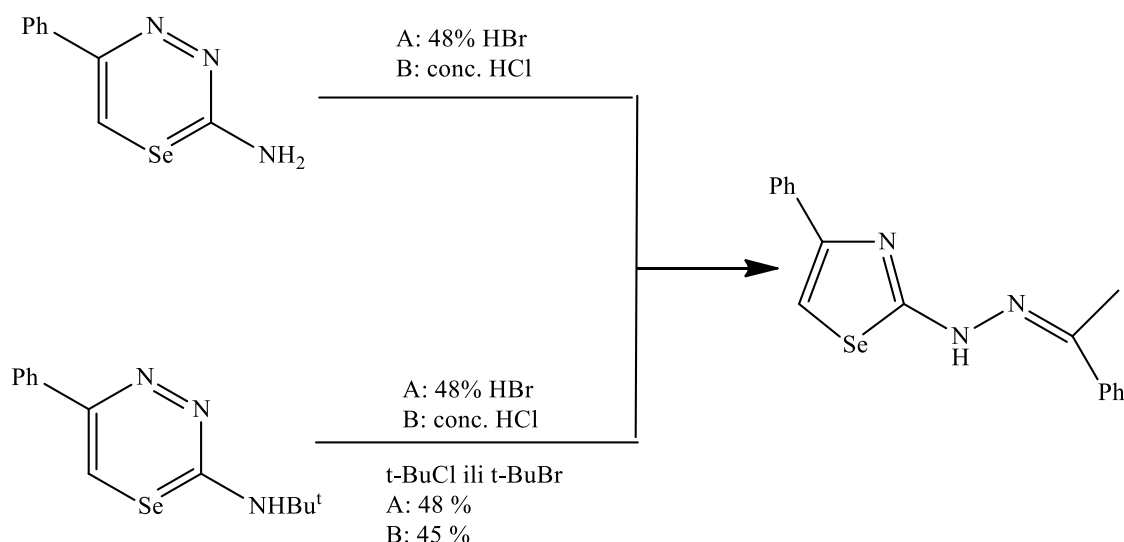
Scheme 2.16 Synthesis of 5-Fluoro-4-(trifluoromethyl) selenazole.

2-Chloro-oxacyclopropanes are isomers with α -halocarbonyl compounds in which both of the carbon atoms in positions **2** and **3** are in the same oxidation state. 2-Chloro-oxacyclopropanes react with selenoamides and selenourea to form 2-aminoselenozoles in the mild conditions, with satisfactory yields (Scheme 2.17)³⁹.



Scheme 2.17 Synthesis of 1,3-selenazole from 2-chloro-oxacyclopropane and selenourea.

Heating of 2-Amino-5-phenyl-1,3,4-(seleno)diazine in the presence of concentrated hydrochloric or hydrobromic acid causes changes in the structure presented in Scheme 2.18. The changes are reflected in disintegration of (seleno)diazine ring followed by cyclization to form a acetophenone-(4-phenyl selenazole-2-yl)hydrazone⁴⁰.



Scheme 2.18 Transformation of 2-amino-5-phenyl-1,3,4-(seleno)diazine to acetophenone-(4-phenyl selenazole-2-yl)hydrazone.

2.1.3.3 Reactivity of 1,3-selenazole

In a comparison of the chemical properties of thiazoles and the selenazoles it can be concluded that they are mutually very similar⁴¹, and small differences exist between the reactivity of thiazoles and the corresponding selenazoles. Nevertheless the 2-position of selenazoles appears to be somewhat less reactive than the 2-position of thiazoles toward nucleophilic reagents.⁴²

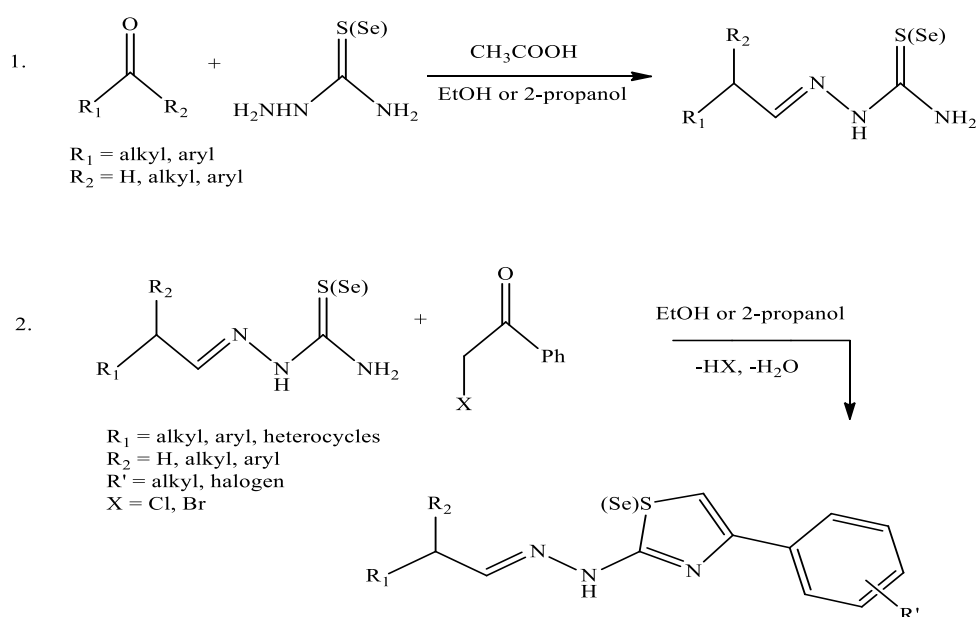
2.1.4 (1,3-thiazol-2-yl)hydrazones and (1,3-selenazol-2-yl)hydrazones

Hydrazones are important compounds because of their wide range of biological and pharmacological activities, primarily antitubercular, analgesic, anticancer, antibacterial, antifungal and antiinflammatory effects, they represent the goal of numerous research in medical chemistry.⁴³⁻⁴⁸ Similarly, thiazoles possess activities and they showed antituberculosic, antifungal, antibacterial, antiparasitic, antioxidant and

anticancer activities⁴⁹⁻⁵³, and potent inhibitory activities against human monoamine oxidase B and histone acetyltransferase⁵⁴⁻⁵⁶. Potential possibility of utilization hydrazone-thiazole derivatives in order to improve therapeutic results attracts the attention in the scientific community during the last decade. Similar studies were carried out with selenazoles-hydrazone derivatives.⁵⁷⁻⁵⁹

2.1.4.1 Synthesis of (1,3-thiazol-2-yl)hydrazones and (1,3-selenazol-2-yl)hydrazones

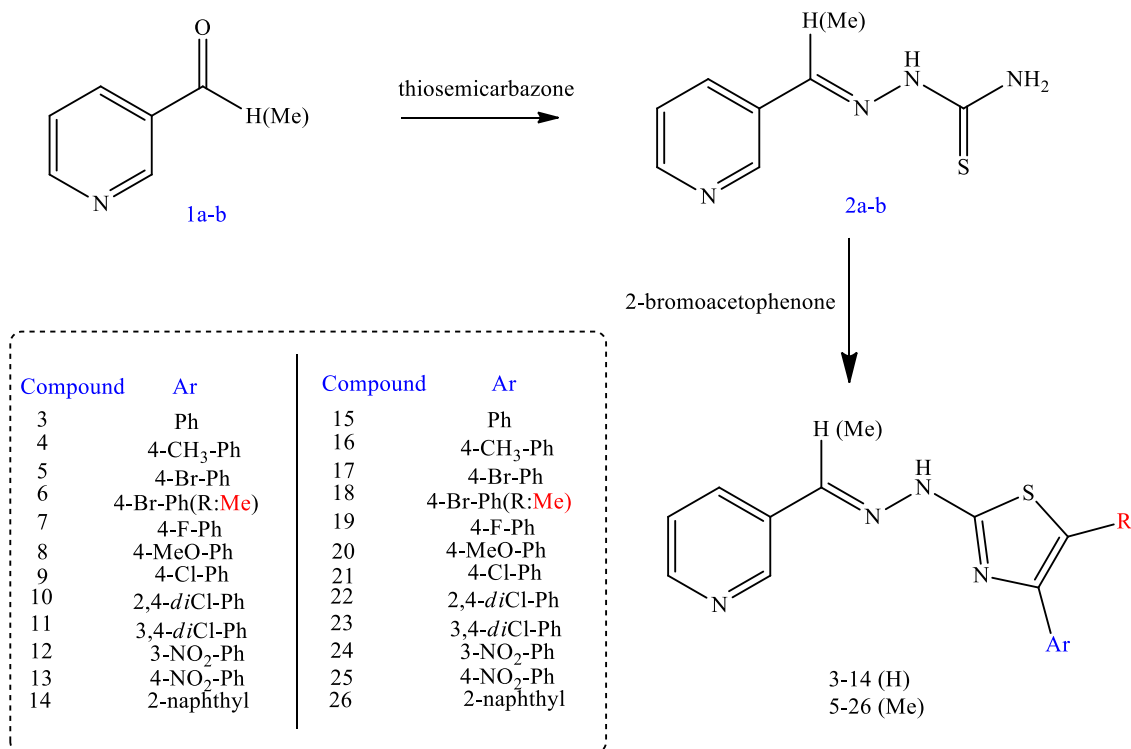
Different carbonyl compounds can react directly with thio(seleno)semicarbazides along with a catalytic amount of acetic acid in ethanol or 2-propanol in order to yield the corresponding thio(seleno)semicarbazone, which further react with correspond α -haloacetophenone to obtain *N*-(4-aryl-thiazole (selenazole)-2-yl) hydrazone product (Hantzsch's reaction, Scheme 2.19)⁶⁰.



Scheme 2.19 *N*-(4-aryl-thiazole (selenazole)-2-yl) hydrazone.

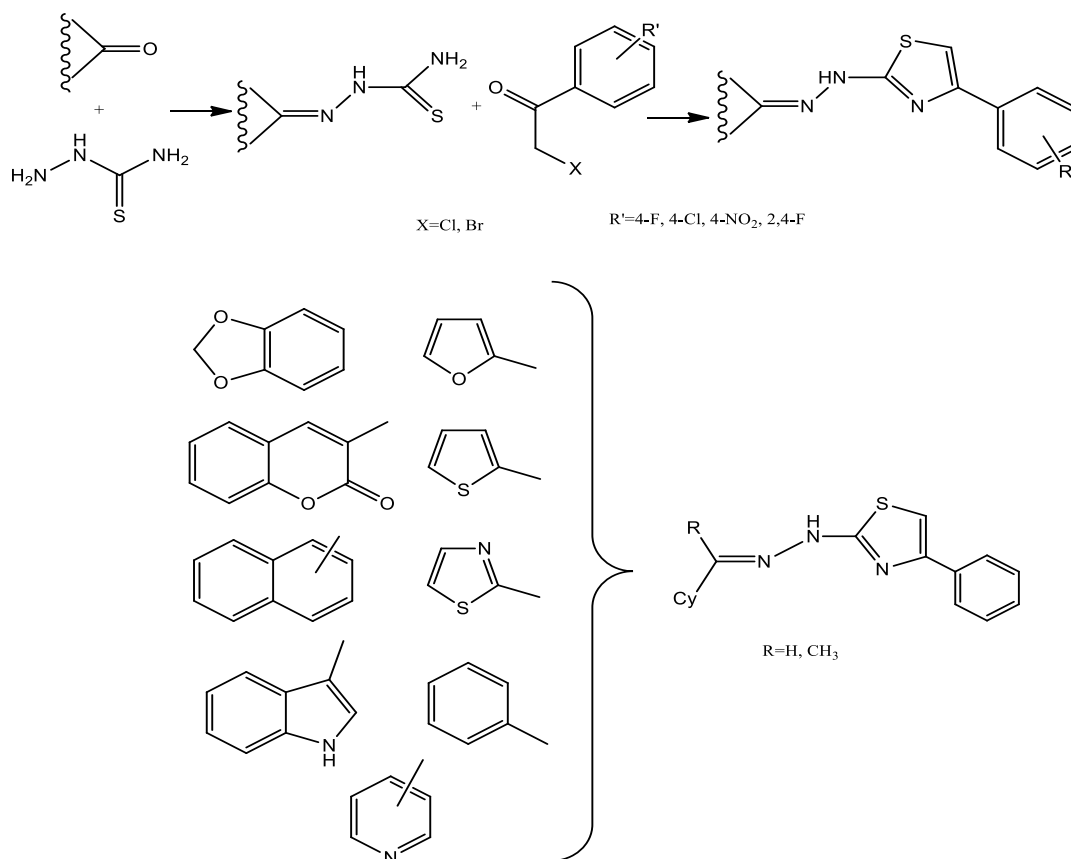
Cardoso et al.⁵² have synthesized a series of 2-(pyridin-2-yl)-1,3-thiazole derivatives, starting from pyridine-2-carboxaldehyde thiosemicarbazone. The reaction is carried out by Hantzsch's mechanism, wherein pyridine-2-carboxaldehyde thiosemicarbazone reacted with a 2-bromoacetophenone in an equimolar ratio with the addition of CaCO_3 . The condensation of thiazole ring takes place, and HBr formed in

this reaction is neutralized with CaCO₃. The reaction is performed in 2-propanol at room temperature in an ultrasonic bath (Scheme 2.20).



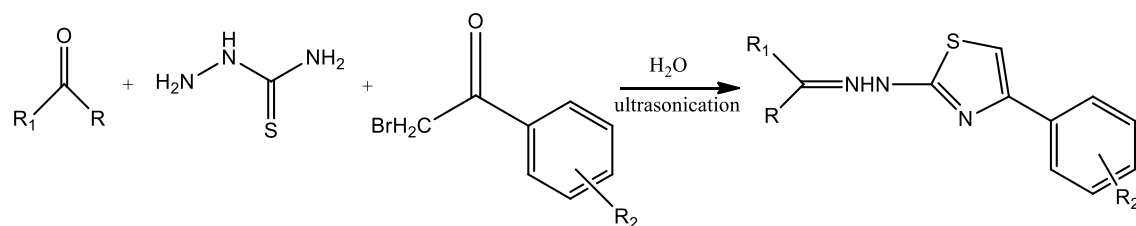
Scheme 2.20 Synthesis of 2-(pyridin-2-yl)-1,3-thiazole.

All compounds were characterized by IR spectroscopy, ¹H NMR and ¹³C NMR spectroscopy, elemental analysis and mass spectrometry, and were in accordance with the proposed structures. The group of Italian and Spanish scientists synthesized a series of (hetero)arylidine-(4-substituents-thiazol-2-yl) hydrazone⁶¹. The carbonyl compounds are converted into a thiosemicarbazone through reaction with thiosemicarbazide in ethanol or 2-propanol, with the addition of a catalytic amount of acetic acid. After recrystallization of hydrazones obtained by Hantzsch's reaction further reacted with the appropriate α -haloacetophenone, resulting in new series of *N*-(4-aryl-thiazole-2-yl) hydrazone. The final products were purified by column chromatography (Scheme 2.21).



Scheme 2.21 Synthesis of *N*-(4-aryl-thiazole-2-yl) hydrazine.

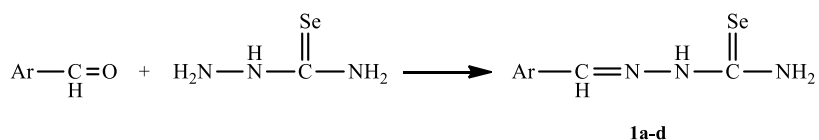
The study of organic reactions in aqueous medium is of great importance for environmental protection and for better understanding of the biochemical processes. Aqueous medium offers many practical and economic advantages as a solvent in the reaction, including low cost, safety and environmental compatibility. Dong-Nun Zhang⁶² was carried out the synthesis of *N*-(4-aryl-thiazole-2-yl) hydrazone by using three-component synthesis. The reaction was performed in an ultrasonic bath at room temperature (Scheme 2.22). The syntheses were also carried out at an raised temperature, but the yields under those conditions were proven to be substantially lower. The use of organic solvents such as ethanol, 2-propanol, acetonitrile and dichloromethane gave lower yields, compared with reaction conducted in an aqueous medium. Nuan-Dong Zhang and colleagues came to the conclusion that the ultrasonic waves can accelerate the reaction. This process avoids the use of organic solvents and catalysts. The method offers several advantages, including better yields, simple experimental procedure, cleaner products and low cost, making it useful and attractive strategy, taking into consideration the economic and environmental benefits.



No.	R/R ₁	R ₂
1:	C ₆ H ₅ /H	H
2:	4-CH ₃ COC ₆ H ₅ /H	H
3:	2-OHC ₆ H ₅ /H	H
4:	2-ClC ₆ H ₅ /H	H
5:	3-ClC ₆ H ₅ /H	H
6:	4-ClC ₆ H ₅ /H	H
7:	2OH, 4-CH ₃ COC ₆ H ₅ /H	H
8:	4-N(CH ₃) ₂ C ₆ H ₅ /H	H
9:	(CH ₂) ₄	H
10:	(CH ₂) ₅	H
11:	2-CH ₃ C ₆ H ₅ /H	4-Cl
12:	(CH ₂) ₅	4-CH ₃

Scheme 2.22 Synthesis of *N*-(4-aryl-thiazole-2-yl) hydrazone by using three-component in aqueous medium

Valentin Zaharia and colleagues⁶³ synthesized a series of new 1,3-selenazoles by Hantzsch's reaction mechanism, and also determined tests in vitro cytotoxicity of two cancer cell lines for those compounds. Synthesized selenosemicarbazones obtained from 2-hydrazinyl-1,3-selenazole derivatives were characterized by IR, NMR, mass spectrometry and elemental analysis. Some of the synthesized compounds showed a significant cytotoxic activity. In the reaction between selenosemicarbazides or benzoyl selenocarbazones with α -halocarbonyl compounds 1,3-selenazoles were obtained (Scheme 2.23 and Scheme 2.24).

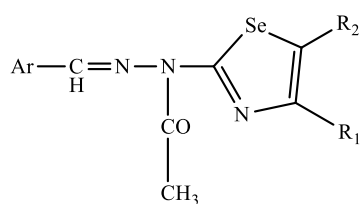
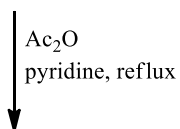
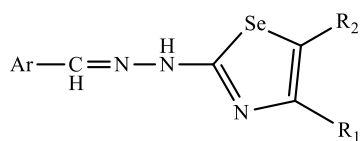
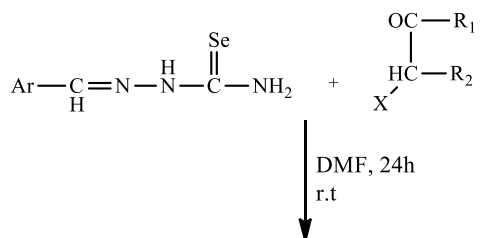
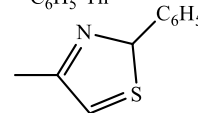


1a Ar
C₆H₅-

1b *p*-Cl-C₆H₅-

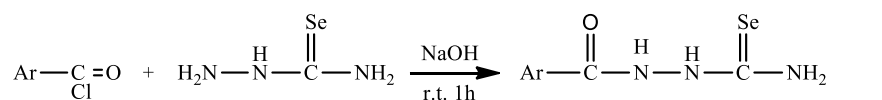
1c *p*-CH₃O-C₆H₄-

1d C₆H₅-Th



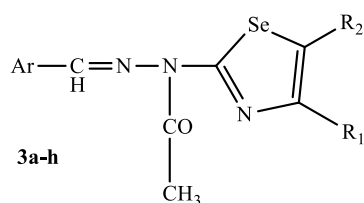
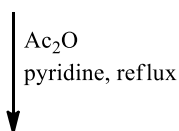
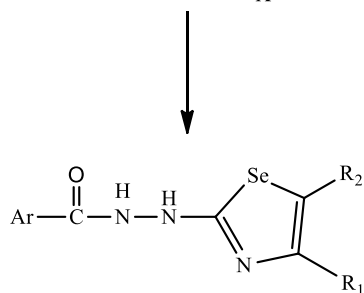
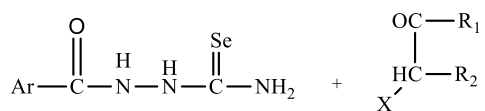
	2a, 3a	2b, 3b	2c, 3c	2d, 3d	2e,3e	2f,3f	2g,3g	2h,3h
Ar	C ₆ H ₅ Cl(<i>p</i>)-	C ₆ H ₄ O CH ₃ (<i>p</i>)-	C ₆ H ₄ O CH ₃ (<i>p</i>)-	C ₆ H ₅ -Th	C ₆ H ₅ -Th			
R₁	CH ₃	CH ₂ Cl	C ₆ H ₅	CH ₃	CH ₃	C ₆ H ₅	CH ₂ Cl	CH ₃
R₂	H	H	H	COOC ₂ H ₅	H	H	H	COCH ₃

Scheme 2.23 Synthesis of 2-hydrazinyl-1,3-selenazoles.



4a-b

Ar
4a C₆H₅-
4b *p*-Cl-C₆H₅-

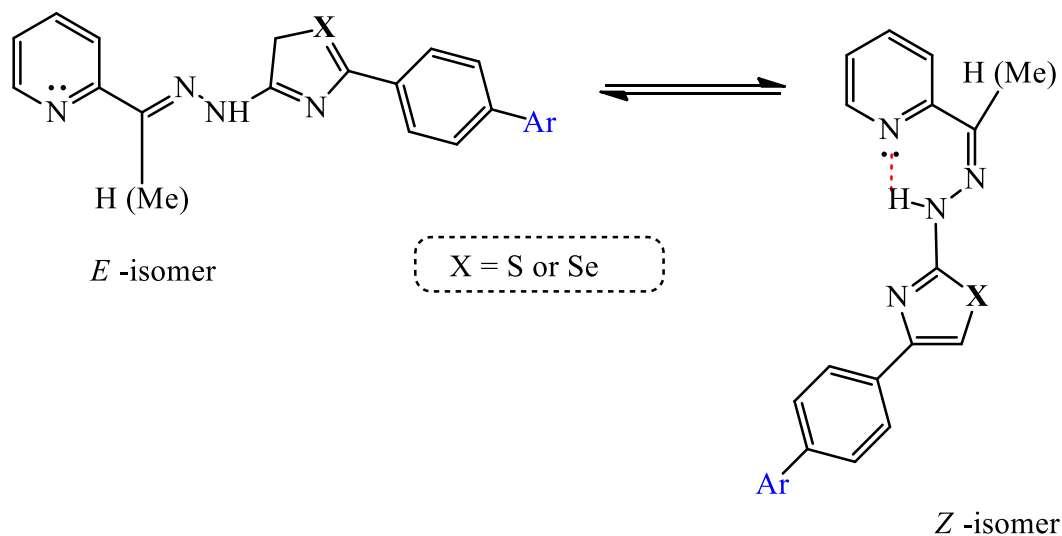


	2a, 3a	2b, 3b	2c, 3c	2d, 3d	2e,3e	2f,3f	2g,3g	2h,3h
Ar	C ₆ H ₅ Cl(<i>p</i>)-	C ₆ H ₄ O CH ₃ (<i>p</i>)-	C ₆ H ₄ O CH ₃ (<i>p</i>)-	C ₆ H ₅ -Th	C ₆ H ₅ -Th			
R ₁	CH ₃	CH ₂ Cl	C ₆ H ₅	CH ₃	CH ₃	C ₆ H ₅	CH ₂ Cl	CH ₃
R ₂	H	H	H	COOC ₂ H ₅	H	H	H	COCH ₃

Scheme 2.24 Synthesis of 2-hydrazinyl-1,3-selenazoles.

2.1.4.2 Isomerisation of (1,3-thiazol-2-yl)hydrazones and (1,3-selenazol-2-yl)hydrazones

Theoretically, all of the compounds may exist in two geometric isomeric forms, *E* and *Z*, and these isomeric forms refer to the imine moiety (C = N) (Scheme 2.25). The results of an experimental study of the existence of intramolecular bonds indicate that the molecules of this type of compound are stabilized in the *Z*-form, due to the formation of an intramolecular hydrogen bond of the type NH---N.



Scheme 2.25 *E* i *Z* isomers of 2-(pyridin-2-yl)-1,3-thiazole.

RSA is a very useful method for testing the condition of the tautomeric equilibrium, as it allows obtaining detailed information on molecular conformations, bond lengths and angles, as well as on intermolecular interactions in solid state. After performing X-ray structural analysis for 2-(2-(Pyridin-2-ylmethylene) hydrazinyl) -4-phenyl-1,3-thiazole, results confirmed that the compound occupies *Z* configuration (Figure 2.7). Namely, formation of intramolecular hydrogen bond between N–NH hydrogen atom and pyridine nitrogen atom in *Z*-isomeric form of pyridine based hydrazones causes significant downfield shift (~ 2–3 ppm) of N–NH hydrogen atom signal in $^1\text{H-NMR}$ spectrum.⁴²

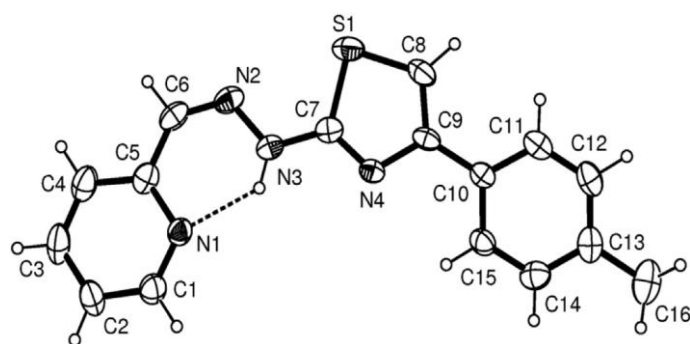


Figure 2.7 ORTEP presentation of 2-(2-(Pyridin-2-ylmethylene) hydrazinyl) -4-phenyl-1,3-thiazole.

2.2 Linear solvation energy relationship (LSER)

2.2.1 Solvatochromism of organic molecules

The position, intensity and shape of the absorption bands in the UV/Vis spectra is influenced by the choice of solvents, the chemical reaction rate and the position of the chemical equilibrium.⁶⁴⁻⁷¹ The influence of solvents on the UV/Vis spectrum, due to the movement and change in the intensity of the absorption band is called solvatochromism. These changes are the result of intermolecular interactions between the solvent and the solution (ion-dipole, dipole-dipole, dipole-induced dipole, hydrogen bonds, etc.). Solvatochromic effects can be *hypsochromic*, blue shift, which means a shift of the absorption maximum to lower wavelengths with increasing solvent polarity (negative solvatochromism), and *bathochromic*, red shift, which means a shift of the absorption maximum to longer wavelengths with increasing solvent polarity (positive solvatochromism).

The energy absorption in the visible and ultraviolet range is determined by the presence of chromophore or chromophore group - which could be a functional group, a carbon group responsible for the UV/VIS absorption of the molecule, *ie.* the double bond C=C, C=C-C=C, C=O, N=N, aromatic rings, *etc.*, or even complex moiety. Any chromophore has a characteristic value corresponding to the maximum absorption wavelength and causes the structure and environment of the molecule. Absorption spectra of multi-atomic molecules are studied from the point of view of the transition of electrons localized in the bonds or to certain functional groups.

Absorption of electromagnetic radiation energy $\Delta E = h\nu$, the molecule moves from primary to excited condition manifested by amplification of vibration or rotation of atomic nuclei or exceed the electronic system to a higher energy level. When the system returns to the ground state, it emits energy that is characteristic of a given substance. The possible electronic transitions are (Figure 2.8):

- $n \rightarrow \pi^*$, when electrons cross the free electron pair of the less stable anti-bonding π^* orbital;
- $\pi \rightarrow \pi^*$, when electrons bonding π orbital taking the less stable anti-bonding π^* orbital;
- $\sigma \rightarrow \sigma^*$, when electrons bonding σ orbital crossing in less stable anti-bonding σ^* orbital.

Electronic transitions of special significance are $n \rightarrow \pi^*$, $\pi \rightarrow \pi^*$ and absorption caused by the transfer of charge.

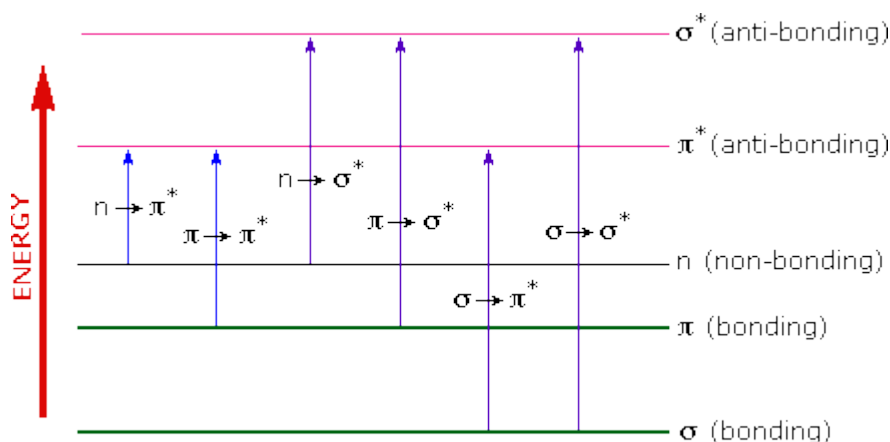


Figure 2.8 Energy level diagrams with electronic transitions⁷²

Electron-donating groups cause shift of absorption maxima to longer wavelengths (bathochromiceffect) and electron-acceptor groupsto smaller wavelengths (hypsochromic effect).Molecules with π -electrons, in which the charge distribution varies considerably in the ground and excited state, have expressed solvahoromatic properties. Compounds which contain π -electrons, can be classified into three different groups according to the idealized structure: aromatic compounds, polyenes (or Poliina) and polymethine.^{73,74}

2.2.2 Solvent effect - multi-parameter approach

The inability to quantitatively express the effect of solvents (through physical constants) on the reactivity of organic compounds and their absorption spectra encouraged the introduction of an empirical scale of the effects of solvents based on reference reactions. In the model, responses that are susceptible to solvents, the empirical measure of the polarity of solvents (solvation power) is expressed. Empirical parameters determined on the basis of a single reaction can't be applied to other systems because it has been shown that the solvent ability to solvatepresent molecules and the ions does not depend only form solvent polarity, but also of all intermolecular interactions.

In order to consider two or more aspects of the solvation, a multi-parameter approach has been applied in which each parameter is relates to a particular interaction in total solvation of the molecule. It allows the prediction of values dependent variable

based on independently variable values and can be applied to a set of data obtained for a large number of well-selected solvents.

Although the separation of the effects of solvents into different types of interactions is of a formal nature, they can't always be separated because of their activity. In general, effects of solvents can be divided into two groups of contributions: specific interaction (donor-acceptor, acid-base with included hydrogen bonds) and non-specific interaction (derived from the action of the solvent as a dielectric continuum).

2.2.2.1 Kamlet-Taft model

Kamlet and *Taft* developed the first multi-parameter correlation equation (2.1),⁷⁵ based on LSER in 1976:

$$A = A_0 + s(\pi_1^* + d\delta) + a\alpha_1 + b\beta_1 \quad (2.1)$$

Size A is a physical-chemical property, which depends on the solvent: the logarithm of the rate constant or equilibrium position or absorption maximum in the UV/Vis, IR, NMR and ESR spectra. A_0 is the extrapolated value of the properties in the vapor phase, or an inert solvent (cyclohexane). Parameter π_1^* is an index of the solvent dipolarity/polarizability and it is the function of its dipole moment $\mu = -0,1 + 4,3\pi_1^*$ (0 (cyclohexane) to 1,00 (DMSO)).⁷⁶ α_1 is a measure of the solvent HBA basicity (0 for non-polar aprotic solvents up to 1 for methanol) and β_1 is a measure of the solvent HBD acidity (0 for non-polar aprotic solvents up to 1 for triamidehexamethylphosphoric acid).⁷⁷ The regression coefficients s , b and a measure the relative susceptibilities of the absorption frequencies to the different solvent parameters.

Kamlet and *Taft* have shown that β , α and π^* may be applied in the correlation analysis by multiple regressions of reaction rates and equilibria, and of spectroscopic data according to eq. (2.2):

$$\nu_{max} = \nu_0 + a\alpha + b\beta + s\pi^* \quad (2.2)$$

The parameter π^* represents polarity/polarizability and is based on the absorption frequencies $\pi \rightarrow \pi^*$ transition of several reference compounds,⁷⁶ ν_0 represents the absorption frequency of the dissolved substance in the reference system, and ν_{max} is the absorption frequency of the compound in a particular solvent.

Kamlet-Taft's approach has a significant success in qualitative estimation of solvent effects on absorption spectra, but there are some disadvantages of this method. Since dipolarity and polarizability of the solvent are represented by only one parameter (π^*), the solvatochromic properties of non-polar substances (which don't establish hydrogen connections with the solvent) can't be adequately described by using the *Kamlet-Taft* scale. The polarizability correction parameter ($d\delta$) is not suitable because it doesn't allow differentiation of the effects of polarizability between two related solvents (aromatic and halogenated hydrocarbons). Another deficiency is the determination of *Kamlet-Taft* parameters by calculating the mean values of the properties of different reference molecules.⁷⁸

2.2.2.2 *Catalán* model

Catalán et al. introduced three alternative scale of polarity SA, SB and SPP, which can be formally linked to the *Kamlet-Taft* parameters α_1 , β_1 , and π_1^* . Determination of each solvatochromic solvent parameter is based on a pair of well-defined homomorphic reference compounds. The need for introducing a fourth polarity scale (SP) it came from the conclusion of *Catalán* and *Hopf*, which showed that the compound ttBP9(3,20-di-tert-butyl-2,2,21,21-tetramethyl-5, 7, 9, 11, 13, 15, 17, 19-docosanone) is sensitive to changes in the polarizability of the medium and isn't sensitive to the acidity, alkalinity and dipolarity of solvents⁷⁹. The dependence of the SPP and SP scale justifies the use of only one of these parameters, which caused the need for the introduction of an additional scale (SdP), which describes the solubility of solvents. SdP is derived from the scale SP and the absorption frequencies of DMANF (2-N, N-dimethylamino-7-nitrofluorene). More elaborated LSER model uses *Catalán* solvent parameters scale,⁸⁰ *i.e.*, eq. (2.4) qualitatively and quantitatively interprets the effect of solvent dipolarity, polarizability, and solvent-solute hydrogen bonding interactions:

$$A = A_o + aSA + bSB + cSP + dSdP \quad (2.3)$$

which if applied to UV-Vis absorption frequencies has the form:

$$\nu_{max} = \nu_o + aSA + bSB + cSP + dSdP \quad (2.4)$$

where SA, SB, SP, and SdP characterize solvent acidity, basicity, polarizability, and dipolarity, respectively. The regression coefficients a – d describe the sensitivity of the absorption maxima to different types of the solvent–solute interactions. Quantitative separation of the non-specific solvent effect (coefficient s ; eq. (2.2)) into polarizability and dipolarity term (coefficients c and d , eq. (2.4)) give more detailed information on electron density distribution over investigated molecule subjected to solvent influences.

2.3 Density Functional Theory (DFT)

The Density Functional Theory (DFT) is a computational method that derives properties of the molecule based on determination of their electron density. The theory was introduced in two papers by Hohenberg and Kohn in 1964, and by Kohn and Sham in 1965^{81,82}. Ever since, number of publications, using DFT calculations for prediction of molecular properties, increases constantly. The density functional theory is presently the most successful and also the most promising approach to compute the electronic structure of matter. When it comes to chemistry, DFT predicts a great variety of molecular properties: molecular structures, vibrational frequencies, atomization energies, ionization energies, electric and magnetic properties, reaction paths, etc.

2.3.1 Fundamental aspects of DFT

The fundamental underlying mathematics of this method is the functional. A functional is a function of a function, and is denoted as follows

$$y = f(x) \quad (2.5)$$

where, the dependent variable (y) depends on one or more single variables. Mathematically, the notation $f(x)$ is read as the "the function of x ".

To understand the DFT theory it is important to introduce the functional denoted as follows

$$y = F[f(x)] \quad (2.6)$$

where, the value of y is in and of itself dependent on another function. The first $f(x)$ function becomes the input for the functional, that is, a function of a function.

The most fundamental parameter in DFT is the electron density $\rho(r)$, and the energy of the molecule is a functional of the electron density. Electron density is a function, with

three variables: x-position, y-position, and z-position of the electrons. Regardless of the number of electrons, the electron density function is always only dependent on those three numbers. The functional (F) of electron density gives the energy of the molecule. The practical advantage is that the mathematics does not spiral out of control as the number of electrons increase.

$$\text{Electron density} = \rho(x, y, z) \quad (2.7)$$

$$\text{Energy} = F[\rho(x, y, z)] \quad (2.8)$$

The goal in DFT is to find the value of the functional F, and it is necessary to make approximations. One of the reasons why there are so many different DFT methods is that there are multiple ways of approximating the functional.

DFT is based on two theorems proved by Hohenberg and Kohn⁸¹ in the 1960s

The first theorem says:

"The ground-state energy from Schrödinger's equation is a unique functional of the electron density."

The second theorem states:

"The electron density that minimizes the energy of the overall functional is the true electron density corresponding to the full solution of the Schrödinger equation."

Using those theorems they were able to develop a more detailed version of the theory, but they did not offer practical way for the calculations. The advanced theory was adapted, in 1965 by Kohn and Sham,⁸² into a practical version of the density functional theory (KS theory). The KS theory, which describes the mathematics of electron densities and their subsequent correlations to molecular energies, is shown in its simplest form as follows

$$E_{\text{DFT}}[\rho] = T[\rho] + E_{\text{ne}}[\rho] + J[\rho] + E_{\text{xc}}[\rho] \quad (2.9)$$

where E is the energy, T is the kinetic energy of the electrons, E_{ne} is the nuclear-electron attraction (Coulombic) energy, J is the electron-electron repulsive (Coulombic) energy, and E_{xc} is the electron electron exchange-correlation energy. Each of these terms is a function of the function ρ , the electron density, which is itself a function of the three positional coordinates (x, y, and z). The first three terms can be determined reasonably well using *ab initio* or semi-empirical methods, but explicit form for electron-exchange-correlation energy, E_{xc} , can not be given.

Minimizing the energy function leads to the Kohn-Sham (KS) equations (2.10-2.13).

$$\left[-\frac{\hbar^2}{2m}\nabla^2 + V_{eff}(\mathbf{r})\right]\Psi_i(\mathbf{r}) = \varepsilon_i\Psi_i(\mathbf{r}) \quad (2.10)$$

$$V_{eff}(\mathbf{r}) = V_{ext}(\mathbf{r}) + V_H(\mathbf{r}) + V_{xc}(\mathbf{r}) \quad (2.11)$$

$$\rho(\mathbf{r}) = \sum_i |\Psi_i(\mathbf{r})|^2 \quad (2.12)$$

$$V_{xc} = \frac{\delta E_{xc}}{\delta \rho(\mathbf{r})} \quad (2.13)$$

Solving the KS equations must be done using iterative technique by self-consistent field method because effective potential V_{eff} depends on $n(\mathbf{r})$, and hence on $\Psi(\mathbf{r})$, which is the solution of the equation. From the eigen-energies and eigen-functions obtained it is possible to get ground state total energy, charge density, vibrational properties, etc. Finding this functional is a very challenging task, and there have been developed different approximate functional.

2.3.2 Methods in DFT

Methods in DFT are complicated and diverse, but can roughly be divided into three classes:

1. Methods that use a local density approximation (LDA). The LDA is determined solely based on the properties of the electron density. The critical assumption of this approximation is that, for a molecule with many electrons in a gaseous state, the density is uniform throughout the molecule (eq 2.14).

$$E_{xc} = \int \rho(\mathbf{r}) \varepsilon_{xc}^{LDA}(\rho(\mathbf{r})) \quad (2.14)$$

where $\varepsilon_{xc}^{LDA}(\rho)$ is the exchange-correlation energy density per electron of a uniform gas with density ρ . The performance of the LDA in calculations is surprisingly good for such a method, but the gross overestimation of the bond energies, and the poor thermochemistry, had diminished its usefulness in dealing with most of the questions of interest in chemistry.

2. Methods that combine the electron density calculations with a gradient correction factor (GGA). In this approach the exchange-correlation functional depends on both the value and the gradient of the electron density (eq. (2.15)):

$$E_{xc} = \int \rho(\mathbf{r}) \varepsilon_{xc}^{GGA}(\rho(\mathbf{r}), \nabla\rho(\mathbf{r})) d\mathbf{r} \quad (2.15)$$

The most common GGA functionals are PW91⁸⁵, PBE⁸⁶ and BLYP⁸⁷.

In general, GGA functionals provide much better results for the calculation of most properties; however, they are not sufficient enough to be useful in the calculation of chemical reaction energies. GGA functionals are also very popular in the solid-state field because they give accurate geometries, elastic properties of periodic solids and qualitatively correct electronic band structures. However, they severely underestimate the electronic band gaps.

3. Methods that are a combination of a Hartree-Fock approximation to the exchange energy and a DFT approximation to the exchange energy, all combined with a functional that includes electron correlation (eqs. 2.16 and 2.17).

$$E_{xc} = \int \rho(\mathbf{r}) \varepsilon_{xc}^{GGA}(\rho(\mathbf{r}), \nabla\rho(\mathbf{r}), \nabla^2\rho(\mathbf{r}), \tau_{KS}(\mathbf{r})) d\mathbf{r} \quad (2.16)$$

$$\tau_{KS}(\mathbf{r}) = -\frac{1}{2} \sum_i |\nabla_i(\mathbf{r})| \quad (2.17)$$

These methods are known as hybrid methods, and are currently the most common and popular DFT method used in practice. A summary of sample methods by name, acronym and type is given in the Table 2.1.

Table 2.1 Summary of sample methods used in DFT.

Method name	Method type	Acronym
Hartree-Fock Slater functional	Hartree-Fock with local density approximation exchange	HFS
Vosko, Wilks, and Nusair	Local Density Approximation (emphasis on electron correlation approximation)	VWN
Becke correlation functional; Lee, Yang, Parr electron exchange functional	Gradient-corrected LDA functional	BLYP
Becke 3-term correlation functional; Lee, Yang, and Parr exchange functional	Hybrid DFT	B3LYP
Perdew 1986 functional	Gradient-corrected LDA functional	P86
Becke 3-term correlation functional; Perdew correlation term	Hybrid DFT	P3P86
Modified Perdew-Wang one parameter hybrid for kinetics	Hybrid DFT	MPW1K

Of all these methods, in terms of practical applications, the B3LYP functional is considered to be the “industry standard”.

2.3.3 Application of DFT

Density functional theory is a general-purpose computational chemistry method, and as such, can be applied to the most systems. With the number of variations of this method (seven of them shown in the table above) – there is no simple guide to the correct choice of a DFT method. However, some general guidelines for the choice of a DFT method are listed below:

1. B3LYP, run with a 6-31G* or better basis set, is on average the best choice of a model chemistry for most systems. B3LYP/6-31G* is particularly good for organic molecules, but less so for metal containing compounds.
2. BLYP with most basis sets is the opposite of B3LYP: not particularly accurate with organics, but provides reasonably good energy values for metal-containing compounds.
3. BLYP and B3LYP methods perform close to the same for determination of charge densities on atoms in molecules.

4. Both gradient-corrected and hybrid methods provide high levels of accuracy in the determination of a geometry optimization.
5. B3LYP methods clearly provide better results for reaction chemistry calculations
6. DFT methods are considered to produce unacceptable results for weak hydrogen bonding interactions.

One important advantage is that DFT scales three-dimensionally, or as N^3 , contrary to *Ab initio* methods that scale as N^4 . DFT calculations are slightly faster with better accuracy. What is most important, DFT methods overcome one of the main disadvantages of *ab initio* methods such as Hartree-Fock: the complete neglect of electron correlation. DFT can also perform calculations on some molecules that are not possible with *ab initio* methods, most notably transition metals. This is a serious advantage considering that a great number of recent studies showed that metal complexes express greater biological activity than free compounds. As biological activity undoubtedly depends on the molecule structure, in order to understand pharmacological activity a lot of investigations based on DFT are successfully developed in the last years.

For a proper understanding of the spectroscopic data a reliable assignment of all vibrational bands, DFT calculations, particularly those based on hybrid functional methods have evolved to a powerful quantum chemical tool for the determination of the electronic structure of molecules.⁸⁴

Compounds containing 1,3-selenazole or 1,3-thiazole rings⁸⁵, and also compound containing hydrazone moiety are separately subject of many research and lot of theoretical calculations has been done. However, investigations of electronic, spectroscopic, geometrical or structural properties of (1,3-selenazole-2-yl)-hydrazones and (1,3-thiazole-2-yl)-hydrazones using quantum mechanical methods are very obscure.⁸⁶⁻⁸⁸

2.4 Introduction to X-ray crystallography⁸⁹

X-ray crystallography is a very useful scientific method used to determine the arrangement of atoms, to obtain detailed information on molecular conformations, bond lengths and angles, as well as on intermolecular interactions in solid state.⁹⁰⁻⁹⁴

The crystal can be defined as a solid state of a substance with a periodic displacement of the motif in a crystal lattice, where in the structural motive can be an atom (ion), and a set of atoms, molecules, a group of molecules, or a combination thereof. One of the main properties of crystals is that they have smooth, properly formed surfaces called flat crystals (facets). The facets are commonly recognized by their shape, consisting of flat faces with sharp angles. The coordinate system of crystals (x, y, z) consists of three imaginary axis that cut at the center of the crystal and are chosen to be parallel to the existing or possible edges of the crystal.

Table 2.2 Classification of crystals according to the length of the crystallographic axes and the angular size between them with given minimal number of elements of symmetry

Crystal system	Axes and axial angles	Minimum number of symmetry elements
Triclinic, a	The three axes of different length which are not perpendicular $a \neq b \neq c \quad \alpha \neq \beta \neq \gamma \neq 90^\circ$	1-fold rotation axis
Monoclinic, m	Three axes of different lengths, one pair of axes is not perpendicular $a \neq b \neq c \quad \alpha = \gamma = 90^\circ \quad \beta > 90^\circ$	2-fold rotation axis or mirror plane
Rhombic, o (orthorhombic)	Three mutually perpendicular axes of different lengths $a \neq b \neq c \quad \alpha = \beta = \gamma = 90^\circ$	Three perpendicular 2-fold rotation axes or two mirror planes
Tetragonal, t	Three mutually perpendicular axes of which are of equal length $a = b \neq c \quad \alpha = \beta = \gamma = 90^\circ$	4-fold rotation axes or roto-inversion axis
Trigonal, r	Three axes of equal length with equal angles that are different from 90° $a = b = c \quad \alpha = \beta = \gamma \neq 90^\circ$	3-fold rotation axes or roto-inversion axis
Hexagonal, h	Two coplanar axes of equal length at an angle of about 120° and a third axis perpendicular to them and different lengths $a = b \neq c \quad \alpha = \beta = 90^\circ \quad \gamma = 120^\circ$	6-fold rotation axis or roto-inversion axis
Cubic, c	Three mutually perpendicular axes of equal length $a = b = c \quad \alpha = \beta = \gamma = 90^\circ$	Four 3-fold rotation axes, two will generate other two

It has been observed that the crystals of the same substance exhibit some mutual similarity and possess certain elements of symmetry, and can be classified according to the length of the crystallographic axes and the size of the angles on six crystal families and seven crystal systems (Table 2.2). Each family contains the same crystal system, the

exception is a hexagonal family that contains two systems: hexagonal and rhombohedral. For each crystal system, the minimum number of elements of symmetry is characteristic. The crystal can always be classified into a triclinic system, but the essence is to determine the highest symmetry and accordingly divide it.

The unit cell is an imaginary parallelepiped containing at least one structural motif. By combining these parallelepipeds in space, the whole structure is being built. In other words, the unit cell is the smallest possible element of a volume having a complete symmetry of the entire structure. The shape and dimensions of the unit cell are determined by the angles between the translation vector (in which directions the translation of the motif is made) and the lengths of these vectors. These sizes are determined by the parameters of the unit cell: the crystallographic axes a , b , c , which are filled with the x -, y - and z -axes of the crystal, and the angles γ (in the plane ab , opposite the c -axis), β (in the plane ac) and α (in the plane bc). The unit cells are also classified into seven existing crystal systems (Table 2.2).

The position of the atom is defined by the fractional coordinates of the atoms, which represent the ratio of the coordinates of the atoms and the length of the corresponding axis. They are calculated as $x = p/a$, $y = q/b$ i $z = r/c$, where p , q , r represent the coordinates of the atom. The possible range of the atomic coordinates is between 0 and 1. Fractional coordinates also define the positions of equivalent atoms in the space. Generally, the atomic coordinates are $x \pm k$, $y \pm l$, $z \pm m$, where are k , l , $m = 0, 1, 2, \dots \infty$.

Bravais lattices are formed as a result of a combination of crystal systems and possible translations of a structural motif. (Figure 2.9). The simplest lattices are called primitive and are designated as P , with the exception of rhombic, which is marked with R . For this type of lattice, translation is exclusively performed for the length of the crystallographic axis, and the points of the grid are located on the sharp edge of the unit cell. Each point on the sharp edge is at the same time the point of the eight adjacent unit cells and each P -lattice. Lattices in which translation is done for half the length of one or more axes are centered. They can be seen as a combination of at least two identical primitive lattices that are moved relative to one another. Depending on the translation vector, they can be classified into face centered (F), basal face centered (C) and body centered (I).

The asymmetric unit is defined as the elementary part of the space for which the fact that the application of symmetry operations can completely fill the space. By applying symmetry operations to an asymmetric unit, the content of the unit cell is obtained, and by stacking unit cells in the space, a crystal structure is being built. When translation-free symmetry elements, expressed as elements of the symmetry of a point group (rotation axis, roto-inversion axis, center of symmetry and mirror plane) affect the unit cells, only 32 combinations are possible, which are designated as point symmetry groups.

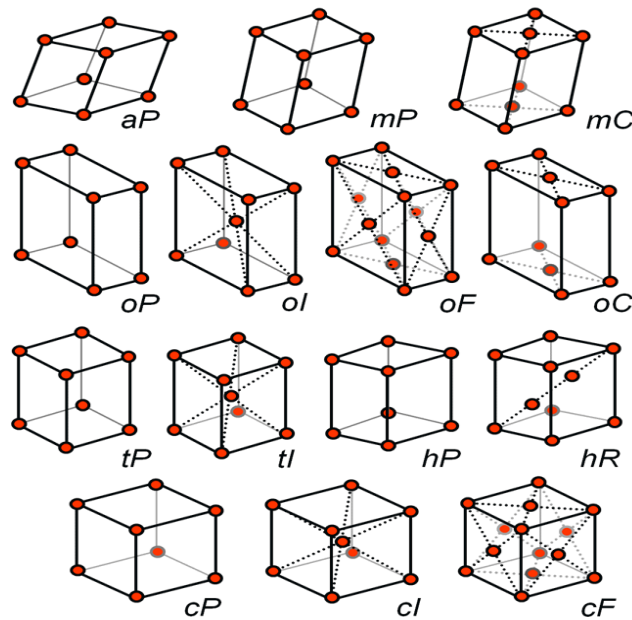


Figure 2.9 The unit cells with corresponding labels of the crystal family (little letter) and Bravais lattice (big letter).

The rotation axes are a combination of rotation and parallel translation with the axis, while the glide plane represents a combination of reflection and translation. By combining Bravais lattice, point groups, axis of rotation and glide plane, 230 crystallographic space groups are obtained. Space group markings begin with the symbol of the Bravais grid, followed by one, two or three markings of the present axes and levels. Space group tags begin with the symbol of the Bravais lattice, followed by one, two or three marks of the present axis and plane.

The crystal lattice can be described as a regular, infinite distribution of points in a space in which each single point has the same environment. If each point of the crystal lattice joins the structural motif, a crystal structure is obtained. Various sets of equidistant levels can be set through the crystal lattice, between which the distance is equal and is called the lattice spacing (d). The plane of the grid is marked with Miller indices,

which are integers, defined as the reciprocal values of the sections of these levels on the crystallographic axes and labeled with hkl .

The basic condition that needs to be fulfilled for the diffraction of electromagnetic radiation in X-ray radiation is nearness of wavelength of radiation and the dimension of the lattice. This condition is satisfied, since the X-rays have a wavelength of about 1 \AA , while the lattice spacings are in the range of $1-10 \text{ \AA}$. When the X-rays fall into a series of points (atoms), they become sources of secondary radiation, and the scattering occurs in all directions, where the scattering refers to an electronic shell.

In Figure 2.10 beams of X-rays falling to adjacent levels are shown. In order for the C and C' rays to be in the same phase, or that there would be constructive interference, it is obvious that A'C' ray should go a long way from the AC ray for the length $1B'2$. The difference of these paths must be equal to the total number of wavelengths, *i.e.* $1B'2 = n\lambda$.

Since $1B' = B'2 = d \sin\theta$, Bragg's law or equation is derived:

$$n\lambda = 2d \sin\theta \quad \text{where } n = 1, 2, 3\dots \quad (2.18.)$$

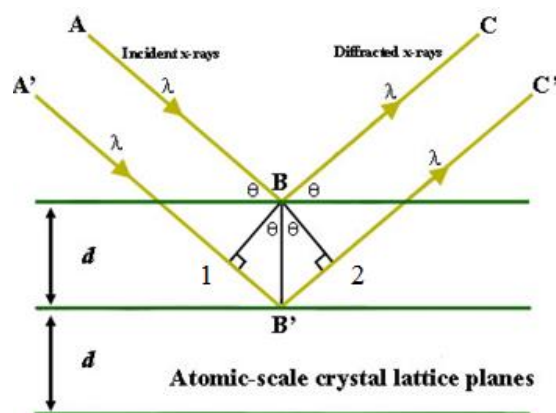


Figure 2.10 Graphic view of the *Bragg's law*.

One of the concluding ideas from Bragg's law is that diffraction is an "arranged event"; three parameters need to be harmonized: the wavelength of the X-rays, λ , the crystal orientation as defined by the angle, θ , and the spacing, d , of the crystal planes under consideration. For a given wavelength and set of planes one can conspire to arrange for diffraction to occur by, for example, continuously changing the orientation, *i.e.* changing θ , until a point arrives when Bragg's law is satisfied: this is precisely when diffraction occurs. If the incident angle differs from Bragg's angle, there is a destructive interference, the rays are not in the phase and they are annulled.

For all experimental techniques, a source of X-ray radiation (usually monochromatic), a diffracted ray detector (film or counter) and a sample (monocrystalline or polycrystalline) is required. The diffraction pattern of the sample contains information on the structure of the compounds that can be obtained by indicating the diffractograms, which involves determining the Miller indexes and the parameters of the unit cell.

After determining the phase of one part or all reflections, different maps are calculated in which an approximate structure of the compound and the coordinates are approximately correct. They need to be pulled out and for that the least squares method is used. By alternating application of this method and calculation maps it is possible to locate all atoms and make a more accurate their coordinates and thermal parameters. As a general indicators of the actual agreement and superior structural model using various indicators of reliability indices: R -factor (R) and weight factor (R_w)

The primary results of determining the crystal structure are the atomic coordinates and their thermal parameters. Atomic displacement parameters are obtained as a result of vibration of the atom, usually due to the temperature change. The isotropic thermal parameters, B and U , are a significant indicator in determining the crystal structure. B can have values between 1 and 10 \AA^2 . Values that deviate from this range indicate an error in a structural model.

The refinement of anisotropic thermal parameters assumes that the vibrations are isotropic, *i.e.* equal in all directions, and the atoms are represented as spheres. However, vibrations of atoms in molecular compounds are, as a rule, anisotropic and can be presented as ellipsoids. After the refinement of the structure with isotropic parameters,

the anisotropic parameters B_{ij} and U_{ij} are separated. On the basis of the atomic coordinates, interatomic distances (lengths) and angles are obtained.

The atomic coordinates are given in the coordinate system of crystals, which for simplicity are translated into orthogonal coordinates. The obtained distances and angles are compared with the literature data. Based on the results, torsional angles, significant geometric parameters describing the conformation of molecules, the mirror plane through the group of atoms, and the angle between two levels can be obtained. Torsional angles are significant in the analysis of nonplanar molecules, and the medium level in the analysis of compounds containing aromatic, planar rings.

The crystal structure, in addition to the coordinates of the atoms, implies the packaging of structural motifs in the crystal lattice. In organic molecules, the packaging depends on intermolecular forces (van der Waals and hydrogen bonds). The length of the hydrogen bond in which the oxygen is the donor is 2.73 Å. When the bonds are strong and short, usually of intramolecular type, they can only be 2.3 Å. The maximum distance of the two O atoms which form the hydrogen bond is 3.1 Å. The usual length of the hydrogen bond between N and O is about 2.9 Å.

2.5 Electrochemistry in analysis of organic compounds

The basis of electrochemistry represents chemical reactions which include an electron (a basic particle of electricity and electric current) as active participant. If the compound receives an electron in the interaction it is reduction, and *vice versa* if the compound gives an electron it is oxidation. The electrode reaction is always carried out at the boundary surface of the electrode-electrolyte⁹⁵.

The basic element of the electrochemical system is an electrochemical cell with, at least, two electrodes (cathode and anode) and the solution of the electrolyte. Electrode reduction is performed on the cathode, and the electrode oxidation is performed on the anode. The electrolyte solution serves as a carrier of organic compound that reacts, but also as a transmitter of electrical energy in the electric circuit of the cell⁹⁵.

Electroanalytical methods are techniques in which analyte is studied by measuring the potential (volts) and/or current (amperes) in an electrochemical cell

containing the analyte. Depending on which aspects of the cell are controlled and which are measured electroanalytical methods can be divided into three main categories:

- potentiometry(the difference in electrode potentials is measured),
- coulometry(the current is measured over time), and
- voltammetry(the current is measured while actively altering the potential).

Due to its high sensitivity, voltametric techniques have been favorable for the investigation of electrochemical behavior of biologically important compounds ⁹⁶.

2.5.1 Voltammetry

Voltammetry is an electroanalytical method in which a time-dependent potential is applied to the electrochemical cell and the resulting current as a function of that potential is measured. The resulting plot of current *versus* applied potential is called a voltammogram, and it is the electrochemical equivalent of a spectrum in spectroscopy, providing quantitative and qualitative information about the species involved in the oxidation or reduction reaction ⁹⁷. A modern voltammetric system consists of three electrodes immersed into a solution of analyte and the basic electrolyte which does not react. A typical electrochemical cell for voltammetry is shown in the Figure 2.11.

Working electrode is the electrode on which the desired phenomenon is examined. The potential on the working electrode can be defined value or can be linearly changed over time. The electrode has a small surface and can be constructed using several different materials: mercury, platinum, gold, silver, and carbon. Mercury is the oldest used material and there are:

- hanging mercury drop electrode(HMDE),
- dropping mercury electrode(DME),
- static mercury drop electrode(SMDE) and
- mercury film electrode

Solid electrodes are constructed using inert metals (platinum, gold, silver), or carbon. Except for the carbon paste electrode, a solid electrode is a disk sealed into the end of an inert support. The carbon paste electrode is made by filling the cavity at the end of the inert support with a paste consisting of carbon particles and viscous oil.

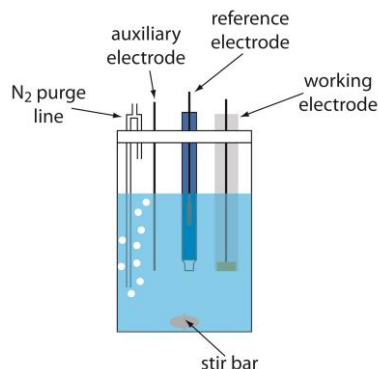


Figure 2.11 Electrochemical cell for voltammetry.

The second electrode is a reference and its potential is known and stable⁹⁸. The reference electrode is introduced into the cell *via* Luggin capillary. The tip of the electrode should be positioned as close as possible to the working electrode, so the resistance of the electrolyte between the electrode and the capillary tip can be reduced to a negligible value. The reference electrode should be separated from the cell solution using electrolytic bridge to prevent leakage of the electrolyte from the cell into the electrolyte of the reference electrode, and *vice versa*.⁹⁵

The third electrode is the auxiliary electrode (counter electrode), which is often a platinum or gold wire, and allows electricity flow through the solution, from the source to the working electrode⁹⁵. The electrode counter is placed at a greater or lesser distance from the working electrode.

There are many different voltammetric techniques. The most common forms of voltammetry currently in use are:

- polarography (voltammetry with the linear change of the potential)
- pulse voltametry (normal and differential)
- cyclic voltammetry and
- stripping voltammetry.

2.5.2 Cyclic voltammetry

Cyclic voltammetry (CV) has become an important and widely used electroanalytical technique in many areas of chemistry. This technique is based on varying the applied potential at a working electrode in both forward and reverse directions (at some scan rate) while monitoring the current. As shown in Fig x2a the

initial scan can start from the initial E in positive direction to the switching potential. In this part oxidation reaction takes place. At the point of switching E the scan is reversed and run in the negative direction. In this part reduction takes place. Depending on the analysis, one full cycle, a partial cycle, or a series of cycles can be performed. The scan rate, in most cases, varies from 0.1 mV s^{-1} to 1.0 V s^{-1} .

The response obtained from a CV for reversible redox system is shown in Figure 2.12.

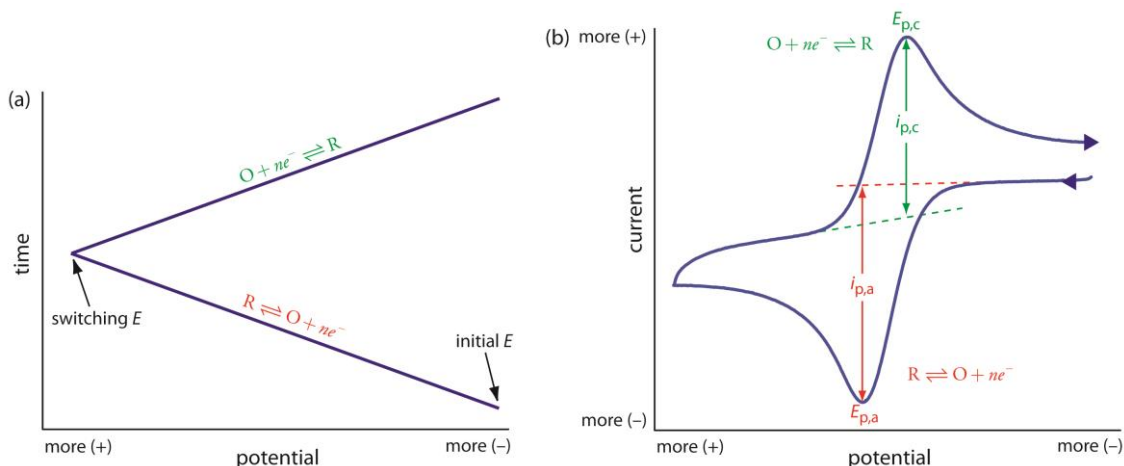


Figure 2.12 Details for cyclic voltammetry; (a) one cycle of the triangular potential-excitation signal showing the initial potential and the switching potential. (b) The resulting cyclic voltammogram showing the measurement of the peak currents and peak potentials.

The important parameters in a cyclic voltammogram are the peak potentials ($E_{p,c}$ and $E_{p,a}$) and peak currents ($i_{p,c}$ and $i_{p,a}$) of the cathodic and anodic peaks, respectively. If the electron transfer process is fast compared with other processes (such as diffusion), the reaction is said to be electrochemically reversible, and the peak separation is:

$$\Delta E = |E_{p,a} - E_{p,c}| \quad (2.19)$$

The peak current is related to the concentration by the Randles–Sevcik equation ($T=25^\circ\text{C}$):

$$i_p = (2.69 \times 10^5) n^{3/2} A D^{1/2} \nu^{1/2} C = KC \quad (2.20)$$

where i_p is the peak current in amperes, A is the electrode area (cm^2), D is the diffusion coefficient ($\text{cm}^2 \text{s}^{-1}$), C is the concentration in mol cm^{-3} , and n is the scan rate in V s^{-1} .¹⁰¹

For a well-behaved system, the anodic and cathodic peak currents are equal, and the ratio $i_{p,a}/i_{p,c}$ is 1.00. The half-wave potential, $E_{1/2}$, is midway between the anodic and cathodic peak potentials.

$$E_{1/2} = (E_{p,a} + E_{p,c})/2 \quad (2.21)$$

Cyclic voltammetry is a very good method to investigate the kinetics of electrochemical reactions. Scanning the potential in both directions provides the opportunity to explore the electrochemical behavior of species generated at the electrode. This is a distinct advantage of cyclic voltammetry over other voltammetric techniques.

2.5.3 Electrochemistry of hydrazones

Many physiologically active hydrazones and their metal complexes find application in the treatment of variety of diseases as tuberculosis, leprosy and mental disorder¹⁰². As oxidation and reduction represents one of many ways in drug metabolism it is, therefore, very useful to elucidate redox properties of such compounds. Electrochemical methods are favorable to obtain this information and successfully used on various biological compounds.

In the literature, there are many published works on the electrochemical reduction of azo and hydrazone compounds. The hydrazones are electroactive compounds. The first systematic electrochemical study of hydrazones was performed by Lund in late 1950s¹⁰³ and since then, there are many published works on the electrochemical reduction of hydrazones^{104–109}. Electrochemical activity of hydrazones has been investigated in both protic, and aprotic solvents. Under aqueous conditions, $\text{C}=\text{N}-\text{NH}$ group converts to $\text{CH}-\text{NH}-\text{NH}$ group by reduction that consists of two-electron, two-proton transfer. In aprotic solvents, like DMF, the hydrolysis of imine is hampered and it is good to examine electrochemical behavior in such conditions¹¹⁰.

Andrieux et al. studied electrochemical reduction of various imines in acetonitrile and DMF and came to conclusion that reduction was one two-electron transfer or two one-electron transfer¹¹⁰. Isse et al. investigated electrochemical reduction of the Schiff bases in DMF and published that self-protonation reaction is involved in the reduction process, while Kononenko et al. claimed that the first wave observed in the electrochemical reduction was an irreversible two-electron transfer reaction and that overall process is controlled by diffusion of the depolarizer to the electrode¹¹¹.

Ozel et al. have demonstrated that some substituted hydrazones have two reduction and two oxidation peaks at platinum electrode in DMF. They proposed an electrode reaction mechanism pathway for these hydrazones. Das et al.⁹⁶ investigated electrochemical properties of some isatin-3-hydrazones and their metal complexes and revealed that electrochemical reduction is influenced by the nature of groups attached to carbon atom ($-N=CR_1R_2$).

By far there are no literature data about electrochemical investigation of 1,3-selenazol-and 1,3-thiazole-2-yl-hydrazones. In this dissertation electrochemical behavior of eighteen hydrazones derivatives and their Cu complexes has been examined. The electrochemical characteristics of investigated compounds may be useful in the future research on their action mechanism as well as pharmacokinetic and pharmacodynamic purposes in biological media, if they find use as drugs.

2.6 Biological activity

Compounds containing nitrogen and sulphur atoms in their structure are the subject of ongoing research in medical chemistry¹¹². A large number of heterocyclic nitrogen or sulphur compounds are interesting targets for the design of different types of drugs.¹¹³⁻¹¹⁶

It is known that thiazoles and selenazoles, and their hydrazone derivatives exhibit a wide spectrum of biological activity and are used as antioxidants, analgesics, anticonvulsants, antidepressants, antiinflammatory and antitubercular agents. In addition, they are used as cardioprotective agents, and they are also known for antihelmintic and anticancer effects.^{9,18,63}

2.6.1 Antimicrobial activity

Antimicrobial resistance is a serious public health problem particularly in hospitals and other health care settings. During the last decade, due to an increase of pathogen resistance, the antimicrobial agents are losing their efficiency. The evolution of bacterial resistance can be attributed to the use and overuse of antibiotics and transmission of resistance within and between individuals. Therefore, there is an urgent need for development of new classes of antimicrobials that may not be as susceptible to bacterial resistance mechanisms as the current drugs.¹¹⁷ The strategy of the pharmaceutical industry is reflected in the changes in the molecular structure of existing antibiotics in order to improve their efficacy. The reason for this is the synthesis and testing of new antimicrobial substances that will have a wide range of effects, will not cause resistance and will show low potential for causing adverse effects. Due to the specificity in the bacteria, there are many antibacterial targets, and the most successful agents work on building a bacterial cell wall, protein synthesis, or replication and DNA transcription.¹¹⁸

The parameters that determine the sensitivity of bacteria and fungi to the existing antimicrobial drugs and new antimicrobial agents in the study are:

- a) Minimal Inhibitory Concentration (MIC),
- b) Minimum Bactericidal Concentration (MBC).

The minimum (or minimal) inhibitory concentration (MIC) is the lowest concentration of a specific chemical that inhibits the growth of a specific microorganism.

The minimum bactericidal concentration (MBC) is the lowest concentration of an antibacterial agent required to kill a particular bacterium. The MBC is identified by determining the lowest concentration of antibacterial agent that reduces the viability of the initial bacterial inoculum by $\geq 99.9\%$.

2.6.1.1 Antimicrobial activity of (1,3-thiazol-2-yl) and (1,3-selenazol-2-yl)hydrazones

Only few studies dealt with the antimicrobial activities of (1,3-thiazol-2-yl) and (1,3-selenazol-2-yl)hydrazones. Chimenti et al. tested a series of 2,4-disubstituted

thiazoles derivatives and against 20 clinical isolates of pathogenic *Candida* spp and revealed a promising inhibitory activity.^{119,120} Łaczkowski et al. tested twenty different thio(seleno)hydrazones for their antimicrobial activity against a panel of reference strains of 27 microorganisms, including Gram-positive bacteria, Gram-negative bacteria, and fungi belonging to yeasts. They showed that investigated compound have fungistatic/fungicidal or bacteriostatic/bactericidal effect.¹²¹

Mbaveng et al. determined the antibacterial activities of a panel of p-toluenesulfonyl-hydrazinethiazoles and hydrazinoselenazoles against different bacterial strains the obtained demonstrated that hydrazinoselenazoles are strong source of inspiration in antibacterial drug discovery.¹⁵

2.6.2 Antioxidant activity

Free radicals are extremely reactive chemical species (molecules, atoms or ions) that can occur in the human organism, even in normal physiological processes. Each organism has the ability to neutralize the production of free radicals by its natural mechanisms, which are found in cells or introduced through a food. Oxidative stress is essentially an imbalance between the production of free radicals and the ability of the body to counteract or detoxify their harmful effects through neutralization by antioxidants¹²². Oxidative stress leads to many pathophysiological conditions in the body. For this reason, optimal antioxidant protection against potentially harmful chemical species is essential for life, and the modern medicine devotes a lot of attention to find new anti-oxidants, "scavengers" of free radicals. The chemical disappearance of free radicals arises due to the tendency for the pairing of unpaired electrons at the last energy level of the atom. In most cases, this process is monitored by the disturbance of the stability of other molecules, and sometimes by the movement of chain reactions that cannot be controlled¹²². The greatest damage is due to the fact that free radicals damage their genetic material when attacking cell membranes, causing the occurrence of various diseases¹²³. Depending on the element that is included in their composition, there are three major groups:

1. Reactive Oxygen Species – ROS;
2. Reactive Nitrogen Species RNS;
3. Reactive Sulfur Species – RSS.

Antioxidants are molecules which can safely interact with free radicals and terminate the chain reaction before vital molecules are damaged. Although there are several enzyme systems within the body that scavenge free radicals, the principle micronutrient (vitamin) antioxidants are vitamin E, beta-carotene, and vitamin C. Additionally, selenium, a trace metal that is required for proper function of one of the body's antioxidant enzyme systems, is sometimes included in this category. The body cannot manufacture these micronutrients so they must be supplied in the diet. Antioxidants operate through different mechanisms:

- As inhibitors of oxidative reactions involving free radicals;
- By interrupting the chain reaction of auto-oxidation of the substrate;
- Through synergy with other antioxidants;
- As metallic ion chelator and/or translating redox active pro-oxidants (iron and copper derivatives) into stable products;
- As inhibitors of pro-oxidative enzymes (e.g. lipoxygenase)¹²⁴.

The product must be stable and less harmful than radicals. If the organism has low levels of antioxidants or low levels of antioxidant enzymes, oxidative stress is created can damage the cells and cause aging, as well as many pathological conditions, such as arterosclerosis, diabetes, and cancer¹²⁵.

2.6.2.1 Antioxidant activity of (1,3-thiazol-2-yl) and (1,3-selenazol-2-yl)hydrazones

Selenium and sulphur inorganic and organic compounds and proteins are well known by their antioxidant properties^{8,118,125-127}. On the other hand, the only study of antioxidant capacity of (1,3-thiazol-2-yl)hydrazones has been done by Shih et al¹²⁸. They showed that thiazole ring contributes to the antioxidant activity of investigated compounds. To the best of our knowledge there is no such study published for (1,3-selenazol-2-yl)hydrazones.

2.6.3 Anticancer activity

Cancer is a class of diseases characterized by the development of abnormal cells that divide uncontrollably and have the ability to infiltrate and destroy normal body

tissue. There are more than 100 different types of malignant tumors, which can occur within certain organs. In order to develop new, applicable anti-cancer drugs, it is necessary to understand the complex mechanisms of the process of carcinogenic and cellular death¹²⁹.

Cell culture has become an indispensable tool to help uncover fundamental biophysical and biomolecular mechanisms by which cells assemble into tissues and organs, how these tissues function, and how that function becomes disrupted in disease. Cell culture is now widely used in biomedical research, tissue engineering, regenerative medicine, and industrial practices. There are two different ways of how cells can be cultured: two-dimensional (2D) and three-dimensional (3D) structures.

2.6.3.1 Activity testing of the compounds on the 2D model

Conventional 2D cell culture relies on adherence to a flat surface to provide mechanical support for the cells (glass or polystyrene petri dish). Presence of nutrients and growth factors in the medium allows for homogenous growth and proliferation¹³⁰. This characteristic makes 2D platforms attractive to biologists and clinical users due to simplicity and efficiency. However, most of these 2D methods do not provide control of cell shape, which determines biophysical cues affecting cell bioactivities *in vivo*. For over a century, two-dimensional (2D) cell cultures have been used as *in vitro* models to study cellular responses to stimulations from biophysical and biochemical cues. Although testing using 2D model help understanding of cell behavior, growing evidence shows that bioactivities resulted from 2D cell culture assay deviate significantly from the *in vivo* response. For instance, some important characteristics of cancer cells cannot be appropriately modeled in 2D cultures¹³¹. To overcome this limitation, novel 3D cell culture platforms are being created to better mimic *in vivo* conditions^{132–134}.

2.6.3.2 Activity testing of the compounds on the 3D model

Cells in our organism perform their biological function in response to the stimulation of a highly complex 3D microenvironment. By choosing suitable microenvironment it is possible to control the tissue formation^{135–137}. A well-designed microenvironment in tissue and cell engineering can be used to promote proliferation, migration, matrix production, and stem cell differentiation. There is a great deal of

evidence that the cells are organized into three-dimensional (3D) models by morphological and physiological parameters much more similar to the parent tumor cells compared to the same cells maintained in the 2D culture¹⁸⁴. Therefore, 3D cultures represent an excellent *in vitro* replacement for animal testing in terms of cell proliferation rate, cell differentiation, gene and protein expression, and cell response to the examined treatment. The introduction of 3D cell culture approaches aimed at modeling the *in vivo* interactions of tissues and organs has opened new possibilities in studying the underlying biochemical and biomechanical signals^{138,139}.

2.6.3.3 Anticancer activity of (1,3-thiazol-2-yl) and (1,3-selenazol-2-yl)hydrazones

While 1,3-thiazoles are well known by their anticancer activity, and the Ayati et al. summarized all the testing that have been done⁹, their selenium analogs have been studied in much less extent. To the best of our knowledge, there are only two systematic anticancer activity studies of 1,3-selenazoles^{63,140}. 1,3-Selenazole has been tested on two human cancer cell lines: DU-145 and Hep-G2 by Zaharia et al.⁶³ and MCF-7 and L1210 by Zhao et al.¹⁴⁰.

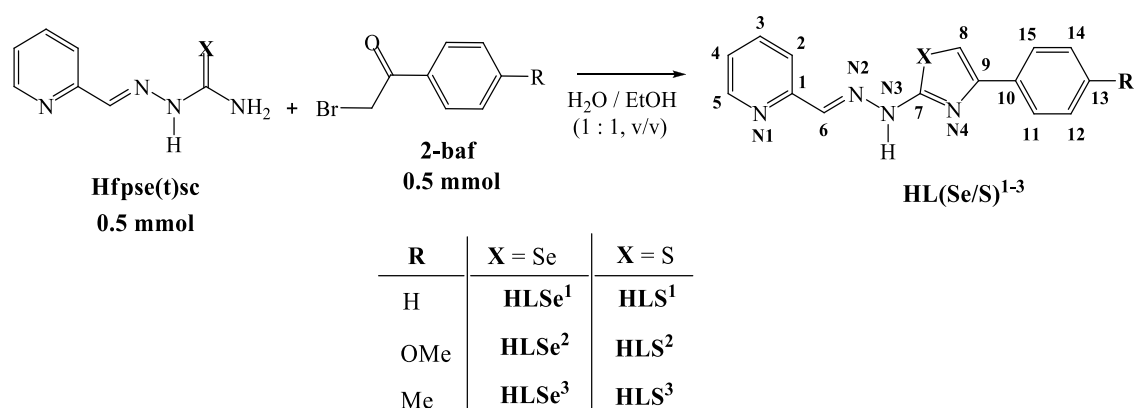
3 EXPERIMENTAL PART

In order to study the synthesis, structure and biological properties, two series of 1,3-seleno(thi)azoles-2-yl-hydrazones were synthesized and characterized. Both series were synthesized by Hantzsch's reaction between the corresponding selenosemicarbazone and 2-bromoacetophenone and its derivatives which in *p*- position contain a methyl or methoxy group. The first series was obtained by reacting mentioned bromo compounds with pyridine-2-carboxaldehyde-seleno(thio)semicarbazone (**Hfpse(t)sc**), while the second series was obtained from nitro (*o*-, *p*- and *m*-) benzaldehyde-selenosemicarbazone (*o*-(*m*-*p*-)**nsesc**).

3.1 Synthesis 1,3-seleno(thi)azoles-2-yl-hydrazones and complexes

3.1.1 General procedure for synthesis first series **HL(Se/S)**¹⁻³

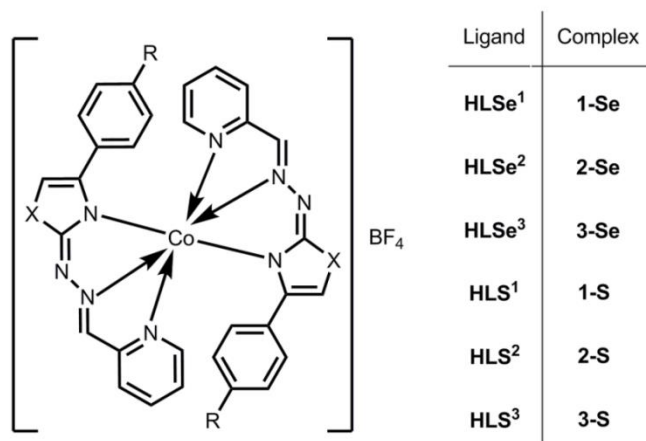
2-Bromoacetophenone (**2-baf**) and its para- methyl or methoxy substituted derivatives (0.5 mmol) was added into suspension of **Hfpse(t)sc** (0.5 mmol) in 20 mL H₂O / EtOH mixture (1 : 1, v/v) and stirred for 3 h at room temperature (Scheme 3.1). Yellow precipitate was filtered off and washed three times with H₂O and EtOH. 2-Formylpyridine selenosemicarbazone(**Hfpse**) and 2-formylpyridine thiosemicarbazone (**Hfptsc**) were obtained by condensation of 2-formylpyridine with selenosemicarbazide/ thiosemicarbazide according to the reported literature procedures^{141,142}.



Scheme 3.1 General procedure for the synthesis of first series 1,3-seleno(thi)azoles-2-yl-hydrazones.

3.1.2 General procedure for synthesis complexes with HL(Se/S)¹⁻³

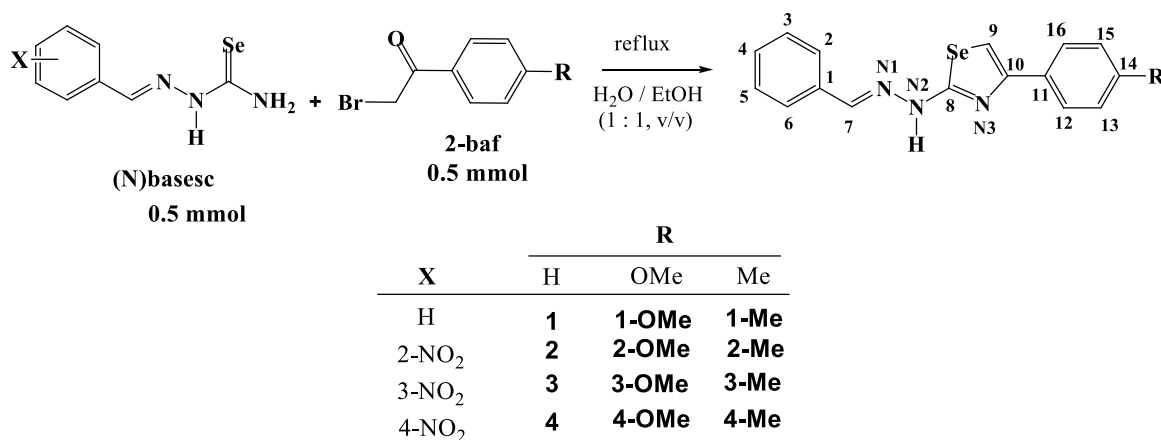
Into suspension of **HL(Se/S)**¹⁻³ (0.30 mmol) in 20 mL of MeOH, solid $\text{Co}(\text{BF}_4)_2 \times 6\text{H}_2\text{O}$ (0.15 mmol) was added. Obtained rotten cherry solution was refluxed for 1 h. After two days emerald colored single crystals were filtered off, washed with cold MeOH and Et₂O. (Scheme 3.2)



Scheme 3.2 Co(III) Complexes of first series 1,3-seleno(thio)azoles-2-yl-hydrazones.

3.1.3 General procedure for synthesis second series

Benzylidene-hydrazine carboselenoamides (**basesc**) and nitro substituted benzylidene-hydrazine carboselenoamides (**Nbasesc**) were suspended (0.5 mmol) were suspended in water/ethanol mixture and the corresponding aromatic α -bromoketone (0.5 mmol) was added. The reaction mixture was heated and stirred for 4 h. After completion of the reaction, monitored by TLC (ethyl acetate/hexane 1:1 v/v), the obtained precipitate was filtered off and washed with cold solvent. (Scheme 3.3)



Scheme 3.3 General procedure for the synthesis of second series 1,3-selenoazoles-2-yl-hydrazones.

3.2 Characterization of synthesized compounds and complexes

Thiosemicarbazide (99 %), potassium selenocyanate (99 %), hydrazine hydrate (99 %), 2-formylpyridine (99 %) and 2-bromoacetophenone (98 %) were obtained from Acros Organics. 2-Bromo-1-(4-methoxyphenyl)ethan-1-one (97 %) and 2-bromo-1-(4-methylphenyl)ethan-1-one (97 %) were obtained from Maybridge. 2-Nitrobenzaldehyde (98%), 3-nitrobenzaldehyde (99%) , 4-nitrobenzaldehyde (98%) and cobalt(II) tetrafluoroborate hexahydrate (99%) was obtained from Aldrich (Sigma-Aldrich Chemie GmbH, Steinheim, Germany). All solvents (reagent grade) were obtained from commercial suppliers and used without further purification.

Elemental analyses (C, H, N, S) were performed by the standard micromethods using the ELEMENTAR Vario EL III CHNS/O analyzer. Infra-red (IR) spectra were recorded on a Thermo Scientific Nicolet 6700 FT-IR spectrometer by the Attenuated Total Reflection (ATR) technique in the region 4000–400 cm^{-1} . Abbreviations used for IR spectra: vs, very strong; s, strong; m, medium; w, weak. The NMR spectra were performed on a Bruker Avance 500 equipped with broad-band direct probe. NMR spectral assignments and structural parameters were obtained by combined use of ^1H homonuclear spectroscopy (2D COSY) and multinuclear proton detected spectroscopy (2D HSQC, 2D HMBC). Chemical shifts are given on δ scale relative to tetramethylsilane (TMS) as internal standard for ^1H and ^{13}C . Abbreviations used for NMR spectra: s, singlet; dd, doublet of doublets; ddd, double double doublet. UV-Vis spectrum was recorded on Uv-1800 Shimadzu spectrophotometer in 250–600 nm range using a quartz cell with 1.0 cm path length. For 2,2-diphenyl-1-picrylhydrazyl (DPPH) scavenging activity, absorbance at 517 nm was measured using a Thermo Scientific Appliskan. Molar conductivity measurement was performed at ambient temperature on the Crison Multimeter MM41. Detailed characterization of both groups of synthesized compounds is given below (Figure 7.1-Figure 7.78):

2-(2-(2-pyridinylmethylene)hydrazinyl)-4-(phenyl)-1,3-selenazole(HLSe¹).

2 Bromoacetophenone (0.10 g; 0.5 mmol) was added into suspension of Hfpsesc (0.11 g; 0.5 mmol) in 20 mL H₂O / EtOH mixture (1:1, v/v) and stirred for 3 h at room temperature. Yellow precipitate was filtered off and washed three times with H₂O and

EtOH. Yield: 0.11 g (68 %). IR (ATR, $\nu_{\max}/\text{cm}^{-1}$): 3054 (w), 2958 (w), 2847 (w), 2714 (m), 1596 (m), 1570 (s), 1480 (s), 1434 (m), 1355 (m), 1261 (s), 1144 (s), 1027 (w), 1001 (w), 923 (w), 893 (w), 766 (m), 700 (s), 656 (w), 591 (w), 515 (w). ^1H NMR (500.26 MHz, DMSO- d_6) δH : 7.30 (t, 1H, $J = 7.2$ Hz), 7.36 (m, 1H), 7.40 (t, 2H, $J = 7.6$ Hz), 7.76(s, 1H), 7.87 (m, 4H), 8.12 (s, 1H), 8.58 (d, 1H, $J = 4.4$ Hz), 12.54 (s, 1H). ^{13}C NMR (126.0 MHz, DMSO- d_6) δC : 108.17, 119.20, 123.70, 125.77, 127.40, 128.60, 135.37, 136.79, 142.26, 149.47, 151.45, 153.16, 170.99. Anal. Calcd for $\text{C}_{15}\text{H}_{12}\text{N}_4\text{Se}$ (%): C, 55.05; H, 3.70; N, 17.12. Found: C, 55.23; H, 3.82; N, 17.29.

2-(2-(2-pyridinylmethylene)hydrazinyl)-4-(4-methoxyphenyl)-1,3-selenazole(HLSe²). HLSe² was synthesized in a similar way to HLSe¹, but using 2-bromo-4'-methoxyacetophenone (0.11 g; 0.5 mmol) instead of 2-bromoacetophenone. Yield: 0.13 g (72 %). IR (ATR, $\nu_{\max}/\text{cm}^{-1}$): 2929 (w), 2832 (w), 2677 (m), 1598 (m), 1574 (s), 1482 (s), 1249 (s), 1028 (m), 843 (w), 666 (w). ^1H NMR (500.26 MHz, DMSO- d_6) δH : 3.78 (s, 3H), 6.95 (d, 2H, $J = 7.0$ Hz), 7.37 (m, 1H), 7.56 (s, 1H), 7.78 (d, 2H, $J = 8.8$ Hz), 7.86 (m, 2H), 8.11 (s, 1H), 8.58 (d, 1H, $J = 4.7$ Hz), 12.49 (s, 1H). ^{13}C NMR (126.0 MHz, DMSO- d_6) δC : 55.10, 105.64, 113.95, 119.19, 123.66, 127.08, 128.60, 136.79, 142.20, 149.45, 153.19, 158.68, 170.94. Anal. Calcd for $\text{C}_{16}\text{H}_{14}\text{N}_4\text{OSe}$ (%): C, 53.79; H, 3.95; N, 15.68. Found: C, 53.48; H, 4.12; N, 15.32.

2-(2-(2-pyridinylmethylene) hydrazinyl)-4-(4-methylphenyl)-1,3-selenazole(HLSe³). HLSe³ was synthesized in a similar way to HSe¹, but using 2-bromo-4'-methylacetophenone (0.11 g; 0.5 mmol) instead of 2-bromoacetophenone. Yield: 0.12 g (69 %). IR (ATR, $\nu_{\max}/\text{cm}^{-1}$): 2970 (w), 2953 (w), 2711 (w), 1601 (m), 1573 (s), 1481 (s), 1433 (m), 1257 (m), 1148 (m), 1039 (w), 818 (w), 667 (w). ^1H NMR (500.26 MHz, DMSO- d_6) δH : 2.30 (s, 3H), 7.19 (d, 2H, $J = 8.0$ Hz), 7.35 (m, 1H), 7.66 (s, 1H), 7.73 (d, 2H, $J = 8.1$ Hz), 7.84 (m, 1H), 7.86 (m, 1H), 8.11 (s, 1H), 8.57 (d, 1H, $J = 4.7$ Hz), 12.54 (s, 1H). ^{13}C NMR (126.0 MHz, DMSO- d_6) δC : 20.79, 106.94, 119.20, 123.68, 125.71, 129.17, 132.65, 136.67, 136.80, 142.21, 149.45, 151.67, 153.18, 170.97. Anal. Calcd for $\text{C}_{16}\text{H}_{14}\text{N}_4\text{Se}$ (%): C, 56.31; H, 4.13; N, 16.42. Found: C, 55.99; H, 3.96; N, 16.45.

2-(2-(2-pyridinylmethylene) hydrazinyl)-4-(phenyl)-1,3-thiazole (HLS¹).

2-Bromoacetophenone (0.10 g; 0.5 mmol) was added into suspension of Hfptsc (0.09 g; 0.5 mmol) in 20 mL H_2O / EtOH mixture (1:1, v/v) and stirred for 3 h at room

temperature. Yellow precipitate was filtered off and washed three times with H₂O and EtOH. Yield: 0.11 g (76 %). IR (ATR, $\nu_{\max}/\text{cm}^{-1}$): 3053 (w), 2953 (w), 2747 (w), 1696 (m), 1570 (s), 1481 (m), 1435 (w), 1262 (m), 1144 (m), 767 (m), 700 (m). ¹H NMR (500.26 MHz, DMSO-*d*₆) δ H: 7.30 (t, 1H, $J = 7.3$ Hz) 7.34 (m, 1H), 7.35 (s, 1H), 7.40 (t, 2H, $J = 7.7$ Hz), 7.85 (m, 4H), 8.08 (s, 1H), 8.57 (d, 1H, $J = 4.4$ Hz), 12.44 (s, 1H). ¹³C NMR (126.0 MHz, DMSO-*d*₆) δ C: 104.19, 119.18, 123.62, 125.55, 127.63, 128.65, 134.58, 136.75, 141.51, 149.45, 150.69, 153.24, 167.84. Anal. Calcd for C₁₅H₁₂N₄S (%): C, 64.26; H, 4.31; N, 19.98; S, 11.44. Found: C, 63.98; H, 4.09; N, 20.17; S, 11.39.

2-(2-(2-pyridinylmethylene)hydrazinyl)-4-(4-methoxyphenyl)-1,3-thiazole (HLS²).

HLS² was synthesized in a similar way to **HLS¹**, but using 2-bromo-4'-methoxyacetophenone (0.11 g; 0.5 mmol) instead of 2-bromoacetophenone. Yield: 0.12 g (74 %). IR (ATR, $\nu_{\max}/\text{cm}^{-1}$): 3186 (w), 3102 (w), 2950 (w), 1567 (s), 1464 (m), 1435 (m), 1353 (m), 1241 (m), 1146 (m), 1030 (w), 912 (w), 832 (m), 732 (m), 696 (m). ¹H NMR (500.26 MHz, DMSO-*d*₆) δ H: 3.78 (s, 3H), 6.97 (d, 2H, $J = 8.9$ Hz), 7.18 (s, 1H), 7.34 (m, 1H), 7.79 (d, 2H, $J = 8.9$ Hz), 7.83 (m, 1H), 7.86 (m, 1H), 8.06 (s, 1H), 8.57 (d, 1H, $J = 5.0$ Hz), 12.38 (s, 1H). ¹³C NMR (126.0 MHz, DMSO-*d*₆) δ C: 55.10, 102.01, 113.98, 119.12, 123.57, 126.85, 127.42, 136.73, 141.36, 149.43, 150.52, 153.24, 158.84, 167.67. Anal. Calcd for C₁₆H₁₄N₄OS (%): C, 61.92; H, 4.55; N, 18.05; S, 10.33. Found: C, 61.66; H, 4.39; N, 18.22; S, 10.56.

2-(2-(2-pyridinylmethylene)hydrazinyl)-4-(4-methylphenyl)-1,3-thiazole (HLS³).

HLS³ was synthesized, by previously published method,^{S143} in a similar way to **HLS¹**, but using 2-bromo-4'-methylacetophenone (0.11 g; 0.5 mmol) instead of 2-bromoacetophenone. Yield: 0.11 g (75 %). IR (ATR, $\nu_{\max}/\text{cm}^{-1}$): 3176 (w), 3109 (w), 3066 (w), 2930 (w), 2850 (w), 2717 (m), 1599 (m), 1573 (vs), 1478 (s), 1456 (w), 1431 (w), 1407 (w), 1360 (w), 1298 (w), 1271 (vs, 1148 (s), 1115 (w), 1089 (w), 1047(m), 1000 (m), 913(m), 879 (w), 839 (w), 789 (w), 766 (w), 726 (m), 681 (m), 637 (w). ¹H NMR (500.26 MHz, DMSO-*d*₆) δ H: 2.31 (s, 3H), 7.21 (d, 2H, $J = 8.0$ Hz), 7.27 (s, 1H), 7.34 (m, 1H), 7.75 (d, 2H, $J = 8.1$ Hz), 7.84 (m, 1H), 7.86 (m, 1H), 8.07 (s, 1H), 8.57 (d, 1H, $J = 4.5$ Hz), 12.40 (s, 1H). ¹³C NMR (126.0 MHz, DMSO-*d*₆) δ C: 20.78, 103.22,

119.13, 123.57, 125.46, 129.18, 131.91, 136.71, 136.88, 141.41, 149.43, 150.71, 153.24, 167.70. Anal. Calcd for C₁₆H₁₄N₄S (%): C, 65.28; H, 4.79; N, 19.09; S, 10.89. Found: C, 65.46; H, 4.84; N, 18.99; S, 10.46.

Synthesis of 1-Se:

Into suspension of **HLSe**¹ (0.10 g; 0.30 mmol) in 20 mL of MeOH, solid Co(BF₄)₂·6H₂O (0.05 g; 0.15 mmol) was added. Obtained rotten cherry solution was refluxed for 1 h. After two days emerald colored single crystals were filtered off, washed with cold MeOH and Et₂O. Yield: 0.07 g (61 %). A_M (1 × 10⁻³ M, MeOH) = 103.2 Ω⁻¹ cm² mol⁻¹. IR (ATR, ν_{\max} /cm⁻¹): 3054 (w), 1600 (m), 1570 (w), 1540 (m), 1479 (m), 1407 (vs), 1345 (s), 1233 (m), 1126 (s), 1103 (m), 1050 (m), 882 (w), 842 (w), 729 (w). ¹H NMR (500.26 MHz, DMSO-*d*₆) δ H: 6.75 (s, 1H), 6.75 (d, 2H, J = 6.4 Hz), 7.29 (ddd, 1H, J = 7.4 Hz, J = 5.9 Hz, J = 1.4 Hz), 7.40 (t, 2H, J = 7.8 Hz), 7.49 (d, 1H, J = 5.3 Hz), 7.58 (ddd, 1H, J = 7.5 Hz, J = 6.4 Hz, J = 1.2 Hz), 7.68 (dd, 1H, J = 8.0 Hz, J = 0.8 Hz), 7.82 (s, 1H), 7.95 (td, 1H, J = 7.7, Hz, J = 1.3 Hz). ¹³C NMR (126.0 MHz, DMSO-*d*₆) δ C: 110.90, 123.68, 125.99, 127.66, 128.89, 129.30, 133.13, 139.52, 141.26, 148.22, 149.33, 159.94, 183.60. Anal. Calcd for C₃₀H₂₂CoN₈Se₂BF₄ (%): C, 45.14; H, 2.78; N, 14.04. Found: C, 45.42; H, 2.54; N, 13.89 %.

Synthesis of 2-Se:

2-Se was synthesized in a similar way to **1-Se**, but using **HLSe**² (0.11 g; 0.30 mmol) instead of **HLSe**¹. XRD quality single crystals were obtained by diffusion of EtOAc vapor into the solution of **2-Se** in DMSO. Yield: 0.07 g (57 %). A_M (1 × 10⁻³ M, MeOH) = 82.4 Ω⁻¹ cm² mol⁻¹. IR (ATR, ν_{\max} /cm⁻¹): 3114 (w), 2962 (w), 2836 (w), 1603 (m), 1526 (m), 1477 (m), 1390 (s), 1340 (s), 1238 (s), 1128 (s), 1053 (s), 886 (m), 831 (m), 742 (w), 671 (w), 515 (w). ¹H NMR (500.26 MHz, DMSO-*d*₆) δ H: 3.89 (s, 3H), 6.65 (d, 2H, J = 8.4 Hz), 6.69 (s, 1H), 6.93 (d, 2H, J = 8.6 Hz), 7.29 (ddd, 1H, J = 7.2 Hz, J = 6.1 Hz, J = 0.9 Hz), 7.50 (d, 1H, J = 5.7 Hz), 7.69 (d, 1H, J = 7.7 Hz), 7.90 (s, 1H), 7.95 (td, 1H, J = 7.9 Hz, J = 0.8 Hz). ¹³C NMR (126.0 MHz, DMSO-*d*₆) δ C: 55.28, 110.57, 112.90, 123.49, 125.29, 125.77, 130.08, 139.11, 141.09, 147.97, 149.17, 159.94, 183.19. Anal. Calcd for C₃₂H₂₆CoN₈O₂Se₂BF₄H₂O (%): C, 43.86; H, 3.22; N, 12.79. Found: C, 43.52; H, 2.93; N, 12.87 %.

Synthesis of 3-Se:

3-Se was synthesized in a similar way to **1-Se**, but using **HLSe³** (0.10 g; 0.30 mmol) instead of **HLSe¹**. Yield: 0.07 g (58 %). A_M (1×10^{-3} M, MeOH) = $110.6 \Omega^{-1} \text{ cm}^2 \text{ mol}^{-1}$. IR (ATR, $\nu_{\text{max}}/\text{cm}^{-1}$): 3128 (w), 3082 (w), 1602 (m), 1530 (m), 1481 (m), 1393 (s), 1342 (s), 1318 (m), 1239 (m), 1131 (m), 1055 (s), 885 (w), 847 (w), 740 (w), 669 (w), 517 (w). ^1H NMR (500.26 MHz, DMSO-*d*₆) δH : 2.46 (s, 3H), 6.62 (d, 2H, $J = 7.7$ Hz), 6.68 (s, 1H), 7.19 (d, 2H, $J = 7.6$ Hz), 7.28 (ddd, 1H, $J = 7.4$ Hz, $J = 5.9$ Hz, $J = 1.4$ Hz), 7.48 (d, 1H, $J = 5.5$ Hz), 7.68 (dd, 1H, $J = 7.9$ Hz, $J = 0.6$ Hz), 7.83 (s, 1H), 7.94 (td, 1H, $J = 7.8$ Hz, $J = 1.3$ Hz). ^{13}C NMR (126.0 MHz, DMSO-*d*₆) δC : 21.05, 110.54, 123.42, 125.71, 127.92, 128.59, 130.16, 138.36, 139.19, 141.05, 148.12, 149.07, 159.85, 183.31. Anal. Calcd for $\text{C}_{32}\text{H}_{26}\text{CoN}_8\text{Se}_2\text{BF}_4$ (%): C, 46.52; H, 3.17; N, 13.56. Found: C, 46.74; H, 2.98; N, 13.82 %.

Synthesis of **1-S**:

1-S was synthesized in a similar way to **1-Se**, but using **HLS¹** (0.08 g; 0.30 mmol) instead of **HLSe¹**. Yield: 0.11 g (65 %). A_M (1×10^{-3} M, MeOH) = $94.4 \Omega^{-1} \text{ cm}^2 \text{ mol}^{-1}$. IR (ATR, $\nu_{\text{max}}/\text{cm}^{-1}$): 3055 (w), 1600 (m), 1570 (w), 1539 (m), 1478 (m), 1396 (s), 1346 (s), 1237 (s), 1129 (s), 1044 (s), 901 (w), 753 (w), 696 (w), 661 (w). ^1H NMR (500.26 MHz, DMSO-*d*₆) δH : 6.56 (s, 1H), 6.77 (d, 2H, $J = 6.9$ Hz), 7.29 (ddd, 1H, $J = 7.3$ Hz, $J = 6.1$ Hz, $J = 1.3$ Hz), 7.42 (t, 2H, $J = 7.7$ Hz), 7.53 (d, 1H, $J = 5.6$ Hz), 7.60 (t, 1H, $J = 7.5$ Hz), 7.66 (d, 1H, $J = 7.4$ Hz), 7.82 (s, 1H), 7.96 (td, 1H, $J = 7.8$ Hz, $J = 1.2$ Hz). ^{13}C NMR (126.0 MHz, DMSO-*d*₆) δC : 108.12, 123.28, 126.06, 127.73, 128.78, 129.54, 131.63, 139.47, 141.27, 147.89, 149.19, 159.81, 180.47. Anal. Calcd for $\text{C}_{30}\text{H}_{22}\text{CoN}_8\text{S}_2\text{BF}_4$ (%): C, 51.15; H, 3.15; N, 15.91; S, 9.10. Found: C, 51.07; H, 3.24; N, 15.72; S, 9.35 %.

Synthesis of **2-S**:

2-S was synthesized in a similar way to **1-Se**, but using **HLS²** (0.09 g; 0.30 mmol) instead of **HSe¹**. Yield: 0.07 g (63 %). A_M (1×10^{-3} M, MeOH) = $102.2 \Omega^{-1} \text{ cm}^2 \text{ mol}^{-1}$. IR (ATR, $\nu_{\text{max}}/\text{cm}^{-1}$): 3148 (w), 3079 (w), 3042 (w), 1602 (m), 1531 (m), 1494 (m), 1394 (s), 1344 (m), 1323 (m), 1243 (s), 1133 (m), 1105 (m), 1049 (m), 1019 (m), 904 (w), 820 (w), 778 (w). ^1H NMR (500.26 MHz, DMSO-*d*₆) δH : 3.23 (s, 3H), 6.47 (s, 1H), 6.65 (d, 2H, $J = 8.6$ Hz), 6.94 (d, 2H, $J = 8.6$ Hz), 7.27 (ddd, 1H, $J = 7.3$ Hz, $J = 6.1$ Hz, $J = 1.3$ Hz), 7.53 (d, 1H, $J = 5.6$ Hz), 7.65 (d, 1H, $J = 7.9$ Hz), 7.87 (s, 1H), 7.94 (td, 1H, $J = 7.8$ Hz, $J = 1.2$ Hz). ^{13}C NMR (126.0 MHz, DMSO-*d*₆) δC : 55.55, 108.06,

113.29, 123.39, 124.01, 126.08, 130.30, 139.33, 141.39, 147.98, 149.29, 160.06, 160.42, 180.45. Anal. Calcd for $C_{32}H_{26}CoN_8O_2S_2BF_4$ (%): C, 50.28; H, 3.43; N, 14.66; S, 8.39. Found: C, 50.55; H, 3.32; N, 14.78; S, 8.07. Anal. Calcd for (%): C, 52.47; H, 3.58; N, 15.30; S, 8.76. Found: C, 52.46; H, 3.39; N, 15.40; S, 8.84.

Synthesis of 3-S:

3-S was synthesized, according to the literature procedure,^{S143} in a similar way to **1-Se**, but using **HLS**³ (0.09 g; 0.30 mmol) instead of **HLSe**¹. Yield: 0.07 g (67 %). A_M (1×10^{-3} M, MeOH) = $89.10 \Omega^{-1} \text{ cm}^2 \text{ mol}^{-1}$. IR (ATR, $\nu_{\text{max}}/\text{cm}^{-1}$): 3548 (w), 3128 (w), 3074 (w), 1603 (m), 1570 (w), 1533 (s), 1486 (m), 1444 (w), 1400 (vs), 1346 (vs), 1326 (w), 1245 (s), 1136 (w), 1055 (m), 935 (w), 906 (m), 846 (w), 811 (m), 766 (m), 676 (w), 637 (w). ¹H NMR (500.26 MHz, DMSO-*d*₆) δ H: 2.46 (s, 3H), 6.50 (s, 1H), 6.64 (d, 2H, ³*J* = 8.0 Hz), 7.21 (d, 2H, ³*J* = 8.0 Hz), 7.28 (ddd, 1H, ³*J* = 7.4 Hz, ³*J* = 5.7 Hz, ³*J* = 1.4 Hz), 7.52 (d, 1H, ³*J* = 5.4 Hz), 7.65 (dd, 1H, ³*J* = 8.0 Hz, ³*J* = 0.8 Hz), 7.82 (s, 1H), 7.99 (td, 1H, *J* = 7.8 Hz, ³*J* = 1.3 Hz). ¹³C NMR (126.0 MHz, DMSO-*d*₆) δ C: 21.19, 107.98, 123.22, 125.98, 128.22, 128.66, 128.84, 138.90, 139.35, 141.01, 148.01, 149.12, 159.91, 180.43. Anal. Calcd for (%): C, 52.47; H, 3.58; N, 15.30; S, 8.76. Found: C, 52.46; H, 3.39; N, 15.40; S, 8.84%.

2-(2-(phenyl) methylene) hydrazynil)-4-(phenyl)-1,3-Selenazole (1)

2-Benzylidene hydrazine carboselenoamide (0.1 g ; 0.4 mmol) in 20 ml H₂O/ ethanol (1:1 v/v) mixture was added 2-bromoacetophenone (0.088 g ; 0.4 mmol). The reaction mixture was heated and stirred for 4 h. The obtained ocher precipitate was filtered off and washed with cold ethanol. Yield: 0.10 g (77 %). Mp: 178–180 °C. IR (ATR, $\nu_{\text{max}}/\text{cm}^{-1}$): 3298 (w), 3139 (w), 3058 (w), 2959 (w), 2852 (w), 1602 (w), 1559 (vs), 1483 (m), 1435 (m), 1347 (w), 1263 (s), 1120 (m), 1040 (w), 1023 (w), 934 (w), 754 (m), 710 (m), 689 (m), 507 (w). ¹H NMR (500.26 MHz, DMSO-*d*₆) δ : 7.29 (t, 1H, H-C14, *J* = 7.2 Hz), 7.34-7.48 (m, 5H, H-C4, H-C3 = H-C5, H-C13 = H-C15), 7.66 (d, 2H, H-C2 = H-C6, *J* = 7.2 Hz), 7.69 (s, 1H, H-C9), 7.85 (d, 2H, H-C12 = H-C16, *J* = 7.2 Hz), 8.09 (s, 1H, H-C7), 12.27 (br. s, 1H, H-N2). ¹³C NMR (126.0 MHz, DMSO-*d*₆) δ : 107.95 (C9), 126.45 (C12 = C16), 126.97 (C2 = C6), 128.01 (C14), 129.25 (C13 = C15), 129.53 (C3 = C5), 130.03 (C4), 135.04 (C1), 136.10 (C11), 142.88 (C7), 151.62 (C10), 171.93 (C8). Anal. Calcd. for $C_{16}H_{13}N_3Se$ (%): C, 58.90; H, 4.02; N, 12.88. Found: C, 58.62; H, 4.22; N, 12.67 %.

2-(2-(phenyl) methylene) hydrazynil)-4-(4-metoxyphenyl)-1,3-Selenazole (1-OMe)

Compound **1-OMe** was synthesized similarly to **1** starting from 2-benzylidene hydrazine carboselenoamide (0.1 g; 0.4 mmol) but instead 2-bromoacetophenone was used 2-bromo-4'-methoxyacetophenone (0.1 g; 0.4 mmol). Ocher solid. Yield: 0.13 g (91 %). Mp: 180–182 °C. IR (ATR, $\nu_{\max}/\text{cm}^{-1}$): 3140 (m), 3062 (m), 3004 (m), 2958 (m), 2905 (m), 2836 (m), 1612 (m), 1572 (vs), 1490 (s), 1436 (m), 1355 (m), 1320 (m), 1300 (m), 1265 (m), 1246 (s), 1175 (m), 1124 (m), 1027 (s), 937 (w), 832 (m), 755 (m), 694 (m), 610 (w), 528 (w). ^1H NMR (500.26 MHz, DMSO- d_6) δ : 3.78 (s, 3H, H-C17), 6.96 (d, 2H, H-C13 = H-C15, $J = 8.7$ Hz), 7.39 (dd, 1H, H-C4, $J = 8.3$ Hz, $J = 6.2$ Hz), 7.44 (t, 2H, H-C3 = H-C5, $J = 7.4$ Hz), 7.51 (s, 1H, H-C9), 7.67 (d, 2H, H-C2 = H-C6, $J = 7.4$ Hz), 7.78 (d, 2H, H-C12 = H-C16, $J = 8.7$ Hz), 8.09 (s, 1H, H-C7), 12.24 (br. s, 1H, H-N2). ^{13}C NMR (126.0 MHz, DMSO- d_6) δ : 55.68 (C17), 105.34 (C9), 114.50 (C12 = C16), 126.86 (C13 = C15), 127.65 (C2 = C6), 128.85 (C11), 129.42 (C3 = C5), 129.89 (C4), 135.00 (C1), 142.80 (C7), 150.78 (C10), 159.21 (C14), 171.70 (C8). Anal. Calcd. for $\text{C}_{17}\text{H}_{15}\text{N}_3\text{OSe}$ (%): C, 57.31; H, 4.24; N, 11.79. Found: C, 57.64; H, 4.35; N, 11.92 %.

2-(2-(phenyl) methylene) hydrazynil)-4-(4-metxylhenyl)-1,3-Selenazole (1-Me)

Compound **1-Me** was synthesized similarly to **1** starting from 2-benzylidene hydrazine carboselenoamide (0.1 g; 0.4 mmol) but instead 2-bromoacetophenone was used 2-bromo-4'-methylacetophenone (0.095 g; 0.4 mmol). Ocher solid. Yield: 0.07 g (51 %). Mp: 174–176 °C. IR (ATR, $\nu_{\max}/\text{cm}^{-1}$): 3143 (m), 3057 (m), 2911 (m), 2859 (m), 1617 (m), 1576 (vs), 1561 (vs), 1492 (m), 1436 (m), 1264 (m), 1039 (m), 823 (m), 751 (m), 689 (m), 611 (w). ^1H NMR (500.26 MHz, DMSO- d_6) δ : 2.31 (s, 3H, H-C17), 7.21 (d, 2H, H-C13 = H-C15, $J = 8.0$ Hz), 7.39 (t, 1H, H-C4, $J = 7.2$ Hz), 7.44 (t, 2H, H-C3 = H-C5, $J = 7.4$ Hz), 7.59 (s, 1H, H-C9), 7.67 (d, 2H, H-C2 = H-C6, $J = 7.4$ Hz), 7.72 (d, 2H, H-C12 = H-C16, $J = 8.0$ Hz), 8.09 (s, 1H, H-C7), 12.26 (br. s, 1H, H-N2). ^{13}C NMR (126.0 MHz, DMSO- d_6) δ : 21.37 (C17), 106.71 (C9), 126.29 (C12 = C16), 126.87 (C2 = C6), 129.43 (C13 = C15), 129.72 (C3 = C5), 129.91 (C4), 133.32 (C11), 134.98 (C1), 137.17 (C14), 142.80 (C7), 151.24 (C10), 171.73 (C8). Anal. Calcd. for $\text{C}_{17}\text{H}_{15}\text{N}_3\text{Se}$ (%): C, 60.00; H, 4.44; N, 12.35. Found: C, 60.23; H, 4.67; N, 12.59 %.

2-(2-(2-nitrophenyl) methylene) hydrazynil)-4-(phenyl)-1,3-Selenazole (2)

Compound **2** was synthesized similarly to **1** starting from 2-(2-nitrobenzylidene) hydrazine carboselenoamide (0.1 g; 0.3 mmol) and 2-bromoacetophenone (0.07 g; 0.3 mmol). Orange solid. Yield: 0.083 g (56 %). Mp: 183–184 °C. IR (ATR, $\nu_{\max}/\text{cm}^{-1}$): 3164 (w), 3115 (w), 3047 (w), 2963 (w), 2851 (m), 2792 (m), 1580 (vs), 1518 (vs), 1481 (m), 1438 (m), 1341 (s), 1297 (m), 1266 (s), 1128 (m), 1043 (m), 1023 (w), 918 (w), 904 (w), 847 (w), 780 (w), 747 (w), 706 (m), 660 (m). ^1H NMR (500.26 MHz, $\text{DMSO-}d_6$) δ : 7.30 (t, 1H, H-C14, $J = 7.3$ Hz), 7.39 (t, 2H, H-C13 = H-C15, $J = 7.7$ Hz), 7.61 (m, 1H, H-C5), 7.74 (s, 1H, H-C9), 7.78 (t, 1H, H-C4, $J = 7.7$ Hz), 7.84 (d, 2H, H-C12 = H-C16, $J = 7.4$ Hz), 8.01 (d, 1H, H-C3, $J = 0.7$ Hz), 8.03 (s, 1H, H-C6), 8.45 (s, 1H, H-C7). ^{13}C NMR (126.0 MHz, $\text{DMSO-}d_6$) δ : 108.77 (C9), 125.35 (C3), 126.45 (C12 = C16), 128.13 (C14), 128.29 (C6), 129.10 (C1), 129.29 (C13 = C15), 130.49 (C5), 134.16 (C4), 135.86 (C11), 137.93 (C7), 148.13 (C2), 151.39 (C10), 171.81 (C8). Anal. Calcd. for $\text{C}_{16}\text{H}_{12}\text{N}_4\text{O}_2\text{Se}$ (%): C, 51.76; H, 3.26; N, 15.09. Found: C, 52.32; H, 2.60; N, 15.14 %.

2-(2-(2-nitrophenyl) methylene) hydrazynil)-4-(4-methoxyphenyl)-1,3-Selenazole (2-OMe)

Compound **2-OMe** was synthesized similarly to **1** starting from 2-(2-nitrobenzylidene) hydrazine carboselenoamide (0.1 g; 0.3 mmol) and 2-bromo-4'-methoxyacetophenone (0.085 g; 0.2 mmol). Orange solid. Yield: 0.104 g (66 %), Mp: 165–166 °C. IR (ATR, $\nu_{\max}/\text{cm}^{-1}$): 3108 (w), 3030 (w), 2954 (w), 2901 (w), 2830 (m), 2654 (m), 2324 (w), 1603 (w), 1569 (s), 1516 (s), 1493 (m), 1441 (m), 1364 (w), 1337 (s), 1307 (m), 1242 (s), 1169 (m), 1126 (m), 1040 (m), 918 (w), 837 (m), 785 (w), 745 (w), 715 (w). ^1H NMR (500.26 MHz, $\text{DMSO-}d_6$) δ : 3.77 (s, 3H, H-C17), 6.95 (d, 2H, H-C13 = H-C15, $J = 8.8$ Hz), 7.54 (s, 1H, H-C9), 7.60 (m, 1H, H-C5), 7.74–7.80 (m, 3H, H-C4 and H-C12 = H-C16), 8.01 (d, 1H, H-C3, $J = 1.0$ Hz), 8.02 (d, 1H, H-C6, $J = 1.0$ Hz), 8.45 (s, 1H, H-C7). ^{13}C NMR (126.0 MHz, $\text{DMSO-}d_6$) δ : 55.79 (C17), 106.30 (C9), 114.63 (C13 = C15), 125.34 (C3), 127.77 (C12 = C16), 128.27 (C6), 128.67 (C11), 129.14 (C1), 130.44 (C5), 134.15 (C4), 137.95 (C7), 148.12 (C2), 150.82 (C10), 159.38 (C14), 171.73 (C8). Anal. Calcd. for $\text{C}_{17}\text{H}_{14}\text{N}_4\text{O}_3\text{Se}$ (%): C, 50.88; H, 3.52; N, 13.96. Found: C, 51.71; H, 1.95; N, 13.98 %.

2-(2-(2-nitrophenyl) methylene) hydrazynil)-4-(4-methylphenyl)-1,3-Selenazole (2-Me)

Compound **2-Mew** was synthesized similarly to **1** starting from 2-(2-nitrobenzylidene) hydrazine carboselenoamide (0.1 g; 0.3 mmol) and 2-bromo-4'-methylacetophenone (0.08 g; 0.3 mmol). Orange solid. Yield: 0.108 g (70 %). Mp: 170–171 °C. IR (ATR, $\nu_{\max}/\text{cm}^{-1}$): 3305 (w), 3156 (w), 3116 (w), 3074 (w), 2971 (w), 2917 (w), 2858 (w), 1569 (vs), 1521 (vs), 1439 (m), 1337 (s), 1294 (m), 1262 (m), 1179 (m), 1125 (m), 1038 (m), 922 (w), 846 (w), 828 (w), 748 (w), 730 (w), 709 (w). ^1H NMR (500.26 MHz, DMSO- d_6) δ : 2.30 (s, 3H, H-C17), 7.19 (d, 2H, H-C13 = H-C15, $J = 8.1$ Hz), 7.58-7.63 (m, 1H, H-C5), 7.64 (s, 1H, H-C9), 7.72 (d, 2H, H-C12 = H-C16, $J = 8.1$ Hz), 7.75-7.80 (m, 1H, H-C4), 8.01 (d, 1H, H-C3, $J = 1.0$ Hz), 8.02 (d, 1H, H-C6, $J = 1.0$ Hz), 8.45 (s, 1H, H-C7). ^{13}C NMR (126.0 MHz, DMSO- d_6) δ : 20.84 (C17), 107.03 (C9), 124.73 (C3), 125.77 (C12 = C16), 127.66 (C6), 128.50 (C1), 129.23 (C13 = C15), 129.84 (C5), 132.55 (C11), 133.53 (C4), 136.80 (C14), 137.30 (C7), 147.50 (C2), 150.71 (C10), 171.21 (C8). Anal. Calcd. for $\text{C}_{17}\text{H}_{14}\text{N}_4\text{O}_2\text{Se}$ (%): C, 53.00; H, 3.66; N, 14.54. Found: C, 52.59; H, 3.18; N, 14.36 %.

2-(2-(3-nitrophenyl) methylene) hydrazynil)-4-(phenyl)-1,3-Selenazole (3)

Compound **3** was synthesized similarly to **1** starting from 2-(4-nitrobenzylidene) hydrazine carboselenoamide (0.1 g; 0.3 mmol) and 2-bromoacetophenone (0.07 g; 0.3 mmol). Orange solid. Yield: 0.108 g (73 %). Mp: 216–218 °C. IR (ATR, $\nu_{\max}/\text{cm}^{-1}$): 3163 (w), 3062 (w), 2962 (w), 2862 (m), 2804 (w), 1608 (w), 1580 (s), 1526 (vs), 1482 (m), 1453 (m), 1345 (s), 1268 (m), 1131 (m), 1093 (w), 928 (w), 734 (m), 704 (m), 673 (w). ^1H NMR (500.26 MHz, DMSO- d_6) δ : 7.30 (t, 1H, H-C14, $J = 7.3$ Hz), 7.39 (t, 2H, H-C13 = H-C15, $J = 7.6$ Hz), 7.71 (t, 2H, ovlp. H-C5 and H-C9, $J = 7.9$ Hz), 7.84 (d, 2H, H-C12 = H-C16, $J = 7.4$ Hz), 8.08 (d, 1H, H-C6, $J = 7.8$ Hz), 8.19 (m, 2H, ovlp. H-C4 and H-C7), 8.45 (s, 1H, H-C2), 12.54 (s, 1H, H-N2). ^{13}C NMR (126.0 MHz, DMSO- d_6) δ : 107.71 (C9), 120.40 (C2), 123.49 (C4), 125.83 (C12 = C16), 127.52 (C14), 128.68 (C13 = C15), 130.49 (C5), 132.31 (C6), 135.23 (C11), 136.33 (C3), 140.02 (C7), 148.34 (C1), 150.86 (C10), 171.30 (C8). Anal. Calcd. for $\text{C}_{16}\text{H}_{12}\text{N}_4\text{O}_2\text{Se}$ (%): C, 51.76; H, 3.26; N, 15.09. Found: C, 51.54; H, 3.00; N, 15.11 %.

2-(2-(3-nitrophenyl) methylene) hydrazynil)-4-(4-methoxyphenyl)-1,3-Selenazole(3-OMe)

Compound **3-OMe** was synthesized similarly to **1** starting from 2-(4-nitrobenzylidene) hydrazine carboselenoamide (0.1 g ; 0.3 mmol) and 2-bromo-4'-methoxyacetophenone

(0.085 g; 0.3 mmol). Orange solid. Yield: 0.112 g (70 %). Mp: 201–203 °C. IR (ATR, $\nu_{\max}/\text{cm}^{-1}$): 3161 (w), 3049 (w), 2958 (m), 2829 (m), 2371 (w), 1581 (s), 1523 (vs), 1489 (m), 1452 (m), 1330 (s), 1320 (m), 1300 (m), 1272 (m), 1245 (s), 1174 (m), 1131 (s), 1032 (m), 930 (w), 834 (m), 752 (w), 731 (w), 675 (w). ^1H NMR (500.26 MHz, DMSO- d_6) δ : 3.77 (s, 3H, H-C17), 6.95 (m, 2H, H-C13 = H-C15), 7.52 (s, 1H, H-C9), 7.71 (t, 1H, H-C5, $J = 8.0$ Hz), 7.76 (m, 2H, H-C12 = H-C16), 8.08 (m, 1H, H-C6), 8.19 (m, 2H, ovlp. H-C4 and H-C7), 8.45 (m, 1H, H-C2), 12.44 (s, 1H, H-N2). ^{13}C NMR (126.0 MHz, DMSO- d_6) δ : 55.16 (C17), 105.05 (C9), 114.00 (C13 = C15), 120.37 (C2), 123.44 (C4), 127.13 (C12 = C16), 127.98 (C11), 130.47 (C5), 132.28 (C6), 136.38 (C3), 140.00 (C7), 148.33 (C1), 150.60 (C10), 158.75 (C14), 171.21 (C8). Anal. Calcd. for $\text{C}_{17}\text{H}_{14}\text{N}_4\text{O}_3\text{Se}$ (%): C, 50.88; H, 3.52; N, 13.96. Found: C, 51.55; H, 3.17; N, 14.12 %.

2-(2-(3-nitrophenyl) methylene) hydrazynil)-4-(4-methylphenyl)-1,3-Selenazole(3 Me)

Compound **3-Me** was synthesized similarly to **1** starting from 2-(4-nitrobenzylidene) hydrazine carboselenoamide (0.1 g; 0.3 mmol) and 2-bromo-4'-methylacetophenone (0.08 g; 0.3 mmol). Orange solid. Yield: 0.106 g (69 %), Mp: 203–206 °C. IR (ATR, $\nu_{\max}/\text{cm}^{-1}$): 3154 (w), 3111 (w), 3046 (w), 2912 (m), 2856 (m), 2363 (w), 1602 (w), 1575 (s), 1523 (vs), 1486 (m), 1448 (m), 1342 (s), 1266 (m), 1177 (w), 1130 (m), 1039 (m), 925 (w), 830 (w), 735 (w), 674 (w). ^1H NMR (500.26 MHz, DMSO- d_6) δ : 2.30 (s, 3H, H-C17), 7.19 (d, 2H, H-C13 = H-C15, $J = 8.0$ Hz), 7.62 (s, 1H, H-C9), 7.71 (m, 3H, ovlp. H-C5 and H-C12 = H-C16), 8.08 (d, 1H, H-C6, $J = 7.8$ Hz), 8.18 (dd, 1H, H-C4, $J = 2.3$ Hz, $J = 0.8$ Hz), 8.20 (s, 1H, H-C7), 8.44 (m, 1H, H-C2), 12.46 (s, 1H, H-N2). ^{13}C NMR (126.0 MHz, DMSO- d_6) δ : 20.82 (C17), 106.54 (C9), 120.37 (C2), 123.44 (C4), 125.74 (C12 = C16), 129.21 (C13 = C15), 130.45 (C5), 132.28 (C6), 132.50 (C11), 136.35 (C3), 136.78 (C14), 140.06 (C7), 148.32 (C1), 150.60 (C10), 171.22 (C8). Anal. Calcd. for $\text{C}_{17}\text{H}_{14}\text{N}_4\text{O}_2\text{Se}$ (%): C, 53.00; H, 3.66; N, 14.54. Found: C, 53.23; H, 3.36; N, 14.59 %.

2-(2-(4-nitrophenyl) methylene) hydrazynil)-4-(phenyl)-1,3-Selenazole (4)

Compound **4** was synthesized similarly to **1** starting from 2-(3-nitrobenzylidene) hydrazine carboselenoamide (0.1 g; 0.3 mmol) and 2-bromoacetophenone (0.07 g; 0.3 mmol). Yellow solid. Yield: 0.102 g (69 %). Mp: 228–230 °C. IR (ATR, $\nu_{\max}/\text{cm}^{-1}$):

3290 (m), 3110 (w), 1584 (w), 1554 (m), 1511 (s), 1440 (w), 1321 (m), 1282 (m), 1146 (w), 1040 (w), 920 (w), 847 (s), 774 (w), 711 (m), 689 (w). ^1H NMR (500.26 MHz, DMSO- d_6) δ : 7.30 (t, 1H, H-C14, $J = 7.3$ Hz), 7.39 (t, 2H, H-C13 = H-C15, $J = 7.6$ Hz), 7.75 (s, 1H, H-C9), 7.84 (d, 2H, H-C12 = H-C16, $J = 7.3$ Hz), 7.88 (d, 2H, H-C2 = H-C6, $J = 8.9$ Hz), 8.16 (s, 1H, H-C7), 8.26 (d, 2H, H-C3 = H-C5, $J = 8.9$ Hz), 12.65 (s, 1H, H-N2). ^{13}C NMR (126.0 MHz, DMSO- d_6) δ : 107.96 (C9), 124.14 (C3 = C5), 125.76 (C12 = C16), 126.99 (C2 = C6), 127.47 (C14), 128.61 (C13 = C15), 135.16 (C11), 139.81 (C7), 140.75 (C1), 147.14 (C4), 150.88 (C10), 171.14 (C8). Anal.Calcd.for $\text{C}_{16}\text{H}_{12}\text{N}_4\text{O}_2\text{Se}$ (%): C, 51.76; H, 3.26; N, 15.09. Found: C, 51.76; H, 3.05; N, 15.10 %.

2-(2-(4-nitrophenyl) methylene) hydrazynil)-4-(4-methoxyphenyl)-1,3-Selenazole(4-OMe)

Compound **4-OMe** was synthesized similarly to **1** starting from 2-(3-nitrobenzylidene) hydrazine carboselenoamide (0.065 g; 0.2 mmol) and 2-bromo-4'-methoxyacetophenone (0.055 g; 0.2 mmol). Single crystals suitable for X-ray diffraction analysis were obtained from acetonitrile solution after two days. Yield: 0.119 g (74 %). Mp: 208–211 °C. IR (ATR, $\nu_{\text{max}}/\text{cm}^{-1}$): 2661 (w), 1587 (m), 1565 (m), 1532 (w), 1512 (s), 1488 (m), 1454 (m), 1376 (w), 1341 (s), 1248 (m), 1172 (m), 1142 (m), 1106 (m), 1044 (m), 1022 (m), 925 (m), 908 (w), 876 (w), 840 (m), 747 (w), 684 (w). ^1H NMR (500.26 MHz, DMSO- d_6) δ : 3.78 (s, 3H, H-C17), 6.95 (d, 2H, H-C13 = H-C15, $J = 8.8$ Hz), 7.56 (s, 1H, H-C9), 7.76 (d, 2H, H-C12 = H-C16, $J = 8.7$ Hz), 7.78 (d, 2H, H-C2 = H-C6, $J = 8.8$ Hz), 8.16 (s, 1H, H-C7), 8.26 (d, 2H, H-C3 = H-C5, $J = 8.8$ Hz) 12.58 (s, 1H, H-N2). ^{13}C NMR (126.0 MHz, DMSO- d_6) δ : 55.15 (C17), 105.49 (C9), 113.99 (C13 = C15), 124.18 (C3 = C5), 127.02 (C2 = C6), 127.12 (C12 = C16), 127.94 (C11), 139.84 (C7), 140.87 (C1), 147.16 (C4), 150.88 (C10), 158.76 (C14), 171.18 (C8). Anal.Calcd.for $\text{C}_{17}\text{H}_{14}\text{N}_4\text{O}_3\text{Se}$ (%): C, 50.88; H, 3.52; N, 13.96. Found: C, 50.80; H, 3.30; N, 14.02 %.

2-(2-(4-nitrophenyl) methylene) hydrazynil)-4-(4-methylphenyl)-1,3-Selenazole (4-Me)

Compound **4-Me** was synthesized similarly to **1** starting from 2-(3-nitrobenzylidene) hydrazine carboselenoamide (0.1 g; 0.3 mmol) and 2-bromo-4'-methylacetophenone (0.08 g; 0.3 mmol). Single crystals suitable for X-ray diffraction analysis were obtained

from acetonitrile solution after three days. Yield: 0.111 g (72 %), Mp: 228–230 °C. IR (ATR, $\nu_{\max}/\text{cm}^{-1}$): 3110 (w), 2922 (w), 2668 (m), 1608 (m), 1587 (s), 1565 (s), 1513 (vs), 1456 (s), 1409 (w), 1374 (w), 1341 (vs), 1320 (s), 1285 (s), 1177 (w), 1144 (m), 1107 (w), 1042 (m), 924 (w), 907 (w), 849 (w), 828 (m), 746 (w). ^1H NMR (500.26 MHz, DMSO- d_6) δ : 2.30 (s, 3H, H-C17), 7.19 (d, 2H, H-C13 = H-C15, $J = 8.0$ Hz), 7.65 (s, 1H, H-C9), 7.72 (d, 2H, H-C12 = H-C16, $J = 8.1$ Hz), 7.88 (d, 2H, H-C2 = H-C6, $J = 8.9$ Hz), 8.16 (s, 1H, H-C7), 8.25 (d, 2H, H-C3 = H-C5, $J = 8.9$ Hz), 12.58 (s, 1H, H-N2). ^{13}C NMR (126.0 MHz, DMSO- d_6) δ : 20.83 (C17), 107.10 (C9), 124.19 (C3 = C5), 125.76 (C12 = C16), 127.03 (C2 = C6), 129.23 (C13 = C15), 132.48 (C11), 136.83 (C14), 139.80 (C7), 140.86 (C1), 147.17 (C4), 150.56 (C10), 171.19 (C8). Anal. Calcd. for $\text{C}_{17}\text{H}_{14}\text{N}_4\text{O}_2\text{Se}$ (%): C, 53.00; H, 3.66; N, 14.54. Found: C, 53.37; H, 3.22; N, 14.70 %.

3.3 X-ray crystallography

The single-crystal X-ray diffraction data were collected on a Gemini S diffractometer (Oxford Diffraction) equipped with a Sapphire CCD detector. Graphite monochromated Mo $K\alpha$ radiation was employed in all experiments. The *CrysAlisPro*¹⁴⁴ was used for raw data integration and reduction. Structures were solved by using *SHELXT*,¹⁴⁵ and refined by *SHELXL-2015*¹⁴⁶ program. The *SHELXLE*¹⁴⁷ was used as a graphical user interface for refinement procedures. All non-hydrogen atoms were refined anisotropically, while hydrogen atoms were treated by a riding model in geometrically idealized positions, with their $U_{\text{iso}} = kU_{\text{eq}}$ of their parent atoms ($k = 1.5$ for CH_3 , 1.2 for all other hydrogen atoms). In complex **2-Se**, hydrogen atoms belonging to water molecule could not be located in the electron density maps.

In complex **3-Se**, the BF_4^- ion is modeled; as disordered between two positions. Common occupational numbers were refined for oxygen atoms belonging to two orientations. Distance and ADP similarity restraints were employed in the refinement to achieve reasonable geometry.

Diffraction pattern of **3-S** specimen showed $6/mmm$ symmetry, however, the structure could not be solved in hexagonal space groups. Closer inspection of the diffraction data revealed several signs of twinning.¹⁴⁸ The structure was solved in trigonal $P3_121$ space group using *SIR92*,¹⁴⁹ but it could not be adequately refined. The

analysis with *TWINROT* in *PLATON*¹⁵⁰ indicated twinning by merohedry with the twin law $-1\ 0\ 0, 0\ -1\ 0, 0\ 0\ 1$. The structure was therefore refined as a four-component twin as described in literature.¹³

Structures were validated with the *PLATON*,¹⁵⁰ and extensive use of the Cambridge Structural Database System.¹⁵³ Crystallographic data for the complexes have been deposited with the Cambridge Crystallographic Data Centre as Supplementary Publication No. CCDC 1523111-1523115. A copy of these data can be obtained, free of charge, via <https://summary.ccdc.cam.ac.uk/structure-summary-form>, or by emailing data_request@ccdc.cam.ac.uk.

3.4 Cyclic voltammetry and spectroelectrochemistry

The cyclic voltammetry experiments were done on a PST050 Voltalab instrument. Three-electrode cell consisted of a glassy carbon (GC) disk electrode (3 mm) polished with alumina suspension before each voltammetric curve, Pt wire counter electrode and a saturated calomel electrode (SCE) as a reference one. Voltammetric measurements were done in a potential range + 1.5 V to – 2.1 V, applying sweep rates from 0.010 V/s to 2 V/s. The solutions of the compounds (0.2 mmoldm⁻³ – 1.2 mmoldm⁻³) were prepared in doubly distilled *N,N*-dimethylformamide (DMF) with tetrabutylammonium perchlorate (TBAP) as supporting electrolyte. The solutions were carefully deaerated by purging nitrogen before an experiment and a strong stream of the gas was maintained during the measurements.

Spectroelectrochemical spectra were recorded on a Cary 100scan UV-visible spectrophotometer with a μ -Autolab type III potentiostat. Herein, spectroelectrochemical cell was constructed by loading a transparent Pt grid working electrode into 1mm path length thin layer channel in the quartz cuvette and mounting the other two electrodes above the channel.

3.5 MS/MSⁿ study

The mass spectrometer used was the LTQ XL linear ion trap (Thermo Fisher Scientific, Waltham, MA, USA) with electrospray ionization (ESI). The results were processed using the Xcalibur® version 2.3 (Thermo Fisher) software package. Tuning of the mass spectrometer was performed automatically. MS and MSⁿ experiments were

performed using standards in methanol at a concentration of $10 \mu\text{g mL}^{-1}$. Standards were delivered by a syringe pump at a flow rate of $10 \mu\text{L min}^{-1}$, and mixed through a T-piece with the LC effluent that contained 99 % of methanol and 1 % of 10 % acidic acid. The mobile-phase flow rate was 0.3 mL min^{-1} . Mass spectra for all the compounds were obtained in positive and negative ESI mode. For all experiments in the positive ESI mode, the source voltage was set at 5 kV. Nitrogen was used as a sheath and auxiliary gas, and values (a scale of arbitrary units in the 0–100 range defined by the LTQ XL system) of their flow rate were 32 and 8 respectively. The capillary temperature was maintained at 350°C . Capillary voltage and tube lens voltage were set at 6 and 75 V, respectively. In negative ESI mode parameters were set as: source voltage was 4 kV, sheath gas flow rate was 32, aux gas flow rate was 8, capillary voltage was -19 V and tube lens voltage was -142 V . Helium was used as the collision gas in the ion trap. The collision energy values were manually optimized for each compound. The maximum inject time for MS experiments was 50 ms and the number of microscans per scan was 2, while for MSⁿ experiments, maximum inject time was 100 ms and number of microscans was 3. Full scan mode was used to acquire mass spectra and to select the precursor ions for product ion spectra.

3.6 Computational methodology

All the quantum chemical calculations for investigated ligands and complexes were performed under the density functional theory (DFT), using the Gaussian 09 program package.¹⁵⁴ Initial geometries of neutral *E*- and *Z*-isomeric form of ligands were optimized with Becke's gradient-corrected exchange correlation in conjunction with the Lee-Yang-Parr correlation functional with three parameters (B3LYP),^{155,156} while the full geometry optimizations of the crystal structures of Co(III) complexes were carried out using BP86 (the Gaussian program specified as BVP86)^{157–159} functional, in the gas phase. Polarized 6-31G(d,p) basis set for Co atom and 6-31G(d) for N, C, O, S, Se and H atoms were used in all theoretical calculations.^{160–163} The stability of optimized geometries was confirmed by the frequency calculations, which were obtained without any imaginary wavenumber values, at the selected level of theory for ligands and complexes. The gas phase calculated molecular structures were re-optimized in DMF and DMSO solvent using the polarisable continuum model

(PCM)¹⁶⁴ with the B3LYP and BVP86 functionals for ligands and complexes, respectively. Theoretical NMR chemical shifts were calculated at DFT/B3LYP(d,p) level of theory using Gauge-Independent Atomic Orbital (GIAO)¹⁶⁵ approximation in DMSO, as a solvent. The absorption spectra and the transition energy evaluations were carried out within time dependent density functional theory (TD-DFT) approach, using B3LYP functional and DMF solvent. Since the parameters for the DMF solvent are not specified in SCRF module in Gaussian program, following the previous studies,^{166,167} the DMF was specified with the parameters: $\epsilon = 36.71$, numeral density = 0.00778 particles \AA^{-3} , $\text{epsinf} = 1.75$, $\text{rsolv} = 2.647 \text{ \AA}$ and $\text{vmol} = 77.4 \text{ cm}^3 \text{ mol}^{-1}$.

In addition, the Fukui function was used to illustrate the electrophilicity of the several atoms of investigated ligands and complexes. Parr and Yang showed that sites in chemical species with the largest values of Fukui Function $f(r)$ are those with higher reactivity. The Fukui $f(r)$ function is defined as:^{168,169}

$$f(r) = \left(\frac{\partial \rho(r)}{\partial N} \right)_v \quad (3.1)$$

where $\rho(r)$ is the total electron density of the molecule, N is the number of electrons and r is the external potential exerted by the nucleus. Thus, the condensed Fukui function of the atom A in a molecule with N electrons can be defined as:

$$f_A^+ = q_N^A - q_{N+1}^A \text{ for nucleophilic attack} \quad (3.2)$$

$$f_A^- = q_{N-1}^A - q_N^A \text{ for electrophilic attack} \quad (3.3)$$

where, q_N^A , q_{N+1}^A and q_{N-1}^A are the electronic population of the atom A in neutral, anionic and cationic forms, respectively. The above the electronic population can be obtained from the natural bond orbital (NBO) calculations.¹⁷⁰

3.7 Multi parameter correlation analysis

The contributions of the solvent-solute interactions on the shifts in UV spectra, *i.e.* interactions with the surrounding media (solvent), were investigated by the use of linear solvation energy relationships (LSER) principles. The effects of solvent dipolarity/polarizability and solvent-solute hydrogen bonding interactions were evaluated by means of the LSER model of Kamlet-Taft¹⁷¹ eq. (3.4):

$$\nu_{\max} = \nu_o + s\pi^* + b\beta + a\alpha \quad (3.4)$$

where ν_{\max} is the absorption maxima shifts, π^* is an index of the solvent dipolarity/polarizability; β is a measure of the solvent hydrogen-bond acceptor (HBA) basicity; α is a measure of the solvent hydrogen-bond donor (HBD) acidity, and ν_o is the regression value in cyclohexane as reference solvent. The solvent parameters used in eq. (3.4) are given in Table 7.1^{172,173}. The regression coefficients s , b and a in eq. (3.4) measure the relative susceptibilities of the absorption frequencies to the solvent effect.

The effects of solvent dipolarity, polarizability and solvent-solute hydrogen bonding interactions were evaluated by means of the linear solvation energy relationship (LSER) model of Catalán⁸⁰, given by eq. (3.5):

$$\nu_{\max} = \nu_o + aSA + bSB + cSP + dSdP \quad (3.5)$$

where SA, SB, SP and SdP characterize solvent acidity, basicity, polarizability and dipolarity of a solvent, respectively; and a to d are the regression coefficients describing the sensitivity of the absorption maximum to the different types of the solvent-solute interactions. The solvent parameters used in eq. (3.4) are given in Table 7.2²². Separation of non-specific solvent effects, term π^* in eq. (3.4), into two terms: dipolarity and polarizability, SP and SdP in eq. (3.5), contribute to advantageous analysis of the solvatochromism of studied compounds.

3.8 Biological experiments

3.8.1 Antimicrobial activity

The antimicrobial activity was determined using four different strains of the Gram-positive bacteria: *Staphylococcus aureus* (ATCC 6538), *Kocuria rhizophila* (ATCC 9341), *Clostridium sporogenes* (ATCC 19404), *Bacillus subtilis* (ATCC 6633), four different strains of the Gram-negative bacteria: *Escherichia coli* (ATCC 25922), *Salmonella enterica* subsp. *enterica* serovar Enteritidis (ATCC 13076), *Proteus hauseri* (ATCC 13315), *Pseudomonas aeruginosa* (ATCC 9027) and three strains of the fungi: *Candida albicans* (ATCC 10231), *Sacharomyces cerevisiae* (ATCC 9763) and *Aspergillus brasiliensis* (ATCC 16404). Antimicrobial activity was determined by well diffusion method.¹⁷⁴ In each Petri dish (90mm diameter) 22 mL of Nutrient agar (Hi Media, Mumbai, India) and 100 μ L of bacterial suspension (10^6 cells/dish) were added, while for antifungal activity in each sterile Petri dish (90 mm diameter) 22 mL of Sabouraud dextrose agar suspension (Torlak, Belgrade, Serbia) was poured and 100 μ L

of fungi (10^5 spores/dish) were added. Eight millimeter diameter well was then punched carefully using a sterile cork borer and 100 μL of test substance (1 mg/100 μL DMSO) were added into each labeled well. Amikacin (30 $\mu\text{g}/100 \mu\text{L H}_2\text{O}$) was used as a positive control for bacteria, nystatin (30 $\mu\text{g}/100 \mu\text{L DMSO}$) was used as a positive control for fungi, while 100 μL of water and DMSO served as a negative controls. The same procedure was repeated for different microorganisms. After the inoculation of the organisms, compounds and controls, the plates were incubated for 24 h at 37 $^\circ\text{C}$ for bacteria and 48 h at 28 $^\circ\text{C}$ for fungi. Antimicrobial activity was determined by measuring the diameter of inhibition zone. Zones of inhibition were recorded in mm.

3.8.2 Antioxidant activity

3.8.2.1 Free-radical scavenging antioxidant assay

The proton donating ability was assayed using a protocol for the determination of radical scavenging activity¹⁷⁵. Compounds were dissolved in pure DMSO and were diluted into ten different concentrations. Commercially available DPPH was dissolved in methanol at a concentration of 6.58×10^{-5} M. Into a 96-well microplate, 140 μL of DPPH solution was loaded and 10 μL DMSO solution of the tested compounds was added, or pure DMSO (10 μL) as the control. The microplate was incubated for 30 min at 25 $^\circ\text{C}$ in the dark and the absorbance was measured at 517 nm. The scavenging activity of the compounds was calculated using the eq. (3.6):

$$\text{Scavenging activity (\%)} = (A_{\text{control}} - A_{\text{sample}})/A_{\text{control}} \times 100 \quad (3.6)$$

where A_{sample} and A_{control} refer to the absorbances at 517 nm of DPPH in the sample and control solutions, respectively. IC_{50} values were calculated from the plotted graph of scavenging activity against the concentrations of the samples. IC_{50} is defined as the total antioxidant concentration necessary to decrease the amount of the initial DPPH radical by 50 %. IC_{50} was calculated for all compounds based on the percentage of DPPH radicals scavenged. Ascorbic acid (vitamin C) was used as the reference compound (positive control) with concentrations from 10 to 500 μM .

3.8.2.2 Total reducing power (TRP) (modified potassium ferricyanide reduction method)

The mixture containing 0.5 mL of phosphate buffer (0.2 M, pH 6.6), 0.5 mL of $K_3[Fe(CN)_6]$ (1%; w/v) and 0.5 mL of the samples (100-1500 μ M) was incubated at 50°C for 20 min. After the addition of 0.5 mL of trichloroacetic acid (TCA, 10%; w/v), 0.5 mL of Milli-Q water and 0.5 mL of $FeCl_3$ (0.1%; w/v), followed by intensive vortexing, the absorbance of the resulting mixture was measured after 60 min at 700 nm against phosphate buffer as blank ¹⁷⁶.

3.8.2.3 Total antioxidant capacity (TAOC) (modified phosphomolybdenum method)

Volume of 0.4 mL of sample solution (50-1000 μ M) was combined with 1.6 mL of reagent solution (0.6 M sulfuric acid, 28 mM sodium phosphate, and 4 mM ammonium molybdate) and resulting mixtures were incubated at 95 °C for 90 min. The cooled reaction mixtures were then centrifuged (3000 rpm for 10 min). The absorbance of the supernatant solution was measured, 1 h after centrifugation, at 695 nm against reagent solution as blank. An increased absorbance in reading in both assays indicated increased antioxidant power, expressed as EC_{50} values (the sample concentration giving absorbance of 0.500 from the graph of absorbance at 700 nm or 695 nm against compound concentration)¹⁷⁷.

3.8.2.4 Oxygen radical absorbance capacity (ORAC) assay

ORAC assay was performed by modified original protocol ¹⁷⁸. Stock solutions of fluorescein substrate (5 μ M) and free radical generator AAPH (0.5 M) were prepared in 75 mM potassium phosphate buffer (pH 7.4). Volume of 100 μ L of sample solutions or Trolox in DMSO (20 μ M) were mixed with 1485 μ L of buffer and 15 μ L of fluorescein solution. The 30 min reaction at 37 °C was initiated by adding 250 μ L of AAPH solution. Fluorescence conditions were as follows: excitation and emission wavelengths 485 and 511 nm, respectively, slits 2 nm. The relative sample ORAC value was expressed as Trolox equivalents (TE).

3.8.3 Anticancer activity

3.8.3.1 Artemia salina cytotoxicity test (I series)

A teaspoon of lyophilized eggs of the brine shrimp *Artemia salina* was added to 1 L of the artificial sea water containing several drops of yeast suspension (3 mg of dry yeast in 5 mL distilled water), and air was passed through the suspension thermostated at 301 K, under illumination for 24 h. The tested substances were dissolved in DMSO. In a glass vial, into 1 mL of artificial sea water 1–2 drops of yeast extract solution (3 mg in 5 mL of distilled water) and 10–20 hatched nauplii were added, and finally solutions of all derivatives to the appropriate concentrations. For each concentration, three determination were performed. The vials were left at 301 K under illumination for 24 h, and afterwards live and dead nauplii were counted. LC₅₀ was defined as the concentration of a drug that causes death of 50 % nauplii. DMSO was inactive under applied conditions.

3.8.3.2 Cell cultures (I series)

Human mammary adenocarcinoma (MCF-7, ATCC® HTB-22) cell line was maintained in DMEM high glucose medium (Dominique Dutscher, 67172 Brumath cedex, France, Cat. No L0102-500), supplemented with heat-inactivated 10% (v/v) fetal bovine serum (FBS, Life Technologies, Paisley, UK, Cat. No 10270-106) and 1% (v/v) penicillin-streptomycin (10,000 units mL⁻¹ and 10,000 µg mL⁻¹, Life Technologies, Paisley, UK, Cat. No 15140-122). Cells were kept at 37 °C in humidified atmosphere containing 5% (v/v) CO₂ during their exponential growing phase and in the course of incubation with investigated compounds. Investigated compound **1** was initially dissolved in DMSO to the stock concentration of 20 mM, whereas CDDP and starting cobalt salt were dissolved in phosphate buffer saline (PBS) to the stock concentration of 5 mM. Further dilutions of the compounds were performed with DMEM medium immediately before each experiment. The ligand HL could not be tested due to low solubility in the culture medium.

3.8.3.3 Annexin-V / propidium iodide (PI) double staining and determination of ED₅₀ concentrations on 2-D tumor model (I series)

MCF-7 cells were seeded in flat bottom 96 well plates (BD Falcon, Cat. No 353072) at a density of 10,000 cells per 0.1 mL of media. Next day, CDDP, **1** and starting cobalt salt were added in a range of six concentrations (1–100 µM), in a volume of 0.1 mL. For controls, non-treated cells, cells treated with 0.5% DMSO and cells

treated with 50 μ M Celastrol (Enzo Life Sciences, Farmingdale, US) were used. After 24 h of incubation, supernatant with non-adherent cells were removed to another plate. Fresh PBS was added to remaining adherent cells afterwards plates were centrifuged on 450g for 10 min. Supernatant was discarded and 200 μ L of trypsin-EDTA (BioWest, Nuaille, France, Cat. No L0930-100) was added to each well. Cells were detached in about 15 min of incubation at 37 °C, afterwards another spinning cycle with supernatant elimination were performed. Finally, previously removed supernatant with non-adherent cells were added to trypsinized cells and stained with Annexin-V-FITC (Immuno Tools, Friesoythe, Germany, Cat. No 31490013) and PI (Miltenyl Biotec Inc, Auburn, USA, Cat. No 130-093-233) in a volumes of 3 μ L. Plates were analyzed on Guava EasyCyte™ micro-capillary flow cytometer (Millipore, Merck, Darmstadt, Germany) using InCyte® software package. Percentages of all cell death events (Annexin-V single-stained, PI single-stained and double-stained cells) were summarized for each of six concentrations,. The computed percentages were plotted against corresponding concentrations on a concentration-response graph. ED₅₀ concentration was calculated as the one that corresponds to half-way of the sigmoidal concentration-dependent curve using asymmetric five-parameter logistic equation (GraphPad Prism 6 software).

3.8.3.4 Evaluation of a single-drug activity on 3-D tumor model (I series)

3-D MCF-7 mamospheres were made in 96 well plates (Corning, Sigma-Aldrich, St. Louis, Mo, USA, Cat. No 4515). Tumors were left to grow for additional four days, afterwards CDDP and **1** were added in concentrations of 100, 10, and 1 μ M. Evaluation has been maintained during eight day incubation period, with media exchanged on day four. Changes in the tumors sizes have been assessed on Celigo® imaging cytometer (Cyntellect, Brooks Life Science Systems, Poway, CA, USA) using Celigo software. Spheroids areas were determined using Celigo software, and growth rates were computed for every other day of incubation by dividing the area on the day-n with the area on the day 0.

3.8.3.5 Evaluation of a combination drug activity on 3-D tumor model (I series)

Spheroids were prepared as described above, and after four day growth drugs were added in combinations. Complex **1** was tested in combinations with CDDP and paclitaxel respectively and together as a three drug combination, with the single-drug

treated spheres as positive controls for each drug in a combination. Treatments lasted for eight days with exchange of media on fourth day. Changes in sizes of spheres were assessed as described above for the days zero, four, and eight of incubation. Computed growth rates for the day eight were used to determine the type of interaction between drugs in combinations expressed as combination indexes (CI) using CalcuSyn software (Biosoft, Cambridge, United Kingdom). The CI value defines type of interaction between drugs as following: for $CI < 0.9$ interaction is synergistic, for $0.9 < CI < 1.1$ interaction is additive, and for $CI > 1.1$ interaction is antagonistic.

3.8.3.6 Antiproliferative activity (II series)

The *in vitro* antiproliferative activity of investigated compounds was evaluated using the protocol of the National Cancer Institute (NCI) of the United States¹⁷⁹. As a model, a panel of six human solid tumor cell lines was used; namely A549 (non-small cell lung), HBL-100, (breast), HeLa (cervix), SW1573 (non-small cell lung), as drug sensitive lines, T-47D (breast) and WiDr (colon) as drug resistant lines. Cells were maintained in 25 cm² culture flasks in RPMI 1640 supplemented with 5% heat inactivated fetal calf serum and 2 mM L-glutamine in a 37 °C, 5% CO₂, 95% humidified air incubator. Exponentially growing cells were trypsinized and re-suspended in antibiotic containing medium (100 units penicillin G and 0.1 mg of streptomycin per mL). Single cell suspensions displaying >97% viability by trypan blue dye exclusion were subsequently counted. After counting, dilutions were made to give the appropriate cell densities for inoculation onto 96-well microtiter plates. Cells were inoculated in a volume of 100 µL per well at densities of 2500 (A549, HBL-100, HeLa and SW1573) or 5000 (T-47D and WiDr) cells per well, based on their doubling times. Compounds to be tested were dissolved in DMSO at an initial concentration of 40 mM. Control cells were exposed to an equivalent concentration of DMSO (0.25% v/v, negative control). Each compound was tested in triplicate at different dilutions in the range of 1-100 µM. The drug treatment was started on day 1 after plating. Drug incubation times were 48 h, after which time cells were precipitated with 25 µL ice-cold trichloroacetic acid (50% w/v) and fixed for 60 min at 4 °C. Then the sulforhodamine B (SRB) assay was performed¹⁸⁰. The optical density (OD) of each well was measured at 530 nm, using BioTek's PowerWave XS Absorbance Microplate Reader. Values were corrected for background OD from wells only containing medium. Antiproliferative activity of the

compounds was expressed as GI₅₀, that is, the concentration of the compound that inhibits 50% of the culture growth.

3.8.4 Monoamine oxidase A/B inhibition

Monoamine oxidase (MAO) A and B inhibition capacities were investigated using a discontinuous fluorimetric assay as described previously with some modifications by using human recombinant membrane-bound MAO purchased from Sigma-Aldrich¹⁸¹. Briefly, assays were conducted in a total assay volume of 100 μL (max. 1% DMSO) using black, flat-bottom 96 well plates (greiner bio-one GmbH, Austria), while pipetting was automated using a EVO freedom pipetting robot (Tecan Trading AG, Switzerland). Remained enzyme activity with inhibitor, either 1 μM (one-point) or concentrations ranging from 0.0001 μM to 10 μM , was assessed in the presence of 2-fold K_M concentrations of kynuramine ($K_M = 30 \mu\text{M}$ for MAO A and $K_M = 20 \mu\text{M}$ for MAO B) in pre-warmed potassium phosphate buffer (50 mM, pH = 7.4). Reactions were started by addition of MAO A (1.25 ng μL^{-1} , 900 units/mL) or MAO B (1.67 ng μL^{-1} , 375 units/mL) and stopped by manual addition of 35 μL sodium hydroxide (2 N) after 20 min. Enzyme activity was determined by detection ($\lambda_{\text{EX}}=320\pm 20 \text{ nm}$, $\lambda_{\text{EM}}=405\pm 20 \text{ nm}$) of 4-hydroxyquinoline using an infinite M1000 Pro microplate reader (Tecan Trading AG, Switzerland). Data were analysed using GraphPad PRISM 6 by plotting relative fluorescence units (RFU) against log inhibitor concentrations and using the implemented non-linear regression “log inhibitor vs. response (three parameters)”. For one-point measurements data were calculated as percentage of control and expressed as mean \pm standard deviation (%). Data were obtained from two (on-point measurements) or at least three (IC₅₀ values) independent experiments, each performed in duplicates.

4 RESULTS AND DISCUSSION

Within this dissertation, two groups of compounds, pyridine-2-carboxaldehyde-seleno(thio)semicarbazone (Scheme 3.3) and nitro (*o*, *p* and *m*) benzaldehyde-selenosemicarbazone (Scheme 3.3) were synthesized, which were tested for biological and antioxidant activity, a particular structure in the solution, and for substances obtained in the form of crystals suitable for RSA and Solid state. In addition, theoretical calculations of elements of geometry, physical and chemical properties, as well as correlation of properties and activities with the structure of synthesized compounds have been carried out.

The first Co(III) complexes with first class of ligands (**Hfpse(t)sc**) were prepared in order to obtain more biological potent derivatives (Scheme 3.2). Finally the comparative structural, electrochemical and DFT studies with sulphur analogues was done to elucidate in more detail the impact of chalcogen atom nature on chemical as well as biological features of these two classes of compounds.

4.1 Pyridine-2-carboxaldehyde-based (1,3-selenazol-2-yl)hydrazones

4.1.1 Synthesis and structural characterization of first series **HL(S/Se)**¹⁻³

Preparation of **HLS**⁽¹⁻³⁾ by reaction of 2-formylpyridine thiosemicarbazone (**Hfptsc**) with appropriate derivative of 2-bromoacetophenone in 2-propanol at room temperature was already described in the literature.⁵² In this procedure CaCO₃ served as a base in order to prevent formation of HBr salts of desired thiazoles. In the case of **HLS**³ single crystals suitable for X-ray diffraction analysis (XRD) were obtained by recrystallization from non-polar solvent mixture (toluene/hexane, 7:3, v/v).⁵² XRD revealed that *Z* isomer of **HLS**³ was obtained. Our attempt to obtain all ligands from chalcogen semicarbazones and corresponding bromoacetophenones in EtOH as a solvent resulted in red precipitates for which, based on results of elemental analysis and molar conductivity measurements, general formula **HL(S/Se)**¹⁻³ × **HBr** can be established. Addition of water in DMF or EtOH solutions of **HL(S/Se)**¹⁻³ × **HBr** caused deprotonation and precipitation of neutral ligands in the form of yellow solids.

The same solvent mixture was applied for preparation of $\mathbf{HL(S/Se)^{1-3}}$. In NOESY spectrum of $\mathbf{HLSe^3}$ there is the same correlation signal which indicates the presence of $E\text{-HLSe}^3$ isomer in $\text{DMSO-}d_6$ solution (Figure 4.1).

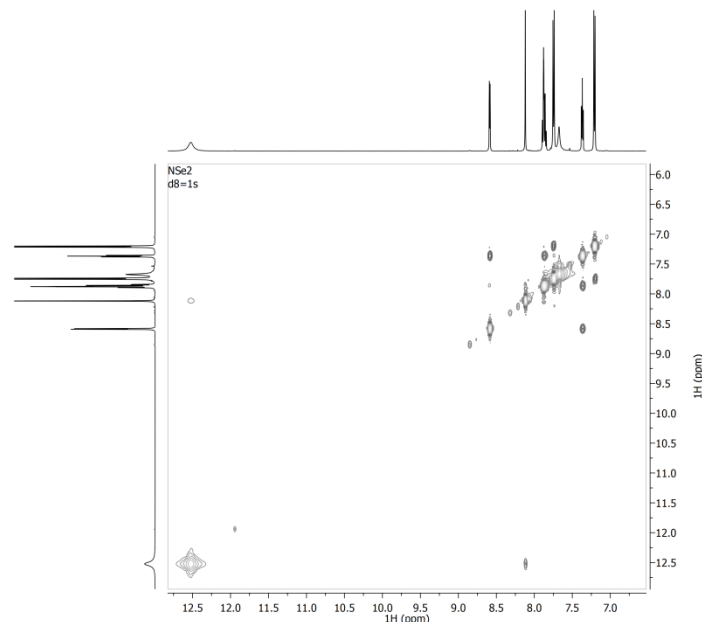


Figure 4.1 2D NOESY spectrum of \mathbf{HLSe}^3 in $\text{DMSO-}d_6$.

Signals of imine hydrogen atom in ^1H NMR spectra of $\mathbf{HL(S/Se)^{1-3}}$ lie in the narrow region 12.38–12.54 ppm which is consistent with existence of E isomeric form of all ligands. Namely, formation of intramolecular hydrogen bond between N–NH hydrogen atom and pyridine nitrogen atom in Z -isomeric form of pyridine based hydrazones causes significant downfield shift ($\sim 2\text{--}3$ ppm) of N–NH hydrogen atom signal.^{182,183} The purity and composition of the ligands $\mathbf{HLSe}^{(1-3)}$ and $\mathbf{HLS}^{(1-3)}$ was confirmed by elemental analysis. Products were soluble in N,N -dimethylformamide (DMF) and dimethyl sulfoxide (DMSO), partially soluble in acetonitrile, chloroform, ethanol and methanol and insoluble in diethyl-ether and water. Structural characterization of the ligands was done NMR spectroscopy (Figure 7.1–Figure 7.26).

4.1.1.1 Crystal structure analysis of \mathbf{HLS}^3

Crystal data and refinement results for the ligand \mathbf{HLS}^3 is summarized in Table 4.1, while molecular structures are depicted in Figure 4.2.

Table 4.1 Data collection and refinement parameters for the crystal structures of the HLS³

HLS ³			
Chemical formula	C ₁₆ H ₁₄ N ₄ S	R_{int}	0.026
Formula weight	294.37	$(\sin \theta/\lambda)_{\text{max}}$ (Å ⁻¹)	0.680
Temperature (K)	294	$R[F^2 > 2\sigma(F^2)]$	0.041
		$wR(F^2)$	0.132
		S	1.08
Wavelength (nm)	0.71073	No. of reflections	3489
Crystal system	Monoclinic	No. of parameters	195
Space group	$P2_1/c$	$\Delta_{\text{max}}, \Delta_{\text{min}}$ (e Å ⁻³)	0.31, –
a, b, c (Å)	7.9329 (4), 8.6465 (3), 21.5857 (9)	Absolute structure	/
α, β, γ (°)	90, 99.822 (4), 90	Absolute structure	/
V (Å ³)	1458.90 (11)	parameter	
Z	4	No. of measured,	12639
		independent and	3489
		observed [$I > 2\sigma(I)$]	2755
μ (mm ⁻¹)	0.22	R_{int}	0.026
Crystal size (mm)	0.70 × 0.17 × 0.07	$(\sin \theta/\lambda)_{\text{max}}$ (Å ⁻¹)	0.680
		$R[F^2 > 2\sigma(F^2)]$	0.041
		$wR(F^2)$	0.132
$T_{\text{min}}, T_{\text{max}}$	0.922, 0.986	S	1.08
		No. of reflections	3489
		No. of parameters	195
No. of measured,	12639	No. of parameters	195
independent and	3489	$\Delta_{\text{max}}, \Delta_{\text{min}}$ (e Å ⁻³)	0.31, –
observed [$I > 2\sigma(I)$]	2755		0.37

The ligand is planar within 0.18 Å and adopts a conformation in which pyridine N4 and azomethine N3, and azomethine N3 and thiazole N1 atoms are mutually in *trans* positions (Figure 4.2 (a)). This implies that conformational rearrangement is necessary for metal binding in an expected and observed tridentate way. Crystal structure of

HLS³(Figure 4.2(b)) is dominated by hydrogen bonds between the N4H groups and pyridine nitrogen atoms that give rise to infinite 1-D chains along *b*-axis. The stacking interactions between neighboring pyridine and tolyl fragments expand these 1-D chains into 2-D supramolecular layers parallel to (001) (Figure 4.2 (c), Table 4.2).

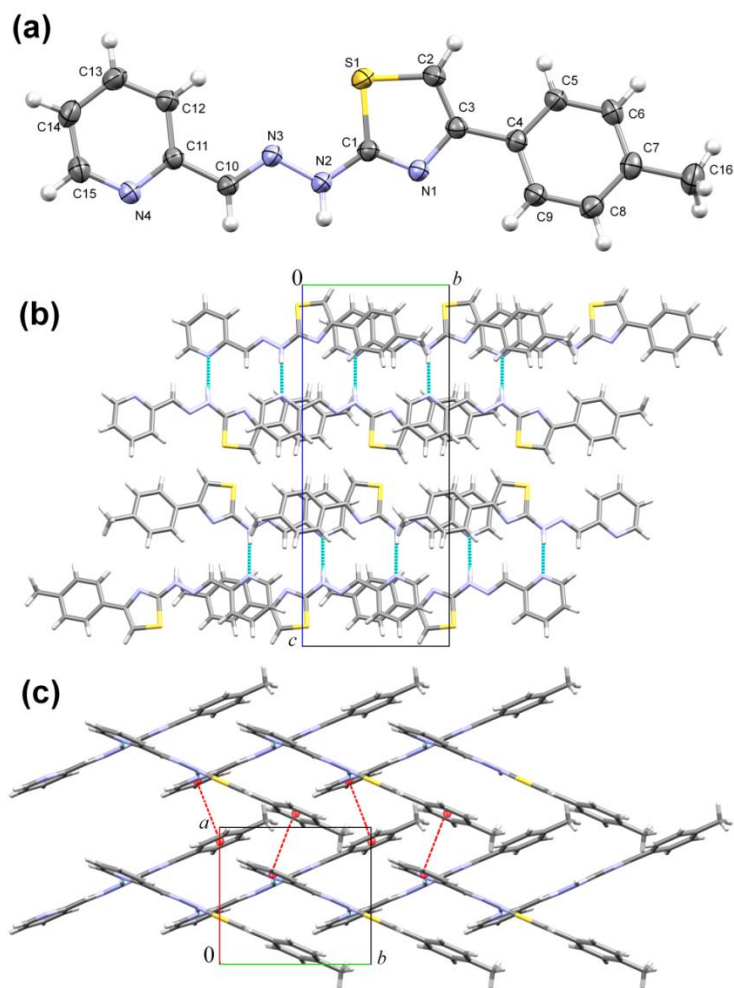


Figure 4.2 (a) Perspective view and labeling of the molecular structure of the ligand HL. Thermal ellipsoids are at the 40% probability level. Selected bond lengths (Å) and angles (°) with SD's in parentheses: N4–C11, 1.342(2); C10–C11, 1.465(2); N3–C10, 1.277(2); N2–N3, 1.3604(19); C1–N2, 1.362(2); N1–C1, 1.300(2); S1–C1, 1.7382(17); S1–C2, 1.7231(19); C2–C3, 1.357(2); C2–S1–C1, 87.88(8); C1–N1–C3, 109.99(13); N1–C1–N2, 123.79(15); N1–C1–S1, 116.05(12); N2–C1–S1, 120.15(12); N3–N2–C1, 116.98(14); C3–C2–S1, 111.26(13); C10–N3–N2, 117.63(14); N3–C10–C11, 119.78(15). (b) Infinite 1-D chains in the crystal structure of HL viewed along the *a*-axis. (c) 2-D supramolecular layers in the crystal structure of HL viewed along the *c*-axis.

Table 4.2 Crystal packing parameters in the crystal structures of **HLS**³

H-bond parameters					
D-H...A	D-H (Å)	H...A (Å)	D...A (Å)	D-H...A (°)	symmetry operation on A
N2-H2...N4	0.87(3)	2.05(3)	2.915(2)	175(2)	1 -x, 1/2 + y, 1/2 -z
π - π interaction parameters					
Cg(I),Cg(J) ^a	α^c (°)	β^d (°)	γ^e (°)	slippage ^f (Å)	symmetry operation on J
Cg1, Cg2	6	16.9	22.6	1.094	-1 + x, -1 + y, z
3.7633(10)					

^a Planes of the rings I/J: ring (1) = N(4),C(11),C(12),C(13),C(14),C(15); ring (2) = C(4),C(5),C(6),C(7),C(8),C(9);

^b Cg-Cg = distance between ring centroids (Å); ^c α = dihedral angle between planes I and J (°); ^d β = angle between Cg(I),Cg(J); vector and normal to plane I (°); ^e γ = angle between Cg(I), Cg(J) vector and normal to plane J (°); ^f Slippage = distance between Cg(I) and perpendicular projection of Cg(J) on ring I (Å).

4.1.2 Synthesis and structural characterization complexes with **HL(Se/S)**¹⁻³

By the reaction of **HL(S/Se)**¹⁻³ and $\text{Co}(\text{BF}_4)_2 \times 6\text{H}_2\text{O}$ in MeOH, the Co(III) Complexes of (1,3-Selen-2-yl)hydrazones and Their Sulphur Analogues (Scheme 3.2). Reactions of **HLSe**⁽¹⁻³⁾ with $\text{Co}(\text{BF}_4)_2 \times 6\text{H}_2\text{O}$ in methanol afforded rotten-cherry coloured solutions. After standing for three days emerald coloured single crystals were filtered off in all cases. Products were soluble in DMSO, DMF, MeOH, EtOH, acetonitrile and chloroform, and insoluble in diethyl-ether, ethyl-acetate and water. Magnetic measurements indicated that the complexes are diamagnetic in nature which allowed their structural characterization by NMR spectroscopy (Figure 7.27–Figure 7.38). Diamagnetic behaviour of obtained complexes indicated that they contain Co(III) ions which are formed during air oxidation of Co(II) ions. Values of molar conductivity of all complexes in methanol suggest that they are 1:1 electrolytes. Elemental analysis showed that the complexes consist of Co^{3+} ion, two deprotonated ligand molecules and BF_4^- ion. Based on these results, the following general formula of the complexes can be postulated: $[\text{Co}(\text{L}_2)]\text{BF}_4$. In the case of complex with **HLSe**², obtained crystals were not of sufficient quality for XRD analysis. Better crystals of **2-Se** were obtained by diffusion of EtOAc into solution of **2-Se** in DMSO. The elemental analysis indicated the presence of one crystal water molecule in the obtained crystals of **2-Se**. For biological investigations, crystalhydrate was used. ¹H-

NMR spectroscopy indicated an absence of N3 proton signal in spectra of all complexes which points to a coordination of corresponding ligands to Co(III) in their anionic form. In the IR spectra of all complexes strong absorption bands around 1050 cm^{-1} were found. These bands originate from BF_4^- ion and were not found in the IR spectra of free ligands.

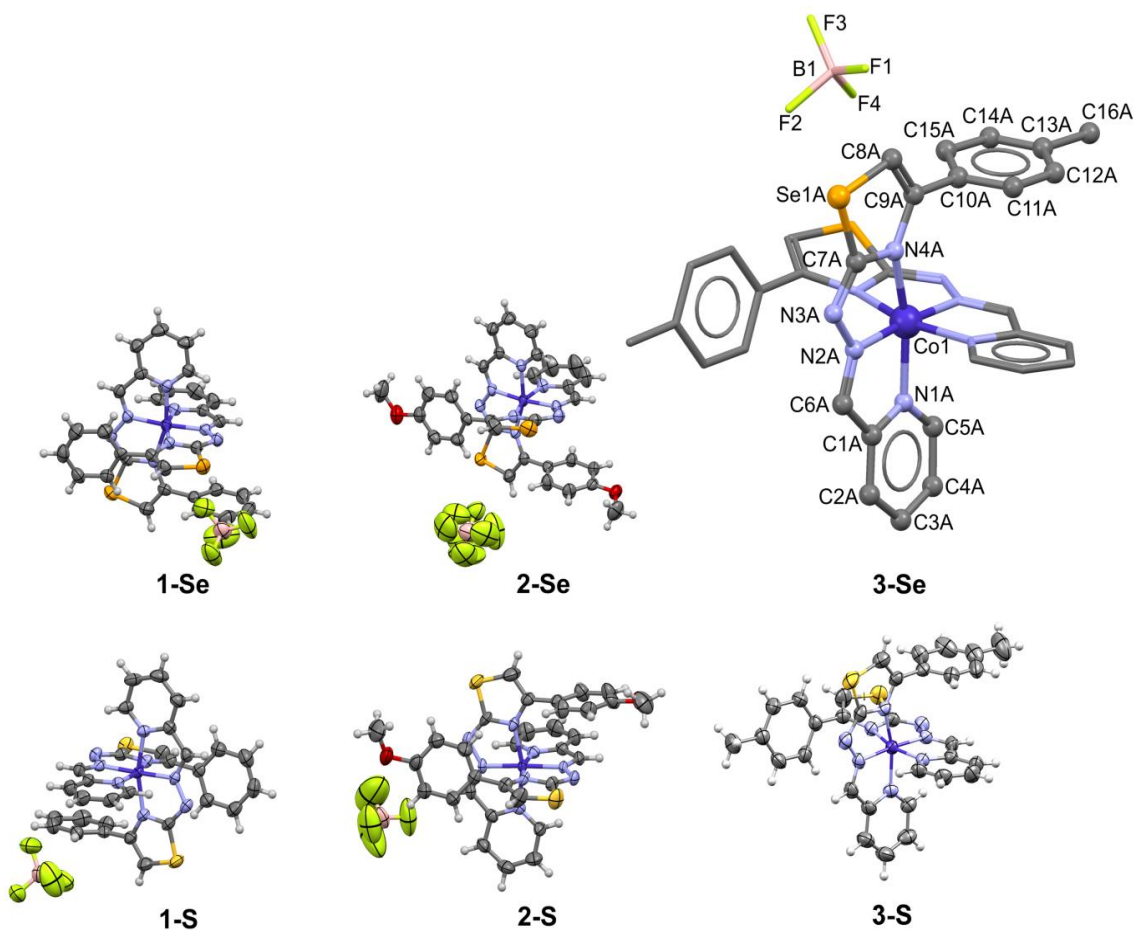


Figure 4.3 Molecular structures of the complexes; Structure of 3-Se is taken as the representative. Atom numbering scheme is given for one ligand. Atoms belonging to other ligand are enumerated in analogous way, with suffix B

A summary of the crystallographic data of the complexes are given in Table 4.3. They are of the octahedral-type, with two meridionally placed ligands, and are therefore chiral. Seemingly, they have approximate C_2 symmetry where the two-fold axis is the bisector of N1A-Co1-N1B angle. Strictly speaking, only in the case of 1-S the deviations from ideal C_2 point group symmetry are not significant, and C_2 symmetry of the cation is identified by SYMMOL algorithm,¹⁸⁴ with continuous symmetry measure of 1.41.^{185,186} Additionally,

Table 4.3 Crystallographic details HLSe¹⁻³

	1-Se	2-Se	3-Se
Chemical formula	C ₃₀ H ₂₂ CoN ₈ Se ₂ ⁺ ·BF ₄ ⁻	C ₃₂ H ₂₆ CoN ₈ O ₂ Se ₂ ⁺ ·BF ₄ ⁻ ·H ₂ O	C ₃₂ H ₂₆ BCoF ₄ N ₈ Se ₂ ·BF ₄
<i>M_r</i>	798.21	874.27	826.27
Crystal system	Tetragonal	Triclinic	Orthorhombic
Space group	<i>I</i> 4 ₁ / <i>a</i>	<i>P</i> -1	<i>P</i> 2 ₁ 2 ₁ 2 ₁
Temperature (K)	294	294	294
<i>a</i> (Å)	19.7293 (5),	11.1149 (3)	9.8772 (2)
<i>b</i> (Å)	19.7293 (5),	11.9728 (5)	15.1645 (4)
<i>c</i> (Å)	30.5890 (17)	13.9147 (5)	22.6936 (4)
<i>α</i> (°)	90	99.814 (3)	90
<i>β</i> (°)	90	96.688 (3)	90
<i>γ</i> (°)	90	104.417 (3)	90
<i>V</i> (Å ³)	11906.6 (9)	1742.49 (11)	3399.11 (13)
<i>Z</i>	16	2	4
<i>μ</i> (mm ⁻¹)	3.09	2.65	2.71
Absorption correction	Analytical	Analytical	Analytical
<i>T</i> _{min}	0.555	0.361	0.422
<i>T</i> _{max}	0.83	0.695	0.592
No. of measured reflections	17246	30249	33384
No. of independent reflections	6849	8296	8168
No. of observed [<i>I</i> > 2σ(<i>I</i>)] reflections	3835	6244	6391
<i>R</i> _{int}	0.059	0.029	0.029
(sin θ/λ) _{max} (Å ⁻¹)	0.683	0.685	0.684
<i>R</i> [<i>F</i> ² > 2σ(<i>F</i> ²)]	0.056	0.045	0.038
<i>wR</i> (<i>F</i> ²)	0.114	0.119	0.096
<i>S</i>	1.01	1.02	1.04
No. of reflections	6849	8296	8168
No. of parameters	415	499	435
No. of restraints	0	118	0
Δρ _{max} (e Å ⁻³)	0.49	0.68	0.55
Δρ _{min} (e Å ⁻³)	-0.38	-0.53	-0.37
Flack <i>x</i>	–	–	-0.015 (3)

Table 4.4 Crystallographic details HLS¹⁻³

	1-S	2-S	3-S
Chemical formula	C ₃₀ H ₂₂ CoN ₈ S ₂ ⁺ ·BF ₄ ⁻	C ₃₂ H ₂₆ CoN ₈ O ₂ S ₂ ⁺ ·BF ₄ ⁻	C ₃₂ H ₂₆ BCoF ₄ N ₈ S ₂
<i>M</i> _r	704.41	764.47	732.47
Crystal system	Tetragonal	Trigonal	Orthorhombic
Space group	<i>I</i> ₄ / <i>a</i>	<i>P</i> 3 ₁ 21	<i>P</i> 2 ₁ 2 ₁ 2 ₁
Temperature (K)	294	293	294
<i>a</i> (Å)	19.7160 (3)	9.2130 (2)	9.8152 (3)
<i>b</i> (Å)	19.7160 (3)	9.2130 (2)	15.3902 (5),
<i>c</i> (Å)	30.3333 (6)	33.5153 (7)	22.2103 (5)
<i>α</i> (°)	90	90	90
<i>β</i> (°)	90	90	90
<i>γ</i> (°)	90	120	90
<i>V</i> (Å ³)	11791.1 (4)	2463.63 (12)	3355.04 (17)
<i>Z</i>	16	3	4
<i>μ</i> (mm ⁻¹)	0.79	0.72	0.70
Absorption correction	Multi-scan	Multi-scan	Multi-scan
<i>T</i> _{min}	0.954	0.953	0.895
<i>T</i> _{max}	1	1	0.946
No. of measured reflections	56667	19412	13706
No. of independent reflections	7345	4013	7148
No. of observed reflections [<i>I</i> > 2σ(<i>I</i>)]	5157	3864	4887
<i>R</i> _{int}	0.050	0.028	0.031
(sin θ/λ) _{max} (Å ⁻¹)	0.686	0.683	0.683
<i>R</i> [<i>F</i> ² > 2σ(<i>F</i> ²)]	0.05	0.054	0.074
<i>wR</i> (<i>F</i> ²)	0.133	0.152	0.188
<i>S</i>	1.02	1.08	1.06
No. of reflections	7345	4013	7148
No. of parameters	415	232	436
No. of restraints	0	35	0
Δρ _{max} (e Å ⁻³)	0.68	1.01	0.63
Δρ _{min} (e Å ⁻³)	-0.45	-0.66	-0.69
Flack <i>x</i>	–	0.45 (3)	-0.018 (12)

the cation in **2-S** lies on a crystallographic two-fold axis, which imposes a perfect C_2 symmetry. In all other cases, no higher symmetry than C_1 was detected within default tolerance ranges. All the complexes consist of a complex cation $[\text{CoL}_2]^+$ and BF_4^- anions. Molecular structures of the complexes, with atom enumeration scheme of **1-Se** as the representative, is given in Figure 4.3 and for **3-S** at Figure 4.4. Thus, each individual crystal contains only one optical isomer of the cation $[\text{CoL}_2]^+$.

They are of the octahedral-type, with two meridionally placed ligands, and are therefore chiral. Seemingly, they have approximate C_2 symmetry where the two-fold axis is the bisector of N1A-Co1-N1B angle. Strictly speaking, only in the case of **1-S** the deviations from ideal C_2 point group symmetry are not significant, and C_2 symmetry of the cation is identified by *SYMMOL* algorithm,¹⁸⁴ with continuous symmetry measure of 1.41^{185,186}. Additionally, the cation in **2-S** lies on a crystallographic two-fold axis imposes a perfect C_2 symmetry. In all other cases, no higher symmetry than C_1 was detected within default tolerance ranges.

Spontaneous resolution of the racemate occurs during crystallization of **3-S**, so that the compound crystallizes as a mixture of enantiopure crystals (conglomerate) in non-centrosymmetric space group $P2_12_12_1$. Octahedral complex cation in **3-S** is comprised of two meridionally placed ligand molecules chelating Co(III) atom, and possesses approximate two-fold symmetry. **HLS**³ molecules are coordinated in an anionic form as tridentate NNN donors, through the pyridine, azomethine and thiazole nitrogen atoms. Distortion from an ideal octahedral geometry in **3-S** is imposed by the ligands' bite angles. In the crystal structure of **3-S** (Figure 4.4), in addition to the electrostatic attraction, cations and tetrafluoroborate anions are connected through hydrogen bonds (Table 4.5).

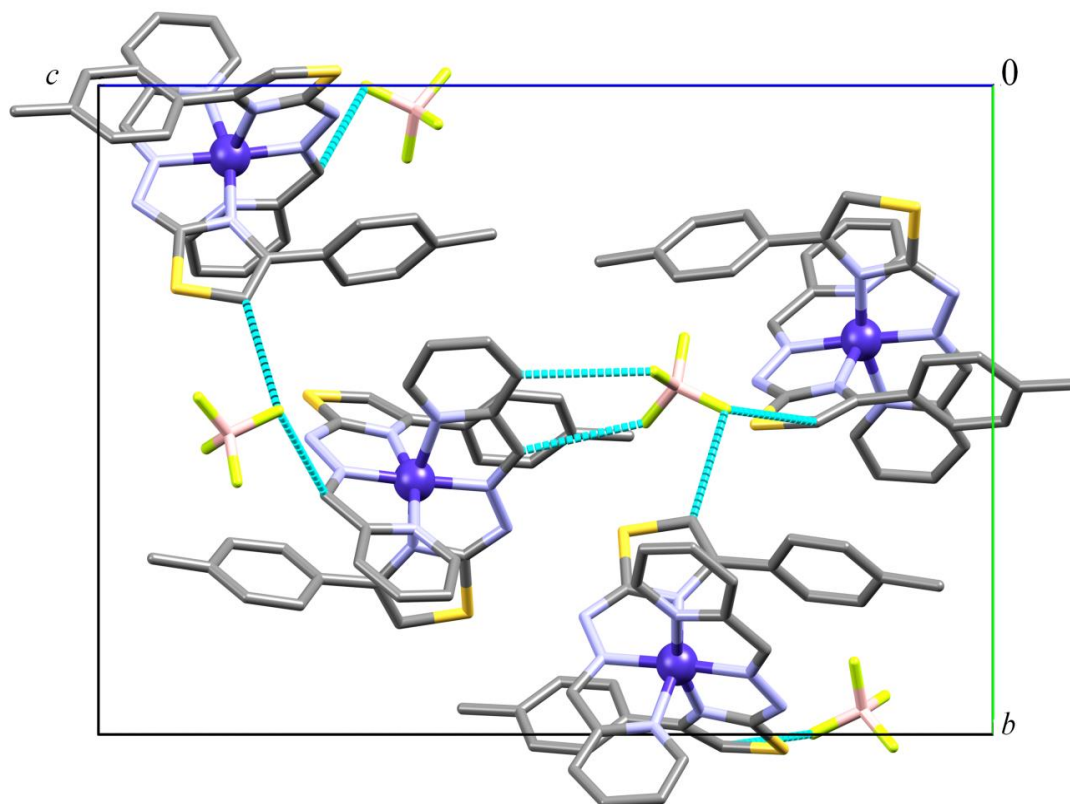


Figure 4.4 Crystal packing in the crystal structure of 3-S viewed along the *a*-axis. H-atoms are omitted for clarity.

Table 4.5 Crystal packing parameters in the crystal structures 3-S

3-S:H-bond parameters

D-H...A	D-H (Å)	H...A (Å)	D...A (Å)	D-H...A (°)	symmetry operation on A
C2-H2...F3	0.93	2.44	3.316(14)	158	$2-x, 1/2+y, 3/2-z$
C10-H10...F4	0.93	2.34	3.236(11)	162	$3/2-x, 1-y, -1/2+z$
C10A-H10A...F1	0.93	2.50	3.405(10)	163	$-1+x, y, z$
C12-H12...F1	0.93	2.48	3.395(11)	171	$3/2-x, 1-y, -1/2+z$

In all five complexes the cobalt atoms are hexacoordinated. The geometry around cobalt atoms is octahedral, and the orthogonal nature of this coordination is clear from the angles between two chelate planes which are in the range $85.24(7)$ – $89.28(5)^\circ$ (Table 4.6; Figure 4.5). Ligands are coordinated in NNN tridentate way through the pyridine nitrogen, azomethine nitrogen, and nitrogen atom of the (selen/thi)azole ring. In that way two fused metallocycles are formed. Metal–ligand bond lengths are in the usual range (Table 4.6), and in all six

complexes the bond between cobalt and azomethine nitrogen atom is the shortest. The observed trend that azomethine nitrogen atom makes shorter bond than pyridine nitrogen atom is already noticed for the similar Schiff base ligands.^{187–189}

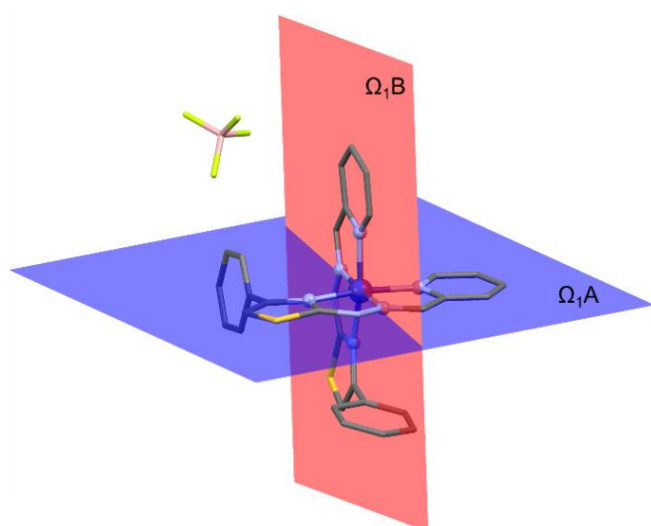


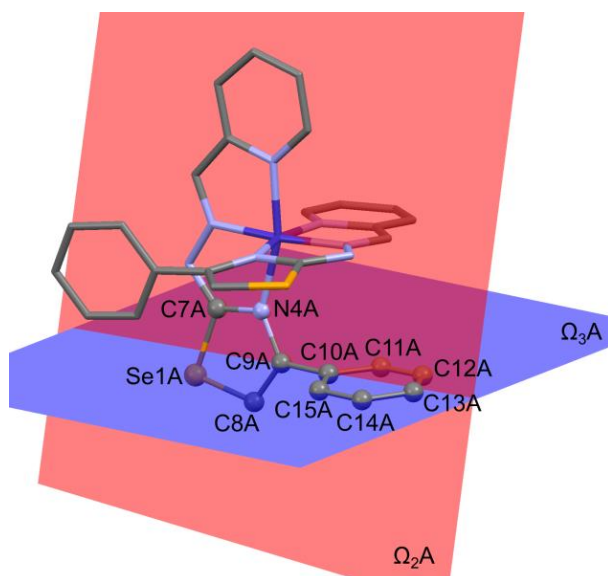
Figure 4.5 Orthogonal nature of ligands coordination seen through chelate planes Ω_1A and Ω_1B .

Ligands are deprotonated at N3 position, which has as a consequence an electron delocalization through C7–N3 and C7–N4 bonds. These bonds are of similar lengths, despite the fact that C7–N3 bond is formally regarded as a double. In comparison to bond lengths in recently published structures of **HLS**^{1, 190} and **Z-HLS**^{3, 52} bond lengths in coordinated ligands change so that C7–N3 is shortened, while C7–N4 is elongated.

It is important to note that the search of the Cambridge Structural Database (CSD) showed that there are no hitherto structurally characterized selenazole hydrazones, and **1-Se**, **2-Se**, and **3-Se** are thus the first crystallographically characterized complexes of selenazole hydrazones. Also, these complexes belong to a very few structurally characterized complexes with ligands coordinated through a selenazole ring,^{191–193} and are so far the first with cobalt(III) as the central atom.

Table 4.6 Selected bond lengths (Å) for the complexes.

	1-Se	2-Se	3-Se	1-S	2-S	3-S
Co1–N1A	1.945(4)	1.965(4)	1.945(3)	1.948(2)	1.948(5)	1.938(6);
Co1–N1B	1.952(4)	1.940(4)	1.950(3)	1.946(2)		1.949(6)
Co1–N2A	1.887(4)	1.890(3)	1.890(2)	1.888(2)	1.886(5)	1.888(5)
Co1–N2B	1.879(3)	1.886(3)	1.885(2)	1.886(2)		1.885(5)
Co1–N4A	1.957(3)	1.949(4)	1.949(3)	1.947(2)	1.948(6)	1.954(6)
Co1–N4B	1.952(3)	1.964(4)	1.950(2)	1.945(2)		1.937(6)
C6A–N2A	1.286(5)	1.296(6)	1.286(4)	1.293(4)	1.302(9)	1.290(10)
C6B–N2B	1.294(5)	1.288(6)	1.301(4)	1.294(3)		1.280(10);
N2A–N3A	1.353(5)	1.341(6)	1.353(4)	1.353(3)	1.359(8)	1.352(9)
N2B–N3B	1.356(5)	1.343(5)	1.341(3)	1.350(3)		1.335(8)
C7A–N3A	1.339(6)	1.327(6)	1.343(4)	1.336(4)	1.320(9)	1.326(10)
C7B–N3B	1.328(6)	1.323(6)	1.342(4)	1.333(4)		1.326(9)
C7A–N4A	1.342(5)	1.354(6)	1.341(4)	1.348(3)	1.346(7)	1.356(9)
C7B–N4B	1.351(5)	1.350(6)	1.341(4)	1.346(3)		1.336(9)
C7A–X1A	1.862(4)	1.864(5)	1.868(3)	1.725(3)	1.707(6)	1.726(9)
C7B–X1B	1.870(5)	1.864(5)	1.867(3)	1.725(3)		
C8A–X1A	1.867(5)	1.875(5)	1.870(4)	1.728(3)	1.729(11)	1.731(9)
C8B–X1B	1.872(5)	1.864(6)	1.871(3)	1.729(3)		1.728(7)
C8A–C9A	1.345(6)	1.336(7)	1.345(5)	1.353(4)	1.326(11)	
C8B–C9B	1.350(6)	1.348(7)	1.343(5)	1.356(4)		
C9A–N4A	1.388(5)	1.395(6)	1.396(4)	1.389(4)	1.393(8)	1.370(9)
C9B–N4B	1.394(6)	1.394(6)	1.401(4)	1.384(4)		1.395(10)

**Figure 4.6** Mean planes through selenazole and phenyl rings in the complex 3-Se

The complexes show some difference regarding the ligand molecules conformations. Namely, (selen/thi)azole ring can deviate from the chelate plane, and magnitudes of the deviations [2.6(2)–15.0(2)°] are not always similar for two ligands (A and B) in the same complex cation. Also, notable feature is the twisting of the terminal (substituted) phenyl ring (Figure 4.6). The angles between mean planes through those rings take values in the range 61.01(16)–88.62(10)°. A search of the CSD for angles between thiazole and phenyl rings, bonded the same as in present ligands, revealed a wide distribution of values, bimodal in nature with peaks around 7 and 45°. Out of 500 hits, only 32 angles were found with values > 60° (Figure 4.7).

It is interesting to note that by doing so, terminal rings belonging to ligand A orient themselves more or less parallel with the chelate plane formed by ligand B, and *vice versa* (Figure 4.8), which is seen from corresponding angles that are in the range of 2.9(3)–12.83(19)°. It seems plausible that the observed conformations result in reduction of steric hindrance. Table 7.3 summarizes dihedral angles between mentioned planes for all complexes.

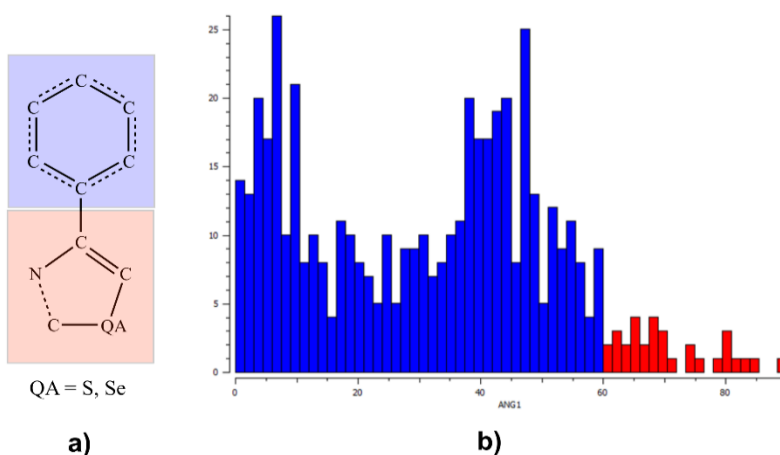


Figure 4.7 (a) Query used in the Cambridge Structural Database (CSD) search; (b) Distribution of dihedral angles, 50 angles (colored in red) out of 500 hits are greater than 60°.

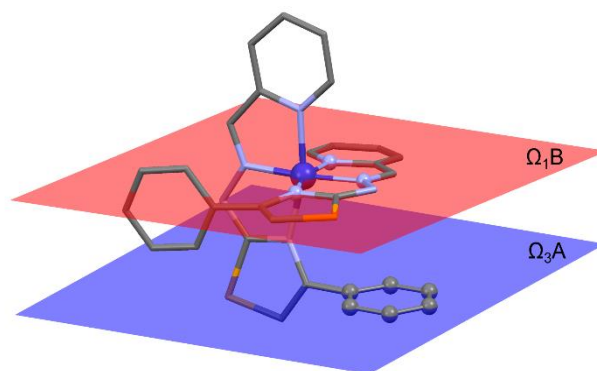


Figure 4.8 Mean planes through phenyl ring of ligand A and chelate plane of ligand B.

No classical hydrogen bonds are found in crystal structures of the complexes, as a consequence of the ligand deprotonation, and thus the lack of hydrogen bond donors. The pairs **1-S-1-Se**, and **3-S-3-Se**, crystallize in the same space groups with similar lattice parameters, and hence can be regarded as isostructural. Complexes **2-S**, **3-S**, and **2-Se** crystallize in non-centrosymmetric space groups, which means that spontaneous resolution of enantiomers occurs during crystallization. However, the crystal of **2-S** studied was twinned by merohedry, and its structure was refined as composed of four twin domains. The refined mass proportions of the domains indicate that specimen under study contained both enantiomers of the complex in approximately equal amounts.

4.1.3 The absorption spectra of $\text{HL}(\text{Se/S})^{1-3}$ and their Co(III) complexes

The absorption spectra of selenazoles $\text{HLSe}^{(1-3)}$ and their sulphur analogues are given in Figure 4.9 a), while their electronic absorption properties are summarized in Table 4.7. The longest wavelength of HLSe^1 was observed at 366 nm, and bathochromic shift (of 4 and 8 nm respectively) was observed upon addition of methyl or methoxy group to the benzene ring. The longest wavelengths of sulphur analogues were observed at about 15 nm smaller values. These results implied both C13-substituents and the nature of chalcogen atom strongly influenced the absorption spectra. Also, hypsochromic shifts of the absorption onset (λ_{onset}) of about 20 nm were observed in the case of thiazoles in comparison to their selenium analogues.

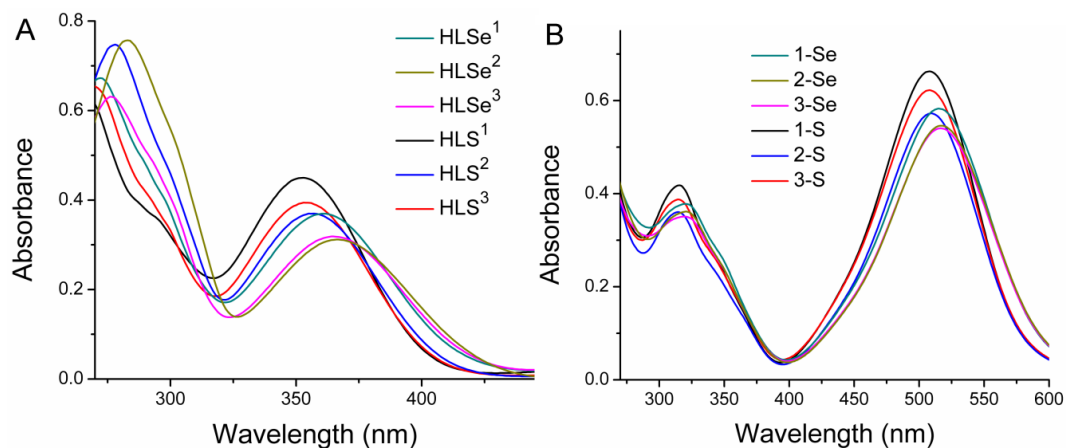


Figure 4.9 UV/Vis spectra of: (A) ligands HLSe(1–3) and HLS(1–3); (B) complexes (1–3)-Se and (1–3)-S.

The electronic absorption spectra of Co(III) complexes are given in Figure 4.9 b). Two absorptions at almost the same wavelengths were found for (1–3)-Se (320 and 516 nm), while in the case of their sulphur analogues, a small bathochromic shift (of 5 and 7 nm, respectively) was noticed (Table 4.8). Selenium atom has the more spatially extended *p*- and *d*-orbitals, compared to those of sulphur atom, which leads to more effective delocalized electrons in conjugated systems of the selenazoles analogs and therefore the λ_{max} value of selenazole ligands and complexes are shifted to a longer wavelength.

Table 4.7 Electronic absorption properties and HOMO–LUMO energy gaps of HLSe^{1–3} and HLS^{1–3}.

Ligand	$\lambda_{\text{abs}}/\text{nm}$	calcd. $\lambda_{\text{max}}/\text{nm}$	$\lambda_{\text{onset}}/\text{nm}^{\text{a}}$ (DMF)	HOMO-LUMO Band gap [eV]	
				onset ^b	TD-DFT ^c
HLSe¹	272, 366	243, 288, 379	421	3.26	3.28
HLSe²	283, 374	254, 295, 396	433	3.12	3.14
HLSe³	277, 370	246, 291, 383	425	3.22	3.24
HLS¹	265, 352	240, 285, 371	402	3.33	3.35
HLS²	278, 358	252, 291, 388	411	3.19	3.20
HLS³	268, 355	244, 288, 376	405	3.29	3.30

^a λ_{onset} are taken as the intersection of spectrum baseline and a tangent line to edge of the absorption band.

^b HOMO–LUMO energy gaps calculated from λ_{onset} . ^c Calculated from λ_{max} , obtain from TD-DFT/B3LYP in DMF solvent, by using equation $E_{\text{gap}} = 1242/\lambda_{\text{max}}^{\text{calc}}$

Table 4.8 Electronic absorption properties and DFT calculation and assignment of λ_{max} (in nm) in DMF for (1–3)-S and (1–3)-Se.

Comp.	$\lambda_{\text{abs}}/\text{nm}$	^{calc.} $\lambda_{\text{max}}/\text{nm}$		HOMO–LUMO Band gap [eV]	
		¹ T _{2g} ← ¹ A _{1g} + LMCT	¹ T _{1g} ← ¹ A _{1g}	$\lambda_{\text{max}}^{\text{a}}$	TD-DFT ^o
1-Se	320, 516	363	507	2.41	2.45
2-Se	320, 517	364	513	2.40	2.47
3-Se	320, 516	363	503	2.41	2.42
1-S	315, 508	359	495	2.44	2.51
2-S	315, 509	360	504	2.44	2.46
3-S	315, 509	360	496	2.44	2.50

^a Calculated from λ_{max} , obtained from TD-DFT/B3LYP/6-31G(d) in DMF solvent, by using Eq1: $E_{\text{gap}} = 1242/\lambda_{\text{max}}^{\text{calc}}$; ^b Calculated from TD-DFT/B3LYP in DMF solvent as $E_{\text{gap}} = E_{\text{HOMO}} - E_{\text{LUMO}}$

4.1.4 Voltammetric and spectroelectrochemical studies

All the ligands and the complexes were voltammetrically studied in DMF using tetrabutylammonium perchlorate (TBAP) as supporting electrolyte. In the available potential range (–2.1 V to +1.5 V) the ligands show mainly one reduction and one oxidation well-defined process (Figure 4.10 A).

The reduction processes for the ligand molecules are located in a 1-e[–] wave at potentials from around –1.6 V. Electrochemical characteristics of the peaks are: $\Delta E_{\text{p}}/\Delta \log v \sim -40$ mV/dec, $I_{\text{p}}/cv^{1/2} \sim \text{const}$, $E_{\text{p}}^{\text{a}} - E_{\text{p}}^{\text{c}} \sim 110$ mV (at $v = 0.1$ V/s). The gain in I_{p}^{R} on repetitive cycling in the amplitude more negative than 0 V is about 80–100% of the starting one, depending on the sweep rate. This is an indication of a chemical instability of the reduced species resulting in a small ill-shaped oxidation peak near 0 V. The nature of this reaction with adsorptive complications was not studied in more detail. This corresponds to an irreversible process (Figure 4.10 A).

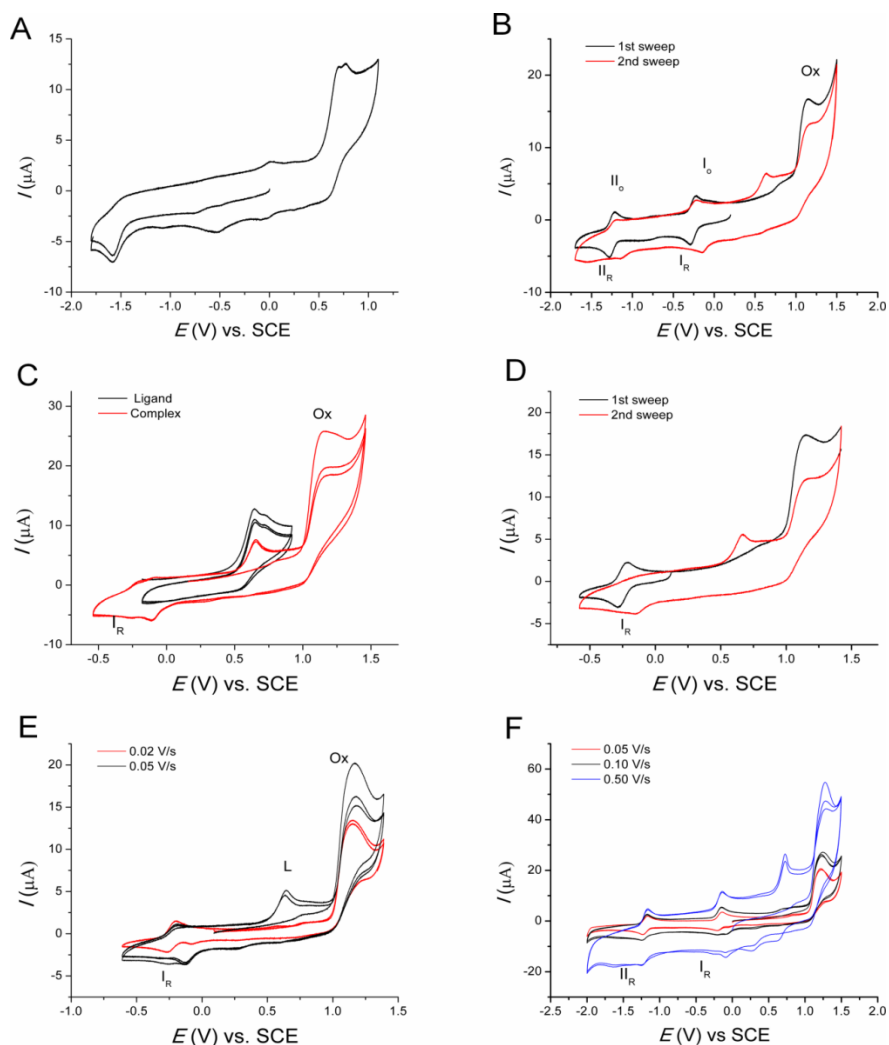


Figure 4.10 Representative cyclic voltammograms of selected substances in DMF + 0.1 M TBAP, GC electrode: (A) HLSe^3 ($c = 0.44 \text{ mM}$, $v = 0.1 \text{ V/s}$). (B) 3-Se ($c = 0.22 \text{ mM}$, $v = 0.1 \text{ V/s}$). Full amplitude and cathodic sweep direction. (C) 2-Se ($c = 0.42 \text{ mM}$) and HLSe^2 ($c = 0.46 \text{ mM}$), $v = 0.1 \text{ V/s}$. Narrow amplitude, anodic direction. (D) 3-Se ($c = 0.22 \text{ mM}$, $v = 0.1 \text{ V/s}$). Narrow amplitude and cathodic sweep direction. (E) 2-S ($c = 0.40 \text{ mM}$) $v = 0.02$ and 0.05 V/s . Narrow amplitude and anodic direction. (F) 2-S ($c = 0.40 \text{ mM}$, $v = 0.05, 0.1$ and 0.5 V/s). Full amplitude and anodic direction.

The voltammogram shows an irreversible oxidation wave at potentials $\sim +0.7 \text{ V}$. The anodic process is complicated by a slow chemical reaction giving rise to a species oxidized at more positive potentials (for $\sim +0.07 \text{ V}$). After these oxidation processes several small peaks appear at the subsequent cathodic sweep pointing to a decomposition of the oxidized species of the products which were not identified.

The potentials of characteristic peaks of all ligands are given in Table 4.9. Similar values of the potential and current functions are due to small differences in the electroactive centres. The one-electron reduction is located at C=N hydrazone group as it is common for these types of compounds. Two-electron oxidations most probably occur at chalcogen and C8 atoms. Fukui function calculations reveal that these centres have the greatest f^- values, which points to their ability of electron donation (*vide infra*).

Table 4.9 Voltammetric characteristics of the ligands at $v = 0.10$ V/s.

Ligand	E_p^R (V)	$I_p/cv^{1/2}$ ^b [$\mu\text{A}/\text{mM}(\text{V}/\text{s})^{1/2}$]	E_p^{Ox} (V)	$I_p/cv^{1/2}$ [$\mu\text{A}/\text{mM}(\text{V}/\text{s})^{1/2}$]
HLSe¹	-1.59	23.9	0.70	67.2
HLSe²	-1.60	23.0	0.65	68.8
HLSe³	-1.60	23.7	0.69	74.7
HLS¹	-1.64	27.0	0.73	68.9
HLS²	-1.66	26.0	0.67	75.1
HLS³	-1.65	23.3	0.70	60.0

All six complexes in DMF show reduction and oxidation processes according to the same pattern, differing slightly in the main current and potential characteristics due to coordination effects.

The typical voltammograms of the complexes recorded in negative direction (reduction processes) are given in Figure 4.10 B. Two pairs of apparently reversible one-electron peaks (at about -0.27 V and -1.27 V) are shown, accompanied by a large oxidation peak at $\sim +1.2$ V. The potentials of the reduction processes are given in Table 4.9. The voltammetric characteristics of both processes with $\Delta E_{p(O/R)}$ from 62 mV (at 0.01 V/s) to ~ 100 mV (at 2 V/s) give the values of heterogeneous rate constants¹⁹⁴ of about $(1-2) \cdot 10^{-4}$ m/s (Table 4.10) which lie at the lower limit of rate constants for reversible systems. In calculations the diffusion coefficient D value of $3.1 \cdot 10^{-10}$ m²/s was used for all the complexes. This value was previously determined for similar bis(ligand) octahedral Fe(III) complexes with ligands based on thiosemicarbazones under the same experimental conditions and was used as a substitute in a lack of true D values for the present complexes.¹⁹⁵

Table 4.10 Values of $k^{0'}$ for the processes I_R and II_R in solutions of complexes calculated according to reference.³⁴

Complexes	$k^{0'}(I_R)$ ^a	$k^{0'}(II_R)$
1-S	$1.4 \cdot 10^{-4} \pm 0.2$	$1.6 \cdot 10^{-4} \pm 0.5$
2-S	$1.6 \cdot 10^{-4} \pm 0.3$	$1.7 \cdot 10^{-4} \pm 0.5$
3-S	$1.4 \cdot 10^{-4} \pm 0.2$	$1.5 \cdot 10^{-4} \pm 0.2$
1-Se	$2.0 \cdot 10^{-4} \pm 0.3$	$1.5 \cdot 10^{-4} \pm 0.2$
2-Se	$1.6 \cdot 10^{-4} \pm 0.4$	$1.6 \cdot 10^{-4} \pm 0.2$
3-Se	$1.6 \cdot 10^{-4} \pm 0.4$	$1.8 \cdot 10^{-4} \pm 0.4$

^a In m/s.

The expected number of reduction processes in the case of Co(III) octahedral complexes with pyridine-based Schiff base ligands containing C=N hydrazono group is four (three one-electron reductions at Co(III) central atom, i.e. Co(III)→Co(0) and one one-electron reduction of C=N group). However, only two reductions (Co(III)→Co(II) and Co(II)→Co(I)) are observed down to –2.0 V which correspond to processes at the central metal atom, as confirmed by spectroelectrochemical experiments (see below). The other reductions are obscured in a huge multi-electron peak arising around the negative potential limit in DMF. Here, similarly to previously reported Fe(III) complexes with heterocyclic chalcogensemicarbazones, the potentials of reduction processes at coordinated ligands are 400–500 mV more negative comparing to the free ones, due to redistribution of negative charge.¹⁹⁶

However, oxidation process is much more complicated and its consequences on the behaviour of the complexes can be seen in consecutive scans. First, current function of the oxidation peak changes from 5-6 times greater than a 1-e⁻ reduction process at low sweep rates to only 4 times greater at high sweep rates. This could mean that with lowering the sweep rate the process changes from two-step 1-e⁻ release at each ligand particle to one-step 2-e⁻ oxidation process at each of the ligands at a close potential. The consequences of these changes can be followed in a subsequent negative sweep using variation of the sweep rate and the amplitude (Figure 4.10 B-F). At sweep rates higher than 0.02 V/s a new species reducible at potentials ~ 150 mV more positive than the peak I_R and II_R replaces partially or completely the starting one (Figure 4.10 B second sweep, Figure 4.10 C-E). At a closer insight into the consequences of the

oxidation process, a new peak at ~ 0.7 V appears belonging to oxidation of the free ligand (Figure 4.10 C) which was released after reduction of this instable complex. In addition, variations of the sweep rates in full potential amplitude reveal the presence of complex homogenous equilibrium coupled to redox processes which is also more pronounced with increasing the sweep rates (Figure 4.10 F). Thus, it can be assumed that oxidation may proceed apparently uncomplicated if enough time to allow necessary reorganization of the oxidized complex is provided (Figure 4.10 E and F). In other words, oxidation might cause temporary disturbances in the molecule which need time to re-establish the previous molecular symmetry. Thus, at low sweep rates this adjustment proceeds in parallel with electron release so the molecule seems to be stable at the end of the oxidation process.

Table 4.11 Voltammetric characteristics of the complexes.*

Complex	$E_p^R(I)$	$E_p^O(I)$	$I_R^I/cv^{1/2}$	$E_p^R(II)$	$E_p^O(II)$	$I_R^{II}/cv^{1/2}$	E_p^{Ox}	$I_{Ox}/cv^{1/2}$
1-Se	-0.27	-0.20	45.0	-1.27	-1.20	43.1	1.16	225
2-Se	-0.30	-0.23	33.0	-1.28	-1.20	33.1	1.14	164
3-Se	-0.28	-0.21	36.1	-1.27	-1.20	33.0	1.16	202
1-S	-0.24	-0.17	37.4	-1.28	-1.21	38.9	1.20	214
2-S	-0.26	-0.20	37.3	-1.29	-1.22	36.0	1.19	189
3-S	-0.26	-0.18	37.5	-1.28	-1.21	37.1	1.20	196

*At $v = 0.10$ V/s. ^a In V. ^b In $\mu\text{A}/\text{mM}(\text{V}/\text{s})^{1/2}$.

The *in situ* spectroelectrochemistry of **3-S** was performed in solution to evaluate the spectral changes between its initial and reduced states. This is of importance for assigning in more details the electrochemical processes.^{197,198} The Co(III) complex **3-S** was dissolved in a DMF solution containing 0.1 M TBAPF₆ and the absorption spectroelectrochemical studies were done using a Pt mesh working electrode. Previously, we recorded the cyclic voltammograms of **3-S** on a Pt electrode (data not shown) and the voltammetric behaviour (i.e. potential, reversibility, current) was identical with GC electrode material. UV-Vis spectroelectrochemical measurements were performed by using a thin-layer electrochemical cell of 1-mm optical path. As already mentioned, **3-S** presents two one-electron reversible reduction waves at -0.26 V and -1.28 V (Table 4.11). Therefore we studied the spectral changes for both reduced forms by

applying potentials slightly more cathodic than the peak potential values (i.e. -0.5 and -1.5 V, respectively).

Upon the first reduction potential -0.5 V, the evolution of the UV-Vis spectra with time were collected and depicted in Figure 4.11. Interestingly, the monitoring of the absorption revealed a fast and nice modification of the electronic transitions when the first reduced state is reached. As shown in Figure 4.11, the main band peaking initially at 509 nm is affected upon the first cathodic reaction. Indeed, it is blue-shifted and increased progressively. The small band at 315 nm tends to vanish. Applying a more cathodic potential (i.e. -1.5 V) corresponding to the second reduction process increases even more the main band which peaks now at 470 nm. In addition, two small bands appeared between 270 and 400 nm after adding this second electron to the complex. After approaching the equilibrium in both cases ($E = -0.5$ V and -1.5 V), an open circuit potential ($E = 0.1$ V) was applied to the system.

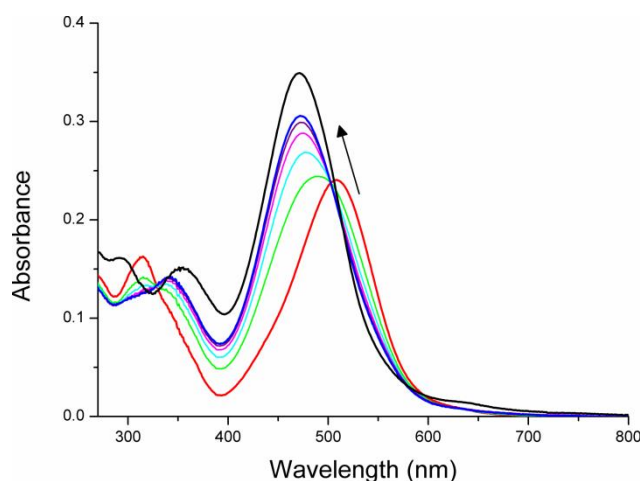


Figure 4.11 Time-resolved UV-Vis spectral changes of 3-S in deoxygenated DMF with 0.1 M TBAPF₆ before (red curve) and after applying the first reduction potential -0.5 V. The arrow indicates the evolution. Blue curve corresponds to the spectrum of the first reduced form. Black curve is the spectrum recorded at equilibrium after applying -1.5 V.

The absorbance recovered with time until the spectral signatures of the complex were as same as the initial state. It confirms the reversibility observed by cyclic voltammetry for the reduction processes and it shows that the reduced species are stable during the timescale of spectroelectrochemical experiments. Whatever, the main band at 509 nm of the initial 3-S complex was attributed to the ligand to metal charge transfer transition (LMCT) as detailed in Table 4.8. The

two reduction processes generate the Co(II) and then Co(I) from the initial Co(III) ion so it makes the LMCT transition more difficult. It explains that this main band was observed at a lower wavelength (i.e. higher energy) compared with that of the initial complex.¹⁹⁷⁻¹⁹⁹ The spectroelectrochemical experiments demonstrate that the cathodic reactions correspond to two successive 1-e⁻ reduction of the central Co(III) atom of the complex.

4.1.5 DFT calculations

The selected DFT/B3LYP/6-31G(d) method for neutral *E*- and *Z*-isomeric form of ligands has been chosen from the consideration of several approaches already applied to similar molecular structures elsewhere.^{200,201} Optimized structures of the ligands are shown in Figure 4.12, and the relevant structural parameters in Table 7.4. Structural data of all optimized molecules correspond reasonably well to the XRD data of available crystal structures. In addition, an evaluation of reliability of theoretical calculations also includes prediction of the planarity of the investigated molecules.

There is a very good agreement between experimental and calculated dihedral angles. By comparing N₃-H bond lengths of **HLS**¹ligand, it can be observed that these bonds are longer in the *Z*-isomer (Table 7.4). The present theoretical method successfully reproduces experimentally observed formation of intramolecular H-bond between N1 of pyridine ring and the proton attached to N3 of hydrazone group CH=N-NH-.⁵² Calculated relative energy shows that *Z*-isomer is more stable than *E*-isomer (Table 4.12). This observation can be explained by the presence of stabilizing effect in *Z*-isomeric form due to a formation of intramolecular H-bond.²⁰²

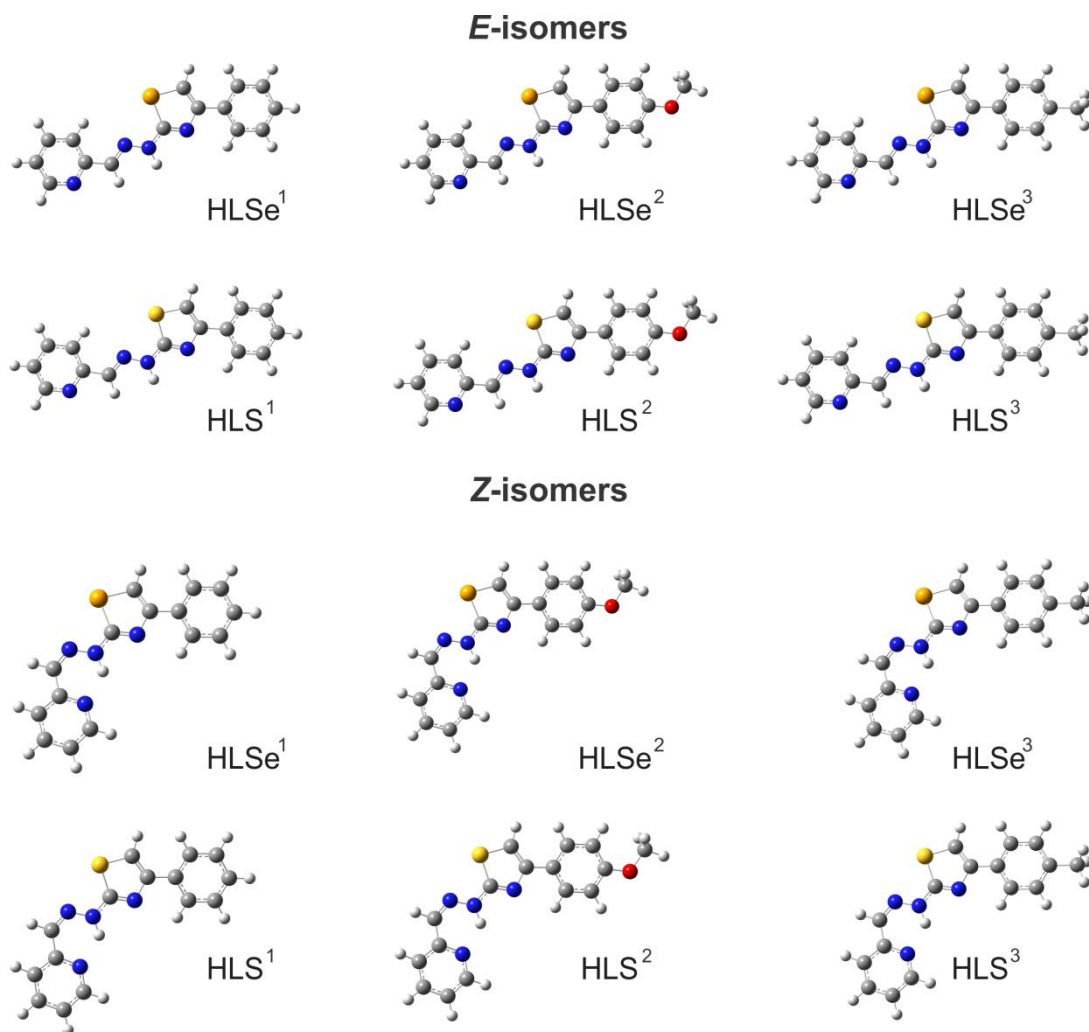


Figure 4.12 DFT optimized structures of the ligands in the gas phase.

Table 4.12 Calculated the relative energy ΔE (kcal/mol) of *E*-1,3-thiazoles and *E*-1,3-selenazoles.

Compound, X=S	<i>E</i> -HLS ¹	<i>Z</i> -HLS ¹	<i>E</i> -HLS ²	<i>Z</i> -HLS ²	<i>E</i> -HLS ³	<i>Z</i> -HLS ³
ΔE (kcal/mol)	2.630 ^a	0.000 ^a	2.571 ^a	0.000 ^a	2.615 ^a	0.000 ^a
	2.212 ^b	0.000 ^b	2.184 ^b	0.000 ^b	2.253 ^b	0.000 ^b

Compound,	<i>E</i> -	<i>Z</i> -HLSe ¹	<i>E</i> -HLSe ²	<i>Z</i> -HLSe ²	<i>E</i> -HLSe ³	<i>Z</i> -HLSe ³
ΔE (kcal/mol)	2.574 ^a	0.000 ^a	2.529 ^a	0.000 ^a	2.496 ^a	0.000 ^a
	2.057 ^b	0.000 ^b	2.053 ^b	0.000 ^b	2.044 ^b	0.000 ^b

DFT/ B3LYP/6-31G(d) calculated the relative energy E , defined as zero-point corrected total energy and with respect to more stable isomeric form.^a In the gas phase; ^b In DMF solvent.

In order to evaluate the basis set influence on the geometry of Co(III) complexes, for the **1-S** complex we have applied two DFT models, B3LYP and BVP86, as well as several basis sets of various complexity. There is a noticeable

tendency for increasing bond length with increasing basis set size (Table 7.6). In fact, the smallest basis set for the metal ion gives the best agreement with the crystallographic data in the case of the Co–N bonds. Consistent with previous studies,²⁰³ the BVP86/6-31g(d,p)/6-31g(d) method gives smallest differences between experimental and calculated values of Co–N bond distances, especially for the Co–N4 bonds (Table 7.5). Optimized structures of complexes are shown in Figure 4.13. Selected structural parameters for all Co(III) complexes are listed in Table 7.6. Structural data of all optimized molecules correspond well to the data obtained from X-ray.

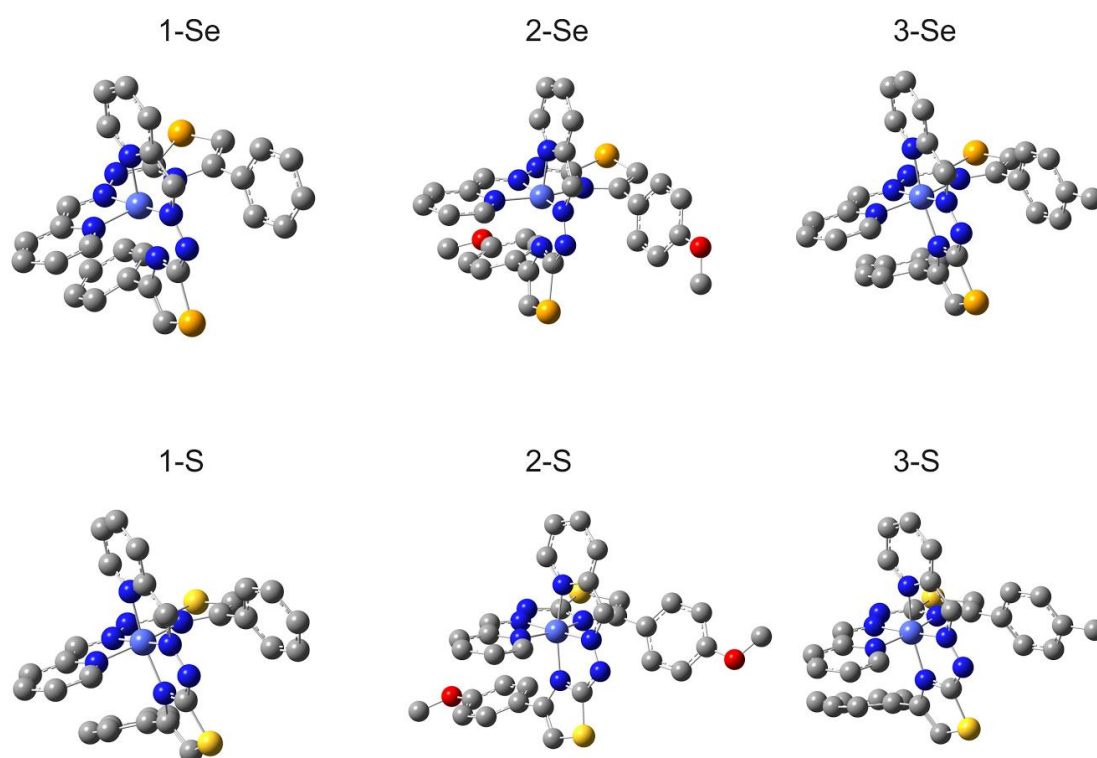


Figure 4.13 DFT optimized structures of Co(III) complexes in the gas phase

Chemical shifts for the complexes were calculated within GIAO approach at DFT/PCM(DMSO)/B3LYP level of theory. Results of theoretically predicted isotropic chemical shifts with respect to tetramethylsilane (TMS) are listed in (Table 7.8) and reveal a good match to the experimental spectroscopic data. Substitutions of Y = H with Y = CH₃, or OCH₃ have an expected influence on proton chemical shifts in *ortho*-position to the substituent Y of the benzene ring (upfield shifts).

Linear regression analysis was applied to estimate the correlation between experimental and calculated values of the chemical shifts. The analysis included experimental and calculated values of all C- sp^2 atoms, as well as, all chemical shifts of the protons attached to C- sp^2 atoms. The resulting linear regression lines were $\delta_{\text{calc.}} = 0.43 + 0.98\delta_{\text{exp.}}$ ($R = 0.98$, the correlation coefficient at confidence level of 95.0%) and $\delta_{\text{calc.}} = 0.24 + 0.97\delta_{\text{exp.}}$ ($R = 0.79$, the correlation coefficient at confidence level of 95.0%) for ^{13}C and ^1H NMR chemical shifts, respectively. Although, both values of R show a significant correlation between experimental and calculated chemical shifts, additional *two-sided t* test has been applied, which confirmed the obtained linear regression results. The linearly scaled calculated values are listed in Table 7.7.

The evaluation of absorption spectra and transition energies was carried out within the time dependent density functional theory (TD-DFT) approach, using B3LYP functional and DMF as solvent. In order to compare the spectral characteristics of Co(III) complexes with 1,3-selenazoles and 1,3-thiazoles as ligands, the absorption spectra, HOMO and LUMO energy levels, and the energies of HOMO-LUMO transitions (E_{gap}) were calculated.

The calculated electronic spectra of free ligands show shoulder bands in the range 240–255 nm (41596–39317 cm^{-1}) and two bands in the range 285–295 nm (35120–33937 cm^{-1}) and 370–395 nm (26929–31939 cm^{-1}). Calculated electronic transitions (λ), oscillator strengths (f) and major MO contributors to the transitions of HLS⁽¹⁻³⁾ and HLSe⁽¹⁻³⁾ ligands are listed in Table 7.8. The shoulder band may be assigned to the $\pi-\pi^*$ transition of the thiazole and selenazole rings.²⁰⁴ The absorption peak in the range 285–295 nm is due to $\pi-\pi^*$ transition of phenyl and pyridine rings.²⁰⁵⁻²⁰⁷ The absorption maxima in the range 370–395 nm correspond to the $\pi-\pi^*$ transition of the azomethine moiety with a contribution of the intraligands $\pi-\pi^*$ transitions.²⁰⁵⁻²⁰⁷ The calculated wavelengths originating from $\pi-\pi^*$ transitions of phenyl, and pyridine rings, as well as those from azomethine moiety, are in good agreement with experimental values (Table 7.4). E_{gap} values of the ligands calculated from λ_{max} by TD-DFT method, are also in good agreement with values obtained by UV-Vis spectroscopy (Table 7.4). Due to higher degree of aromaticity of selenazole in comparison to thiazole, it can be

expected for Se-heterocycles to be more stable and less reactive. Calculated relative energies of the ligands indeed show that selenazoles are more stable than their thiazole analogs (Table 4.12). Also, all the selenazoles have the smaller values of E_{gap} than their sulphur analogs (Table 4.7), which indicates the lower reactivity of 1,3-selenazoles and explains the bathochromic shifts of absorption maxima.

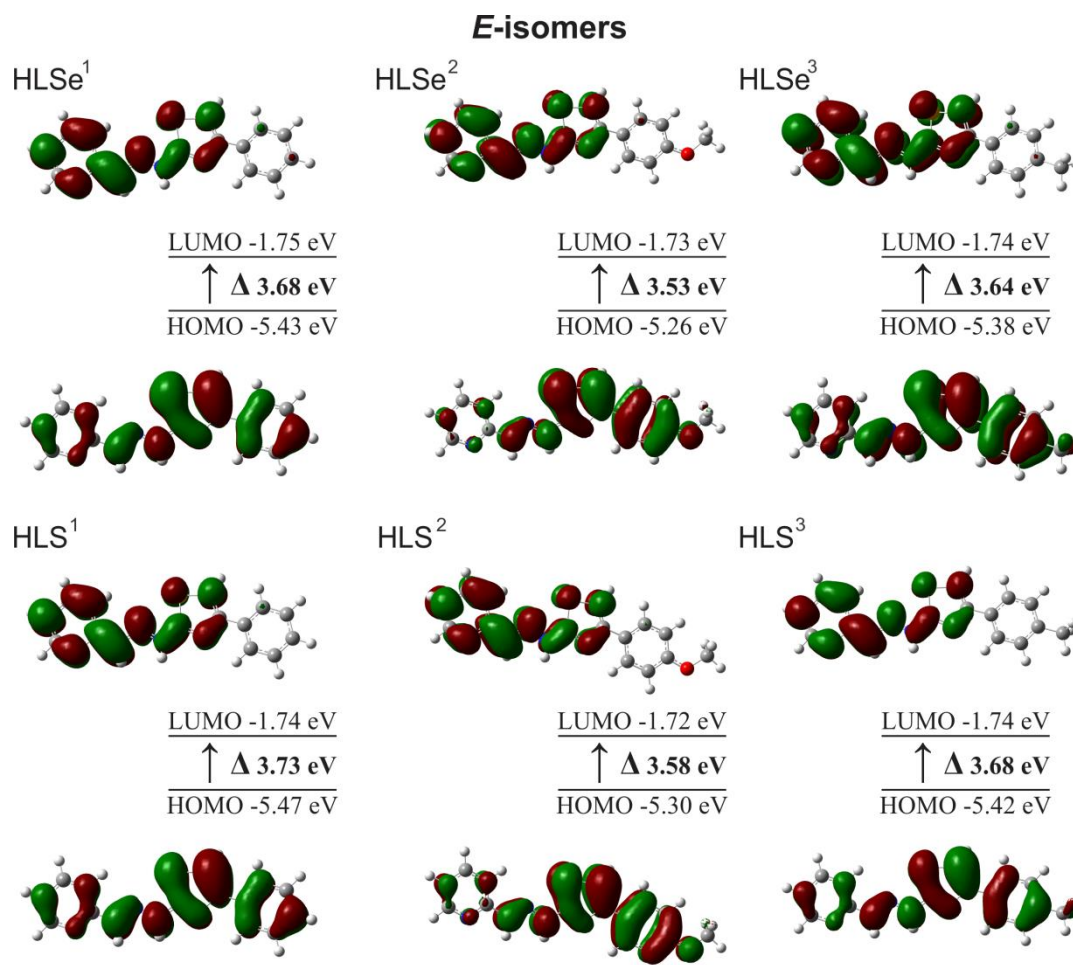


Figure 4.14 Graphical representation of calculated HOMO, LUMO and HOMO-LUMO transition of *E*-1,3-thiazoles and *E*-1,3-selenazoles in DMF solvent

Graphic representations of calculated HOMO, LUMO and HOMO-LUMO transitions for ligands are shown in Figure 4.14. The HOMOs of all ligands are delocalized mainly at the azomethine group, heterocyclic ring and phenyl group, whereas the LUMOs are delocalized on the pyridine ring, azomethine group and the heterocyclic ring. The presence of electron releasing substituent (methyl- or

methoxy-) of the thioazole and selenazole attached phenyl ring, destabilizes HOMO and LUMO orbitals and decreases the energy gap (Figure 4.14). Energetically the most favourable $\pi-\pi^*$ absorptions (370–395 nm) occur from HOMO→LUMO transitions^{205–207} (Table 7.8).

Since the intraligand $\pi-\pi^*$, ligand to metal charge transfer (LMCT), or spin-forbidden transitions may cause broadening or masking of d-d bands or even their disappearance²⁰⁸ in the experimental absorption spectra of complexes, additional information could be obtained using the results of TD-DFT calculations, as discussed below.

The ground state of Co(III) ion in octahedral low-spin complexes is 1A_g arising from $(t_{2g})^6$ electronic configuration. The one-electron excited states $^1T_{1g}$, $^3T_{1g}$, $^1T_{2g}$ and $^3T_{2g}$ derive from $(t_{2g})^5 (e_g)^1$ electronic configuration, of which both spin-triplet states lying at lower energy than the singlets. Therefore, UV-VIS spectra of Co(III) ion in strong ligand field of O_h symmetry have the following assignments of d–d transitions: two spin allowed $\nu_1: ^1T_{1g} \leftarrow ^1A_{1g}$; $\nu_2: ^1T_{2g} \leftarrow ^1A_{1g}$ and two spin forbidden $\nu_3: ^3T_{1g} \leftarrow ^1A_{1g}$; $\nu_4: ^3T_{2g} \leftarrow ^1A_{1g}$.²⁰⁹ Calculated electronic spectra of approximate octahedral(1–3)-Se and (1–3)-S complexes in DMF show two principal spin allowed bands. The first ones, relatively sharp around 20 000 cm^{-1} (500 nm), were assigned to $^1T_{1g} \leftarrow ^1A_{1g}$ transition, while the second ones, broad around 30 000 cm^{-1} (360 nm), were assigned to $^1T_{2g} \leftarrow ^1A_{1g}$. The electronic spectral assignments of the complexes are given in Table 4.8. E_{gap} values of complexes obtained via TD-DFT calculated from λ_{max} are also in a good agreement with experimental data (Table 4.7).

Ligand to metal charge transfers can be divided in four classes: $\nu_1: \pi \rightarrow t_{2g}$ (π^*), $\nu_2: \pi \rightarrow e_g$ (σ^*), $\nu_3: \sigma \rightarrow t_{2g}$ (π^*) and $\nu_4: \sigma \rightarrow e_g$ (σ^*) in order of increasing energy. For d^6 complexes, only ν_2 (25000–45000 cm^{-1}) and ν_4 (above 45000 cm^{-1}) transitions are spin allowed. In the investigated complexes $\pi \rightarrow e_g$ (σ^*) transition can be the reason for broadening of the d-d band around 30000 cm^{-1} (360 nm). The important contribution can be assigned to the intervening sigma bond, which can be formed by donation of the nitrogen lone pairs (azomethine group) to the empty d orbital of the metal ion.^{205–207} Presence of intraligand $\pi-\pi^*$ transitions may also cause a broadening of the absorption bands. Calculated electronic transitions

(λ), oscillator strengths (f) and major MO contributors to the transitions of (1–3)-Se and (1–3)-S complexes are listed in Table 7.9.

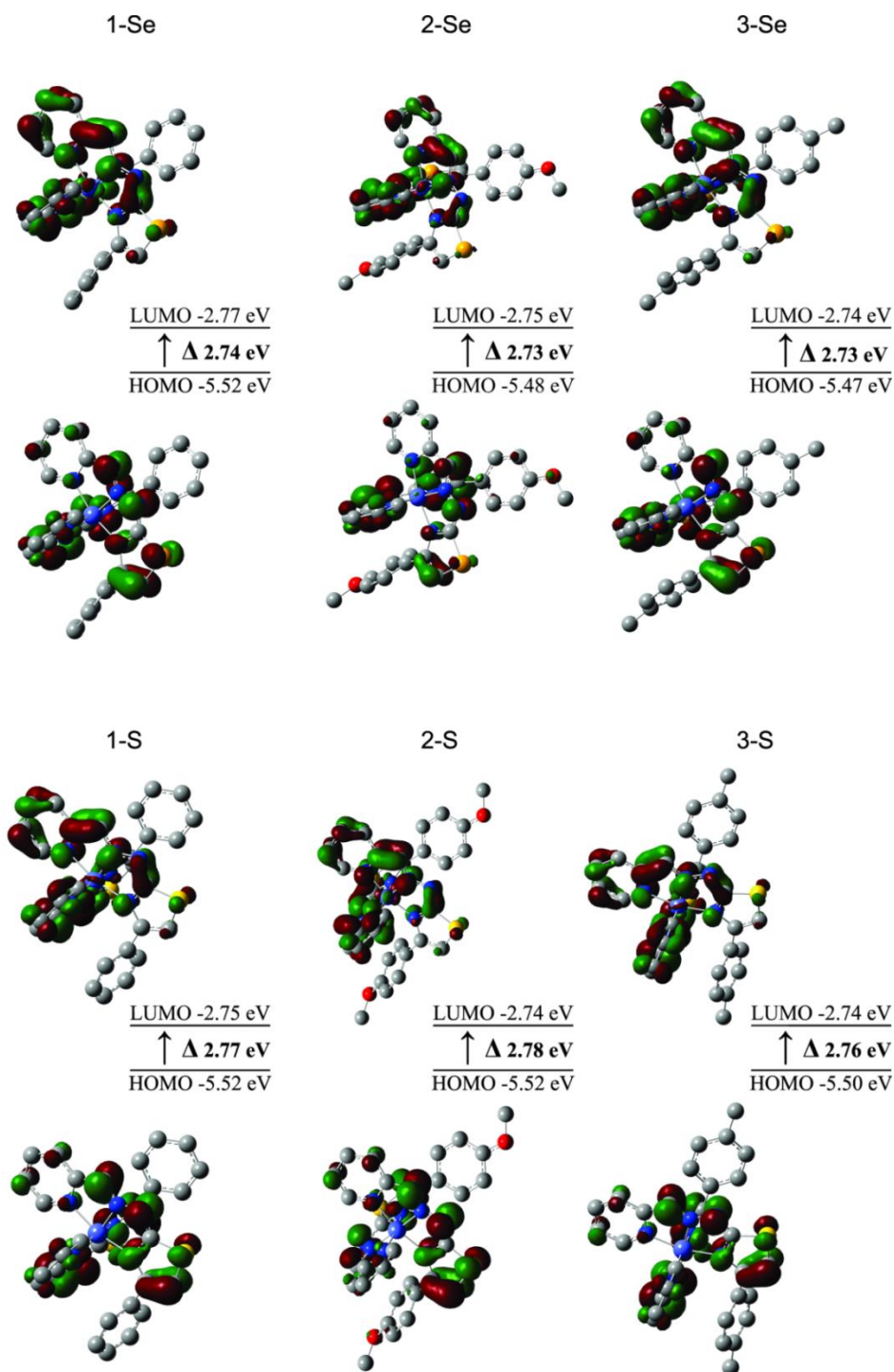


Figure 4.15 Graphic representation of calculated HOMO, LUMO and HOMO-LUMO transition of Co(III) complexes with E-1,3-thiazoles and E-1,3-selenazoles as ligands, in DMF solvent.

Graphic representations of calculated HOMO, LUMO and HOMO-LUMO transitions for complexes are shown in Figure 4.15. The LUMO orbitals of all Co(III) complexes are delocalized mainly at the azomethine group, metal centre, and pyridine ring. The main contribution to the HOMO orbitals of all Co(III) complexes derives from the heterocyclic ring, azomethine group, and metal centre.

It is known that DFT exchange-correlation functionals overestimate the energy of HOMO orbital and underestimate the energy of LUMO orbital. The HOMO eigenvalues predicted by hybrid functionals are generally better than those predicted by nonhybrid functionals, and their accuracy depend on the included percentages of Hartree-Fock exchange.²¹⁰ DFT/B3LYP calculated energies of HOMO orbitals for Co(III) complexes are in good agreement with experimental data.

Fukui functions

Fukui functions (f) provide information about atoms in a molecule that have increased tendency to either lose or accept an electron. This allows evaluating the nucleophilic and electrophilic behaviour of each atom in a molecule. The greatest values of Fukui functions calculated by NBO charges at DFT/DMF of investigated ligands are reported in Table 7.10. The f^- measures reactivity with respect to electrophilic attack or the tendency of the molecule to donate electrons, while f^+ measures reactivity related to nucleophilic attack or the propensity of a molecule to accept electrons. The highest value of f^- for the ligands is at Se/S and C8 indicating the zone for transfer of electron, while the highest value of f^+ is associated with N2 and C6 showing the ability for a back donation through the N2=C6 zone of hydrazone group.

Table 4.13 Electrochemical properties and energies of HOMO orbitals of (1–3)-S and (1–3)-Se.

Compound	E1/2ox/[eV] ^a	HOMO/eV	
		CV ^b	DFT ^c
1-Se	0.532	-5.33	-5.52
3-Se	0.513	-5.31	-5.47
2-Se	0.500	-5.30	-5.48
1-S	0.568	-5.37	-5.52
2-S	0.540	-5.34	-5.52
3-S	0.554	-5.35	-5.50

^aV vs Fc/Fc⁺ in DMF containing 0.1 M TBAP as supporting electrolyte at a scan rate of 100 mV/s. GC working electrode. ^bEHOMO (eV) = -4.8 - (Eonset - E1/2(Fc/Fc⁺)).²⁰⁷ ^cEHOMO (eV) calculated from TD-DFT/DMF calculations.

4.1.6 Biological activity

4.1.6.1 Antimicrobial activity

The antimicrobial activity of the (1,3-thiazol-2-yl)hydrazones and (1,3-selenazol-2-yl)hydrazones and its Co(III) complexes was examined against four Gram-negative bacteria *P. hauseri*, *P. aeruginosa*, *E. coli*, *S. enterica* and four Gram-positive bacteria: *S. aureus*, *C. sporogenes*, *B. subtilis* and *K. rhizophila* (Table 4.14). Antifungal activity of investigated compounds was examined against *A. brasiliensis*, *C. albicans* and *S. cerevisiae* (Table 4.15).

Table 4.14 Antibacterial activity of investigated compounds tested by the disc-diffusion method.

Compound	Inhibition zone diameter ^a (mm)							
	<i>P. hauseri</i>	<i>P. aeruginosa</i>	<i>E. coli</i>	<i>S. enterica</i>	<i>S. aureus</i>	<i>C. sporogenes</i>	<i>B. subtilis</i>	<i>K. rhizophila</i>
HLSe¹	10	10	10	10	10	10	10	10
HLSe²	10	10	12	14	12	12	12	14
HLSe³	10	12	12	12	10	10	12	12
HLS¹	n.a. ^b	n.a.	n.a.	n.a.	n.a.	n.a.	n.a.	n.a.
HLS²	n.a.	n.a.	n.a.	n.a.	n.a.	n.a.	n.a.	n.a.
HLS³	n.a.	n.a.	n.a.	n.a.	n.a.	n.a.	n.a.	n.a.
1-Se	24	24	26	24	26	24	24	28
2-Se	28	26	28	26	26	28	26	30
3-Se	26	24	28	26	26	26	24	28
1-S	22	20	30	28	20	24	26	30
2-S	26	24	32	24	24	24	26	32
3-S	32	34	32	28	32	30	30	32
Amikacin	22	20	38	22	28	20	20	22

^aIncluding diameter of disc (8 mm); ^b n.a. – not active

From the results of antimicrobial activity investigation the impact of chalcogen atom identity on activity of organic ligand can be clearly seen. Namely, none of the sulphur ligands did show any activity against bacteria, while the activity against fungi was never higher in comparison to their selenium isosters. In the case of selenium ligands **HLSe**⁽¹⁻³⁾, substitutions on benzene ring often resulted in increased activity of the corresponding ligand in comparison to **HLSe**¹ on all bacterial and fungi strains. The similar effect was found for **HLS**⁽¹⁻³⁾ on all investigated fungi strains. Complex formation enhanced to a great extent the activity of organic ligands against bacterial strains investigated. The trend found for the ligands is also valid for the complexes: **1-Se** and **1-S** were less active corresponding complexes.

Table 4.15 Antifungal activity of investigated compounds tested by the disc-diffusion method (inhibition zone size including disc/mm)

Compound	Inhibition zone diameter ^a (mm)		
	<i>A. brasiliensis</i>	<i>C. albicans</i>	<i>S. cerevisiae</i>
HLSe ¹	10	16	18
HLSe ²	12	16	22
HLSe ³	12	22	28
HLS ¹	9	9	10
HLS ²	10	16	14
HLS ³	9	12	12
1-Se	16	30	22
2-Se	12	18	14
3-Se	16	20	18
1-S	22	26	22
2-S	n.a. ^b	12	12
3-S	18	24	20
Nystatin	30	32	52

^a Including diameter of disc (8 mm); ^b n.a. – not active

The most potent thiazole complex appears to be **3-S**, while in the case of selenazoles the most active complex was **2-Se**. Contrary to ligands, in the case of Co(III) complexes it was not possible to establish a strict correlation of impact of isosteric replacement on antibacterial activity. Only in the case of **2-S** and **2-Se** sulphur analogue was more active on all investigated bacterial strains. **3-Se** was more active than **3-S** on all bacterial strains except *E. coli* and *K. rhizophila*,

while **1-S** showed better activities against *E. coli*, *S. eneterica*, *B. subtilis* and *K. rhizophila* and its selenium analogue was more active against *P. hauseri*, *P. aeruginosa*, *S. aureus* and *C. sporogenes*.

Despite few exceptions, a complex formation resulted in more active chemical species regarding antifungal activity, with few. Complexation of **HLS²** with Co(III) resulted in **2-S** which showed no activity against *A. brasiliensis* and reduced activity against two other fungi strains. Reduced activity was also noticed for **2-Se** on *S. cerevisiae*. Slightly reduced activity was observed for **3-Se** in comparison to its parent ligand. The most active complexes on fungi strains were **1-Se** and **1-S** (with no substituents on benzene ring). The activity of **1-Se** against *C. albicans* was almost the same as in the case of nystatin (Table 4.15).

4.1.6.2 Acute lethality study

Results of acute toxicity test on brine shrimp (*Artemia salina*) are presented in Table 4.16. While DMSO itself did not cause changes in viability of treated nauplii at any of five tested concentrations, treatment with $K_2Cr_2O_7$ induced high incidence of lethality. Nauplii revealed different level of sensitivity toward (1,3-thiazol-2-yl)hydrazones and (1,3-selenazol-2-yl)hydrazones. Namely, our results showed that selenium compounds exhibited significantly reduced toxicity in comparison to their isosters. The most toxic were ligands without substituents at benzene ring (**HLS¹** and **HLSe¹**), while the most toxic sulphur base complex was **1-S**. In the case of selenium based complexes **1-Se** and **3-Se** showed the same level of toxicity, while the most toxic was **2-Se**.

Table 4.16 LC₅₀ values of the *A. salina* cytotoxic activity and IC₅₀ of the DPPH free-radical scavenging activity of investigated compounds

Compound	LC ₅₀ (μM) <i>A. salina</i>	Compound	LC ₅₀ (μM) <i>A. salina</i>
HLS¹	60.64 ± 9.23	HLSe¹	94.73 ± 6.56
HLS²	144.99 ± 11.23	HLSe²	137.15 ± 13.10
HLS³	70.62 ± 7.04	HLSe³	120.14 ± 12.45
1-S	35.49 ± 5.74	1-Se	72.66 ± 7.32
2-S	66.71 ± 10.11	2-Se	62.92 ± 8.89
3-S	42.21 ± 9.87	3-Se	72.41 ± 9.63
$K_2Cr_2O_7$	248.14 ± 16.85		

4.1.6.3 Free-radical scavenging activity

Selenium and sulphur inorganic and organic compounds and proteins are well known by their antioxidant properties.^{8,127,211,212} On the other hand, there is only one study of antioxidant capacity of (1,3-thiazol-2-yl)hydrazones while to the best of our knowledge there¹⁹⁰ is no such study published for (1,3-selenazol-2-yl)hydrazones. The proton donating ability of investigated compounds was assayed using a protocol for the determination of radical scavenging activity, the 2,2-diphenyl-1-picrylhydrazyl (DPPH) method.²¹³ IC₅₀ values were calculated from the plotted graph of scavenging activity against the concentrations of the samples. IC₅₀ is defined as the total antioxidant necessary to decrease the initial DPPH radical by 50%. IC₅₀ was calculated for all compounds based on the percentage of DPPH radicals scavenged. Ascorbic acid was used as the reference compound (positive control) with concentrations from 50 to 500 µg mL⁻¹. The obtained results (Table 4.17) revealed that selenium compounds were better antioxidants in comparison to their sulphur isosters, without exception. Both selenium and sulphur ligands with unsubstituted benzene rings showed best antioxidant activity in corresponding series. Benzene ring substitution with both electron donation (Me) and electron withdrawing properties (OMe) resulted in less active compounds. This effect was more pronounced for OMe derivatives. The Co(III) complexes followed the same trend. It is interesting to notice that there is a total overlap between free-radical scavenging activity and cytotoxicity. Namely, the compounds showing the more pronounced free-radical scavenging activity were the most cytotoxic.

Table 4.17 LC₅₀ values of the *A. salina* cytotoxic activity and IC₅₀ of the DPPH free-radical scavenging activity of investigated compounds

Compound	IC ₅₀ (µM) DPPH assay	Compound	IC ₅₀ (µM) DPPH assay
HLS¹	81.97 ± 7.66	HLSe¹	50.74 ± 7.85
HLS²	298.60 ± 18.14	HLSe²	125.28 ± 15.22
HLS³	151.12 ± 13.59	HLSe³	73.15 ± 8.18
1-S	48.93 ± 6.81	1-Se	18.86 ± 4.93
2-S	146.51 ± 16.64	2-Se	70.67 ± 9.54
3-S	71.71 ± 5.37	3-Se	42.33 ± 6.41
		Ascorbic acid	79.38 ± 8.52

Co(III) complexes showed better activities than the corresponding ligands. Our results are challenging the previously postulated hypothesis regarding the mode of action of (1,3-thiazol-2-yl)hydrazones²¹² and other hydrazone derivatives,²¹³ which indicate an interaction of hydrazone hydrogen atom with DPPH radical. Namely, the coordination of **HLS**⁽¹⁻³⁾ to Co(III) resulted in their deprotonation, which was shown by the results of single crystal X-ray diffraction experiments. On the other hand there is no other acidic hydrogen atom present in Co complexes. It seems that sulphur and selenium atoms are the cause for free-radical scavenging activity in Co(III) complexes.

4.1.6.4 Anticancer activity

Comparison of anticancer activity on 2-D and 3-D cell models

Investigation on anti-cancer activity of **3-S** was initiated by evaluation of its ability to induce cell death in a classical MCF-7 2-D monolayer culture over 24 h of incubation. CDDP was chosen as our reference compound, as it is currently the most efficient metal complex administered in treatments of various types of cancer²¹⁴. The activity of the ligand **HLS**³ could not be tested due to its low solubility in the cell culture medium. Starting cobalt salt after 24 h of incubation exhibited very low cytotoxic activity and did not reach ED₅₀ value in the range of applied concentrations (up to 100 µM). As represented in Figure 4.16, treatment with **3-S** induced higher incidence of cell death compared to CDDP. Contrary to CDDP, activity of **3-S** displayed a wide plotted concentration-response curve. This implies there is a broad concentration of **3-S** to achieve the desired treatment effect while avoiding a toxic threshold i.e. a characteristic of a drug of good therapeutic index²¹⁵.

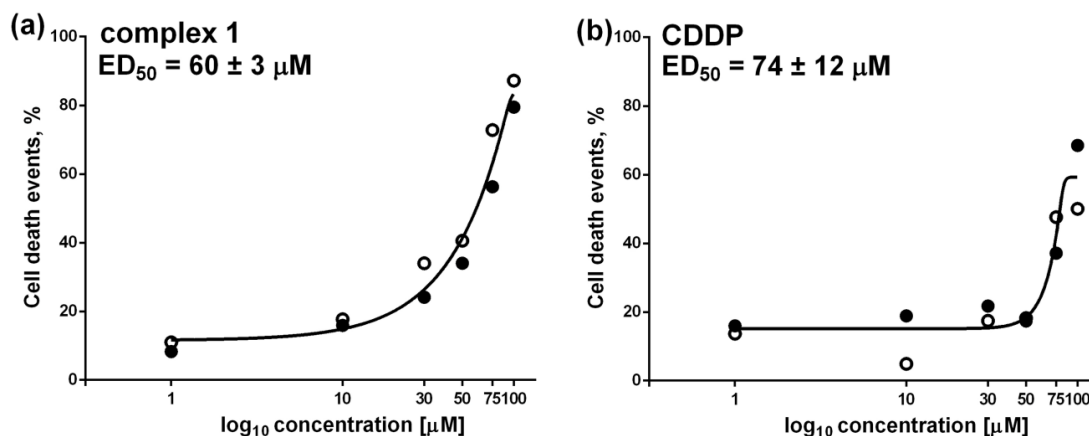


Figure 4.16 Concentration-response curves and ED₅₀ values for 3-S (a) and CDDP (b) on 2-D MCF-7 cell model after 24 h of incubation. Results are presented as percentage of cell death events determined by means of Annexin-V/PI double staining in two independent experiments (open and closed circles) and asymmetric five-parameter sigmoidal curve computed for both replicates in GraphPad Prism software.

The next step was to examine activity of **3-S** and CDDP in a 3-D cell model. 3-D culture models are *in vitro* derived tissues which mimic *in vivo* tumors in respect to gradient of nutrients, oxygen and metabolites within themselves²¹⁶. Therefore, 3-D models serve as a unique screening platform for drug effectiveness in a function of multiple parameters such as drug concentration, molecular weight, kinetics, charge, solubility, diffusion, metabolism, and sequestration²¹⁷.

Changes in 3-D cultures can be analyzed regarding two parameters: size and morphology. Due to insufficiency of mass transport through cellular barriers, there are three concentric zones clearly distinguished within newly developed spheroid: necrotic core (black circle located in the center of sphere, consisted of dead cells), quiescent zone (transparent dark gray rim that surrounds necrotic core), and proliferating zone (transparent light gray located on the outer edge). Sizes and mutual ratio of these zones got altering over the days of incubation, thus in non-treated spheroids necrotic core is getting bigger with quiescent zone significantly thinned and completely suppressed to the very edge of the sphere (Figure 4.17). Spheroids treated with CDDP showed concentration-dependent changes in both parameters (Figure 4.17). Concentration of 100 μM induced reduction in spheroid size already after second day of incubation, together with markedly expanded necrotic core and loss of proliferating zone. Size of those spheroids remained unchanged over the time of incubation, but zones became

unrecognizable with development of strikingly crispy edges. CDDP at concentration of 10 μM induced growth regression almost equivalent to that achieved with 100 μM , but morphological transformation was far less prominent. Thus, at the fourth day, 3-D cultures subjected to concentration of 10 μM still had well defined edge and preserved thin proliferation zone. Spheroids incubated with 1 μM of CDDP were the least affected in both growth rate and morphological changes.

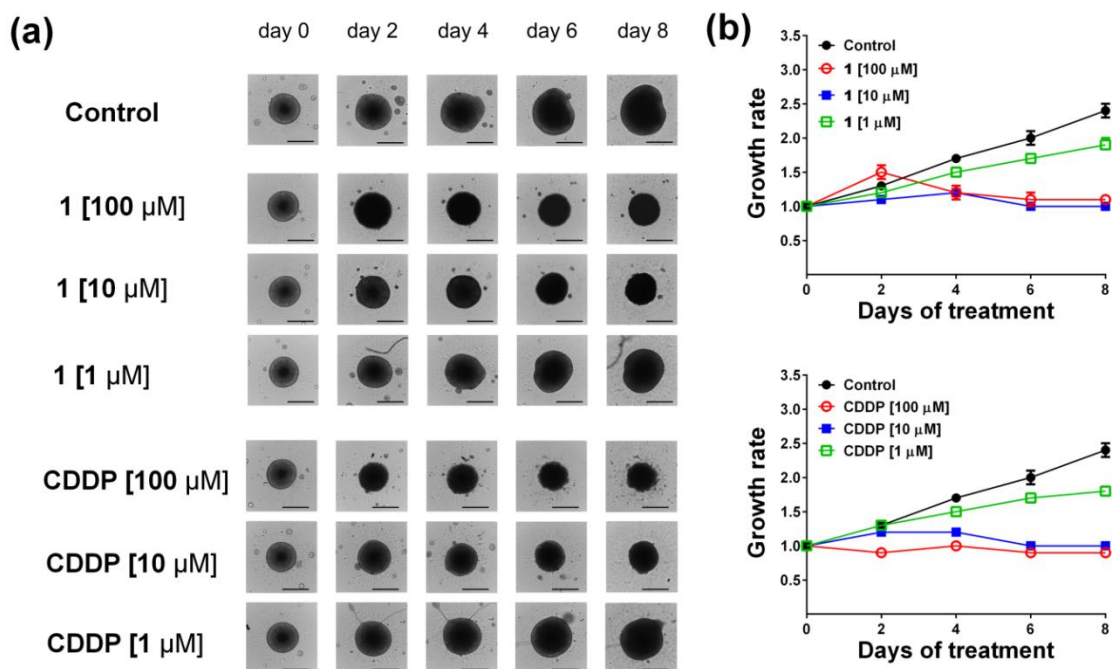


Figure 4.17 (a) MCF-7 3-D culture changes in growth and morphology induced by the treatment with either 1 or CDDP added in three concentrations over the 8-day incubation period. Images have been acquired every other day, starting from day 0 on the Celigo imaging cytometer using Celigo software. Scale bar: 500 μm . (b) Changes in growth rate of MCF-7 spheroids treated with either 1 or CDDP applied in concentrations of 100 μM (open circle), 10 μM (full square), and 1 μM (open square), and non-treated control (full circle). Growth rate was determined by means of spheroid area established with Celigo software, and afterwards computed for every other day of the 8-day incubation period by dividing the area on the day-n with the area on the day 0. Results are presented as the mean \pm SD of two replicates of independent experiments.

The highest (100 μM) applied concentration of **3-S** initially induced an increase in size of 3-D culture accompanied with complete loss of recognizable zones within its architecture, demonstrating a mighty drug activity. Starting on the fourth incubation day, those spheroids were displaying a decrease in size, thus on day eight, their growth rate was almost equal to the one obtained after CDDP treatment at the same concentration (1.08 ± 0.03 and 0.95 ± 0.01 for **3-S** and CDDP, respectively). Spheroids incubated with

a median concentration of **3-S** (10 μM) were gradually losing their zonal segregation. At day two, a necrotic core was still distinctive, while the quiescent zone was dark and glazy with complete disappearance of any proliferation rim. Two days later, the necrotic core could be barely identified, while on day six, spheroid zonal organization was completely obliterated. Nevertheless, those two concentrations of **3-S** induced almost the same activity on 3-D cultures, but morphological transformations registered in spheroids treated with concentration of 10 μM were vigorous to a lesser extent. As for CDDP, the lowest tested concentration of **3-S** (1 μM) did not produce any substantial growth rate inhibition. However, due to the delayed growth, the ratio between necrotic core and quiescent zone at day eight was approximately the same as seen on day four in control 3-D cultures.

The differences in response to treatment with **3-S** on monolayer or spheroids at 10 and 100 μM provide a full insight into benefit of drug testing on 3-D model. Since 2-D culture of adherent cells is considered today as completely unrealistic formation where all cells are equally exposed to applied treatment, it is not surprising that promising results gained from *in vitro* evaluation are frequently not confirmed during *in vivo* assessment. Here, concentration of 10 μM achieved almost the same activity on 3-D model as concentration of 100 μM on 2D, a result completely unforeseen according to percentages of cell death scored with those concentrations on 2-D (Figure 4.16 and Figure 4.17 (a)). Thus, our results confirm that **3-S** is a compound with potentially high therapeutic index, and by careful dose titration, the desired impact should not be compromised with side effects.

Combination treatment

The strategy of combination treatment implies acting upon different targets in order to improve therapeutic effect as well as to interfere with development of drug resistance which tumor cells can easily acquire in case of single drug therapy. Major disadvantage of combination treatment includes interactions at the level of side effects. Such interaction demands dose reduction for each drug given in combination so to avoid serious toxic complications. We evaluated here the possibility of assenting interaction of **3-S** with paclitaxel, nowadays one of mostly used drugs for the treatment of breast cancer²¹⁸. On the other hand, CDDP was revealed as effective for the treatment of

locally advanced breast cancer, metastatic breast cancer and triple-negative breast cancers²¹⁹.

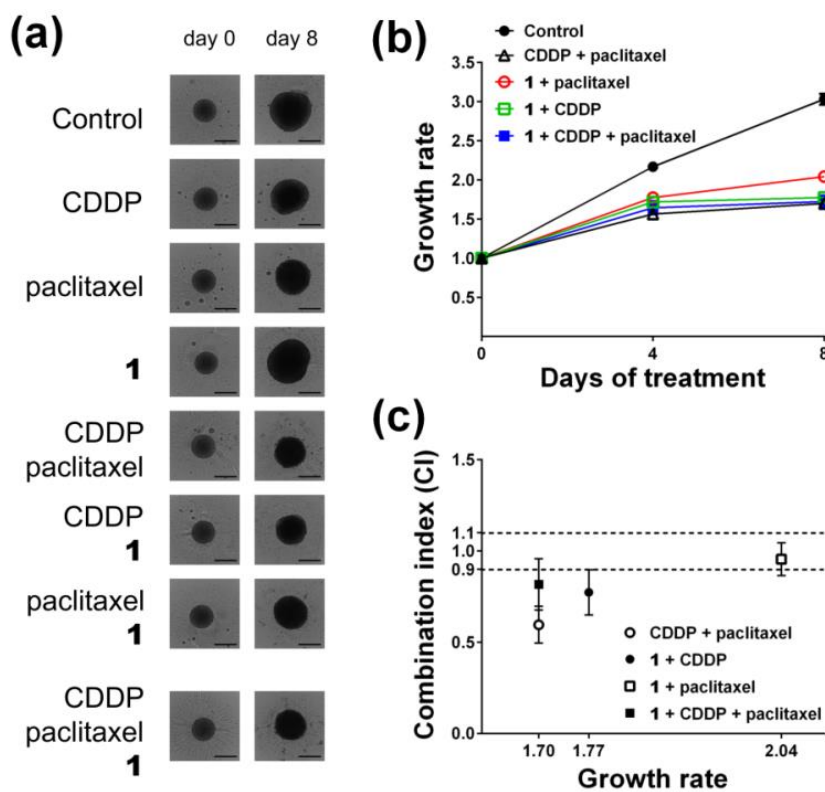


Figure 4.18 (a) MCF-7 3-D culture changes in growth and morphology induced by the treatment with different combinations of 1, CDDP and paclitaxel. Images have been acquired every other day, starting from day 0 on the Celigo imaging cytometer using Celigo software. Scale bar: 500 μm . (b) Changes in growth rate of MCF-7 spheroids treated with combination of CDDP and paclitaxel (open triangle), combination of 1 and paclitaxel (open circle), combination of 1 and CDDP (open square), combination of 1 with CDDP and paclitaxel (closed square), and non-treated control (full circle). Growth rate was determined by means of spheroid area established with Celigo software, and afterwards computed for days 4 and 8 by dividing the area on the day-n with the area on the day 0. Results are presented as the mean \pm SD of two replicates of independent experiments. (c) Type of interactions between drugs in combination treatments expressed by means of Combination index (CI), where $CI < 0.9$ indicates on synergistic, $0.9 < CI < 1.1$ indicates on additive, and $CI > 1.1$ indicates on antagonistic type of interaction. Results are presented as the mean \pm SD of two replicates of independent experiments.

The least effective concentrations of 3-S and CDDP confirmed in the single-treatment experiment were used (1 μM , Figure 4.17) in planning of combination treatments in respect of the general approach that implies dose reduction of drugs in combination, while paclitaxel was investigated in concentration of 1 nM also

determined as the concentration with lowest activity in the tested range between 1-100 nM (data not shown). As shown in Figure 4.18, combination of paclitaxel with **3-S** was the least effective when compared to other three combinations. However, the true type of interaction within combinations becomes evident when represented by the combination index (CI, Figure 4.18 (c)). Combination of **3-S** with CDDP revealed synergistic interaction whereas **3-S** in combination with paclitaxel acted additively with less efficient inhibition of spheroid growth. CDDP with paclitaxel in combination performed synergistically against MCF-7 3-D model, while the addition of **3-S** to the triple combination did not help to gain any improvement of the overall effect of two conventional drugs, but additionally did not reduce it either. Different type of interactions defined for **3-S** and CDDP when they were separately combined with paclitaxel, remains a strong indication that those two metal complexes do not share the same target. Their combination deserves further investigation on this and other 3-D models tested in various concentration ratios.

4.2 Nitro (*o*, *p* and *m*) benzaldehyde-based (1,3-selenazol-2-yl)hydrazones

4.2.1 Synthesis and characterization of second series 1-4 (OMe, Me)

Twelve benzylidene-based (1,3-selenazol-2-yl)hydrazones (Scheme 3.3) were prepared *via* Hantzsch type condensation of corresponding selenosemicarbazones with a series of 4-substituted α -bromoacetophenones. Compounds **4-OMe** and **4-Me** crystallized as single crystals suitable for X-ray diffraction analysis (XRD) which indicated *E*-configuration of the imine bond (*vide infra*).

Synthesis of the compounds **1** and **1-Me** was previously published, but without spectral characterization²²⁰. Literature data for melting points of **1** and **1-Me** significantly differ from our data²²⁰. Structures of all synthesized compounds were confirmed by elemental analysis, NMR and IR spectroscopy and mass spectrometry data. 1D and 2D NMR spectra are given in Figure 7.39-Figure 7.78. The influence of substituents on both phenyl rings, A and B, on NMR chemical shifts of corresponding hydrogen and carbon atoms was observed. As expected, in the ¹H NMR spectra of all compounds the signal of H-N2 is the most downfielded. Substitution of the phenyl rings had negligible influence on chemical shift of a proton from 1,3-selenazole ring, thus the signal of the proton H-C9 in the ¹H NMR spectra of all compounds appeared in

the narrow range (7.51–7.71 ppm). Introduction of NO₂ group on the phenyl ring A, which has negative inductive and negative resonance effect, caused downfield shift of signals of all protons in the ring in comparison to signals of corresponding protons in the ¹H NMR spectra of compounds from set 1. Also, chemical shift of H-C7 protons was affected by this substitution, where for all compounds from set 2, with NO₂ group in ortho-position, significant shift to lower field was observed. Introduction of methyl group on the phenyl ring B, which is electron donating group by induction, caused shielding effect of all protons from the ring B, where signals of protons H-C13 and H-C15 were the most affected in the ¹H NMR spectra of all methyl derivatives. The electronic effects of methoxy group, which is a withdrawer by induction and an electron donor by resonance, is determined by its position. Since it participates in delocalization of pi electrons from the phenyl ring B, it functions as strong electron donor. This is again mostly reflected on chemical shifts of H-C13 and H-C15 protons in the ¹H NMR spectra of all methoxy derivatives, where these protons are shielded and thus their signals are upfielded. Electronic effects of substituents have the similar impact on chemical shifts of corresponding carbon atoms in ¹³C NMR spectra.

4.2.2 Analysis of crystal structures

Crystal data, data collection and refinement parameters for the compounds **4-OMe** and **4-Me** are summarized in Table 4.18.

Molecular structures of compound **4-Me** and **4-OMe** with the atom numberings are given in Figure 4.19, crystal packing motifs are depicted in Figure 4.20, while selected bond lengths and bond angles are presented in Table 4.19.

Table 4.18 Crystallographic data of 4-Me and 4-OMe.

Structure	4-Me	4-OMe
<i>Brutto</i> formula	C ₁₇ H ₁₄ N ₄ O ₂ Se	C ₁₇ H ₁₄ N ₄ O ₃ Se
Formula weight (g mol ⁻¹)	385.28	401.28
Crystal color and habit	Orange prism	Brown prism
Crystal dimensions (mm)	0.33 × 0.26 × 0.21	0.30 × 0.21 × 0.20
Space group	<i>Pbcn</i>	<i>Pbca</i>
<i>a</i> (Å)	11.4924(3)	11.8767(6)
<i>b</i> (Å)	7.9189(4)	13.5795(7)
<i>c</i> (Å)	35.9317(19)	20.3707(11)
<i>V</i> (Å ³)	3270.0(3)	3285.4(3)
<i>Z</i>	8	8
μ (CuK α) (mm ⁻¹)	3.263	3.218
Absorption correction	Multi-scan	Multi-scan
<i>F</i> (000)	1552	1616
θ max (°)	74.000	76.014
No. refl. measured	7934	9975
No. refl. unique	3212	3383
No. refl. observed [<i>I</i> > 2 σ (<i>I</i>)]	2562	2912
<i>R</i> _{int}	0.0395	0.0229
<i>R</i> _{σ}	0.0601	0.0315
Parameters	227	239
<i>R</i> ₁ [<i>I</i> > 2 σ (<i>I</i>)]	0.0461	0.0319
<i>wR</i> ₂ , all	0.1414	0.0964
<i>S</i>	1.054	1.044
ρ _{max} , ρ _{min} (eÅ ⁻³)	0.46, -0.68	0.25, -0.34

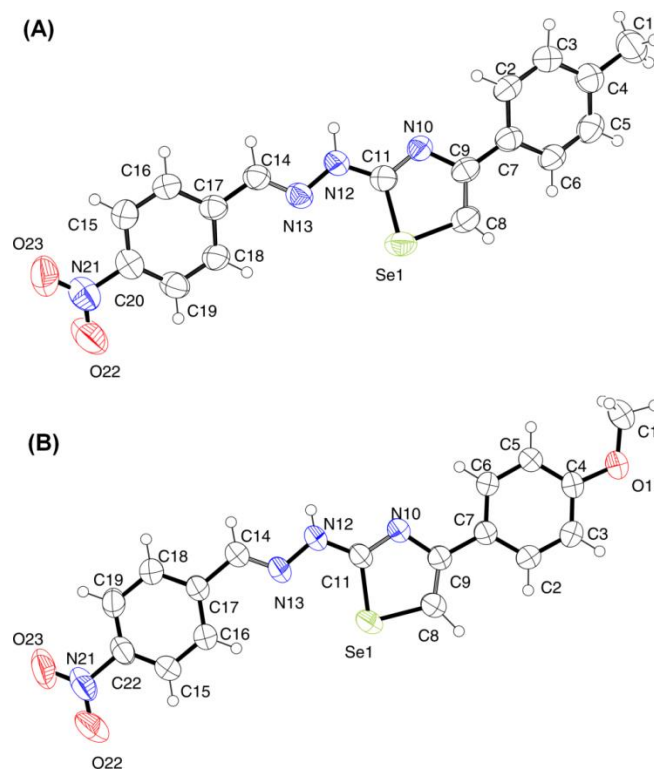


Figure 4.19 ORTEP drawings of the molecular structures of compounds 4-Me (A) and 4-OMe (B) with labeling of non-H atoms. Displacement ellipsoids are shown at the 50% probability level and H atoms are drawn as spheres of arbitrary radii.

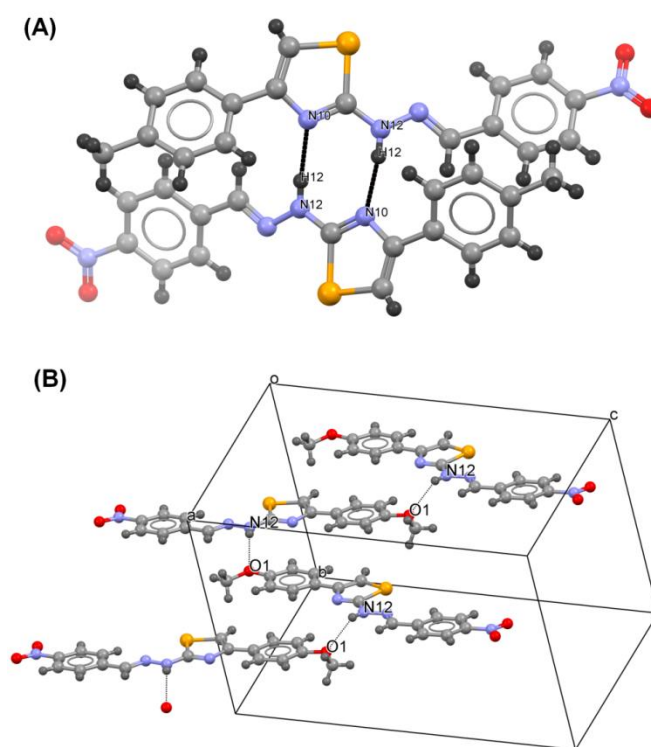


Figure 4.20 Crystal packing diagrams of compound 4-Me (A) and 4-OMe (B).

Table 4.19 Selected experimentally obtained (XRD) and calculated (DFT) bond lengths (Å) and angles (°) for **4-Me** and **4-OMe**.

	4-Me (XRD)	4-Me (DFT)	4-OMe (XRD)	4-OMe (DFT)
C7–C9	1.475(5)	1.476	1.475(3)	1.476
C8–C9	1.353(5)	1.368	1.351(3)	1.369
C8–Se1	1.871(5)	1.874	1.873(2)	1.876
C9–N10	1.388(4)	1.391	1.391(2)	1.391
C11–N10	1.300(5)	1.291	1.290(2)	1.292
C11–N12	1.348(5)	1.375	1.361(3)	1.375
C11–Se1	1.872(4)	1.887	1.8808(19)	1.886
C14–N13	1.277(4)	1.290	1.271(3)	1.290
C14–C17	1.451(4)	1.459	1.463(3)	1.459
N12–N13	1.358(4)	1.338	1.354(2)	1.337
N21–O23	1.212(5)	1.232	1.214(3)	1.232
N21–O22	1.218(6)	1.232	1.222(3)	1.232
C9–C8–Se1	111.6(3)	111.16	111.86(16)	111.60
C8–C9–N10	116.0(3)	116.20	116.55(18)	116.20
C8–C9–C7	126.9(3)	125.90	125.85(19)	126.00
N10–C9–C7	117.1(3)	117.90	117.59(17)	117.80
N10–C11–N12	121.3(3)	122.10	124.32(18)	122.00
N10–C11–Se1	115.2(3)	116.30	116.57(15)	116.30
N12–C11–Se1	123.6(3)	121.70	119.11(14)	121.70
N13–C14–C17	121.8(3)	121.20	119.71(19)	121.10
C11–N10–C9	113.4(3)	112.80	112.22(16)	112.80
C11–N12–N13	120.4(3)	120.60	117.09(17)	120.60
C14–N13–N12	115.4(3)	119.10	118.96(17)	119.10
O23–N21–O22	122.6(4)	124.60	123.6(2)	124.60
O23–N21–C20	119.0(4)	117.70	118.4(2)	117.70
O22–N21–C20	118.4(4)	117.70	118.0(2)	117.70
C8–Se1–C11	83.76(16)	83.20	82.79(9)	83.20

The geometries of the selenazole rings in both structures reveal no unusual parameters when compared with the set of related structures from the current version of CSD²²¹. Analysis of the interplanar angles defined by the least square plane of the selenazole ring and the least square planes of both phenyl rings reveals a certain level of planarity in the structure of **4-OMe** unlike in **4-Me** (Table 4.20). Visually this result is depicted in Figure 4.21, which displays an overlay of molecular structures of **4-Me** and

4-OMe. The torsion angle Se1–C11–N12–N13 [$-7.3(4)^\circ$ in **4-Me** and $1.3(3)^\circ$ in **4-OMe**] reveals the *cis*-orientation of the N13 with respect to the selenium (and, consequently, *trans*-orientations with respect to the N10) in both structures, which are therefore conformationally prone to act as *N,Se* bidentate ligands in possible metal coordination. Basic crystallographic packing motif in the structure of **4-Me** is a distinct paddle wheel-like centrosymmetric molecular dimer formed by the hydrogen bond N12–H12 \cdots N10^{*i*} [$i = 1-x, y, 1/2-z$; d (N12–H): 0.86 Å, d (H \cdots N10): 2.01 Å, d (N12 \cdots N10): 2.857(5) Å, angle: 168°] of the graph set notation R 2,2 (8) (Figure 4.20A). The paddlewheel axis running through Se1 and C11 of both involved molecules is roughly parallel with the crystallographic *a*-axis. In the structure of (roughly planar) **4-OMe** crystal packing is guided by a single hydrogen bond N12–H12 \cdots O1^{*ii*} [$ii = 1/2+x, y, 1/2-z$; d (N12–H): 0.81(4) Å, d (H \cdots O1): 2.48 (3) Å, d (N12 \cdots O1): 3.202 (3) Å, angle: $150(3)^\circ$] through which the *zig-zag* oriented molecules are connected into the “endless” chains parallel to the crystallographic *ac* plane (Figure 4.20 B).

Table 4.20 Angles between the selenazole ring least square plane and phenyl rings least square planes.

Se1-C8-C9-N10-C11	4-Me ($^\circ$)	4-OMe ($^\circ$)
C2-C3-C4-C5-C6-C7	30.18 (15)	4.94 (10)
C15-C16-C17-C18-C19-C20	24.86 (15)	6.03 (11)

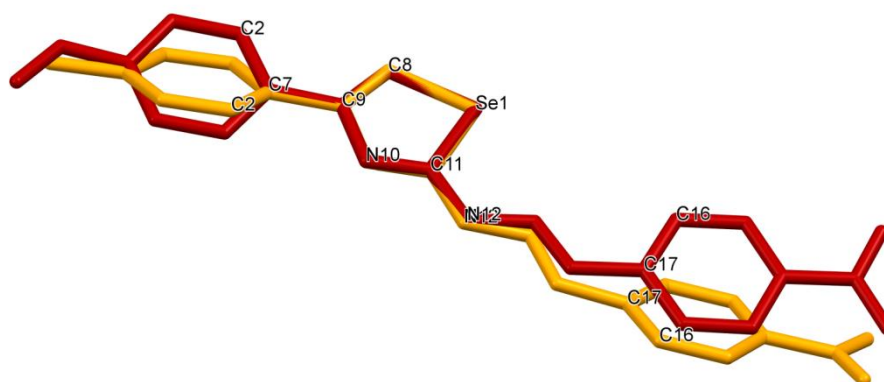


Figure 4.21 Structural superposition of **4-Me** (yellow) and **4-OMe** (red).

4.2.3 Cyclic voltammetry (CV)

All compounds were studied voltammetrically in DMSO using TBAP as supporting electrolyte. Results of CV study are given in Table 4.21. Examples of cyclic voltammograms of compounds **1–4** are given in Figure 4.22. In the investigated potential range (+1.0V to –2.0 V) **1**, **1-OMe** and **1-Me** show mainly one reduction and one oxidation peak. Reduction peak around –1.40 V is caused by reduction of imine group of the ligand. The peak at around +0.40 V can be attributed to the oxidation of chalcogen or C8 atoms. Both electrochemical processes were coupled with a chemical reaction (EC mechanism), as there were no peaks in the reverse scan. For the oxidation peaks there were a few peaks of small intensities at the subsequent cathodic sweep as a result of decomposition of the oxidized species ¹⁹.

Table 4.21 Voltammetric characteristics of the the benzylidene-based (1,3-selenazol-2-yl)hydrazones^a

Comp.	$E_p^{R(I)^b}$	$I_p/cv_{1/2}$	$E_p^{O(I)}$	$I_p/cv_{1/2}$	$E_p^{R(II)}$	$I_p/c_{v^{1/2}}$	$E_p^{O(II)}$	$I_p/c_{v^{1/2}}$	$E_p^{Ox(II)}$	$I_p/cv^{1/2}$	E_{HOM} (CV)	E_{HOMO} (DFT)
1	/	/	/	/	-1.45	2.1	/	/	+0.33	39.1	-4.90	-5.34
1-Me	/	/	/	/	-1.50	2.9	/	/	+0.28	38.4	-4.85	-5.20
1-OMe	/	/	/	/	-1.59	2.3	/	/	+0.31	26.6	-4.88	-5.30
2	-1.26	6.8	-1.27	4.1	-1.46	5.3	-1.39	12.7	+0.40	23.2	-4.97	-5.49
2-Me	-1.27	13.2	-1.23	2.3	-1.49	6.6	-1.39	13.9	+0.36	24.0	-4.93	-5.31
2-OMe	-1.25	11.3	-1.26	3.6	-1.47	10.6	-1.40	15.5	+0.43	23.0	-5.00	-5.43
3	-1.18	10.7	-1.20	4.2	-1.40	16.8	-1.33	22.2	+0.42	25.7	-4.99	-5.51
3-Me	-1.20	4.2	-1.19	5.4	-1.40	17.9	-1.33	4.3	+0.42	18.9	-4.99	-5.32
3-OMe	-1.21	13.1	-1.19	4.6	-1.44	14.9	-1.32	21.3	+0.42	20.2	-4.99	-5.45
4	-1.29	25.3	/	/	-1.38	3.5	-1.32	21.3	+0.41	35.8	-4.98	-5.46
4-Me	-1.27	25.3	/	/	-1.39	2.4	-1.32	19.4	+0.40	34.8	-4.97	-5.28
4-OMe	-1.30	26.2	/	/	-1.39	2.2	-1.31	18.9	+0.37	33.5	-4.94	-5.40

^a In DMSO containing 0.1 M TBAP at $v = 100$ mV/s; ^b E_{vs} ferrocene/ferrocenium couple (Fc/Fc⁺) in V; ^c in $\mu A/mM(V/s)^{1/2}$; ^d in eV, $E_{HOMO} = -4.8 - (E - E_{Fc})$, $E_{Fc} = +0.23V$

Cyclic voltammograms of nitro derivatives show additional both reduction and oxidation peaks. Reduction peak at around -1.20 V corresponds to reversible one-electron reduction of the radical anion of the nitro group which is commonly known in aprotic solvents²²². Since the intensities of the reverse scan currents are decreased the mechanism of the reaction is also EC. Additional oxidation peak at around -1.35 V belongs to reversible one-electron oxidation of imine group. The oxidation peak is invisible for **1**, **1-Me** and **1-OMe** which means that the presence of strong electron withdrawing nitro group enables oxidation of the anion²²³. The intensities of the reverse scan are increased by 20-30% implying the ECE nature of the reaction mechanism. Peak currents were correlated with the square root of scan rate (20–500 mV/s) and the linear relationship was obtained which indicates diffusion controlled process on the electrode surface.

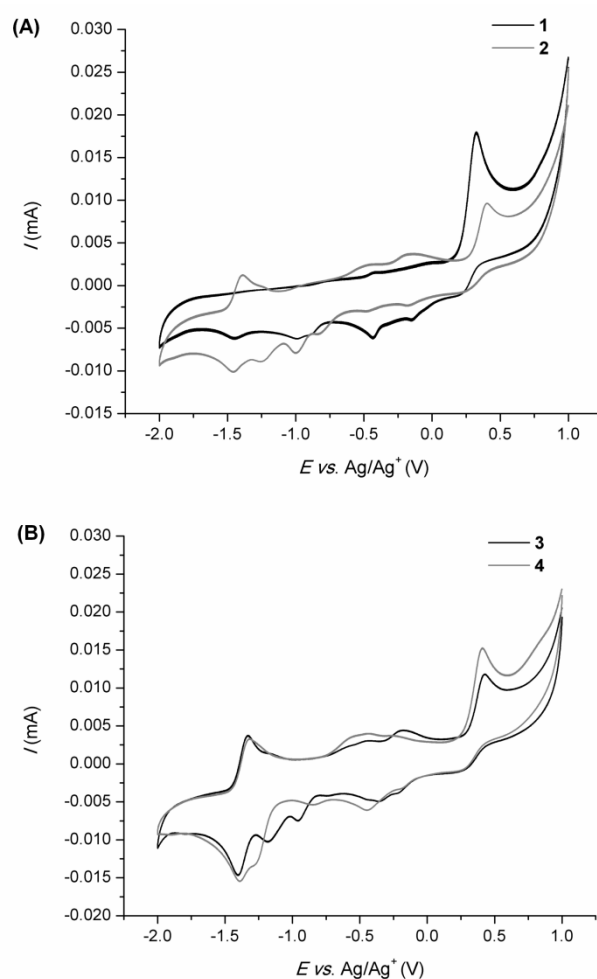


Figure 4.22 Cyclic voltammograms of compounds 1 and 2 (A) and 3 and 4 (B).

4.2.4 MS/MSⁿ analysis

The mass spectral fragmentation of investigated compounds was studied in order to gain a better understanding of their behavior, and should reflect position dependent substituent influence on fragmentation mechanism. Mass spectra were recorded in the range of $m/z = 50$ to 600 in positive and negative electrospray ionization mode (example of mass spectra are given in Figure 4.23 and Figure 4.24). Tandem mass spectrometry was performed with collision energy optimized for each compound and transition in order to obtain stable and abundant fragments. Detection of the analytes was based on the isolation of the protonated molecule, $[M+H]^+$ or deprotonated molecule $[M-H]^-$, and fragmentation schemes are shown in Figure 4.25 and Figure 4.26-Figure 4.34.

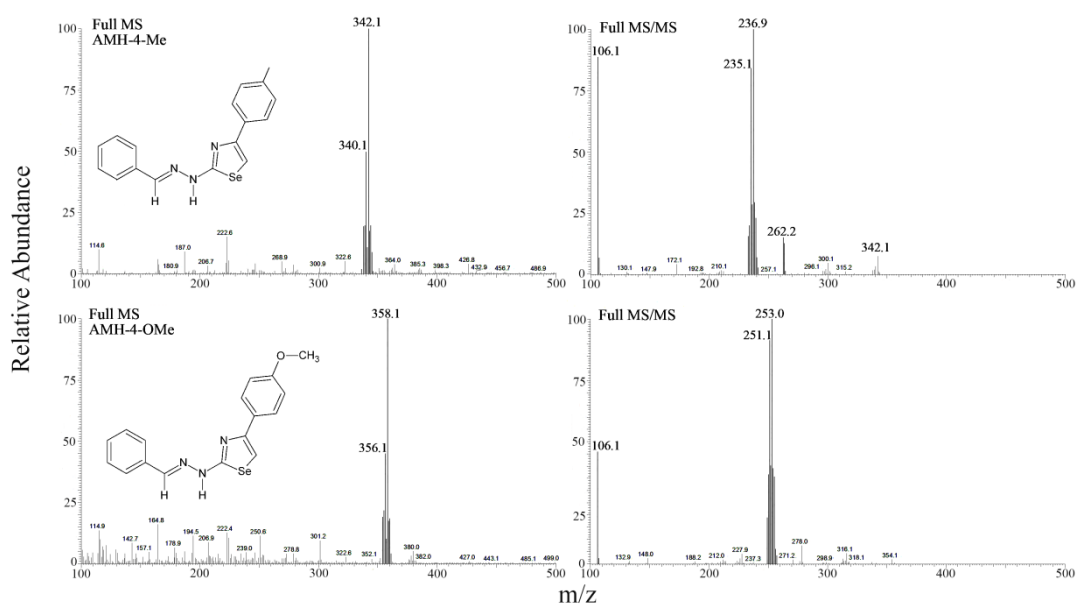


Figure 4.23 Full MS/MS spectra of 1-Me (top) and 1-OMe (bottom)

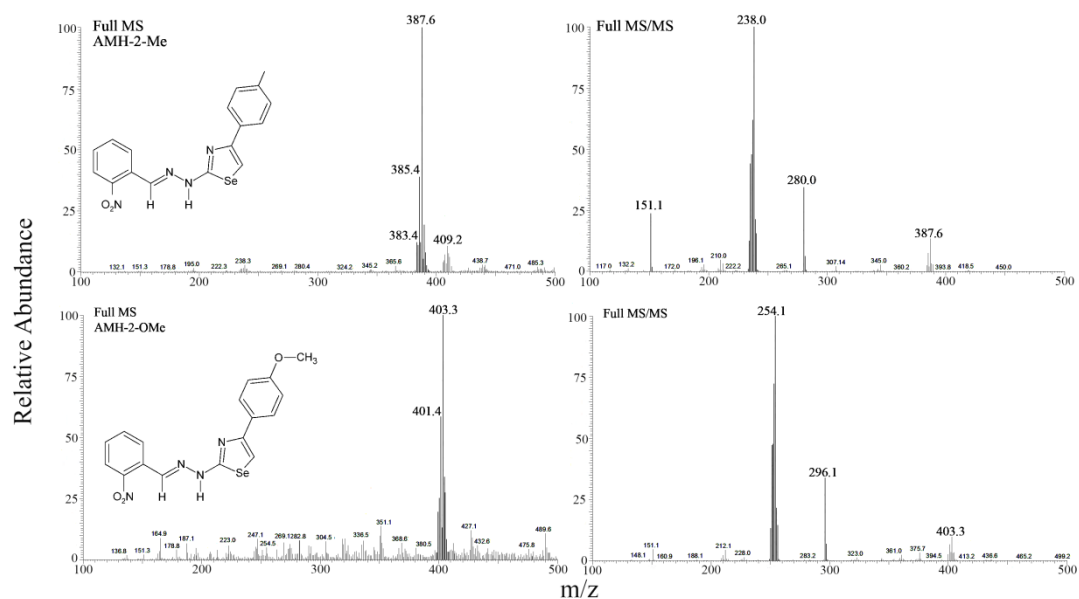


Figure 4.24 Full MS/MS spectra of 2-Me (top) and 2-OMe (bottom).

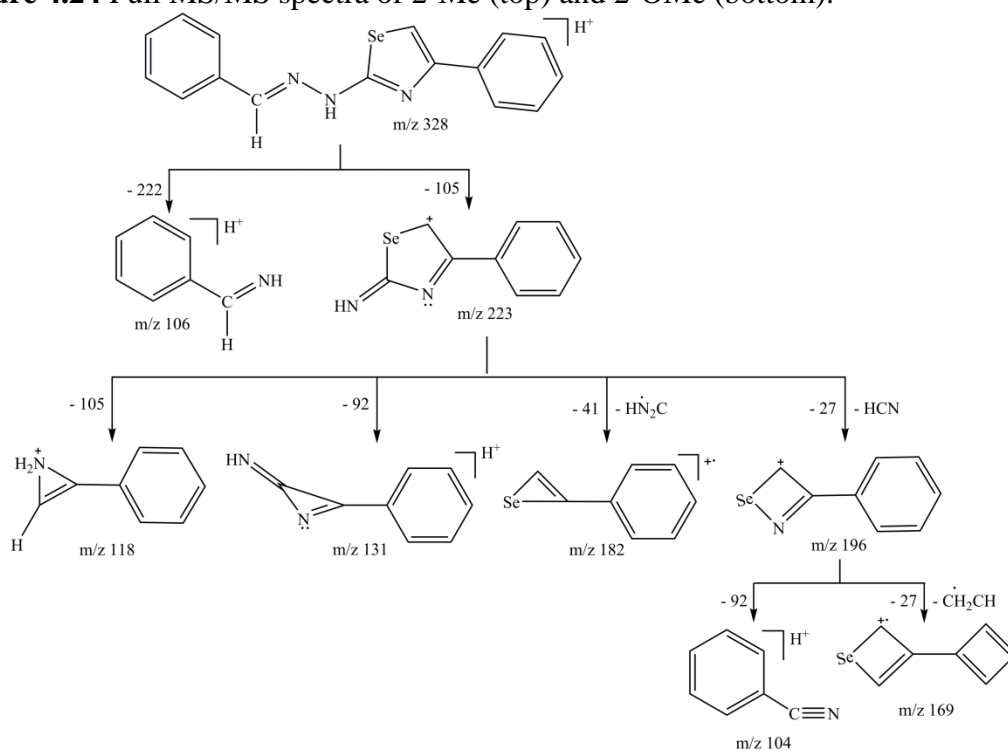


Figure 4.25 Common fragmentation paths of compound 1.

Full MS² spectrum of ion at m/z 328 in the mass spectrum of **1** revealed two fragment ions: the most intense peak at m/z 223, 2-amino-4-phenyl-2,5-dihydro-1,3-selenazol-5-yl cation, and phenylmethaneimine, an ion observed at m/z 106. By further fragmentation of the daughter ion, m/z 223, fragments at m/z 118, 131, 182 and 196

were detected. The most abundant ion in MS² spectrum, at m/z 196 (3-phenyl-4*H*-1,2-selenazet-4-ylum ion) was obtained by the loss of 27 Da (HCN). Subsequent fragmentation of m/z 196 ion, observed in MS⁴ spectrum, produced two fragments: protonated benzonitrile (m/z 104) and 3-(cyclobuta-1,3-dienyl)-2*H*-selenet-2-ylum (m/z 169).

Compounds **1-Me** and **1-OMe** were fragmented in a similar fashion like **1** and main fragmentation pathways are presented in Figures 4.26 and Figure 4.27. In the first fragmentation step of **1-OMe** and **1-Me**, similar fragments were obtained to ones found for **1**. MS² analysis of **1-OMe** revealed two major fragments at m/z 106, obtained by the hemolytic cleavage of C=N-N bridging single bond, and ion at m/z 253, obtained by the loss of 105 Da (Figure 4.26).

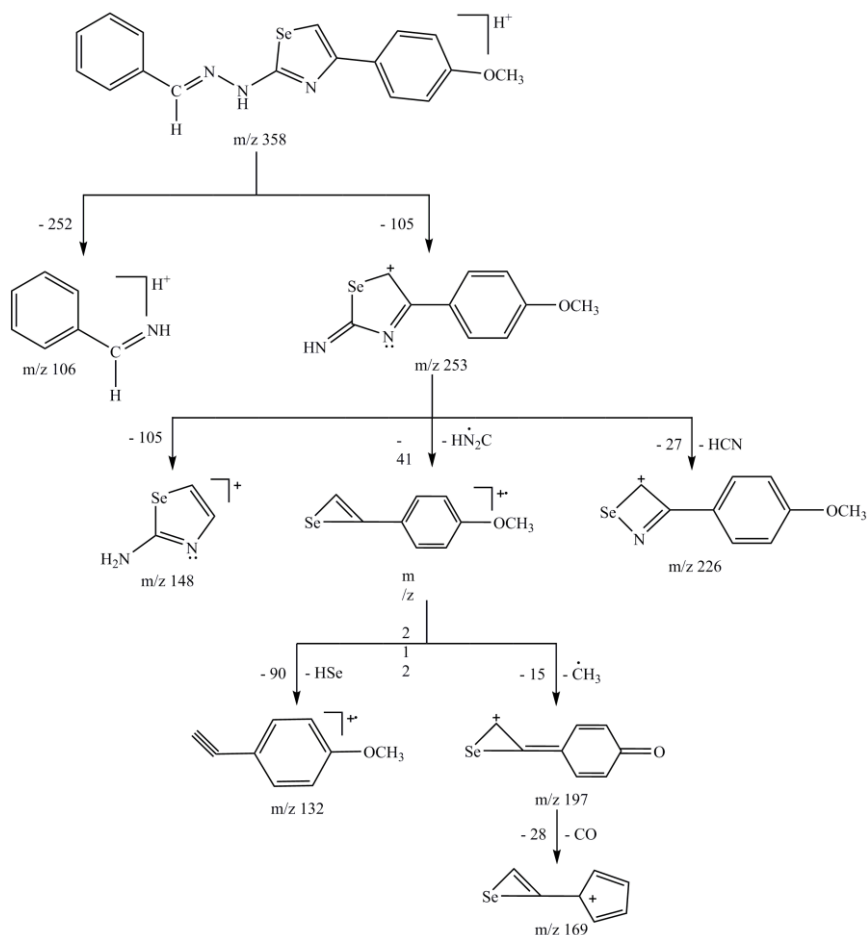


Figure 4.26 Common fragmentation paths of **1-OMe**.

Further fragmentation of the daughter ion at m/z 253 resulted in the subsequent loss of HCN, HN_2C radical and phenylmethaneimine producing the fragments at m/z

226, 212 and 148. Fragment at the m/z 212 was further fragmented and ions at m/z 132 and 197 were obtained. Ion at m/z 132, 1-ethynyl-4-methoxybenzene ion, was produced by expulsion of selenium monohydride (hydrogen selenide) ion from m/z 212. Homolytic cleavage of the O-CH₃ generated the second ion obtained through MS⁴ analysis of the ion at m/z 212, ion at m/z 197 (3-(4-oxocyclohexa-2,5-dien-1-ylidene)seleniran-2-ylum cation). Expulsion of carbon monoxide from the m/z 197 produce 1-(seleniren-2-yl)cyclopenta-2,4-dien-1-ylum cation (Figure 4.26).

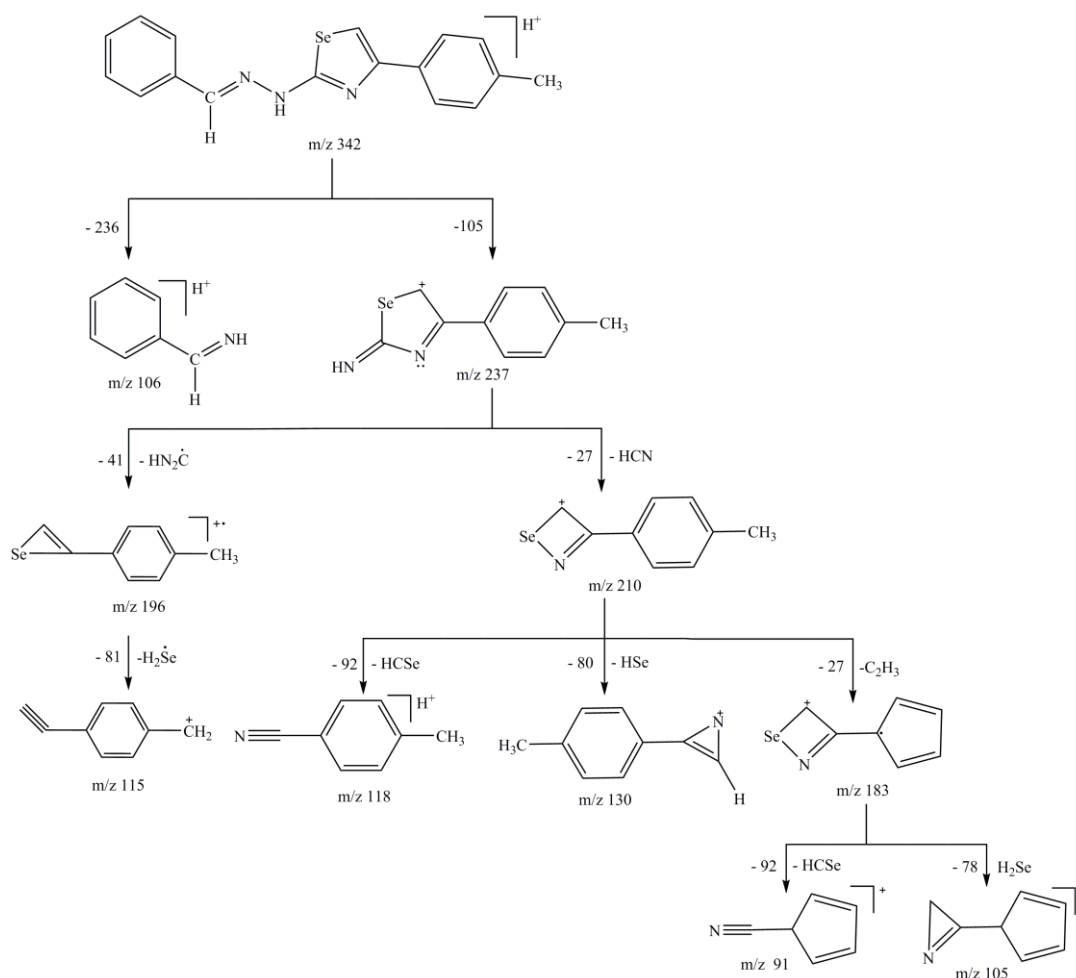


Figure 4.27 Common fragmentation paths of 1-Me.

Compound **1-Me** in the first fragmentation step, analogously to **1** and **1-OMe**, reveals two major fragments at m/z 106, obtained by the homolytic cleavage of C=N-N bridging single bond, and ion at m/z 237, obtained by the loss of 105 Da (Figure 4.27). Subsequent loss of HCN and H₂CN from the fragment at m/z 237 produced ions at m/z 210 and 196. Further fragmentation of ion at m/z 210 reveals ions at m/z 118, 130 (1-ethynyl-4-methylbenzene), and ion at m/z 183. In the final step of fragmentation the m/z

91 and 105 ions were obtained from m/z 183 (Figure 4.27). On the other hand loss of H_2Se radical from m/z 196 gave (4-ethynylphenyl)methyl cation (m/z 115). According to the difference in fragmentation paths of **1-OMe** and **1-Me** large influence of electronic substituent effects, i.e. low electron-donating for methyl and moderate for methoxy group, was observed.

Compounds **2**, **3** and **4** are the ones with variable position of nitro group: 2-, 3- and 4-position in the phenyl ring A and without Y substituent on the phenyl ring B. Schematic overview of proposed complex fragmentation path is given on Figure 4.28. Complex fragmentation path mainly arise from position dependent influences of electronic effect of *nitro*-group. Three characteristic fragmentation processes were observed for this group of studied compounds: (1) breakage of N-N single bond with concomitant loss of 4-nitrophenylmethaneimine (149 Da) producing 4-phenyl-1,3-selenazol-2-amine fragment (m/z 224); (2) a similar process to the one described, where different process of bond scission produce visible protonated 4-nitrophenylmethaneimine ion (m/z 151); (3) specific fragmentation which occurs through elimination organic fragment containing selenium (107 Da) forming an 2-(2-(2-, 3- and 4-nitrobenzylidene)hydrazono)-1-phenylethan-1-ylum ion (m/z 266), which after loss of nitro group produce 3-benzyl-4-phenyl-1,2-diazete (m/z 220). Characteristic fragmentations, noted for ion m/z 224, were defined by the loss of the H_2CN and H_2CN_2 radicals producing deprotonated 3-phenyl-4*H*-1,2-selenazet-4-ilyium ion (m/z 196) and 2-phenylselenirene (m/z 182) observed in the course of the fragmentation of all three studied compounds. Additionally loss of hydrogen selenide from m/z 182 ion produced benzonitrile (m/z 102) found for all three compounds.

Third group of compounds, i.e. **2-OMe**, **3-OMe** and **4-OMe**, contains electron-donating group with moderate effect capable to compensate electron-accepting properties of nitro group present in the phenyl ring A. Schematic overview of proposed complex fragmentation paths is given on Figure 4.29. MS^2 spectrum of ion m/z 403, molecular ion of compounds **2-OMe**, **3-OMe** and **4-OMe**, revealed that three ions were produced: the most intense peak at m/z 254 obtained by the loss of 4-nitrophenylmethaneimine, protonated nitro substituted phenylmethaneimine ion at m/z 151 and methyl(4-(2-((2-, 3- and 4-nitrobenzylidene)hydrazono)-ethylidene)cyclohexa-2,5-dienylidene)oxonium ion at m/z 296 obtained by the loss of organic fragment

containing selenium. Further fragmentation of m/z 296 takes place by elimination of the nitro group producing the *N*-benzylidene-2-(4-methoxyphenyl)-1*H*-azirin-1-amine ion at m/z 250 (found for **2-OMe**, **3-OMe** and **4-OMe**). On the other hand loss of fragment 58, produce 2-(cyclobuta-1,3-dienylethynyl)-1-(2- and 4-nitrobenzylidene)diazenium ion at m/z 238. Further fragmentations of m/z 250 and m/z 238 ions (found only for **2-OMe**) gave six fragments: m/z 134, m/z 148 and m/z 235 from former and m/z 148, m/z 207 and m/z 223 from the later one.

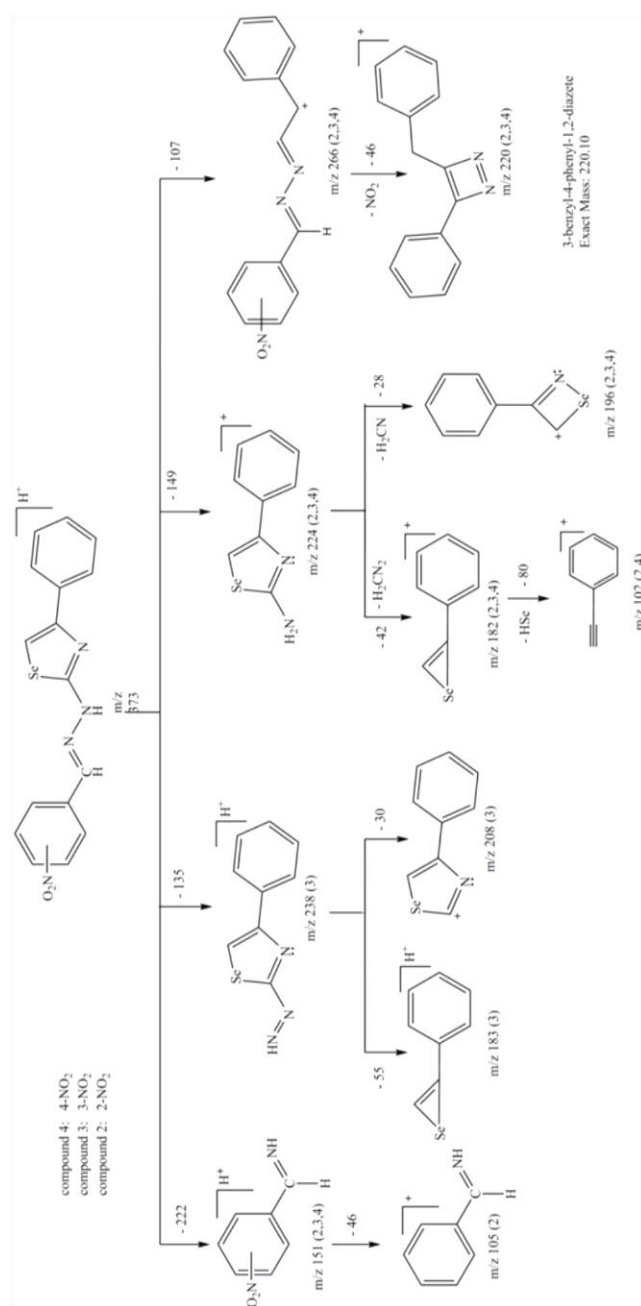


Figure 4.28 Common fragmentation paths of 2, 3 and 4.

Full mass MS² spectrum of ion at m/z 387, molecular ion observed for **2-Me**, **3-Me** and **4-Me**, revealed that three fragments were produced: the most intense peak at m/z 238 obtained by the loss of 4-nitrophenylmethaneimine, protonated nitro substituted phenylmethaneimine ion (m/z 151) and specific fragmentation, performed by the loss of organic selenium group, which produced 3-(2-(2-, 3- and 4-nitrobenzylidene)hydrazinyl)-2-phenyl-2*H*-azirine ion (m/z 280) (Figure 4.30). Further fragmentation of ion at m/z 280, for all three compounds, was accomplished by the loss off nitro group producing 3-(2-benzylidenehydrazinyl)-2-phenyl-2*H*-azirine ion (m/z 234). Specific fragmentation of the ion at m/z 280 to the ion at m/z 178 was observed for **2-Me**.

The daughter ion, m/z 238 is further fragmented by loosing hydrogen cyanide and protonated HCN to produce base peak at m/z 210 and m/z 196, i.e. 3-*p*-tolyl-4*H*-1,2-selenazet-4-ylum and 2-*p*-tolylselenirene ions, respectively. Fragment at m/z 307 (2-(2-(2-nitrobenzylidene)hydrazinyl)-4-*p*-tolylazete ion) obtained by the loss of hydrogen selenide was only noted for **2-Me**. Further fragmentations of ion at m/z 307 took place by elimination of nitric acid producing 2-(2-benzylidenehydrazinyl)-4-*p*-tolylazete (m/z 260) and loss of 135 Da, producing protonated 2-diazenyl-4-*p*-tolylazete structure (m/z 172). The m/z 151 ion, analog to previous compounds, was obtained by scission of N-N bond and elimination of 4-(4-methyphenyl)-1,3-selenazol-2-amine.

Fragmentations of deprotonated molecular ions, [M-H]⁻, of all compounds are simpler and reflect the most acidic hydrogen removal. Common fragmentation scheme for compound **1**, **1-OMe** and **1-Me** is presented in Figure 4.31. MS² spectrum of ion m/z 326 [M-H]⁻ revealed one fragment ion at m/z 222, deprotonated 4-phenyl-1,3-selenazole-2-amine, obtained by the loss of phenylmethaneimine fragment. The daughter ion m/z 222 was further fragmented and three fragments were obtained. The most abundant fragment, ion at m/z 119, 2*H*-selenete-2-ide, was obtained by the loss of 103 Da. Fragments at m/z 143, 5-phenyl-4*H*-imidazole, and at m/z 196, 3-phenyl-2*H*-1,2-selenazete were obtained by loosing hydrogen selenide and hydrogen cyanide, respectively. In a similar fashion deprotonated molecular ions of **1-OMe** and **1-Me** were fragmented in the first step. Two subsequent steps of fragmentation were found for **1-OMe**: loss of selen from ion m/z 252 produce deprotonated m/z 173 ion, which after expulsion of methyl group gave 4-(4*H*-imidazol-4-ylidene)cyclohexa-2,5-dienone ion

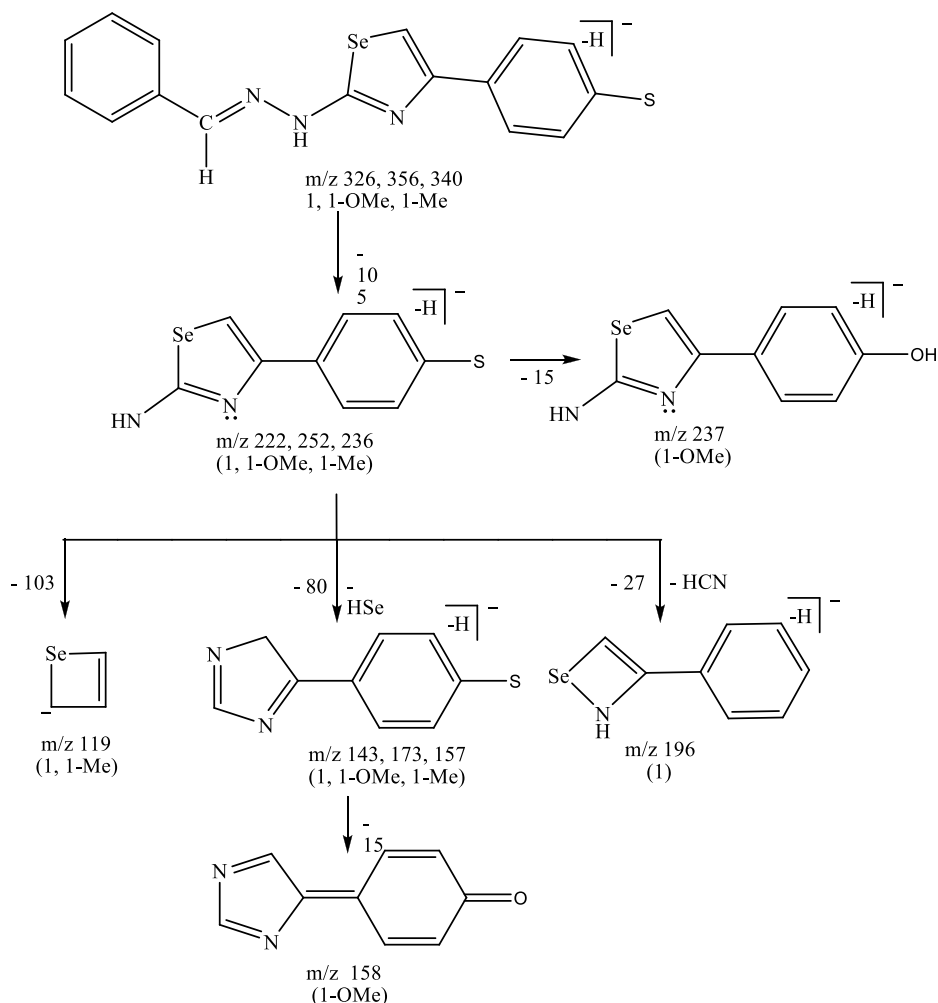


Figure 4.31 Common fragmentation pathway of 1, 1-O-Me and 1-Me.

Fragmentation products of *nitro*-substituted selenazoles **2-4**, in MS² spectrum of [M-H]⁻ ion showed presence of two fragments: deprotonated 4-phenyl-1,3-selenazol-2-amine (m/z 223) common fragment for **2** and **4** and 4-phenyl-1,3-selenazole (m/z 208) fragment obtained for **3**, obtained by the loss of nitro-substituted fragments with molecular weights 148 and 163, respectively (Figure 4.32). Subsequent loss of 104 and 80 Da (hydrogen selenide) from the ion at m/z 223 gave 2*H*-selenete-2-ide (m/z 119) and 4-phenylazete-2-amine (m/z 143), respectively.

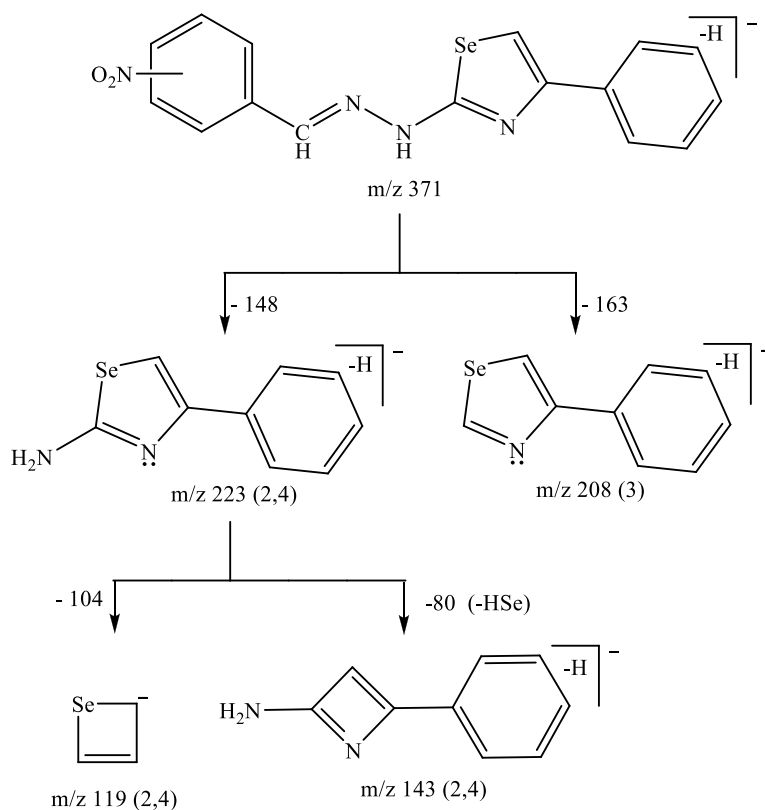


Figure 4.32 Common fragmentation paths of 2, 3 and 4.

Fragmentation of **2-OMe**, **3-OMe** and **4-OMe** took place in a similar manner by losing nitro-substituted phenylmethanimine fragment producing 4-(4-methoxyphenyl)-1,3-selenazol-2-amine ion (m/z 253) for **4-OMe** and **2-OMe**. Ions at m/z 238 and 223 were fragments obtained for **3-OMe** (Figure 4.33). Further fragmentation of ion at m/z 253 is accompanied by elimination methyl group and hydrogen selenide produced 4-(4-methoxyphenyl)-1,3-selenazole (m/z 238) and 4-(4-methoxyphenyl)azet-2-amine (m/z 173), respectively. Third fragment obtained from ion at m/z 253 was obtained by the loss of 133 Da producing an ion at m/z 119. Forthcoming loss of amide fragment from ion at m/z 173 produced 2-(4-methoxyphenyl)azete ion (m/z 158). Common fragmentation pattern of **2-Me**, **3-Me** and **4-Me** is shown in Figure 4.34. Two fragmentation routes were observed in the first fragmentation step of $[M-H]^-$ ion for studied compounds: elimination of 163 and 148 Da fragments produced 4-*p*-tolyl-1,3-selenazole (m/z 222), the only fragment obtained for **3-Me**, and 4-*p*-tolyl-1,3-selenazol-2-amine (m/z 237), the common fragment obtained for **2-Me** and **4-Me**, respectively. Further fragmentation of m/z 237 ion took place by elimination of C_2NHSe and hydrogen selenide to produce 2*H*-selenete-2-ide

(m/z 119) and 4-*p*-tolylazete-2-amine (m/z 157), respectively. Subsequent loss of 41 Da from m/z 157 produce *p*-tolylacetylene ion (m/z 116).

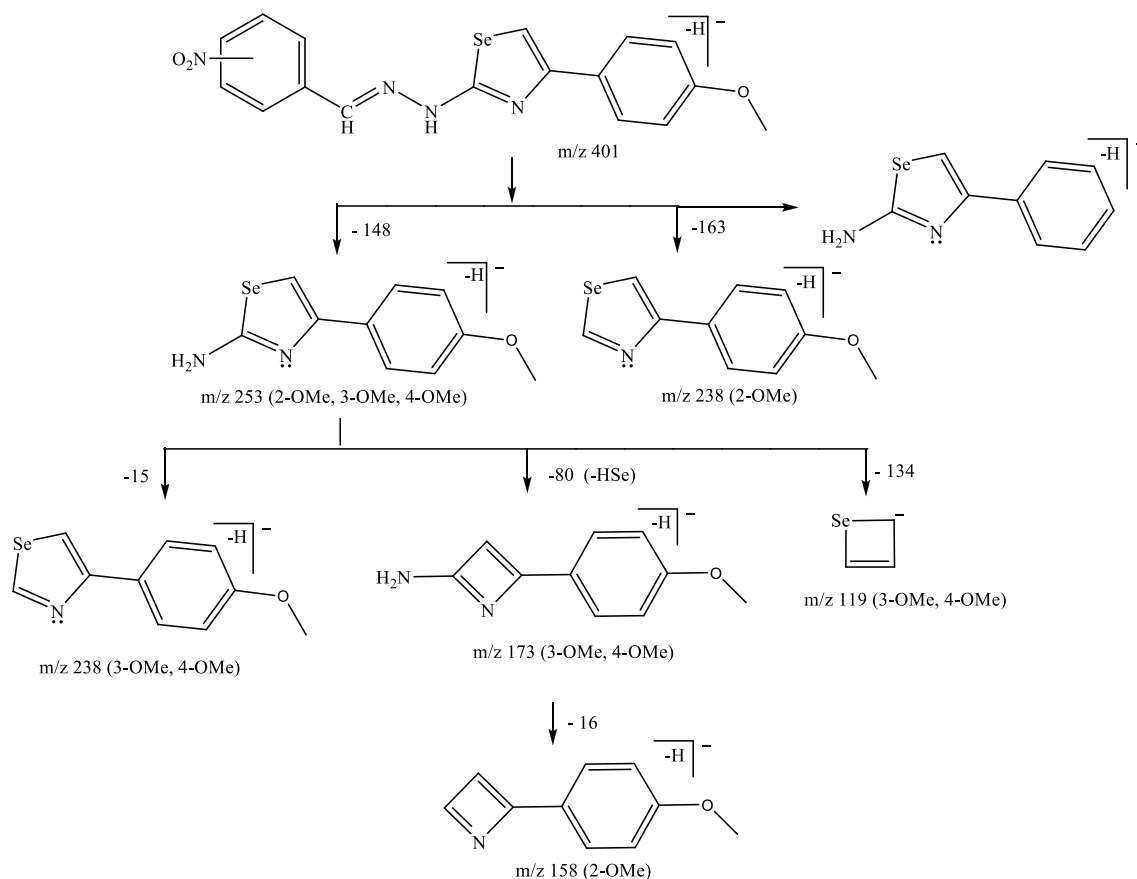


Figure 4.33 Common fragmentation paths of 2-O-Me, 3-O-Me and 4-O-Me.

Similarity of fragmentation pattern allows recognition of four groups of studied selenazoles: first - compounds **1**, **1-O-Me** and **1-Me**, compounds **2**, **3** and **4** (second); compounds **2-Me**, **3-Me** and **4-Me** (third) and compounds **2-O-Me**, **3-O-Me** and **4-O-Me** (fourth group). Fragmentation pathways of studied compounds and MSⁿ spectra obtained reflects influences of both substituents from benzylidene part of molecule, for *ortho*-, *meta*- and *para*-position of nitro group, and substituent on phenyl group present in 4-position of 1,3-selenazole ring.

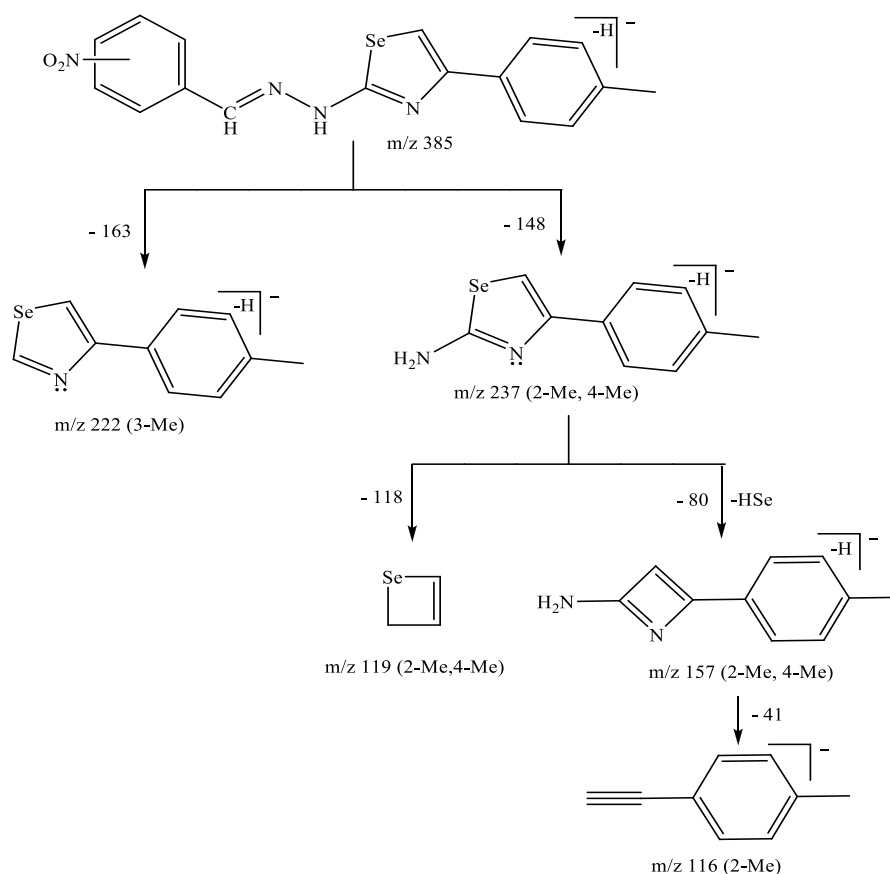


Figure 4.34 Common fragmentation paths of 2-Me, 3-Me and 4-Me.

In the MS spectrum of **1** ($C_{16}H_{13}N_3Se$, exact mass is 327.03) the base signal at $m/z = 328.14$ was assigned to protonated molecular ion, $[M + H]^+$. The signal of sodium adduct, $[M + Na]^+$ appeared at $m/z = 349.98$, and similar sodium adducts of other investigated compounds were found. As a further step in definition of fragmentation mechanism, peak at m/z 328.03 (representing $[M + H]^+$) was selected for collision-induced dissociation (CID) and further mass spectral analysis. Fragments containing selenium were easily recognized by the complex isotope pattern. Common fragmentation scheme of compound **1** is presented on Figure 4.25. For compounds **1**, **1-Me** and **1-OMe** fragmentation behavior was very comparable. In the first fragmentation step two major fragments are obtained for this group of compounds, first ion obtained by the hemolytic cleavage of C=N-N bridging single bond, ion at m/z 106, and second ion obtained by the loss of 105 Da. Further fragmentation of the ion $[M+H-105]^+$ was also common for this group of compounds and three major ions were produced by the loss of 105, 41 and 27 Da. Intensities of obtained ions were the same

for the compounds **1** and **1-Me** while for the compound **1-OMe**, ion at m/z 106 was half the size in comparison to the same ion obtained by fragmentation of the other two compounds.

Fragmentations of other three groups of compounds were very similar in the first fragmentation step (MS^2). From the protonated molecular ion three fragments were produced: the peak obtained by the loss of 4-nitrophenylmethaneimine, protonated nitro substituted phenylmethaneimine ion at m/z 151, fragment obtained by the loss of 149 Da and fragment obtained by the loss of organic fragment containing selenium, 107 Da. Subsequent fragmentations of obtained ions are also very similar but still influenced by the substituent on the phenyl ring B.

The influence of position of nitro group in phenyl ring A on fragmentation mechanism is most dominant for compounds where nitro group is located in the *para* position (**4**, **4-Me**, **4-OMe**). For this group of compounds intensity of molecular ion was the weakest in comparison to the other nitro substituted selenazoles, and also in the first stage of mass fragmentations besides common fragments a one specific fragment was obtained. Ion intensities of obtained common fragments differ from the ion intensities obtained for compounds where nitro group is in the *meta* and *ortho*-position.

In the negative ionization mode common fragmentation for the compounds **1**, **1-Me** and **1-OMe** is the loss of phenylmethaneimine fragment of 104 Da. Further fragmentation product ions depend on the substituent on the phenyl ring B. Fragmentation of selenoazoles with nitro group at *meta* and *ortho* position of the phenyl ring A was characterized by the loss of the 148 Da as the most abundant fragment in the first fragmentation step. Further common fragmentation was the loss of the 80 Da. For compounds with nitro group at *para* position of phenyl ring A the most abundant ion in the first fragmentation step was obtained by the loss of 163 Da.

In general, fragmentation of studied compounds is sensitive to the appropriate proton-donating/proton-accepting capabilities of the particular sites which proved that local electronic density distribution is an important factor determining fragmentation mode of studied compounds.

4.2.5 Solvatochromism

It is well known that spectral behavior of a molecule, *i.e.* position, intensity and shape of absorption bands, depends on the properties of solvent used. It was shown that

the study of the solvent effects on the absorption spectra allows assessment of fundamental molecular properties ²²⁴. In general it was accepted that more planar structure supports higher contribution of extended π -electron delocalization and thus bathochromic shift is a consequence. Solvatochromic behavior of a series of 12 benzylidene-based(1,3-selenazol-2-yl)hydrazones was investigated with presumption that studied π -conjugated systems could show different sensitivities towards solvent and substituent effects.

The absorption spectra of the investigated compounds were recorded in twenty three solvents of different polarity, absorption frequency maxima, ν_{\max} , are given in Table 4.22 and the characteristic spectra in DMSO and ethanol are shown in Figure 4.35. Main absorbance bands appeared in the region 300-500 nm. According to experimental and theoretical results it was postulated that these bands correspond to π - π^* transition. The data from Table 4.22 indicate that ν_{\max} values were largely affected by both substituent and solvent effect, which is clearly observed from wide range of ν_{\max} difference (in the range 20–70 nm).

The absorption maxima of compound **1**, **1-OMe** and **1-Me** appeared at higher ν_{\max} values, while highest bathochromic shift showed compound with electron-acceptor substituents in both *ortho*- and *para*-position, *i.e.* **2**, **2-OMe** and **2-Me** and **4**, **4-OMe** and **4-Me**, respectively, suggesting a more pronounced ICT.

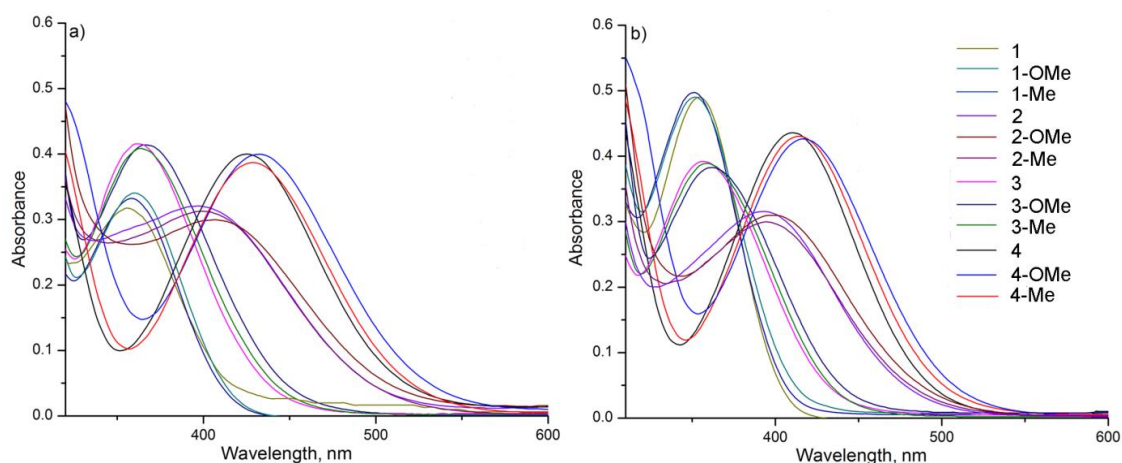


Figure 4.35 Absorption spectra of benzylidene-based (1,3-selenazol-2-yl)hydrazones in (A) DMSO and (B) EtOH.

The absorption maxima is well separated into four groups of compounds where the most influential factor determining shift of UV maxima shift is *nitro* group position. The introduction of the substituent of different electronic properties contributes to the positive solvatochromism, found for **1-OMe** and **1-Me**, and hypsochromic (blue) shift for other compounds. Solvent dependent spectral shifts are influenced by non-specific (dipolarity/polarizability) and specific (HBA/HBD) solvent-solute interactions, and the absorption spectra showed relatively high dependence on both solvent and substituent effects²²⁵. Due to the appropriate conjugation over cross-conjugated imino bridges, the ICT process was observed to be high to moderate in the absorption spectra of these compounds.

4.2.5.1 LSER analysis of UV data

The contribution of specific and nonspecific solvent-solute interactions was quantitatively evaluated by the use of LSER eq. (2.1 and 2.2). The LSER concept, developed by Kamlet and Taft, is very successful methodology used for quantitative treatments of solvation effects. This treatment assumes attractive/repulsive solvent/solute interactions and enables an estimation of the ability of the solvated compounds to interact with solvent. Correlation results obtained by the use Kamlet-Taft model are given in Table 4.23. Presented results indicate that the solvatochromic behaviors are complex due to diversity of contribution of both solvent and substituent effects. From the results given in Table 4.23 it can be noticed that in the most cases specific solvent effect is a factor of the highest contribution to UV-Vis spectral shifts of studied hydrazones. The negative sign of coefficients *s* and *b*, except for **2**, **2-Me**, **3**, **3-Me**, **4** and **4-Me** for coefficient *s*, and **2** and **2-Me** for coefficient *b*, indicates bathochromic (red) shift with increasing solvent dipolarity/polarizability and hydrogen-bond accepting capability. This suggests better stabilization of the electronic ground state relative to excited state with increasing solvent polarity and basicity. Highest (positive) values of coefficients *s* and *b* were noticed for **2** which indicates significance of *ortho*-position of strong electron-accepting nitro group. Positive sign of coefficient *a*, except negative found for **2** and **2-Me**, indicates hypsochromic (blue) shift with increasing solvent hydrogen donating capability.

Table 4.22 Absorption maxima shifts, ν_{\max} (10^{-3} cm^{-1}), of investigated (1,3-selenazol-2-yl)hydrazones in selected solvents

Solvent/Compound	1	1-	1-Me	2	2-OMe	2-Me	3	3-	3-Me	4	4-	4-Me
Methanol (MeOH)	28.82	28.29	28.10	24.45	24.13	24.78	28.29	27.74	28.01	24.66	24.33	24.48
Ethanol (EtOH)	28.01	28.49	28.21	25.48	25.13	25.38	28.09	27.66	27.86	24.39	24.01	24.15
2-Propanol (iPrOH)	28.74	28.17	28.62	25.38	25.06	25.28	28.01	27.51	27.89	24.15	23.95	24.04
1-Butanol	28.65	28.49	28.29	25.32	24.88	25.13	27.86	27.70	27.86	24.21	23.89	24.18
Isobutanol (iBuOH)	28.65	28.41	28.39	25.29	25.32	25.35	27.80	27.61	27.78	24.20	24.05	24.07
3-Methylbutanol (iPeOH)	28.57	28.41	28.41	25.12	25.53	25.16	27.88	27.86	27.85	24.39	24.09	24.34
2-Methoxyethanol (2ME)	28.49	28.71	28.90	25.48	24.97	25.32	28.86	27.66	28.25	24.18	23.78	23.92
2-Chloroethanol (2CE)	29.59	29.50	29.50	28.25	27.78	27.97	29.24	28.78	28.86	27.03	26.60	26.99
Hexane (Hex)	29.41	29.50	29.50	25.41	25.06	25.41	26.77	28.17	27.17	23.92	24.63	23.31
Toluene	28.57	28.93	28.90	25.19	24.78	25.28	28.45	27.74	27.93	24.48	24.01	24.27
Diethylether	28.65	28.57	28.45	25.42	24.47	26.05	27.34	27.69	27.40	23.24	24.00	22.72
1,4-Dioxane (dioxane)	28.57	28.49	28.32	25.99	24.49	26.06	27.76	27.65	27.63	23.97	23.84	23.41
Tetrahydrofuran (THF)	28.99	28.90	27.74	25.00	24.69	24.97	28.01	27.55	27.74	24.07	23.75	23.92
Chloroform (Chl)	28.65	28.62	29.20	25.06	24.66	24.94	28.25	27.47	27.66	24.45	23.89	24.10
Dichloromethane (DCM)	29.07	29.07	28.65	25.45	25.03	25.32	28.69	27.86	28.05	24.69	24.30	24.48
Acetonitrile (AcN)	28.99	28.99	27.78	26.18	25.74	25.97	28.53	28.29	28.33	24.84	24.51	24.69
Ethyl acetate (EtAc)	28.99	28.90	27.90	26.01	24.41	26.16	27.68	27.81	27.57	23.74	23.78	23.22
2-Pyrrolidone (2-Pyr)	28.65	27.78	28.74	25.22	24.72	24.97	27.82	27.51	27.62	23.58	23.28	23.50
1-Methyl-2-pyrrolidone	28.01	27.93	27.78	28.17	22.68	28.09	27.62	27.47	27.47	24.33	24.04	24.33
<i>N,N</i> -Dimethylformamide	28.25	27.17	27.40	25.51	24.69	25.28	27.93	27.55	27.70	24.04	23.56	23.81
Dimethyl sulfoxide (DMSO)	28.01	27.93	27.86	25.25	24.63	25.03	27.66	27.36	27.51	23.56	23.12	23.26
Formamide (F)	28.57	28.49	28.33	25.19	25.19	25.19	28.13	27.74	28.01	23.84	23.67	23.84
<i>N</i> -Methylformamide (NMF)	28.42	28.49	28.41	25.85	25.05	25.72	28.31	27.63	28.01	24.82	23.58	24.68

This suggests better stabilization of the ground state relative to the excited state. Results of correlation obtained according to Kamlet–Taft equation indicate that low sensitivity to solvent effects was noticed for **1**. Low change of coefficients *s* and *a*, related to non-specific and HBD solvent effects, were noticed for **1-OMe** and **1-Me** with respect to **1**.

Table 4.23 Results of LSER correlations for investigated benzylidene-based (1,3-selenazol-2-yl)hydrazones obtained by the use of the Kamlet–Taft eq (3.4)

Comp.	$\nu_0 \times 10^{-3}$ (cm^{-1})	$s \times 10^{-3}$ (cm^{-1})	$b \times 10^{-3}$ (cm^{-1})	$a \times 10^{-3}$ (cm^{-1})	R^a	Sd^b	F^c	Solvent excluded from correlation ^d
1	29.28 ± 0.11	-0.54 ± 0.15	-0.99 ± 0.16	0.66 ± 0.11	0.93	0.17	27.83	EtOH, Chl, THF, EtAc, 2ME, 2-Py
1-OMe	29.37 ± 0.16	-0.86 ± 0.21	-1.27 ± 0.18	0.70 ± 0.11	0.93	0.23	28.31	2-Py, MeOH, AcN, EtAc, THF
1-Me	29.42 ± 0.12	-0.68 ± 0.16	-1.16 ± 0.16	0.62 ± 0.15	0.94	0.17	29.28	Chl, THF, DMF, MeOH, 2CE, AcN
2	23.62 ± 0.29	2.41 ± 0.37	2.86 ± 0.35	-2.46 ± 0.24	0.96	0.25	44.56	2-CE, THF, 2-Pyr, DMSO, Hex, DCM, Chl, NMF, DMF
2-OMe	25.32 ± 0.26	-0.75 ± 0.37	-1.84 ± 0.37	2.52 ± 0.29	0.93	0.39	26.36	MeOH, Chl, DMSO, DMF AcN, THF
2-Me	25.43 ± 0.08	0.52 ± 0.12	1.05 ± 0.12	-1.68 ± 0.11	0.97	0.11	67.16	2CE, DMSO, THF, Toluene, 2-Pyr, NMP, DMF, 2-ME
3	27.86 ± 0.18	1.03 ± 0.22	-1.64 ± 0.17	1.24 ± 0.13	0.96	0.17	42.37	F, THF, Chl, Hex, DMF, MeOH, iPrOH, Toluene
3-OMe	28.04 ± 0.037	-0.41 ± 0.052	-0.43 ± 0.058	0.41 ± 0.05	0.96	0.06	46.54	Chl, AcN, 2-CE, iPrOH, MeOH, DMF, NMP
3-Me	27.75 ± 0.089	0.63 ± 0.12	-1.16 ± 0.11	1.06 ± 0.076	0.97	0.092	69.32	Chl, F, AcN, THF DCM, Hex, MeOH, EtOH
4	24.16 ± 0.23	1.60 ± 0.39	-2.88 ± 0.45	2.47 ± 0.27	0.93	0.33	28.4	F, Chl, Hexane, NMP, DCM,
4-OMe	24.59 ± 0.09	-0.85 ± 0.12	-0.76 ± 0.13	0.59 ± 0.10	0.94	0.13	36.99	NMP, Chl, 2CE, AcN
4-Me	23.52 ± 0.23	0.81 ± 0.34	-1.84 ± 0.33	2.75 ± 0.26	0.95	0.34	34.44	NMP, F, DMF, Chl, MeOH, EtOH, AcN

^a Correlation coefficient; ^b Standard deviation; ^c Fisher test of significance; ^d abbreviation for the solvents are given in Table 7.1.

Small increase of coefficient *b* were obtained with introduction of moderately/weak electron-donating methoxy and methyl group. Other hydrazones with nitro group, irrespectively to position of this group, showed higher sensitivity for compounds with X = 2, 3- and 4-NO₂ and Y = H (Scheme 3.3), while for Y =

OCH₃ electron-donating capability compensate electron-density depletion caused by nitro group. Differences in the sign and the values of solvatochromic coefficients, found for **2**, **2-OMe** and **2-Me**, are the results of balanced interplay of primary *ortho*-substituent effects and the molecular geometry. *ortho*-Nitro substituent exerts larger influences on ν_{\max} shifts due to contribution of polar effects (inductive/field), resonance and steric effects. Similarity of polar and resonance could be expected for *ortho*- and *para*-nitro substituted compounds. Steric effect includes all those phenomena, which result in structural changes at measured sites, such as bond lengths and angles, and due to size of the *ortho*-substituent. *ortho*-Nitro substituent could, by adjustment of the orientation of its dipole, through the space electrostatically and by hydrogen bonding effect to stabilize surrounding positive charges without direct interaction (through the space induced π -polarization).

Appropriate regularity of the sign of solvatochromic coefficients change could be observed for compounds with *meta*- and *para*-nitro group, while large differences were noticed with respect to *ortho*-substituted compounds. Higher sensitivity of ν_{\max} shift in *para*-nitro substituted compounds is the result of directional transmission of substituent effect which contributes to more effective charge separation. The sensitive balance of both electronic substituent effect of *para*-nitro substituent and π -electronic interaction in methyl and methoxy substituted moieties contributes to decrease of non-specific and HBD solvent/solute interactions found for **4-OMe** and **4-Me**. The only exception is **4-Me** with higher contribution of HBD effect.

Results of the quantitative separation of the non-specific solvent effect into polarizability and dipolarity term (coefficients *c* and *d*, respectively), performed by using Catalán equation, are given in Table 4.3.

The results obtained by the use of Catalán equation provide better understanding of attractive/repulsive solvent/solute interactions, and enables an estimation of their appropriate contribution to ν_{\max} shift. The correlation results, given in Table 4.24, confirmed conclusions obtained according to the results from Kamlet-Taft equation (Table 4.23). Specific solvent interactions are the principal factors influencing the shift of ν_{\max} , whereas solvent dipolarity and polarizability have moderate to low contribution, except in the case of **1** and **2**. Specific solvent-solute interactions realized through hydrogen bonding, *i.e.* HBD effect can be attributed mainly to the non-bonded nitrogen

electrons, while solvent basicity (HBA) could be established with generated positive charge at molecular structure. Negative values of the coefficient *b*, except for **2** and **2-Me**, indicate moderate to high contribution of the solvent acidity to the stabilization of the excited state. Long-range transmission of substituent effects, which supports the larger polarization, enhances hydrogen bonding capabilities of carbonyl oxygen atoms.

Table 4.24 Correlation results of investigated benzylidene-based (1,3-selenazol-2-yl)hydrazones according to Catalán eq. (3.5)

Comp.	$\nu_0 \times 10^{-3}$ (cm^{-1})	$c \times 10^{-3}$ (cm^{-1})	$d \times 10^{-3}$ (cm^{-1})	$b \times 10^{-3}$ (cm^{-1})	$a \times 10^{-3}$ (cm^{-1})	R^a	Sd^b	F^c	Solvent excluded from correlation ^d
1	31.65 ± 0.38	-3.68 ± 0.55	-0.13 ± 0.16	-0.79 ± 0.15	0.64 ± 0.20	0.94	0.13	21.65	EtOH, 2CE, THF, DCM, MEOH
1-OMe	30.15 ± 0.61	-0.26 ± 0.13	-1.79 ± 0.18	-1.23 ± 0.36	1.98 ± 0.29	0.95	0.23	26.30	1-BuOH, EtOH, F
1-Me	29.14 ± 0.70	-0.55 ± 0.22	-1.40 ± 0.16	-1.11 ± 0.4	1.47 ± 0.38	0.95	0.24	25.80	MeOH, F, EtOH, 1-BuOH
2	20.77 ± 1.18	3.75 ± 1.52	2.85 ± 0.59	1.83 ± 0.48	-4.02 ± 0.57	0.93	0.37	14.72	2-CE, Hex, THF, DMF DMSO, DCM, Toluene
2-OMe	25.90 ± 1.13	-1.71 ± 1.61	1.28 ± 0.44	-2.47 ± 0.42	4.05 ± 0.57	0.94	0.38	24.92	MeOH, F, NMP, THF, 2-ME
2-Me	23.45 ± 0.53	0.81 ± 0.62	1.81 ± 0.24	0.71 ± 0.18	-1.95 ± 0.26	0.94	0.12	16.51	2-CE, Hex, THF, DMF, EtOH, DMSO, DCM, THF, Toluene, NMP
3	28.12 ± 0.62	-1.65 ± 0.94	2.12 ± 0.27	-1.74 ± 0.23	1.88 ± 0.31	0.97	0.22	47.58	F, Toluene, THF, MeOH
3-OMe	28.12 ± 0.27	0.11 ± 0.44	-0.34 ± 0.15	-0.71 ± 0.10	0.49 ± 0.11	0.95	0.08	27.00	2-CE, Chl, AcN, Dioxane, Toluene
3-Me	27.65 ± 0.61	-0.47 ± 0.91	1.11 ± 0.21	-0.76 ± 0.20	0.88 ± 0.26	0.94	0.17	20.99	Toluene, F, MeOH, DMSO, Chl, NMP
4	23.21 ± 1.12	1.75 ± 1.63	0.91 ± 0.46	-2.44 ± 0.31	4.39 ± 0.82	0.93	0.38	14.85	F, MeOH, EtOH, 2-ME, THF
4-OMe	25.47 ± 1.06	-0.97 ± 1.63	0.09 ± 0.44	-1.92 ± 0.40	4.37 ± 0.64	0.93	0.39	11.57	Toluene, F, MeOH, 2ME, EtOH, Chl, nBuOH
4-Me	22.58 ± 1.42	1.70 ± 2.07	1.19 ± 0.57	-2.28 ± 0.64	3.69 ± 0.46	0.92	0.48	11.64	F, MeOH, 2ME, 3-MeBu, THF, iPrOH, iBuOH

^a Correlation coefficient; ^b Standard deviation; ^c Fisher test of significance; ^d abbreviation for the solvents are given in Table 7.2.

Negative values of the coefficient c , obtained for **1**, **1-OMe**, **1-Me**, **4-OMe**, **3**, **3-Me** and **2-OMe**, and coefficient d , for **1**, **1-OMe**, **1-Me** and **3-OMe**, indicate higher contribution of the dipolarity/polarizability effects to the stabilization of the excited state. The noticeable contribution of solvent polarizability indicates that the overall π -electronic density shifts take place by two cooperative mechanisms: overall π -network and polarization of localized π -unit. Interaction of selenazole ring, which acts as an electron-acceptor, with the substituents of different electronic properties causes variation in the mobility of the π -electrons, and thus, wide range of coefficients c and d values were found. The sensitive balance of both electronic substituent effect and π -electronic interaction in defined π -unit contributes to highest extent of polarizability in the case of **1** and **2**.

A greater extent of resonance interaction could be operative in two distinct π -resonance units: substituted benzylideneamino and 4-arylidene-1,3-selenazole moieties. In that context, methoxy substituent exerts larger π -electron delocalization supported by electron-accepting selenazole ring. The electron donating substituent, present in selenazole moiety, participates in electron delocalization over causing electron-density shift to nitro substituted benzylideneamino structure contributing to lower polarizability, *i.e.* coefficient c of -0.55 (**1-Me**), -0.97 (**4-OMe**) and 0.11 (**3-OMe**) (Table 4.3).

Effect of solvent dipolarity, assigned with d term, showed complex behavior, with the highest value found for compound **2**. Dipolar solvent–solute interactions lead to blue shift, except for **1**, **1-OMe**, **1-Me** and **3-OMe**, when a moderate and strong electron-acceptor are present at both side of investigated compounds. Higher contribution of the solvent dipolar effect, in compounds with substituent displaying high electron-accepting character could be due to balanced contribution of two similarly oriented effects: electronic substituent effect and presence of nitro substituent on the phenyl ring A. Synergism of these effects cause charge separation and creation of differently oriented local/overall dipolar structure. The better stabilization of the excited state was found mostly for compounds **1**, **1-OMe**, **1-Me** and **3-OMe**, which indicates that directional shift of substituent causes more effective charge separation.

4.2.6 DFT and TD-DFT calculations

4.2.6.1 Evaluation of electronic transitions and ICT

Electronic properties of investigated molecules were studied by calculation of absorption spectra, the HOMO and LUMO energy levels and energy of HOMO - LUMO transitions (E_{gap}). All vertical excitation energies were computed at the PCM/TD-DFT/B3LYP/6-31G(d,p) optimized ground-state geometries, in DMSO, EtOH and THF solvents.

Table 4.25 The experimental (λ_{abs}) and calculated absorption maxima (λ^*), obtained by the use of TD/DFT method, of (1,3-selenazol-2-yl)hydrazones in DMSO, EtOH and THF.

	DMSO		EtOH		THF	
	λ_{abs} (nm)	λ^* (nm)	λ_{abs} (nm)	λ^* (nm)	λ_{abs} (nm)	λ^* (nm)
1	357	368	357	365	345	369
	270	287	272	286	272	287
	263	246	264	246	232	246
1-OMe	359	382	355	381	348	390
	282	309, 299	276	308, 298	279	313, 304
	244	250		250	212	250
1-Me	358	371	351	372	346	373
	276	291	271	292	273	292
	223	248	203	248	214	248
2	396	520	392	519	400	519
	568	364	280	364	286	365
		284	252	284	258	287
2-OMe	406	553	398	553	405	554
	364	382	282	382	290	385
	282	296	263	295	263	295
2-Me	400	530	394	529	400	530
	286	370	282	370	285	372
	-	290	256	290	258	291
3	475	513	356	511	357	509
	362	366	268	365	277	364
	273	267		266	266	275
3-OMe						266
	366	552	362	550	360	549
	283	401	278	400	286	398
3-Me		292		292	271	286
	364	525	359	523	360	521
	276	377	270	376	277	375
4		271		271		280
						271
	424	/ 514	410	/ 513	416	/ 509
4-OMe	290	378	283	378	286	380
		285	245	290	247	290
				285		
4-Me	432	/ 544	416	/ 543	421	/ 541
	286	394	283	394	284	396
		313	257	312	276	314
4-OMe				295		295
	430	/ 523	414	/ 523	418	/ 520
	291	384	286	384	284	386
4-Me		294	249	293	251	293

The calculated absorption maxima of *E*-benzylidene-based (1,3-selenazol-2-yl)hydrazones are compared with the experimental values (Table 4.25), while oscillator strengths (*f*) and composition of calculated bands are listed in Table 7.12.

Influence of substituents and solvents are estimated by comparing the calculated values of absorption maxima, frontier molecular orbital energies (E_{LUMO} , E_{HOMO}) and E_{gap} (Table 4.26). Molecular orbital plots and energy levels of the HOMO, the LUMO and HOMO-LUMO transitions of investigated compounds in DMSO are depicted in Figure 4.36, while analog plots for all compounds in EtOH and THF are given in Figure 7.79 and Figure 7.80, respectively.

Table 4.26 Calculated energies of the HOMO and LUMO orbitals and energy gap (in eV) for *E*-(1,3-selenazol-2-yl)hydrazones in DMSO, EtOH and THF, obtained by TD/DFT.

	1	1-Me	1-OMe	2	2-Me	2-OMe
DMSO						
E_{LUMO}	-1.55	-1.54	-1.53	-2.71	-2.71	-2.70
E_{HOMO}	-5.34	-5.30	-5.20	-5.49	-5.43	-5.31
E_{gap}	3.79	3.76	3.66	2.78	2.72	2.61
EtOH						
E_{LUMO}	-1.53	-1.54	-1.53	-2.71	-2.71	-2.70
E_{HOMO}	-5.34	-5.29	-5.19	-5.49	-5.43	-5.30
E_{gap}	3.80	3.75	3.66	2.78	2.72	2.60
THF						
E_{LUMO}	-1.53	-1.52	-1.51	-2.70	-2.69	-2.69
E_{HOMO}	-5.31	-5.26	-5.16	-5.48	-5.41	-5.28
E_{gap}	3.78	3.74	3.65	2.78	2.72	2.59
	3	3-Me	3-OMe	4	4-Me	4-OMe
DMSO						
E_{LUMO}	-2.79	-2.79	-2.79	-2.67	-2.67	-2.67
E_{HOMO}	-5.51	-5.45	-5.32	-5.46	-5.40	-5.28
E_{gap}	2.72	2.66	2.54	2.79	2.73	2.62
EtOH						
E_{LUMO}	-2.79	-2.79	-2.78	-2.67	-2.67	-2.66
E_{HOMO}	-5.51	-5.45	-5.32	-5.46	-5.40	-5.28
E_{gap}	2.72	2.66	2.54	2.79	2.73	2.62
THF						
E_{LUMO}	-2.77	-2.77	-2.76	-2.65	-2.65	-2.65
E_{HOMO}	-5.51	-5.45	-5.31	-5.46	-5.39	-5.27
E_{gap}	2.74	2.68	2.55	2.80	2.74	2.62

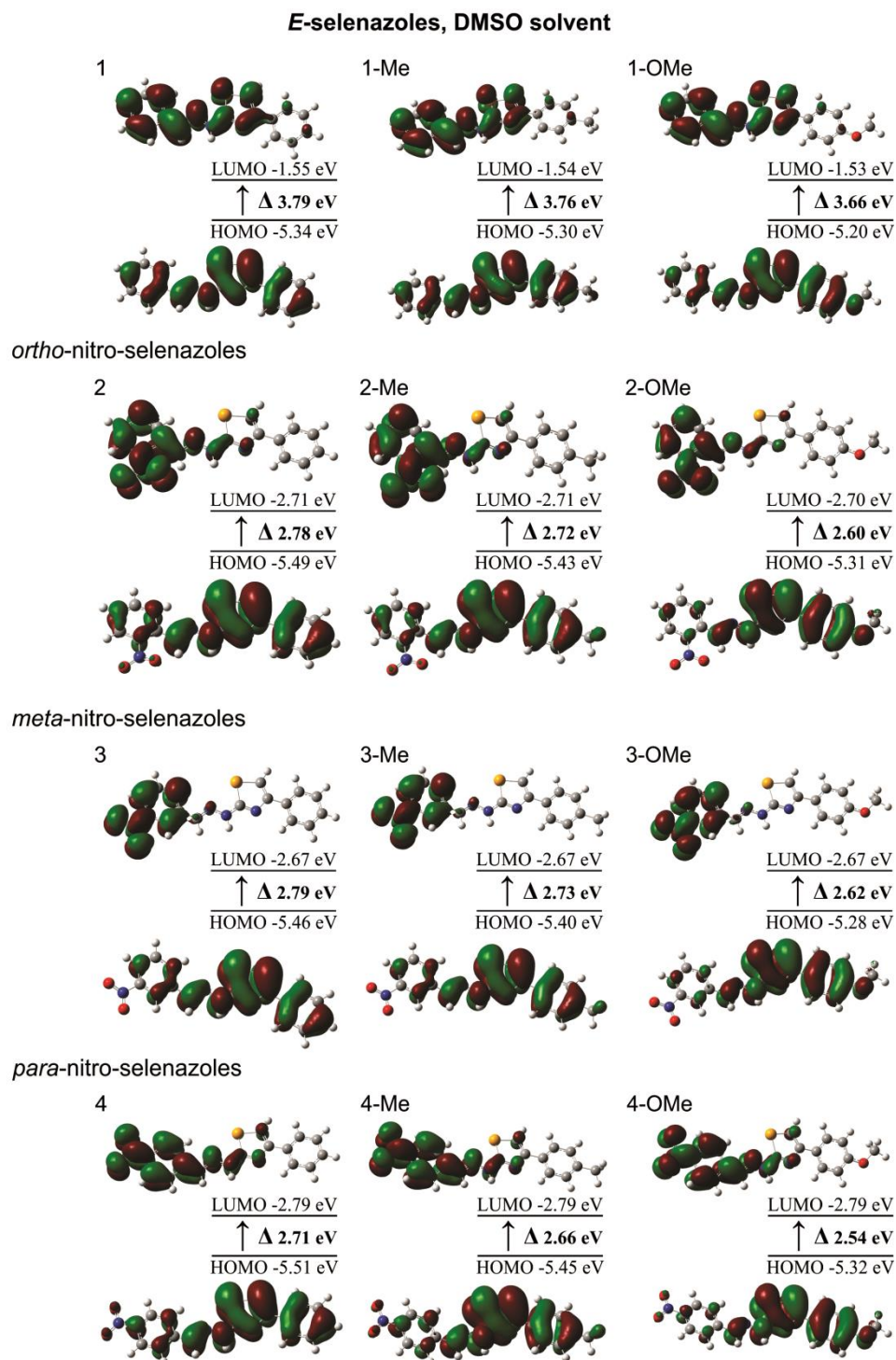


Figure 4.36 Molecular orbital plots and energy levels of the HOMO, the LUMO and HOMO-LUMO transitions of the benzylidene-based (1,3-selenazol-2-yl)hydrazones in DMSO.

The main difference between compounds **1**, **1-OMe** and **1-Me** and nitro-substituted (1,3-selenazol-2-yl)hydrazones derives from stabilization of LUMO orbital in the

presence of nitro group. Influence of nitro group is clearly reflected in red shifted HOMO-LUMO transitions of all nitro-substituted (1,3-selenazol-2-yl)hydrazones in comparison to compounds **1**, **1-OMe** and **1-Me**. The different position of nitro group on the phenyl ring A causes the certain changes in frontier molecular orbital energies. As it is well known, electron acceptor group, such as nitro-group, adjacent to the aromatic ring, decreases the electron density on the ring through a resonance withdrawing effect. If an acceptor is in a *para* or *ortho* position, the certain stabilization is expected through the corresponding resonance structures. The change of the position of the nitro-group from *para* to *ortho* and *meta* destabilizes both HOMO and LUMO orbitals. A relatively small increase in HOMO orbital energies can be negligible. Destabilization of the LUMO orbitals by 0.1 eV when nitro substituent changes position from *para* to *ortho* or *meta* position, induces an increase of the energy gap. In all molecules with *para* and *ortho*-nitro substituents, the LUMO orbitals are mainly located on the aromatic rings A and hydrazone bridges. In the case of molecules containing the nitro group in *meta*-position, the LUMO orbitals are mainly located on the aromatic rings A with smaller participation of the hydrazone bridges. The HOMO orbitals are located on selenazole rings, phenyl rings B and hydrazone bridges (Figure 4.36, Figure 7.79 and Figure 7.80).

The presence of electron donating substituents (-Me and -OMe) on the phenyl rings B, destabilize HOMO orbitals and decrease the energy gap. Since -OMe group is stronger electron donating group in comparison to -Me group, the selenazole analogs with OMe substituted phenyl rings B have the smallest energy gap. In a series of -H, -Me and -OMe substituents, the calculated values of the absorption maxima show increasing (red shifted) trend.

For investigated nitro-substituted (1,3-selenazol-2-yl)hydrazones calculated absorption spectra are very similar for DMSO and EtOH, but slightly different for THF. Calculated energy values indicate that THF destabilized the LUMO energy level, which resulted in higher values of energy gap and blue-shifted absorption maxima.

Fukui functions

For the investigation of molecular reactivity Fukui function was applied. This model relies on Parr and Yang^{226,227} theory that sites in chemical species with the largest values of Fukui Function $f(r)$ are those with higher reactivity. The Fukui

$f(r)$ function can be defined as the change in electron density upon a change in the number of electrons (eq. 3.1), where $\rho(r)$ is the total electron density of the molecule, N is the number of electrons and $v(r)$ is the external potential exerted by the nucleus. The condensed Fukui function evaluated reactivity of compounds towards nucleophilic and electrophilic (eqs. 3.2 and 3.3, respectively).

The partial atomic charges for investigated compounds were calculated using the natural bond orbital analysis (NBO) at the ground state geometry in DMSO solvent. Calculated values of Fukui functions are listed in Table 4.27 and Table 4.28.

According to the values of f^+ for **1**, **1-OMe** and **1-Me** (Table 4.27), the most reactive sites upon nucleophilic attack are C7 and N1 atoms which are directly bonded atoms to form imino group. On the other hand, N6 atom, as well as Se1 and C9 atoms which are directly bonded atoms within 1,3-selenazole ring are the most favorable for electrophilic attack. The same influence of substituents at phenyl ring was observed in the case of pyridine-based analogues¹⁹. In a series of -H, -CH₃ and -OCH₃ substituents of phenyl ring, reactivity of C7 and N1 sites upon nucleophilic attack show increasing trend. In the same series, values of f^- decrease for Se1 and N6 sites, but increase for C9 atom.

Table 4.27 Selected highest values of the condensed Fukui functions (f^+ and f^-) for unsubstituted (1,3-selenazol-2-yl)hydrazones, considering DFT/DMSO/NBO charges according to eqs. (3.2) and (3.3).

Comp.		N1	N2	C1	C7	C9	Se1	C6
1	f^+	0.119	-0.001	0.024	0.133	0.060	0.091	0.073
	f^-	0.001	0.111	-0.007	0.077	0.119	0.169	0.028
1-Me	f^+	0.122	0.000	0.025	0.134	0.057	0.089	0.074
	f^-	-0.001	0.101	-0.008	0.072	0.122	0.168	0.026
1-OMe	f^+	0.124	0.000	0.026	0.135	0.055	0.086	0.075
	f^-	-0.004	0.081	-0.008	0.062	0.126	0.161	0.021

The nucleophilic reactivity site order of *ortho*-nitro substituted (1,3-selenazol-2-yl)hydrazones (Table 4.28) is O(NO₂) > N4 > C5 > N1, without any influence of Y substituents, while electrophilic attack is favorable for Se1, C9, N2 and C7 sites.

Table 4.28 Selected highest values of the condensed Fukui functions (f^+ and f^-) for the nitro substituted (1,3-selenazol-2-yl)hydrazones, considering DFT/DMSO/NBO charges according to eqs. (3.2) and (3.3).

Compound		N1	N2	C5	C7	C9	Se1	N4	O(NO ₂)
2	f^+	0.075	0.015	0.081	0.010	0.019	0.034	0.093	0.168
	f^-	-0.009	0.092	0.001	0.083	0.123	0.172	0.000	0.012
2-Me	f^+	0.075	0.015	0.081	0.010	0.019	0.034	0.093	0.168
	f^-	-0.010	0.081	0.002	0.076	0.125	0.169	0.000	0.011
2-OMe	f^+	0.075	0.015	0.082	0.009	0.019	0.034	0.094	0.169
	f^-	-0.010	0.060	0.002	0.062	0.125	0.157	0.000	0.009
		N1	N2	C1	C7	C9	Se1	N4	O(NO ₂)
4	f^+	0.081	0.017	0.085	0.017	0.020	0.036	0.080	0.153
	f^-	-0.010	0.089	-0.017	0.082	0.122	0.171	0.000	0.016
4-Me	f^+	0.080	0.017	0.085	0.016	0.020	0.035	0.080	0.154
	f^-	-0.010	0.078	-0.016	0.075	0.125	0.168	0.000	0.015
4-OMe	f^+	0.080	0.017	0.085	0.016	0.020	0.035	0.080	0.154
	f^-	-0.011	0.058	-0.013	0.061	0.124	0.156	0.000	0.012
		N1	N2	C6	C7	C9	Se1	N4	O(NO ₂)
3	f^+	0.042	0.009	0.123	-0.001	0.010	0.017	0.100	0.183
	f^-	-0.007	0.098	0.022	0.081	0.124	0.175	0.000	0.008
3-Me	f^+	0.042	0.009	0.123	-0.001	0.010	0.017	0.101	0.182
	f^-	-0.008	0.087	0.020	0.075	0.127	0.172	0.000	0.007
3-OMe	f^+	0.042	0.009	0.123	-0.001	0.010	0.017	0.101	0.183
	f^-	-0.009	0.066	0.016	0.062	0.127	0.160	0.000	0.006

Substitution of hydrogen atom by Me and OMe group leads to increasing reactivity only for C9 atom. From the values of *para*-nitro substituted (1,3-selenazol-2-yl)hydrazones reported in Table 4.28, the reactivity site order for the nucleophilic attack is O(NO₂) > C1 > N1, while N4 and changes in Y substituent do not have influence on reactivity of these centers. The order of reactive electrophilic sites is Se1 > C9 > N2. Reactivity of C7 and C9 sites increases due to substitution of Y = H with Y = Me, OMe. The results for *meta*-nitro substituted (1,3-selenazol-2-yl)hydrazones (Table 4.28) show similar trend as

for *para*-nitro substituted (1,3-selenazol-2-yl)hydrazones. The most reactive sites upon nucleophilic attack are oxygen atoms and carbon atom in opposite position of nitro group. Electrophilic sites and influence of Y substituents on their reactivity are the same as in the case of *para*-nitro substituted (1,3-selenazol-2-yl)hydrazones.

4.2.7 Biological activity

4.2.7.1 Antimicrobial activity

The antimicrobial activity of investigated compounds was examined against four Gram-negative, four Gram-positive bacteria and three fungi strains. In respect of antibacterial activity, the most potent were compounds from the set 1 (Table 4.29).

Table 4.29 Antibacterial activity of investigated benzylidene-based (1,3-selenazol-2-yl)hydrazones tested by the disc-diffusion method.

Comp.	Inhibition zone diameter (mm) ^a							
	<i>P.</i> <i>hauseri</i>	<i>P.</i> <i>aeruginosa</i>	<i>E.</i> <i>coli</i>	<i>S.</i> <i>enterica</i>	<i>S.</i> <i>aureus</i>	<i>C.</i> <i>sporogenes</i>	<i>B.</i> <i>subtilis</i>	<i>K.</i> <i>rhizophila</i>
1	12	12	10	10	12	12	10	10
1-Me	12	10	10	10	10	12	10	10
1-OMe	14	12	10	10	10	12	10	10
2	n.a. ^b	n.a.	n.a.	n.a.	n.a.	n.a.	n.a.	n.a.
2-Me	n.a.	n.a.	n.a.	n.a.	n.a.	n.a.	n.a.	n.a.
2-OMe	n.a.	n.a.	n.a.	n.a.	n.a.	n.a.	n.a.	n.a.
3	10	10	9	9	10	10	9	9
3-Me	10	10	9	9	10	10	9	9
3-OMe	10	10	9	9	10	10	10	9
4	9	10	9	9	10	10	9	9
4-Me	9	9	9	9	10	9	9	9
4-OMe	n.a.	n.a.	n.a.	n.a.	n.a.	n.a.	n.a.	n.a.
Amikacin	22	20	38	22	28	20	20	22

^a Including diameter of disc (8 mm); ^b n.a. – not active.

Ortho substitution of benzene ring (set 2) resulted in inactive compounds. In the case of *metasubstitution*, almost equal antibacterial activity of all three derivatives from set 3 was observed. Similar level of activity was noticed for **4** and **4-Me**, while **4-OMe** was inactive against all bacterial strains investigated. In the case of antifungal activity, **1** was

the most active compound against *A. niger*, **3-OMe** and **4** were the most active against *C. albicans*, while **2** and **2-Me** showed selectivity to *C. albicans* (Table 4.30).

Table 4.30 Antifungal activities of benzyldene-based (1,3-selenazol-2-yl)hydrazones

Compound	Inhibition zone diameter (mm) ^a		
	<i>A. niger</i>	<i>C. albicans</i>	<i>S. cerevisiae</i>
1	16	12	10
1-OMe	12	10	10
1-Me	10	12	10
2	n.a. ^b	14	n.a.
2-OMe	9	12	12
2-Me	n.a.	12	n.a.
3	9	12	9
3-OMe	10	16	10
3-Me	9	14	9
4	10	16	9
4-OMe	10	12	9
4-Me	10	14	9
Nystatin	30	32	52

^a Including diameter of disc (8 mm); ^b n.a. – not active

4.2.7.2 In vitro antioxidant capacity (AOC)

To study the possible AOC of investigated compounds their radical scavenging activity, the oxygen radical absorption capacity and reduction ability was done in series of four *in vitro* tests. The DPPH[•] assay has been widely used in assessment of the free radical-scavenging activity of various synthetic compounds, because of its ease and convenience. When an antioxidant scavenges these stable free radical by hydrogen radical or electron donation the purple DPPH assay solutions decolorized. ORAC test assay measures the loss of fluorescein fluorescence due to its oxidation by a radical formed by the breakdown of AAPH over time¹⁷⁸. Antioxidant suppresses this reaction by hydrogen atom transfer. Trolox, a water soluble vitamin E analog, serves as a positive control for quantification of antioxidant activity present by its normalization to equivalent Trolox units. The reducing power of a substance may serve as a significant indicator of its potential antioxidant activity. For measurement of the reductive ability, the Fe(III)→Fe(II) transformation with the formation of Perl's Prussian blue color complex¹⁷⁶, as well as the Mo(VI)→Mo(V) transformation with the formation of a green phosphate/Mo(V) complex¹⁷⁷, in the presence of examined compounds was

investigated. Consequently, increase in absorbance of the reaction mixture indicated the reducing power of the tested compounds.

In our previous study pyridine-based analogues (HLSe¹, HLSe² and HLSe³) of compounds from set 1 were tested in DPPH test and the activities were compared with vitamin C ¹⁹. Unsubstituted derivative, HLSe¹ appeared to be the most active, while addition of –OMe and –Me substituents resulted in less active species. The same trend was observed in the case of their benzylidene-based analogues from set 1 (Table 4.31), but with significant difference in terms of activity. Namely, all three derivatives showed significantly stronger free-radical scavenging activity than vitamin C, especially **1**, which was one order of magnitude more active than the standard.

Table 4.31 Antioxidant capacity of investigated benzylidene-based (1,3-selenazol-2-yl)hydrazones and the standard.

Compound	IC ₅₀ (μM) ^a	EC ₅₀ (μM) ^b		TE
	DPPH*	TAOC	TRP	ORAC
1	8.63 ± 1.66	648 ± 55	990 ± 92	0.752 ± 0.05
1-OMe	54.26 ± 4.54	548 ± 53	806 ± 85	0.736 ± 0.06
1-Me	45.06 ± 6.53	603 ± 61	966 ± 88	0.650 ± 0.07
2	21.9 ± 5.6	357 ± 41	390 ± 48	0.824 ± 0.07
2-OMe	40.5 ± 3.8	433 ± 39	560 ± 53	0.816 ± 0.07
2-Me	20.2 ± 4.3	416 ± 45	470 ± 41	0.768 ± 0.05
3	173.5 ± 11.6	325 ± 38	420 ± 45	0.896 ± 0.06
3-OMe	298.1 ± 14.8	632 ± 50	488 ± 46	0.864 ± 0.07
3-Me	151.6 ± 10.1	571 ± 45	480 ± 50	0.826 ± 0.05
4	44.8 ± 2.3	433 ± 43	376 ± 51	0.925 ± 0.08
4-OMe	79.2 ± 3.9	645 ± 53	398 ± 44	0.920 ± 0.07
4-Me	40.1 ± 4.7	579 ± 51	495 ± 48	0.916 ± 0.07
vitamin C	79.1 ± 1.8	140 ± 10	155 ± 39	0.966 ± 0.07

^a IC₅₀ - concentration providing 50% of radicals scavenging activity; ^bEC₅₀ - Concentration providing 0.500 of absorbance; The lower IC₅₀ or EC₅₀ value the higher the antioxidant capacity; Values are given as means ± standard deviations (n = 3).

Addition of nitro group on the phenyl ring A reduced the activity of **2**, **4** and **4-OMe** to some extent, while this effect was the strongest for set 3 which is the only series of compounds with lower activity than vitamin C. In all three sets of compounds containing nitro group, the order of activities changed from H > Me > OMe (set 1) to Me > H > OMe (sets 2-4), but activity of non-substituted and Me-derivatives was almost the same in the case of *ortho* and *para* substitution. Compounds **2-OMe**, **2-Me** and **4-Me** are the only nitro-containing compounds which showed better activity than their non-substituted analogues.

To the best of our knowledge ORAC, TAOC, and TRP tests have been performed for the first time for evaluation of AOC of some 1,3-selenazole based compounds. While activities in both tests, evaluating reduction ability, were negligible (Table 4.31), activities of all investigated compounds were greater than vitamin C in ORAC test. Again, the series without nitro substituent showed the best activity, but **1-Me** appeared to be the most active compound. Methyl derivatives showed the best activities in all three series. In contrast to DPPH test, compounds having nitro group in *ortho* position showed the weakest activities. Based on results presented in Table 4.31 it was possible to establish simple structure-activity relationship. The order of activities of compounds from the sets is: set 1 > set 2 > set 3 > set 4, while in each set the order of activity is Me > OMe > H.

4.2.7.3 Antiproliferative effects

While 1,3-thiazoles are well known by their anticancer activity⁹, their selenium analogues have been studied in much less extent. To the best of our knowledge, there are only two systematic anticancer activity studies of 1,3-selenazoles^{14,63}. Herein we performed the *in vitro* antiproliferative activity of the benzylidene based 1,3-selenazoles on a panel of six human solid tumor cell lines: A549, HBL-100, HeLa, SW1573, T-47D and WiDr (Table 4.32).

In our study, **1** showed moderate activity ($GI_{50} = 10-100\mu\text{M}$) when tested against A549, HBL-100, HeLa and SW1573 cell lines, and good activity ($GI_{50} = 1-10\mu\text{M}$) against T-47D and WiDr cell lines. Substitution on B phenyl ring reduced activity in set **1** since **1-Me** and **1-OMe** were inactive ($GI_{50} > 100\mu\text{M}$) against five cell lines. In contrast, the introduction of a nitro group in the phenyl ring A significantly influenced

the antiproliferative activity of analogs **2-4** against A549, HBL-100, HeLa and SW1573 cells. The same trend was observed for nitro analogues of **1-Me** and **1-OMe** on all six cell lines with one exception. Namely, **4-Me** remained inactive against all six cell lines similarly to **1-Me**. The most potent compounds were **2** and **2-Me**, which showed good activity against A549, HeLa, SW1573 and WiDr cells. However, GI₅₀ values obtained on T-47D cell line were very close to 10 μM. Also, a good activity was noticed for **3** on A549 cells, **3-OMe** on SW1573 cells and **4** against T-47D and WiDr cells. Some of the activities exhibited by benzylidene-based (1,3-selenazol-2-yl)hydrazones were comparable or even better than values obtained for positive control 5-fluorouracil, the blockbuster anticancer drug.

Table 4.32 Antiproliferative activities of benzylidene-based (1,3-selenazol-2-yl)hydrazones.

Compound	GI ₅₀ (μM)					
	A549	HBL-100	HeLa	SW1573	T-47D	WiDr
1	28.0 ± 7.1	91 ± 12	41.0 ± 9.5	24 ± 8	6.4 ± 0.9	4.8 ± 0.8
1-Me	n.d. ^a	n.d.	n.d.	47 ± 3	n.d.	n.d.
1-OMe	n.d.	n.d.	n.d.	42.0 ± 7.7	n.d.	n.d.
2	4.9 ± 1.5	21.0 ± 8.6	6.0 ± 0.7	5.3 ± 0.6	12.0 ± 1.5	5.0 ± 0.9
2-Me	8.8 ± 2.2	95.0 ± 8.1	7.4 ± 1.4	4.6 ± 1.2	13.0 ± 1.3	8.2 ± 1.0
2-OMe	22.0 ± 5.6	n.d.	49 ± 12	46 ± 10	36 ± 8.6	22.0 ± 2.3
3	6.1 ± 0.8	28.0 ± 0.8	24.0 ± 7.1	16.0 ± 4.8	52 ± 13	40.0 ± 0.6
3-Me	44 ± 15	60.0 ± 9.5	31.0 ± 4.0	18.0 ± 4.5	46.0 ± 9.7	55 ± 19
3-OMe	52 ± 1	n.d.	26 ± 2	8.4 ± 0.2	67.0 ± 2.2	n.d.
4	16.0 ± 3.5	n.d.	31.0 ± 8.5	23.0 ± 1.2	6.3 ± 1.1	6.9 ± 1.3
4-Me	n.d.	n.d.	n.d.	n.d.	n.d.	n.d.
4-OMe	16.0 ± 5.3	47 ± 13	33 ± 10	26 ± 17	66 ± 17	n.d.
5-fluorouracil	n.d.	4.0 ± 0.7	15.0 ± 4.7	4.6 ± 1.5	47 ± 18	49.0 ± 6.7

^a n.d. - not determined (GI₅₀ > 100 μM).

4.2.7.4 Monoamine oxidase A/B inhibition capacity

With the well-known representative's phenelzine or iproniazid, two hydrazine derivatives as non-selective MAO inhibitors are used as antidepressants in the class of

MAO inhibitors. Based on that, numerous thiazol-2-ylhydrazones were developed to obtain isoform-selective MAO inhibitors²²⁸, while related hydrazone-selenazoles have so far not been investigated in this context to best of our knowledge. Consequently, we investigated the MAO inhibition capacities of our structurally related (1,3-selenazol-2-yl)hydrazones. In a prescreening, we found most promising inhibition capacities for compounds **1** and **4** with percental MAO inhibition >70% at a concentration of 1 μ M (Table 4.33), while substitution on B phenyl ring tend to results in reduced MAO inhibition potency for these two representatives (e.g. **1** vs. **1-Me** and **1-OMe**).

Further more detailed characterization revealed nanomolar activity. The most potent compound **4**, bearing a *meta* nitro-group, showed IC₅₀ values of 73 nM and 258 nM for MAO B and MAO A, respectively. Surprisingly, compound **1** demonstrated high MAO B preference (IC₅₀ = 252 nM) with no inhibition of MAO A (IC₅₀> 10 000 nM).

Table 4.33 Monoamine oxidase (MAO) A/B inhibition capacities of benzylidene-based (1,3-selenazol-2-yl)hydrazones.

Compound	% Inhibition ^a (at 1 μ M)	
	MAO A	MAO B
1	-6.8 \pm 12.6	89.4 \pm 1.5
1-Me	12.7 \pm 3.5	23.4 \pm 17.1
1-OMe	32.4 \pm 3.3	33.0 \pm 11.6
2	26.5 \pm 3.7	64.8 \pm 6.1
2-Me	17.2 \pm 1.9	22.1 \pm 8.7
2-OMe	28.0 \pm 4.0	35.9 \pm 11.2
3	32.7 \pm 6.2	57.5 \pm 11.4
3-Me	13.4 \pm 2.4	7.4 \pm 27.0
3-OMe	31.2 \pm 1.6	23.8 \pm 7.7
4	71.9 \pm 3.5	96.3 \pm 0.5
4-Me	22.1 \pm 2.1	48.1 \pm 2.9
4-OMe	49.4 \pm 1.3	42.5 \pm 19.0

^a Percental inhibition calculated from remained enzyme activity normalized to control (=100%). Values are given as means \pm standard deviations (n = 2, global fit).

5 CONCLUSIONS

In order to study the structural and solvatochromic properties, as well as the influence of the structure on the biological activity, six pyridine (1,3-thiazol/selenazol-2-yl) hydrazones (**HL(S/Se)**¹⁻³) and their metal complexes (**(1-3)-(S/Se)**), as well as twelve benzyliden (1,3-selenazol-2-yl) hydrazones (**1-4**, **(1-4)-OMe**, **(1-4)-Me**) have been synthesized.

Within the first series of six pyridine derivatives and their complexes, results of XRD confirmed bonding of pyridine and imine nitrogen atoms, which is well known coordination behaviour of pyridyl-based hydrazone ligands. 1,3-Selenazole ring contains two donor atoms capable of coordinating to Co(III) ions forming a chelate ring. XRD revealed a coordination of hard nitrogen atom instead of soft selenium atom to metal centre making (1,3-selenazol-2-yl)hydrazones NNN tridentate chelators.

UV-Vis spectral characterization in DMF was supported by TD-DFT calculations. Values of λ_{\max} for selenazole derivatives are shifted bathochromically. Calculated values of E_{gap} for selenazoles are smaller than for their sulphur analogues which correlate to bathochromic shifts of λ_{\max} for selenazole derivatives. Energetically the most favourable ligand absorptions originate from HOMO→LUMO transitions. The HOMOs orbitals of all ligands and complexes are delocalized mainly at the azomethine group and selen/thiazole ring. These orbitals are also found at the benzene ring of the ligands and on Co atoms in the complexes. LUMOs of the ligands are delocalized on pyridine ring, azomethine group and selen/thiazole ring. Methyl- and methoxy- substituents of benzene ring destabilize HOMO and LUMO orbitals and decrease the energy gap due to electron releasing effect. The LUMO orbitals of **(1-3)-Se** and **(1-3)-S** are delocalized mainly at the azomethine group, metal centre, and pyridine ring.

Electrochemical study of investigated sulphur and selenium ligands, supported by calculation of Fukui functions, indicate one-electron reduction process of C=N hydrazono group and one two-electron oxidation of C8-chalcogen bond. Totally, four-electron oxidations observed in the case of all complexes indicate that C8-chalcogen bond is a possible oxidation site, while only two reversible reduction processes observed were attributed to

Co(III)→Co(II) and Co(II)→Co(I) reductions. Further possible reduction sites (Co(I) and C=N) are supposed to be at even lower potentials, outside the potential window applied in our CV experiments.

The investigation of free-radical scavenging activity of all substances within the first series indicates that selenium based compounds are more potent than corresponding sulphur analogues. The strong influence of substituents on benzene ring on free-radical scavenging activity was observed. Non-substituted derivatives appeared to be the most active ones in the case of all ligands and their complexes. **HLSe**² and **HLS**² were the only investigated compounds less active than the reference compound vitamin C.

Antimicrobial activity assay indicates that **HLSe**⁽¹⁻³⁾ were more active than corresponding sulphur compounds on all bacteria and fungi strains investigated. Preparation of Co(III) complexes enhanced ligands' antibacterial activity. Despite the fact that sulphur based complexes reached almost the same level of antibacterial activity as their selenium analogues, results of acute lethality assay indicate the significantly smaller cell toxicity of Co(III) (1,3-selenazol-2-yl)hydrazone complexes, which makes them promising candidates for future antibacterial drug development.

Results of anticancer activity of **1-S**, investigated using the standard monolayer 2-D and 3-D spheroid model, reveal that **1-S** is more potent inducer of cell death than CDDP after 24 h incubation on MCF-7 2-D model, whereas both drugs achieved inhibition of 3-D MCF-7 spheres growth in almost the same extent after eight days of incubation. However, the difference in morphological changes of spheroids subjected to CDDP and **1** was the primary indication that those two compounds do not share the same mechanism of activity, supported by the results of combination treatment. The evidence that these two metal complexes in combination resulted with synergistic interaction might, at first glance, discards the assumption stated above. However, their discordant interaction with paclitaxel contributed to hypothesize on the diversity of CDDP and **1-S** mechanisms for their anticancer effect. Although this is the first study on anticancer property of **1-S**, current results strongly approve its further testing onto other cancer models, especially the underlying mechanism of synergistic interaction with CDDP.

A focused library of twelve benzyldene-based (1,3-selenazol-2-yl)hydrazones was synthesized to study the impact of substituents on both A and B phenyl rings on structure, solvatochromism, electrochemical properties, antimicrobial and antioxidant activity. The results showed that fragmentation of compounds is sensitive to the appropriate proton-donating/proton-accepting capabilities of the particular sites which proved that local electronic density distribution is an important factor determining fragmentation mode of studied compounds. The results of LSER analysis provide better understanding of attractive/repulsive solvent/solute interactions, and showed diversity of solvent and substituents on to ν_{\max} shift in UV-Vis spectra. Largest specific interactions through solvent hydrogen bond donating effect were achieved with *ortho*- and *para*-nitro substituted (1,3-selenazol-2-yl)hydrazones exerting bathochromic shifts for **2** and **2-Me**, while hypsochromic were found for others. UV-Vis spectral characterization in the twenty three solvents of different polarity was supported with TD-DFT calculations.

From the crystal structure of **4-Me** and **4-OMe** and optimized geometries of investigated compounds, it was evident that significant change in torsion angles was observed which determine extent of π,π -conjugation and ICT as well. The change of position of the nitro-group from *para* to *ortho* and *meta* destabilized both HOMO and LUMO orbitals, while small influence of solvent effect was observed. Energetically the most favorable absorptions originate from HOMO→LUMO transitions. The HOMO orbitals of (1,3-selenazol-2-yl)-hydrazones are delocalized mainly at the 1,3-selenazole moieties, phenyl rings B and hydrazone bridges, while LUMO orbitals are delocalized at phenyl rings A.

Antioxidant capacity study, including radical scavenging activity, the oxygen radical absorption capacity and reduction ability, indicated that mechanism of action of investigated compounds under applied experimental conditions is not based on their reduction power. Namely, compounds possessed excellent antioxidant properties in DPPH and ORAC assays, since most of the compounds showed better activities than Vitamin C. In the case of DPPH assay addition of nitro substituent reduced the activity of compounds from sets 2–4 (with few exceptions) and changed the order of Y substituents impact in comparison to activity of compounds from set 1. In the case of ORAC assay it was possible to establish simple structure- activity relationship. Namely,

methyl and methoxy substituents potentiate, while addition of nitro group reduces the activity.

Study of 12 benzylidenebased (1,3-selenazol-2-yl)hydrazones compounds in screening on MAO B inhibition revealed that **1** and **4** possess IC₅₀ values in nanomolar concentration range. Docking studies showed that KCCN1 is additional target for **1** and **4**, which indicates their possible multi targeting properties for the treatment of neurodegenerative disorders. Antiproliferative activity screening indicates that **2** and **2-Me** are the most potent anticancer agents among investigated compounds with better activity than that of the positive control 5-fluorouracil. Docking studies point to 5-NT and EIF4E as possible cancer-related targets.

6 REFERENCES

- 1 A. Imramovsky, J. Kozic, M. Pesko, J. Stolarikova, J. Vinsova, K. Kralova and J. Jampilek, *Sci. World J.*, 2014, **2014**, 1–11.
- 2 P. Karegoudar, M. S. Karthikeyan, D. J. Prasad, M. Mahalinga, B. S. Holla and N. S. Kumari, *Eur. J. Med. Chem.*, 2008, **43**, 261–267.
- 3 S. K. Bharti, G. Nath, R. Tilak and S. K. Singh, *Eur. J. Med. Chem.*, 2010, **45**, 651–660.
- 4 H. Mohammad, A. S. Mayhoub, M. Cushman and M. N. Seleem, *J. Antibiot. (Tokyo)*, 2015, **68**, 259–266.
- 5 N. P. de Sá, C. M. de Lima, C. I. Lino, P. J. S. Barbeira, L. de M. Baltazar, D. A. Santos, R. B. de Oliveira, E. Mylonakis, B. B. Fuchs and S. Johann, *Antimicrob. Agents Chemother.*, 2017, **61**.
- 6 F. Chimenti, B. Bizzarri, E. Maccioni, D. Secci, A. Bolasco, R. Fioravanti, P. Chimenti, A. Granese, S. Carradori, D. Rivanera, D. Lilli, A. Zicari and S. Distinto, *Bioorg. Med. Chem. Lett.*, 2007, **17**, 4635–4640.
- 7 A. M. Youssef, A. Malki, M. H. Badr, R. Y. Elbayaa and A. S. Sultan, *Med. Chem.*, 2012, **8**, 151–62.
- 8 C. M. Weekley and H. H. Harris, *Chem. Soc. Rev.*, 2013, **42**, 8870.
- 9 A. Ayati, S. Emami, A. Asadipour, A. Shafiee and A. Foroumadi, *Eur. J. Med. Chem.*, 2015, **97**, 699–718.
- 10 S. . Ueda, H. . b Terauchi, K. . Suzuki, A. . Yano, M. . Matsumoto, T. . Kubo, H. . Minato, Y. . Arai, J.-I. . Tsuji and N. . Watanabe, *Bioorganic Med. Chem. Lett.*, 2005, **15**, 1361–1366.
- 11 H. van der Goot, J. C. Eriks, R. Leurs and H. Timmerman, *Bioorganic Med. Chem. Lett.*, 1994, **4**, 1913–1916.
- 12 V. Zaharia, A. Ignat, B. Ngameni, V. Kuete, M. L. MOUNGANG, C. N. Fokunang, M. Vasilescu, N. Palibroda, C. Cristea, L. Silaghi-Dumitrescu and B. T. Ngadjui, *Med. Chem. Res.*, 2013, **22**, 5670–5679.
- 13 M. Hong, Y. Yang, C. Li, L. Xu, D. Li and C. Li, *RSC Adv.*, 2015, **5**, 102885–102894.
- 14 H. C. Zhao, Y. P. Shi, Y. M. Liu, C. W. Li, L. N. Xuan, P. Wang, K. Zhang and B. Q. Chen, *Bioorganic Med. Chem. Lett.*, 2013, **23**, 6577–6579.
- 15 A. T. Mbaveng, A. G. Ignat, B. Ngameni, V. Zaharia, B. T. Ngadjui and V. Kuete, *BMC Pharmacol. Toxicol.*, 2016, **17**, 3.
- 16 K. Z. Łaczkowski, K. Motylewska, A. Baranowska-Łaczkowski, A. Biernasiuk, K. Misiura, A. Malm and B. Fernandez, *J. Mol. Struct.*, 2016, **1108**, 427–437.
- 17 A. T. Mbaveng, A. G. Ignat, B. Ngameni, V. Zaharia, B. T. Ngadjui and V. Kuete, *BMC Pharmacol. Toxicol.*, 2016, **17**, 3.
- 18 A. Z. Al-Rubaie, S. A. S. Al-Jadaan, S. K. Muslim, E. A. Saeed, E. T. Ali, A. K. J. Al-Hasani, H. N. K. Al-Salman and S. A. M. Al-Fadal, *J. Organomet. Chem.*, 2014, **774**, 43–47.
- 19 N. R. Filipović, H. Elshaflu, S. Grubišić, L. S. Jovanović, M. Rodić, I. Novaković, A. Malešević, I. S. Djordjević, H. Li, N. Šojić, A. Marinković and T. R. Todorović, *Dalt. Trans.*, 2017, **46**, 2910–2924.
- 20 A. Šmelcerović, K. Tomović, Ž. Šmelcerović, Ž. Petronijević, G. Kocić, T. Tomašić, Ž. Jakopin and M. Anderluh, *Eur. J. Med. Chem.*, 2017, **135**, 491–516.
- 21 M. J. Kamlet, J. L. M. Abboud and R. W. Taft, in *Progress in Physical Organic Chemistry*, ed. R. W. Taft, John Wiley & Sons, New York, 1981, pp. 485–630.

- 22 J. Catalán, *J. Phys. Chem. B*, 2009, **113**, 5951–5960.
- 23 T. Eicher and S. Hauptmann, *The Chemistry of Heterocycles: Structure, Reactions, Synthesis, and Applications*, John Wiley & Sons, 2003.
- 24 V. Savić, *Hemija heterocikličnih jedinjenja*, Farmaceutski fakultet, Beograd, 2011.
- 25 in *Heterocyclic Chemistry at a Glance*, John Wiley & Sons, Ltd, Chichester, UK, 2012, pp. 107–121.
- 26 J. B. Julio Alvarez-Builla, Juan Jose Vaquero, *Modern Heterocyclic Chemistry*, 2011.
- 27 R. Kluger and K. Tittmann, *Chem. Rev.*, 2008, **108**, 1797–1833.
- 28 A. Hantzsch and J. H. Weber, *Berichte der Dtsch. Chem. Gesellschaft*, 1887, **20**, 3118–3132.
- 29 M. Ochiai, Y. Nishi, S. Hashimoto, Y. Tsuchimoto and D.-W. Chen, *J. Org. Chem.*, 2003, **68**, 7887–7888.
- 30 A. G. Belyuga, V. S. Brovarets and B. S. Drach, *Russ. J. Gen. Chem.*, 2004, **74**, 1418–1422.
- 31 M. Narender, M. S. Reddy, V. P. Kumar, V. P. Reddy, Y. V. D. Nageswar and K. R. Rao, *J. Org. Chem.*, 2007, **72**, 1849–1851.
- 32 E. Bulka, 1963, pp. 343–364.
- 33 Y. Chen, F. Tian, M. Song and S. Lu, *Heteroat. Chem.*, 2008, **19**, 211–214.
- 34 H. Below, W.-D. Pfeiffer, K. Geisler, M. Lalk and P. Langer, *European J. Org. Chem.*, 2005, **2005**, 3637–3639.
- 35 C. Madhu, N. R. Panguluri, N. Narendra, V. Panduranga and V. V. Sureshbabu, *Tetrahedron Lett.*, 2014, **55**, 6831–6835.
- 36 W. Davies, J. A. Maclaren and L. R. Wilkinson, *J. Chem. Soc.*, 1950, 3491.
- 37 E. Bulka, K.-D. Ahlers and E. Tuček, *Chem. Ber.*, 1967, **100**, 1459–1464.
- 38 E. Klingsberg, *J. Am. Chem. Soc.*, 1963, **85**, 2685–2685.
- 39 J. Gasteiger and C. Herzig, *Tetrahedron*, 1981, **37**, 2607–2611.
- 40 W. D. Pfeiffer and E. Bulka, *Chemiker-Ztg*, 1991, **115**, 361–363.
- 41 T. Takahashi and J. Shibasaki, *YAKUGAKU ZASSHI*, 1949, **69**, 496–497.
- 42 J. Haginiwa, *YAKUGAKU ZASSHI*, 1948, **68**, 195–197.
- 43 S. Rollas and Ş. G. Küçükgülzel, *Molecules*, 2007, **12**, 1910–1939.
- 44 A. Kajal, S. Bala, N. Sharma, S. Kamboj and V. Saini, *Int. J. Med. Chem.*, 2014, **2014**, 761030.
- 45 G. Verma, A. Marella, M. Shaquiquzzaman, M. Akhtar, M. R. Ali and M. M. Alam, *J. Pharm. Bioallied Sci.*, 2014, **6**, 69–80.
- 46 K. Padmini, P. J. Preethi, M. Divya, P. Rohini, M. Lohita, K. Swetha and P. Kaladar, *Int. J. Pharma Res. Rev.*, 2013, **2**, 43–58.
- 47 M. Asif and A. Husain, *J. Appl. Chem.*, 2013, **2013**, 1–7.
- 48 V. J. Negi, *Int. J. Pharm. Chem.*, 2013, **2**, 12–13.
- 49 A. Arshad, H. Osman, M. C. Bagley, C. K. Lam, S. Mohamad and A. S. M. Zahariluddin, *Eur. J. Med. Chem.*, 2011, **46**, 3788–3794.
- 50 A. M. Vijesh, A. M. Isloor, V. Prabhu, S. Ahmad and S. Malladi, *Eur. J. Med. Chem.*, 2010, **45**, 5460–5464.
- 51 F. Chimenti, B. Bizzarri, A. Bolasco, D. Secci, P. Chimenti, S. Carradori, A. Granese, D. Rivanera, N. Frishberg, C. Bordón and L. Jones-Brando, *J. Med. Chem.*, 2009, **52**, 4574–4577.
- 52 M. V. de O. Cardoso, L. R. P. de Siqueira, E. B. da Silva, L. B. Costa, M. Z.

- Hernandes, M. M. Rabello, R. S. Ferreira, L. F. da Cruz, D. R. Magalhães
 Moreira, V. R. A. Pereira, M. C. A. B. de Castro, P. V. Bernhardt and A. C. L.
 Leite, *Eur. J. Med. Chem.*, 2014, **86**, 48–59.
- 53 M.-H. Shih, Y.-S. Su and C.-L. Wu, *Chem. Pharm. Bull. (Tokyo)*, 2007, **55**,
 1126–35.
- 54 F. Chimenti, B. Bizzarri, E. Maccioni, D. Secci, A. Bolasco, P. Chimenti, R.
 Fioravanti, A. Granese, S. Carradori, F. Tosi, P. Ballario, S. Vernarecci and P.
 Filetici, *J. Med. Chem.*, 2009, **52**, 530–536.
- 55 F. Chimenti, E. Maccioni, D. Secci, A. Bolasco, P. Chimenti, A. Granese, O.
 Befani, P. Turini, S. Alcaro, F. Ortuso, M. C. Cardia and S. Distinto, *J. Med.*
Chem., 2007, **50**, 707–712.
- 56 P. Chimenti, A. Petzer, S. Carradori, M. D’Ascenzio, R. Silvestri, S. Alcaro, F.
 Ortuso, J. P. Petzer and D. Secci, *Eur. J. Med. Chem.*, 2013, **66**, 221–227.
- 57 K. J. Wilson, C. R. Illig, N. Subasinghe, J. B. Hoffman, M. J. Rudolph, R. Soll,
 C. J. Molloy, R. Bone, D. Green, T. Randall, M. Zhang, F. A. Lewandowski, Z.
 Zhou, C. Sharp, D. Maguire, B. Grasberger, R. L. DesJarlais and J. Spurlino,
Bioorg. Med. Chem. Lett., 2001, **11**, 915–8.
- 58 L. Yurttaş, Y. Özkay, H. Karaca Gençer and U. Acar, *J. Chem.*, 2015, **2015**, 1–7.
- 59 D. González Cabrera, F. Douelle, T.-S. Feng, A. T. Nchinda, Y. Younis, K. L.
 White, Q. Wu, E. Ryan, J. N. Burrows, D. Waterson, M. J. Witty, S. Wittlin, S.
 A. Charman and K. Chibale, *J. Med. Chem.*, 2011, **54**, 7713–7719.
- 60 F. Chimenti, D. Secci, A. Bolasco, P. Chimenti, A. Granese, S. Carradori, M.
 Yáñez, F. Orallo, M. L. Sanna, B. Gallinella and R. Cirilli, *J. Med. Chem.*, 2010,
53, 6516–6520.
- 61 D. Secci, A. Bolasco, S. Carradori, M. D’Ascenzio, R. Nescatelli and M. Yáñez,
Eur. J. Med. Chem., 2012, **58**, 405–417.
- 62 D.-N. Zhang, J.-T. Li, Y.-L. Song, H.-M. Liu and H.-Y. Li, *Ultrason. Sonochem.*,
 2012, **19**, 475–478.
- 63 V. Zaharia, A. Ignat, B. Ngameni, V. Kuete, M. L. MOUNGANG, C. N. Fokunang,
 M. Vasilescu, N. Palibroda, C. Cristea, L. Silaghi-Dumitrescu and B. T. Ngadjui,
Med. Chem. Res., 2013, **22**, 5670–5679.
- 64 C. Reichardt, *Solvents and Solvent Effects in Organic Chemistry*, Wiley-VCH,
 Weinheim, 3th ed., 2003.
- 65 E. S. Amis and J. F. Hinton, *Solvent Effects on Chemical Phenomena, vol I*,
 Academic Press, New York, 1973.
- 66 E. M. Kosower, *An Introduction to Physical Organic Chemistry*, Wiley, New
 York, 1968.
- 67 J. Kakabadse, *Solvent Problems in Industry*, Elsevier Applied Science Publishers,
 London, 1984.
- 68 Y. Marcus, *Ion Solvation*, Wiley, Chichester, 1985.
- 69 M. H. Abraham, *Pure Appl. Chem.*, 1985, **57**, 1055–1064.
- 70 M. H. . G. Abraham and R. W. P. L.; Abboud, J.-L. M.; Doherty, R. M.; Taft,
Can. J. Chem., 1988, **66**, 2673–2686.
- 71 K. A. Connors, *Chemical Kinetics-The Study of Reaction Rates in Solution*, VCH
 Publishers, Weinheim, 1990.
- 72 S. Sagadevan and P. Murugasen, *J. Cryst. Process Technol.*, 2014, **04**, 99–110.
- 73 S. Dähne and F. Moldenhauer, in *Progress in Physical Organic Chemistry*, ed. R.
 W. Taft, John Wiley & Sons, Inc., Hoboken, NJ, USA, 1985, pp. 1–130.

- 74 J. Fabian and H. Hartman, *J. Mol. Struct.*, 1975, **27**, 67–78.
- 75 M. J. Kamlet, J. L. M. Abboud, M. H. Abraham and R. W. Taft, *J. Org. Chem.*, 1983, **48**, 2877–2887.
- 76 M. J. Kamlet, J. L. Abboud and R. W. Taft, *J. Am. Chem. Soc.*, 1977, **99**, 6027–6038.
- 77 R. W. Taft and M. J. Kamlet, *J. Am. Chem. Soc.*, 1976, **98**, 2886–2894.
- 78 F. Riedel and S. Spange, *J. Phys. Org. Chem.*, 2012, **25**, 1261–1268.
- 79 J. Catalán and H. Hopf, *European J. Org. Chem.*, 2004, 4694–4702.
- 80 J. Catalán, *J. Phys. Chem.*, 2009, **113**, 5951–5960.
- 81 P. Hohenberg and W. Kohn, *Phys. Rev.*, 1964, **136**, B864–B871.
- 82 W. Kohn and L. J. Sham, *Phys. Rev.*, 1965, **140**, A1133–A1138.
- 83 P. Hao, J. Sun, B. Xiao, A. Ruzsinszky, G. I. Csonka, J. Tao, S. Glindmeyer and J. P. Perdew, *J. Chem. Theory Comput.*, 2013, **9**, 355–363.
- 84 I. B. Cozar, A. Pîrnău, L. Szabo, N. Vedeanu, C. Nastasă and O. Cozar, *Rom. J. Phys.*, 2016, **61**, 1265–1275.
- 85 F. T. Burling and B. M. Goldstein, *J. Am. Chem. Soc.*, 1992, **114**, 2313–2320.
- 86 K. Z. Łączkowski, J. Anusiak, M. Świtalska, K. Dzitko, J. Cytarska, A. Baranowska-Łączkowska, T. Plech, A. Paneth, J. Wietrzyk and J. Białczyk, *Med. Chem. Res.*, 2018, **27**, 1131–1148.
- 87 M. Ghorbanloo, R. Bikas and G. Małecki, *Inorganica Chim. Acta*, 2016, **445**, 8–16.
- 88 M. Alam, M. J. Alam, S. A. A. Nami, D. Lee, M. Azam and S. Ahmad, *J. Mol. Struct.*, 2016, **1108**, 411–426.
- 89 L. Karanović and D. Poleti, *Rendgenska strukturna analiza*, Zavod za udžbenike i nastavna sredstva, 2003.
- 90 D. Mendoza-Espinosa, G. Ung, B. Donnadiu and G. Bertrand, *Chem. Commun.*, 2011, **47**, 10614–10616.
- 91 S. Yousuf, H. Siddiqui, R. Farooq and M. I. Choudhary, *Acta Crystallogr. Sect. E Struct. Reports Online*, 2012, **68**.
- 92 Manju, P. Joshi and D. Kumar, *Russ. J. Coord. Chem.*, 2014, **40**, 445–459.
- 93 A. S. Thakar, H. B. Friedrich, K. T. Joshi and G. E. Maguire, *South African J. Chem.*, 2015, **68**, 39–44.
- 94 Y. Gu, X. Fei, Y. Lan, B. I. N. Shi, B. Zhang and G. Jia, *Structure*, 2010, **7**, 305–312.
- 95 A. Despić, *Elektrohemijske tehnike i tehnologije*, Srpska akademija nauke i umetnosti, Beograd, 2005.
- 96 G. K. R. Das*, A. Saxena, S. Saxena, *J. Adv. Electrochem.*, 2015, **1**, 19–24.
- 97 David T Harvey, *Modern Analytical Chemistry*, Boston, MA, 1999.
- 98 D. . Skoog, D. M. West and F. J. Holler, *Fundamentals of Analytical Chemistry*, Saunders College Publishing, Philadelphia, 1996.
- 99 R. Holze, *Berichte der Bunsengesellschaft für Phys. Chemie*, 1994, **98**, 1350–1350.
- 100 J. Wang, *Analytical Electrochemistry*, John Wiley & Sons, Inc., Hoboken, NJ, USA, 2006.
- 101 A. J. Bard and L. R. Faulkner, *Electrochemical Methods, Fundamentals and Applications*, John Wiley & Sons, 2001.
- 102 R. B. Singh, P. Jain and R. P. Singh, *Talanta*, 1982, **29**, 77–84.
- 103 H. Lund, A. Sundholm, A. Magnéli, B. Högberg, P. Kneip and H. Palmstierna,

- Acta Chem. Scand.*, 1959, **13**, 249–267.
- 104 E. Biçer and C. Arat, *Croat. Chem. Acta*, 2009, **82**, 583–593.
- 105 S. Çakir, E. Biçer, M. Odabasoglu and Ç. Albayrak, *J. Braz. Chem. Soc.*, 2005, **16**, 711–717.
- 106 G. Visbal, G. San-Blas, A. Maldonado, Á. Álvarez-Aular, M. V. Capparelli and J. Murgich, *Steroids*, 2011, **76**, 1069–1081.
- 107 H. Shirinzadeh, A. D. Yılmaz, M. Gümüştas, S. Süzen, S. Özden and A. S. Özkan, *Comb. Chem. High Throughput Screen.*, 2010, **13**, 619–627.
- 108 R. J. Abdel-Jalil, E. Q. El Momani, M. Hamad, W. Voelter, M. S. Mubarak, B. H. Smith and D. G. Peters, *Monatshefte für Chemie - Chem. Mon.*, 2010, **141**, 251–258.
- 109 H. M. Fahmy and M. H. Elnagdi, *Electrochim. Acta*, 1978, **23**, 255–260.
- 110 A. D. Özel, Zehra Durmus, Ibrahim Yılmaz, A. Çukurovalı and E. Kılıç1, *Acta Chim. Slov.*, 2009, **56**, 797–806.
- 111 V. N. D. L. V Kononenko, V. D. Bezuglyi, *Zh. Obs. Khim.*, 1968, **38**, 2153–2159.
- 112 X.-H. Liu, J.-Q. Weng and C.-X. Tan, *J. Chem.*, 2013, **2013**, 1–5.
- 113 X.-H. Liu, C.-X. Tan, J.-Q. Weng and H.-J. Liu, *Acta Crystallogr. Sect. E Struct. Reports Online*, 2012, **68**, o493–o493.
- 114 N.-B. Sun, J.-Q. Fu, J.-Q. Weng, J.-Z. Jin, C.-X. Tan and X.-H. Liu, *Molecules*, 2013, **18**, 12725–12739.
- 115 N.-B. Sun, Y.-X. Shi, X.-H. Liu, Y. Ma, C.-X. Tan, J.-Q. Weng, J.-Z. Jin and B.-J. Li, *Int. J. Mol. Sci.*, 2013, **14**, 21741–21756.
- 116 M. Alam, G. Verma, M. Shaquiquzzaman, A. Marella, M. Akhtar and M. Ali, *J. Pharm. Bioallied Sci.*, 2014, **6**, 69.
- 117 A. Borges, C. Ferreira, M. J. Saavedra and M. Simões, *Microb. Drug Resist.*, 2013, **19**, 256–265.
- 118 R. C. Finch, D. Greenwood, S. R. Norrby, R. J. Whitley and J. R. Lentino, *Clin. Infect. Dis.*, 2004, **38**, 1197–1197.
- 119 F. Chimenti, D. Secci, A. Bolasco, P. Chimenti, A. Granese, S. Carradori, M. D’Ascenzio, M. Yáñez and F. Orallo, *Medchemcomm*, 2010, **1**, 61.
- 120 F. Chimenti, B. Bizzarri, A. Bolasco, D. Secci, P. Chimenti, A. Granese, S. Carradori, M. D’Ascenzio, D. Lilli and D. Rivanera, *Eur. J. Med. Chem.*, 2011, **46**, 378–382.
- 121 K. Z. Łączkowski, K. Motylewska, A. Baranowska-Łączkowska, A. Biernasiuk, K. Misiura, A. Malm and B. Fernández, *J. Mol. Struct.*, 2016, **1108**, 427–437.
- 122 H. Sies, *Exp. Physiol.*, 1997, **82**, 291–5.
- 123 M. Valko, M. Izakovic, M. Mazur, C. J. Rhodes and J. Telsler, *Mol. Cell. Biochem.*, 2004, **266**, 37–56.
- 124 M. Carocho and I. C. F. R. Ferreira, *Food Chem. Toxicol.*, 2013, **51**, 15–25.
- 125 N. Hermans, P. Cos, L. Maes, T. De Bruyne, D. Vanden Berghe, A. J. Vlietinck and L. Pieters, *Curr. Med. Chem.*, 2007, **14**, 417–430.
- 126 S. A. Soto-Rodriguez, N. Simões, D. A. Jones, A. Roque and B. Gomez-Gil, *J. Microbiol. Methods*, 2003, **52**, 101–14.
- 127 R. R. Ramoutar and J. L. Brumaghim, *Cell Biochem. Biophys.*, 2010, **58**, 1–23.
- 128 M.-H. Shih, Y.-S. Su and C.-L. Wu, *Chem. Pharm. Bull. (Tokyo)*, 2007, **55**, 1126–1135.
- 129 D. Hanahan and R. A. Weinberg, *Cell*, 2000, **100**, 57–70.

- 130 R. Edmondson, J. J. Broglie, A. F. Adcock and L. Yang, *Assay Drug Dev. Technol.*, 2014, **12**, 207–218.
- 131 S.-W. Choi, Y.-C. Yeh, Y. Zhang, H.-W. Sung and Y. Xia, *Small*, 2010, **6**, 1492–1498.
- 132 E. Figallo, C. Cannizzaro, S. Gerecht, J. A. Burdick, R. Langer, N. Elvassore and G. Vunjak-Novakovic, *Lab Chip*, 2007, **7**, 710.
- 133 M. MONDRINOS, R. DEMBZYNSKI, L. LU, V. BYRAPOGU, D. WOOTTON, P. LELKES and J. ZHOU, *Biomaterials*, 2006, **27**, 4399–4408.
- 134 Y. Wang, E. Bella, C. S. D. Lee, C. Migliaresi, L. Pelcastre, Z. Schwartz, B. D. Boyan and A. Motta, *Biomaterials*, 2010, **31**, 4672–4681.
- 135 D. T. Scadden, *Nature*, 2006, **441**, 1075–1079.
- 136 J. A. Burdick and G. Vunjak-Novakovic, *Tissue Eng. Part A*, 2009, **15**, 205–219.
- 137 G. H. Underhill and S. N. Bhatia, *Curr. Opin. Chem. Biol.*, 2007, **11**, 357–366.
- 138 L. Gu and D. J. Mooney, *Nat. Rev. Cancer*, 2016, **16**, 56–66.
- 139 D. Huh, G. A. Hamilton and D. E. Ingber, *Trends Cell Biol.*, 2011, **21**, 745–754.
- 140 H.-C. Zhao, Y.-P. Shi, Y.-M. Liu, C.-W. Li, L.-N. Xuan, P. Wang, K. Zhang and B.-Q. Chen, *Bioorg. Med. Chem. Lett.*, 2013, **23**, 6577–6579.
- 141 T. R. Todorović, A. Bacchi, D. M. Sladić, N. M. Todorović, T. T. Božić, D. D. Radanović, N. R. Filipović, G. Pelizzi and K. K. Anđelković, *Inorganica Chim. Acta*, 2009, **362**, 3813–3820.
- 142 W. Yi, C. Dubois, S. Yahiaoui, R. Haudecoeur, C. Belle, H. Song, R. Hardré, M. Réglie and A. Boumendjel, *Eur. J. Med. Chem.*, 2011, **46**, 4330–4335.
- 143 H. Elshafly, S. Bjelogrić, C. D. Muller, T. R. Todorović, M. Rodić, A. Marinković and N. R. Filipović, *J. Coord. Chem.*, 2016, **69**, 3354–3366.
- 144 2014.
- 145 G. M. Sheldrick, *Acta Crystallogr. Sect. A Found. Adv.*, 2015, **71**, 3–8.
- 146 G. M. Sheldrick, *Acta Crystallogr. Sect. C Struct. Chem.*, 2015, **71**, 3–8.
- 147 C. B. Hübschle, G. M. Sheldrick and B. Dittrich, *J. Appl. Crystallogr.*, 2011, **44**, 1281–1284.
- 148 R. Herbst-Irmer and G. M. Sheldrick, *Acta Crystallogr. Sect. B Struct. Sci.*, 1998, **54**, 443–449.
- 149 A. Altomare, G. Cascarano, C. Giacovazzo and A. Guagliardi, *J. Appl. Crystallogr.*, 1993, **26**, 343–350.
- 150 A. L. Spek, *Acta Crystallogr. Sect. D Biol. Crystallogr.*, 2009, **65**, 148–155.
- 151 H. D. Flack and M. Wörle, *J. Appl. Crystallogr.*, 2013, **46**, 248–251.
- 152 H. D. Flack and G. Bernardinelli, *Acta Crystallogr. Sect. A Found. Crystallogr.*, 1999, **55**, 908–915.
- 153 C. R. Groom and F. H. Allen, *Angew. Chemie Int. Ed.*, 2014, **53**, 662–671.
- 154 M. J. Frisch, G. W. Trucks, H. B. Schlegel, G. E. Scuseria, M. A. Robb, J. R. Cheeseman, G. Scalmani, V. Barone, B. Mennucci, G. A. Petersson, H. Nakatsuji, M. Caricato, X. Li, H. P. Hratchian, A. F. Izmaylov, J. Bloino, G. Zheng, J. L. Sonnenberg, M. Hada, M. Ehara, K. Toyota, R. Fukuda, J. Hasegawa, M. Ishida, T. Nakajima, Y. Honda, O. Kitao, H. Nakai, T. Vreven, J. A. Montgomery Jr., J. E. Peralta, F. Ogliaro, M. Bearpark, J. J. Heyd, E. Brothers, K. N. Kudin, V. N. Staroverov, R. Kobayashi, J. Normand, K. Raghavachari, A. Rendell, J. C. Burant, S. S. Iyengar, J. Tomasi, M. Cossi, N. Rega, J. M. Millam, M. Klene, J. E. Knox, J. B. Cross, V. Bakken, C. Adamo, J. Jaramillo, R. Gomperts, R. E. Stratmann, O. Yazyev, A. J. Austin, R. Cammi, C.

- Pomelli, J. W. Ochterski, R. L. Martin, K. Morokuma, V. G. Zakrzewski, G. A. Voth, P. Salvador, J. J. Dannenberg, S. Dapprich, A. D. Daniels, Ö. Farkas, J. B. Foresman, J. V. Ortiz, J. Cioslowski and D. J. Fox, 2009.
- 155 A. D. Becke, *J. Chem. Phys.*, 1993, **98**, 5648–5652.
- 156 C. Lee, W. Yang and R. G. Parr, *Phys. Rev. B*, 1988, **37**, 785–789.
- 157 J. P. Perdew, *Phys. Rev. B*, 1986, **33**, 8822–8824.
- 158 A. D. Becke, *Phys. Rev. A*, 1988, **38**, 3098–3100.
- 159 S. H. Vosko, L. Wilk and M. Nusair, *Can. J. Phys.*, 1980, **58**, 1200–1211.
- 160 V. A. Rassolov, J. A. Pople, M. A. Ratner and T. L. Windus, *J. Chem. Phys.*, 1998, **109**, 1223.
- 161 V. A. Rassolov, M. A. Ratner, J. A. Pople, P. C. Redfern and L. A. Curtiss, *J. Comput. Chem.*, 2001, **22**, 976–984.
- 162 P. C. Hariharan and J. A. Pople, *Theor. Chim. Acta*, 1973, **28**, 213–222.
- 163 M. M. Francl, *J. Chem. Phys.*, 1982, **77**, 3654.
- 164 G. Scalmani and M. J. Frisch, *J. Chem. Phys.*, 2010, **132**, 114110.
- 165 N. T. Abdel Ghani and A. M. Mansour, *J. Mol. Struct.*, 2011, **991**, 108–126.
- 166 L. Miao, Y. Yao, F. Yang, Z. Wang, W. Li and J. Hu, *J. Mol. Struct. THEOCHEM*, 2008, **865**, 79–87.
- 167 E. S. Böes, P. R. Livotto and H. Stassen, *Chem. Phys.*, 2006, **331**, 142–158.
- 168 Y. Li and J. N. S. Evans, *J. Am. Chem. Soc.*, 1995, **117**, 7756–7759.
- 169 R. G. Parr and W. Yang, *Functional Theory of Atoms and Molecules*, Oxford University Press, New York, 1989.
- 170 E. D. Glendening, A. E. Reed, J. E. Carpenter and F. Weinhold, .
- 171 K. Hofmann, K. Schreiter, A. Seifert, T. Ruffer, H. Lang and S. Spange, *New J. Chem.*, 2008, **32**, 2180.
- 172 M. J. Kamlet, J. L. M. Abboud, M. H. Abraham and R. W. Taft, *J. Org. Chem.*, 1983, **48**, 2877–2887.
- 173 Y. Marcus, *Chem. Soc. Rev.*, 1993, **22**, 409.
- 174 C. Perez, M. Pauli and P. Bazerque, *Acta Biol. Med. Exp.*, 1990, **15**, 113–115.
- 175 R. L. Prior, X. Wu and K. Schaich, *J. Agric. Food Chem.*, 2005, **53**, 4290–4302.
- 176 M. Oyaizu, *Japanese J. Nutr. Diet.*, 1986, **44**, 307–315.
- 177 P. Prieto, M. Pineda and M. Aguilar, *Anal. Biochem.*, 1999, **269**, 337–341.
- 178 B. Ou, M. Hampsch-Woodill and R. L. Prior, *J. Agric. Food Chem.*, 2001, **49**, 4619–4626.
- 179 P. Skehan, R. Storeng, D. Scudiero, A. Monks, J. McMahon, D. Vistica, J. T. Warren, H. Bokesch, S. Kenney and M. R. Boyd, *J. Natl. Cancer Inst.*, 1990, **82**, 1107–12.
- 180 P. O. Miranda, J. M. Padrón, J. I. Padrón, J. Villar and V. S. Martín, *ChemMedChem*, 2006, **1**, 323–329.
- 181 L. Meiring, J. P. Petzer and A. Petzer, *Bioorg. Med. Chem. Lett.*, 2013, **23**, 5498–5502.
- 182 C. R. Kowol, W. Miklos, S. Pfaff, S. Hager, S. Kallus, K. Pelivan, M. Kubanik, É. A. Enyedy, W. Berger, P. Heffeter and B. K. Keppler, *J. Med. Chem.*, 2016, **59**, 6739–6752.
- 183 N. R. Filipović, S. Bjelogrić, A. Marinković, T. Ž. Verbić, I. N. Cvijetić, M. Senčanski, M. Rodić, M. Vujčić, D. Sladić, Z. Striković, T. R. Todorović and C. D. Muller, *RSC Adv.*, 2015, **5**, 95191–95211.
- 184 T. Pilati and A. Forni, *J. Appl. Crystallogr.*, 1998, **31**, 503–504.

- 185 T. Pilati and A. Forni, *J. Appl. Crystallogr.*, 2000, **33**, 417–417.
- 186 H. Zabrodsky, S. Peleg and D. Avnir, *J. Am. Chem. Soc.*, 1993, **115**, 8278–8289.
- 187 M. Alagesan, N. S. P. Bhuvanesh and N. Dharmaraj, *Dalt. Trans.*, 2013, **42**, 7210.
- 188 V. M. Leovac, V. I. Češljević, L. S. Vojinović-Ješić, V. Divjaković, L. S. Jovanović, K. M. Szécsényi and M. V. Rodić, *Polyhedron*, 2009, **28**, 3570–3576.
- 189 M. V. Rodić, V. M. Leovac, L. S. Jovanović, V. Spasojević, M. D. Joksović, T. Stanojković, I. Z. Matić, L. S. Vojinović-Ješić and V. Marković, *Eur. J. Med. Chem.*, 2016, **115**, 75–81.
- 190 M.-H. Shih, Y.-S. Su and C.-L. Wu, *Chem. Pharm. Bull. (Tokyo)*, 2007, **55**, 1126–1135.
- 191 C. Kleeberg and M. Bröring, *Polyhedron*, 2010, **29**, 507–513.
- 192 E. Ruiz, X. Tang, Y.-J. Li and M. M. Muir, *J. Crystallogr. Spectrosc. Res.*, 1993, **23**, 791–794.
- 193 B.-B. Xu, P. Shi, Q.-Y. Guan, X. Shi and G.-L. Zhao, *J. Coord. Chem.*, 2013, **66**, 2605–2614.
- 194 R. S. Nicholson, *Anal. Chem.*, 1965, **37**, 1351–1355.
- 195 L. Bjelica and L. Jovanović, *J. Electroanal. Chem. Interfacial Electrochem.*, 1986, **213**, 85–110.
- 196 C. R. Kowol, E. Reisner, I. Chiorescu, V. B. Arion, M. Galanski, D. V. Deubel and B. K. Keppler, *Inorg. Chem.*, 2008, **47**, 11032–11047.
- 197 D. Tomco, F. R. Xavier, M. M. Allard and C. N. Verani, *Inorganica Chim. Acta*, 2012, **393**, 269–275.
- 198 M. van der Meer, Y. Rechkemmer, U. Frank, F. D. Breitgoff, S. Hohloch, C.-Y. Su, P. Neugebauer, R. Marx, M. Dörfel, J. van Slageren and B. Sarkar, *Chem. - A Eur. J.*, 2016, **22**, 13884–13893.
- 199 I. Yilmaz, H. Temel and H. Alp, *Polyhedron*, 2008, **27**, 125–132.
- 200 T. Murai, K. Yamaguchi, F. Hori and T. Maruyama, *J. Org. Chem.*, 2014, **79**, 4930–4939.
- 201 N. Günay, E. Tarcan, D. Avcı, H. Cömert, K. Esmer and Y. Atalay, *Concepts Magn. Reson. Part A*, 2009, **34A**, 297–304.
- 202 H. Tavakol, *Struct. Chem.*, 2011, **22**, 1165–1177.
- 203 H. Hirao, *J. Phys. Chem. A*, 2011, **115**, 9308–9313.
- 204 S. E. H. Etaiw, D. M. Abd El-Aziz, E. H. Abd El-Zaher and E. A. Ali, *Spectrochim. Acta Part A Mol. Biomol. Spectrosc.*, 2011, **79**, 1331–1337.
- 205 H. N. Ly, D. J. R. Brook and O. Oliverio, *Inorganica Chim. Acta*, 2011, **378**, 115–120.
- 206 S. Mukherjee, S. Chowdhury, A. P. Chattopadhyay and H. Stoeckli-Evans, *Polyhedron*, 2010, **29**, 1182–1188.
- 207 D. Sek, M. Siwy, K. Bijak, M. Grucela-Zajac, G. Malecki, K. Smolarek, L. Bujak, S. Mackowski and E. Schab-Balcerzak, *J. Phys. Chem. A*, 2013, **117**, 10320–10332.
- 208 L. A. Berben and J. R. Long, *Inorg. Chem.*, 2005, **44**, 8459–8468.
- 209 P. F. Rapheal, E. Manoj, M. R. P. Kurup and E. Suresh, *Polyhedron*, 2007, **26**, 607–616.
- 210 G. Zhang and C. B. Musgrave, *J. Phys. Chem. A*, 2007, **111**, 1554–1561.
- 211 E. Mukwevho, Z. Ferreira and A. Ayeleso, *Molecules*, 2014, **19**, 19376–19389.
- 212 M. Iwaoka and K. Arai, *Curr. Chem. Biol.*, 2013, **7**, 2–24.

- 213 R. L. Prior, X. Wu and K. Schaich, *J. Agric. Food Chem.*, 2005, **53**, 4290–4302.
- 214 L. Kelland, *Nat. Rev. Cancer*, 2007, **7**, 573–584.
- 215 P. Y. Muller and M. N. Milton, *Nat. Rev. Drug Discov.*, 2012, **11**, 751–761.
- 216 D. R. Grimes, C. Kelly, K. Bloch and M. Partridge, *J. R. Soc. Interface*, 2014, **11**, 20131124–20131124.
- 217 R.-Z. Lin and H.-Y. Chang, *Biotechnol. J.*, 2008, **3**, 1172–1184.
- 218 S. Griffin, G. Dunn, S. Palmer, K. Macfarlane, S. Brent, A. Dyker, S. Erhorn, C. Humphries, S. White, W. Horsley, L. Ferrie and S. Thomas, *Health Technol. Assess. (Rockv)*, 2009, **13**.
- 219 B. S. Yadav, *World J. Clin. Oncol.*, 2014, **5**, 125.
- 220 E. Bulka, H.-G. Patzwaladt, F.-K. Peper and H. Beyer, *Chem. Ber.*, 1961, **94**, 1127–1137.
- 221 C. R. Groom, I. J. Bruno, M. P. Lightfoot and S. C. Ward, *Acta Crystallogr. Sect. B Struct. Sci. Cryst. Eng. Mater.*, 2016, **72**, 171–179.
- 222 D. S. Silvester, A. J. Wain, L. Aldous, C. Hardacre and R. G. Compton, *J. Electroanal. Chem.*, 2006, **596**, 131–140.
- 223 A. J. Fry and R. G. Reed, *J. Am. Chem. Soc.*, 1969, **91**, 6448–6451.
- 224 C. Reichardt, *Solvents and Solvent Effects in Organic Chemistry*, Wiley-VCH Verlag GmbH & Co. KGaA, Weinheim, FRG, 2002.
- 225 M. P. Rančić, I. Stojiljković, M. Milošević, N. Prlainović, M. Jovanović, M. K. Milčić and A. D. Marinković, *Arab. J. Chem.*, 2016.
- 226 R. G. Parr and W. Yang, *J. Am. Chem. Soc.*, 1984, **106**, 4049–4050.
- 227 W. Yang, R. G. Parr and R. Pucci, *J. Chem. Phys.*, 1984, **81**, 2862–2863.
- 228 S. Carradori and R. Silvestri, *J. Med. Chem.*, 2015, **58**, 6717–6732.

7 APPENDIX

Table 7.1 Solvent parameters used in Kamlet–Taft equation^{172,173}.

Solvent	π^*	α	β
Methanol	0.6	0.66	0.98
Ethanol	0.54	0.75	0.86
2-Propanol	0.48	0.84	0.76
2-Butanol	0.4	0.8	0.69
Cyclohexanol	0.45	0.84	0.66
Benzyl alcohol	0.98	0.52	0.6
2-Methoxyethanol	0.71	0	0
2-Chloroethanol	0.46	0.53	1.28
1,2-dimethoxyethane (DME)	0.53	0.41	0
Toluene	0.54	0.11	0
Dichloromethane (DCM)	0.82	0.1	0.13
Acetone	0.71	0.43	0.08
Cyclohexanone (ChO)	0.76	0.53	0
Ethyl acetate (EtAc)	0.55	0.45	0
Formamide (F)	0.97	0.48	0.71
Dimethylformamide (DMF)	0.88	0.69	0
Dimethylacetamide (DMAc)	0.88	0.76	0
1-Methyl-2-pyrrolidinone (NMP)	0.92	0.77	0
Acetonitrile (AcN)	0.75	0.4	0.19
DMSO	1	0.76	0
THF	0.58	0.55	0
2-Pyrrolidone (2-Pyr)	0.85	0.77	0.36

Table 7.2 Solvent parameters ²²used in Catalán equation^a

Solvent	SP	SdP	SA	SB
Ethanol	0.633	0.783	0.4	0.658
Methanol	0.608	0.904	0.605	0.545
1-Propanol	0.658	0.748	0.367	0.782
2-Propanol	0.633	0.808	0.283	0.83
1-Butanol	0.674	0.655	0.341	0.809
Isobutanol	0.657	0.684	0.311	0.828
2-Metoxyethanol	0.6996	0.8952	0.36	0.56
2-Chloroethanol	0.7704	0.9736	0.56	0.38
Diethyl ether	0.617	0.385	0	0.562
Diisopropyl ether	0.625	0.324	0	0.657
Cyclohexane	0.683	0	0	0.073
Heptane	0.635	0	0	0.083
Pentane	0.593	0	0	0.073
Dioxane	0.737	0.312	0	0.444
Acetonitrile	0.645	0.974	0.044	0.286
<i>N,N</i> -Dimethylformamide	0.759	0.977	0.031	0.613
Dimethyl sulfoxide	0.83	1	0.072	0.647
Formamide	0.814	1.006	0.549	0.414

^a Catalán parameters for *trans*-1,2-dichloroethene are not available

Table 7.3 Selected dihedral angles (°) for complexes.

	1-S	2-S	1-Se	2-Se	3-Se
$\angle(\Omega_1A \ \Omega_1B)$	89.28(5)	85.26(13)	89.33(8)	85.24(7)	88.28(7)
$\angle(\Omega_1A \ \Omega_2A)$	6.72(16)	5.7(5)	5.5(2)	2.6(2)	10.1(2)
$\angle(\Omega_1B \ \Omega_2B)$	5.16(14)	–	6.6(3)	15.0(2)	10.40(18)
$\angle(\Omega_2A \ \Omega_3A)$	88.62(10)	86.5(3)	81.99(14)	84.70(14)	78.75(10)
$\angle(\Omega_2B \ \Omega_3B)$	82.86(9)	–	87.62(14)	61.01(16)	73.43(11)
$\angle(\Omega_1A \ \Omega_3B)$	4.45(18)	10.5(4)	10.60(19)	10.7(2)	12.83(19)
$\angle(\Omega_1B \ \Omega_3A)$	9.90(13)	–	4.7(3)	2.9(3)	3.18(19)

Ω_1A and Ω_1B are chelate planes A and B defined as mean planes through atoms Co1 N1A N2A N4A, and Co1 N1B N2B N4B, respectively.

Ω_2A and Ω_2B are (selen/thi)azole planes A and B defined mean planes through atoms N4A C7A S1A/Se1A C8A C9A, and N4B C7B S1B/Se1B C8B C9B, respectively.

Ω_3A and Ω_3B are planes through terminal phenyl rings A and B defined mean planes through atoms C10A > C15A, and C10B > C15B, respectively.

Table 7.4 Elements of DFT optimized geometries of *E*- and *Z*-isomers of ligands compared with available crystal structure data.

Compound, X=S	HLS ^{1*}	HLS ^{2*}	HLS ^{3*}	HLS ^{1*}	HLS ^{2*}	HLS ^{3*}
	<i>E</i> -isomer			<i>Z</i> -isomer		
Bond (Å)						
N ₄ -C ₇	1.289	1.289	1.298 (1.300) ^a	1.299	1.300	1.299 (1.265) ^b
N ₄ -C ₉	1.389	1.390	1.389 (1.388) ^a	1.388	1.388	1.388 (1.373) ^b
X ₁ -C ₇	1.759	1.758	1.758 (1.738) ^a	1.762	1.761	1.762 (1.700) ^b
X ₁ -C ₈	1.746	1.747	1.746 (1.723) ^a	1.744	1.746	1.745 (1.690) ^b
C ₁ -C ₆	1.465	1.465	1.465 (1.465) ^a	1.462	1.462	1.462 (1.414) ^b
C ₆ -N ₂	1.287	1.288	1.288 (1.277) ^a	1.298	1.298	1.298 (1.260) ^b
N ₂ -N ₃	1.344	1.343	1.344 (1.360) ^a	1.337	1.336	1.337 (1.337) ^b
N ₃ -H	1.019	1.019	1.019 (0.872) ^a	1.026	1.026	1.026 (0.860) ^b
Angle (°)						
C ₇ -N ₄ -C ₉	110.77	110.85	110.80 (109.98) ^a	110.84	110.84	110.84 (109.82) ^b
C ₇ -X ₁ -C ₈	87.33	87.35	87.37 (87.87) ^a	87.35	87.35	87.35 (87.76) ^b
Torsion (°)						
X ₁ -C ₈ -C ₉ -C ₁₀	179.90	180.00	180.00 (178.83) ^a	179.89	179.93	179.89 (178.21) ^b
N ₄ -C ₉ -C ₁₀ -C ₁₁	2.07	2.82	-0.74 (-12.51) ^a	5.98	5.59	4.86 (4.46) ^b
X ₁ -C ₇ -N ₃ -N ₂	-0.13	-0.10	-0.07 (-0.85) ^a	0.21	0.29	0.04 (4.69) ^b
N ₁ -C ₁ -C ₆ -N ₂	179.98	179.88	179.98 (-175.82) ^a	-0.33	-0.21	-0.30 (3.75) ^b
C ₁ -C ₆ -N ₂ -N ₃	179.94	179.96	179.90 (179.93) ^a	0.13	0.05	0.21 (-0.25) ^b

Table 7.5 Continued

Compound, X=Se	HLSe ^{1*}	HLSe ^{2*}	HLSe ^{3*}	HLSe ^{1*}	HLSe ^{2*}	HLSe ^{3*}
	<i>E</i> -isomer			<i>Z</i> -isomer		
Bond (Å)						
N ₄ -C ₇	1.293	1.293	1.292	1.293	1.294	1.294
N ₄ -C ₉	1.391	1.392	1.392	1.390	1.390	1.390
X ₁₁ -C ₇	1.890	1.888	1.890	1.893	1.893	1.892
X ₁₁ -C ₈	1.876	1.877	1.877	1.875	1.875	1.875
C ₁ -C ₆	1.465	1.465	1.465	1.462	1.462	1.462
C ₆ -N ₂	1.287	1.287	1.287	1.298	1.298	1.298
N ₂ -N ₃	1.344	1.343	1.343	1.337	1.336	1.337
N ₃ -H	1.019	1.019	1.019	1.027	1.026	1.026
Angle (°)						
C ₇ -N ₄ -C ₉	112.75	112.78	112.78	112.88	112.95	112.84
C ₇ -X ₁ -C ₈	83.19	83.20	83.16	83.20	83.22	83.23
Torsion (°)						
X ₁ -C ₈ -C ₉ -C ₁₀	-179.99	-179.90	-179.94	179.90	179.96	179.86
N ₄ -C ₉ -C ₁₀ -C ₁₁	-1.02	5.15	0.24	6.78	6.37	6.25
X ₁ -C ₇ -N ₃ -N ₂	-0.01	0.00	-0.08	0.17	0.15	0.18
N ₁ -C ₁ -C ₆ -N ₂	-179.88	-180.00	179.94	-0.20	-0.23	-0.25
C ₁ -C ₆ -N ₂ -N ₃	-179.98	-179.99	179.98	0.09	0.14	0.14

* Optimized geometries obtained by the use of DFT calculations with the B3LYP/6-31G(d) basis set

^a Crystal structure data obtained from X-ray diffraction analysis in the present work

^b Crystal structure data taken from literature^{S35}

Table 7.6 Comparison of average values of the theoretically calculated Co–N bond lengths (in Å) and N–Co–N angles (in °) obtained for the complex 1-S, using two DFT functionals with several basis sets and experimental measured values.

functionals / basis sets	Co– N ₁	Co– N ₂	Co– N ₄	N–Co–N	
				<i>trans</i>	<i>cis</i>
b3lyp / 6-31g(d,p) ^a / 6-31g(d) ^a	1.966	1.899	1.976	167.83	90.38
b3lyp / 6-31g(2d,2p) ^b / 6-31g(d,p) ^b / 6-31g(d) ^b	1.966	1.899	1.977	167.83	90.38
b3lyp/ LanL2DZ-epc ^c / 6-31g(d) ^c	1.977	1.909	1.992	167.83	90.38
bvp86 / 6-31g(d,p) ^d / 6-31g(d) ^d	1.944	1.888	1.958	168.02	90.37
bvp86 / LanL2DZ-epc ^e / 6-31g(d) ^e	1.960	1.902	1.981	168.08	90.37
bvp86 / cc-pVTZ ^f / 6-31g(d) ^f	1.958	1.900	1.973	167.67	90.39
measured ^g	1.947	1.887	1.946	167.17	90.41

^a B3LYP functional with 6-31g(d,p) on Co and 6-31g(d) on all others atoms

^b B3LYP functional with 6-31g(2d,2p) on Co, 6-31g(d,p) on N atoms and 6-31g(d) on all others atoms

^c B3LYP functional with LanL2DZ-epc on Co and 6-31g(d) on all others atoms

^d BVP86 functional with 6-31g(d,p) on Co and 6-31g(d) on all others atoms

^e BVP86 functional with LanL2DZ-epc on Co and 6-31g(d) on all others atoms

^f BVP86 functional with cc-pVTZ on Co and 6-31g(d) on all others atoms

^g Experimental Co-N bond lengths

Table 7.7 Comparison of average values of the experimental and theoretical calculated Co–N bond lengths (in Å) and N–Co–N angles (in °) obtained for the (1–3)-Se and (1–3)-S complexes

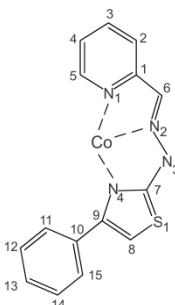
Compound		1-Se [*]	2-Se [*]	3-Se [*]
Bond (Å)				
Co–N ₁		1.946 (1.949) ^a	1.945 (1.953) ^a	1.947 (1.948) ^a
Co–N ₂		1.884 (1.883) ^a	1.884 (1.888) ^a	1.886 (1.888) ^a
Co–N ₄		1.973 (1.955) ^a	1.971 (1.957) ^a	1.960 (1.950) ^a
Angle (°)				
N–Co–N	<i>trans</i>	168.10 (166.97) ^a	168.13 (166.58) ^a	167.75 (167.05) ^a
	<i>cis</i>	90.40 (90.42) ^a	90.35 (90.42) ^a	90.37 (90.42) ^a

Compound		1-S [*]	2-S [*]	3-S [*]
Bond (Å)				
Co–N ₁		1.944 (1.944) ^a	1.944 (1.948) ^a	1.944 (1.946) ^b
Co–N ₂		1.888 (1.887) ^a	1.887 (1.886) ^a	1.889 (1.888) ^a
Co–N ₄		1.958 (1.946) ^a	1.967 (1.948) ^a	1.956 (1.943) ^a
Angle (°)				
N–Co–N	<i>trans</i>	168.02 (167.17) ^a	168.27 (-) ^a	167.89 (167.33) ^a
	<i>cis</i>	90.37 (90.41) ^a	90.39 (-) ^a	90.37 (90.41) ^a

^{*} Optimized geometries obtained by the use of DFT calculations with the B3LYP/6-31G(d) basis set

^a Crystal structure data obtained from X-ray diffraction analysis in the present work.

Table 7.8 Average values of experimental and calculated chemical shifts (δ in ppm), coupling constants (J in Hz) and assignments of the signals in ^1H and ^{13}C NMR spectra of (1–3)-Se and (1–3)-S complexes

1-S	^1H			^{13}C				
	Exp.	Calc.	Calc. ^{scaled}	Exp.	Calc.	Calc. ^{scaled}		
	H-C ₈	6.56 (s, 1H)	6.12	6.60	C ₈	108.12	114.46	106.39
	H- C _{11,15}	6.77 (d, 2H, $^3J = 6.9$)	7.14	6.81	C ₂	123.28	118.82	121.24
	H-C ₁₃	7.29 (ddd, 1H, $^3J = 7.3$, $^3J = 6.1$, $^3J = 1.3$)	7.76	7.31	C ₄	126.06	120.78	123.97
	H- C _{12,14}	7.42 (t, 2H, $^3J = 7.7$)	7.63	7.44	C _{11,15}	127.73	126.13	125.61
	H-C ₅	7.53 (d, 1H, $^3J = 5.6$)	8.18	7.54	C _{12,14}	128.78	123.11	126.63
	H-C ₄	7.60 (t, 1H, $^3J = 7.5$)	7.16	7.61	C ₁₀	129.54	127.68	127.38
	H-C ₂	7.66 (d, 1H, $^3J = 7.4$)	7.55	7.67	C ₁₃	131.63	125.18	129.43
	H-C ₆	7.82 (s, 1H)	8.15	7.83	C ₆	139.47	134.94	137.11
	H-C ₃	7.96 (td, 1H, $^3J = 7.8$, $^3J = 1.2$)	7.87	7.96	C ₃	141.27	136.65	138.87
					C ₉	147.89	147.56	145.36
					C ₅	149.19	146.47	146.64
					C ₁	159.81	154.59	157.04
					C ₇	180.47	179.14	177.29

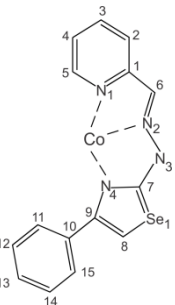
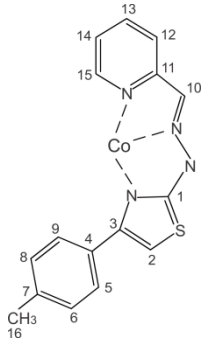
1-Se	^1H			^{13}C				
	Exp.	Calc.	Calc. ^{scaled}	Exp.	Calc.	Calc. ^{scaled}		
	H-C ₈	6.75 (s, 1H)	6.33	6.79	C ₈	110.90	118.78	109.11
	H- C _{11,15}	6.75 (d, 2H, $^3J = 6.4$)	7.27	6.79	C ₂	123.68	119.27	121.64
	H-C ₁₃	7.29 (ddd, 1H, $^3J = 7.4$, $^3J = 5.9$, $^3J = 1.4$)	7.75	7.31	C ₄	125.99	120.80	123.90
	H- C _{12,14}	7.40 (t, 2H, $^3J = 7.8$)	7.65	7.42	C _{11,15}	127.66	125.69	125.54
	H-C ₅	7.49 (d, 1H, $^3J = 5.3$)	8.07	7.51	C _{12,14}	128.89	123.46	126.74
	H-C ₄	7.58 (ddd, 1H, $^3J = 7.5$, $^3J = 6.4$, $^3J = 1.2$)	7.08	7.59	C ₁₀	129.30	129.71	127.14
	H-C ₂	7.68 (dd, 1H, $^3J = 8.0$, $^3J = 0.8$)	7.33	7.69	C ₁₃	133.13	124.65	130.90
	H-C ₆	7.82 (s, 1H)	7.87	7.83	C ₆	139.52	134.13	137.16
	H-C ₃	7.95 (td, 1H, $^3J = 7.7$, $^3J = 1.3$)	7.76	7.95	C ₃	141.26	136.29	138.86
					C ₉	148.22	148.26	145.69
					C ₅	149.33	146.17	146.77
					C ₁	159.94	154.17	157.17
					C ₇	183.60	186.75	180.36

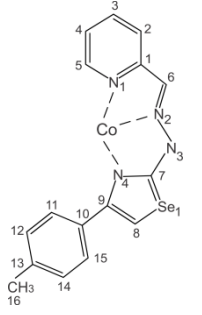
Table 7.7 Continued

2-S	¹ H			¹³ C			
	Exp.	Calc.	Calc. ^{scaled}	Exp.	Calc.	Calc. ^{scaled}	
H-C ₁₆	3.23 (s, 3H)	4.11	-	C ₁₆	55.55	55.05	-
H-C ₈	6.47 (s, 1H)	6.15	6.52	C ₈	108.06	113.97	106.33
H- C _{11,15}	6.65 (d, 2H, ³ J= 8.6)	7.16	6.69	C ₂	123.39	118.78	121.35
H- C _{12,14}	6.94 (d, 2H, ³ J=8.6)	6.94	6.97	C ₄	126.08	120.81	123.99
H-C ₄	7.27 (ddd, 1H, ³ J = 7.3, ³ J = 6.1, ³ J = 1.3)	7.08	7.29	C _{12,14}	113.29	109.28	111.45
H-C ₅	7.53 (d, 1H, ³ J= 5.6)	8.08	7.54	C _{11,15}	130.30	127.12	128.12
H-C ₂	7.65 (d, 1H, ³ J=7.9)	7.28	7.66	C ₁₀	124.01	120.45	121.96
H-C ₆	7.87 (s, 1H)	7.92	7.87	C ₁₃	160.42	154.37	157.64
H-C ₃	7.94 (td, 1H, ³ J = 7.8, ³ J = 1.2)	7.76	7.94	C ₆	139.33	133.99	136.97
				C ₃	141.39	136.34	138.99
				C ₉	147.98	148.03	145.45
				C ₅	149.29	145.89	146.73
				C ₁	160.06	154.09	157.29
				C ₇	180.45	179.63	177.27

2-Se	¹ H			¹³ C			
	Exp.	Calc.	Calc. ^{scaled}	Exp.	Calc.	Calc. ^{scaled}	
H-C ₁₆	3.89 (s, 3H),	4.13	-	C ₁₆	55.28	55.10	-
H-C ₈	6.69 (s, 1H)	6.27	6.73	C ₈	110.57	118.25	108.79
H- C _{11,15}	6.65 (d, 2H, ³ J= 8.4)	7.17	6.69	C ₂	123.49	119.12	121.45
H- C _{12,14}	6.93 (d, 2H, ³ J=8.6)	6.94	6.96	C ₄	125.77	120.66	123.68
H-C ₄	7.29 (ddd, 1H, ³ J = 7.2, ³ J = 6.1, ³ J = 0.9)	7.06	7.31	C _{12,14}	112.90	109.15	111.07
H-C ₅	7.50 (d, 1H, ³ J= 5.7)	8.07	7.52	C _{11,15}	130.08	127.41	127.91
H-C ₂	7.69 (d, 1H, ³ J=7.7)	7.32	7.70	C ₁₀	125.29	121.63	123.21
H-C ₆	7.90 (s, 1H)	7.90	7.90	C ₁₃	159.94	154.30	157.17
H-C ₃	7.95 (td, 1H, ³ J = 7.9, ³ J = 0.8)	7.76	7.95	C ₆	139.11	133.74	136.76
				C ₃	141.09	136.20	138.70
				C ₉	147.97	148.19	145.44
				C ₅	149.17	146.17	146.62
				C ₁	159.94	154.24	157.17
				C ₇	183.19	186.37	179.96

Table 7.7 Continued

3-S	¹ H			¹³ C				
	Exp.	Calc.	Calc. ^{scaled}	Exp.	Calc.	Calc. ^{scaled}		
	H-C ₁₆	2.46 (s, 3H)	2.67	-	C ₁₆	21.19	23.26	-
	H-C ₈	6.50 (s, 1H)	6.10	6.55	C ₈	107.98	113.93	106.25
	H-C _{11,15}	6.64 (d, 2H, ³ J= 8.0)	7.06	6.68	C ₂	123.22	118.83	121.19
	H-C _{12,14}	7.21 (d, 2H, ³ J=8.0)	7.45	7.23	C ₄	125.98	120.68	123.89
	H-C ₄	7.28 (ddd, 1H, ³ J = 7.4, ³ J = 5.7, ³ J = 1.4)	7.17	7.30	C _{12,14}	128.22	123.95	126.09
	H-C ₅	7.52 (d, 1H, ³ J = 5.4)	8.19	7.53	C _{11,15}	128.66	125.96	126.52
	H-C ₂	7.65 (dd, 1H, ³ J=8.0, ³ J = 0.8)	7.55	7.66	C ₁₀	128.84	124.95	126.69
	H-C ₆	7.82 (s, 1H)	8.19	7.83	C ₁₃	138.90	136.82	136.55
	H-C ₃	7.99 (td, 1H, J = 7.8, ³ J = 1.3)	7.86	7.99	C ₆	139.35	134.75	136.99
					C ₃	141.01	136.48	138.62
					C ₉	148.01	147.58	145.48
					C ₅	149.12	146.50	146.57
					C ₁	159.91	154.65	157.14
					C ₇	180.43	179.11	177.25

3-Se	¹ H			¹³ C				
	Exp.	Calc.	Calc. ^{scaled}	Exp.	Calc.	Calc. ^{scaled}		
	H-C ₁₆	2.46 (s, 3H)	2.68	-	C ₁₆	21.05	23.17	-
	H-C _{11,15}	6.62 (d, 2H, ³ J= 7.7)	7.05	6.66	C ₈	110.54	118.41	108.76
	H-C ₈	6.68 (s, 1H)	6.24	6.72	C ₂	123.42	118.82	121.38
	H-C _{12,14}	7.19 (d, 2H, ³ J=7.6)	7.44	7.21	C ₄	125.71	120.63	123.63
	H-C ₄	7.28 (ddd, 1H, ³ J = 7.4, ³ J = 5.9, ³ J = 1.4)	7.14	7.30	C _{12,14}	127.92	123.74	125.79
	H-C ₅	7.48 (d, 1H, ³ J = 5.5)	8.13	7.50	C _{11,15}	128.59	126.54	126.45
	H-C ₂	7.68 (dd, 1H, ³ J _{14,15} =7.9, ³ J = 0.6)	7.53	7.69	C ₁₀	130.16	126.11	127.99
	H-C ₆	7.83 (s, 1H)	8.08	7.84	C ₁₃	138.36	136.43	136.02
	H-C ₃	7.94 (td, 1H, ³ J = 7.8, ³ J = 1.3)	7.83	7.94	C ₆	139.19	134.51	136.84
					C ₃	141.05	136.38	138.66
					C ₉	148.12	147.51	145.59
					C ₅	149.07	146.51	146.52
					C ₁	159.85	154.56	157.08
					C ₇	183.31	185.69	180.07

Exp. - Experimental ¹H and ¹³C NMR chemical shifts. Calc. - Calculated ¹H and ¹³C NMR chemical shifts at PCM(DMSO)DFT/B3LYP/6-31G(d,p)/6-31G(d) level of theory with respect to TMS. Calculated chemical shifts of TMS at PCM(DMSO)DFT/B3LYP/6-31G(d) have values 190.11 ppm for ¹³C and 32.17 ppm for ¹H. Calc.scaled - the linearly scaled calculated values (Calc.) by applied the correlation between the experimental and the calculated (Calc.) chemical shifts. Linear Regression was applied at experimental and calculated chemical shifts of all C-*sp*² atoms and the best fit straight line corresponding to $\delta_{\text{calc.}} = 0.43 + 0.98\delta_{\text{exp.}}$ (R=0.98). Resulting linear regression line for all protons attached to C-*sp*² atoms has form $\delta_{\text{calc.}} = 0.24 + 0.97\delta_{\text{exp.}}$ (R=0.79).

Table 7.9 TD-DFT/B3LYP calculated electronic transitions (absorption maxima λ_{\max} in cm^{-1} and nm), oscillator strengths (f) and major MO contributors in percent of *E*-1,3-thiazoles and *E*-1,3-selenazoles in DMF solvent.

Compound	No.	λ_{\max}		f	MO major contributors					
					Transition	%	Transition	%	Transition	%
HLSe¹	1	26409	379	0.4185	HOMO→LUMO	98				
	2	33331	300	0.0336	H-1→LUMO	29	HOMO→L+1	67		
	3	34349	291	0.3009	H-1→LUMO	18	HOMO→L+1	10	HOMO→L+2	68
	4	34721	288	0.7809	H-1→LUMO	49	HOMO→L+1	20	HOMO→L+2	28
	5	35498	282	0.0012	HOMO→L+4	97				
	6	35791	279	0.0011	H-3→LUMO	96	H-3→L+1	2		
	7	37511	267	0.0180	H-2→LUMO	36	H-2→L+1	10	HOMO→L+3	48
	8	38554	259	0.0033	H-2→LUMO	61	HOMO→L+3	30	H-1→L+1	5
	9	40536	247	0.0010	H-4→LUMO	48	H-1→L+2	11	HOMO→L+5	21
	10	40855	245	0.0003	H-6→LUMO	93	H-6→L+1	4	H-6→L+5	2
	11	41080	243	0.1792	H-4→LUMO	14	H-1→L+1	74	HOMO→L+3	4
	12	41508	241	0.0124	H-5→LUMO	14	H-1→L+2	39	HOMO→L+5	20
	13	42081	238	0.0553	H-5→LUMO	76	HOMO→L+5	15	H-1→L+2	3
	14	42358	236	0.0031	H-3→L+2	98				
	15	42894	233	0.0078	H-2→L+1	45	H-1→L+3	16	HOMO→L+3	14

Compound	No.	λ_{\max}		f	MO major contributors					
					Transition	%	Transition	%	Transition	%
HLSe²	1	25265	396	0.2651	HOMO→LUMO	99				
	2	31939	313	0.7786	H-1→LUMO	97				
	3	33518	298	0.0635	HOMO→L+1	51	HOMO→L+2	45		
	4	33937	295	0.3403	HOMO→L+1	43	HOMO→L+2	50		
	5	34772	288	0.0012	HOMO→L+3	16	HOMO→L+4	80		
	6	35844	279	0.0011	H-4→LUMO	97	H-4→L+1	2		
	7	36815	272	0.0776	HOMO→L+3	65	HOMO→L+4	13		
	8	38740	258	0.0838	H-2→LUMO	87	H-3→LUMO	3	HOMO→L+3	5
	9	39271	255	0.1111	H-1→L+1	78	H-7→LUMO	3	HOMO→L+5	8
	10	39317	254	0.1567	H-3→LUMO	44	H-1→L+2	39	H-7→LUMO	5
	11	40076	250	0.0651	H-3→LUMO	31	H-1→L+2	37	HOMO→L+5	24
	12	40818	245	0.0042	H-6→LUMO	74	H-5→LUMO	14	HOMO→L+5	5
	13	40864	245	0.0173	H-6→LUMO	20	H-5→LUMO	55	HOMO→L+5	11
	14	42371	236	0.0047	H-4→L+1	18	H-4→L+2	79		
	15	42382	236	0.1043	H-5→LUMO	20	H-1→L+2	11	HOMO→L+5	36

Table 7.8 Continued

Compound	No.	λ_{\max}	f	MO major contributors						
				Transition	%	Transition	%	Transition	%	
HLSe³	1	26090	383	0.3747	HOMO→LUMO	99				
	2	33211	301	0.2759	H-1→LUMO	72	HOMO→L+1	25		
	3	34055	294	0.4179	H-1→LUMO	10	HOMO→L+1	41	HOMO→L+2	45
	4	34382	291	0.5260	H-1→LUMO	15	HOMO→L+1	31	HOMO→L+2	51
	5	35311	283	0.0002	HOMO→L+4	98				
	6	35855	279	0.0011	H-3→LUMO	96	H-3→L+1	2		
	7	37186	269	0.0184	H-2→LUMO	31	H-2→L+1	10	HOMO→L+3	54
	8	38227	262	0.0034	H-2→LUMO	67	HOMO→L+3	25	H-1→L+1	5
	9	40268	248	0.0031	H-4→LUMO	28	H-1→L+2	19	HOMO→L+5	17
	10	40620	246	0.2442	H-4→LUMO	20	H-1→L+1	65		
	11	40837	245	0.0001	H-6→LUMO	93	H-6→L+1	3	H-6→L+5	2
	12	41150	243	0.0228	H-5→LUMO	24	H-1→L+2	31	HOMO→L+5	25
	13	41374	242	0.0370	H-5→LUMO	67	H-4→LUMO	13		
	14	42404	236	0.0030	H-3→L+2	97				
	15	42714	234	0.0184	H-4→LUMO	14	H-2→L+1	33	H-1→L+3	15

Compound	No.	λ_{\max}	f	MO major contributors						
				Transition	%	Transition	%	Transition	%	
HLS¹	1	26929	371	0.5163	HOMO→LUMO	98				
	2	33732	296	0.0289	H-1→LUMO	28	HOMO→L+1	69		
	3	34672	288	0.1744	H-1→LUMO	12	HOMO→L+2	77	HOMO→L+1	6
	4	35120	285	0.7943	H-1→LUMO	57	HOMO→L+1	22	HOMO→L+2	18
	5	35771	280	0.0011	H-3→LUMO	97				
	6	37773	265	0.0125	H-2→LUMO	34	H-2→L+1	11	HOMO→L+3	50
	7	38737	258	0.0027	H-2→LUMO	64	HOMO→L+3	28	H-1→L+1	4
	8	39026	256	0.0000	HOMO→L+5	98				
	9	40905	244	0.0001	H-4→LUMO	52	H-1→L+2	14	HOMO→L+4	16
	10	41596	240	0.2430	H-1→L+1	82	H-4→LUMO	8	HOMO→L+3	3
	11	42015	238	0.0178	H-6→LUMO	15	H-1→L+2	36	HOMO→L+4	30
	12	42379	236	0.0030	H-3→L+2	97				
	13	42522	235	0.0000	H-5→LUMO	92	H-5→L+1	3	H-5→L+4	2
	14	42961	233	0.0088	H-2→L+1	44	H-1→L+3	19	HOMO→L+3	15
	15	43833	228	0.0010	H-8→LUMO	96				

Table 7.8 Continued

Compound	No.	λ_{\max}		f	MO major contributors						
					Transition	%	Transition	%	Transition	%	
HLS²	1	25753	388	0.3256	HOMO→LUMO	99					
	2	32179	311	0.7855	H-1→LUMO	97					
	3	33823	296	0.0235	HOMO→L+1	39	HOMO→L+2	56			
	4	34343	291	0.3198	HOMO→L+1	54	HOMO→L+2	38			
	5	35859	279	0.0011	H-4→LUMO	97	H-4→L+1	2			
	6	36989	270	0.0837	HOMO→L+3	77	H-2→LUMO	5	H-2→L+1	7	
	7	38315	261	0.0000	HOMO→L+5	97					
	8	39135	256	0.0100	H-2→LUMO	87	H-1→L+1	8	HOMO→L+3	3	
	9	39499	253	0.0018	H-3→LUMO	14	H-1→L+1	33	H-1→L+2	26	
	10	39653	252	0.3091	H-3→LUMO	19	H-1→L+1	43	H-1→L+2	24	
	11	40442	247	0.0881	H-3→LUMO	36	H-1→L+2	28	HOMO→L+4	31	
	12	42342	236	0.0030	H-4→L+1	19	H-4→L+2	78			
	13	42448	236	0.0637	H-3→LUMO	16	H-1→L+3	18	HOMO→L+4	33	
	14	42458	236	0.0016	H-6→LUMO	90	H-6→L+1	3	H-6→L+4	2	
	15	42935	233	0.0362	H-2→L+1	10	H-1→L+3	49	HOMO→L+4	20	

Compound	No.	λ_{\max}		f	MO major contributors						
					Transition	%	Transition	%	Transition	%	
HLS³	1	26561	376	0.4682	HOMO→LUMO	99					
	2	33538	298	0.3203	H-1→LUMO	77	HOMO→L+1	19			
	3	34393	291	0.2010	HOMO→L+1	30	HOMO→L+2	62	H-1→LUMO	4	
	4	34726	288	0.5796	H-1→LUMO	17	HOMO→L+1	48	HOMO→L+2	33	
	5	35769	280	0.0011	H-3→LUMO	97					
	6	37426	267	0.0134	H-2→LUMO	29	H-2→L+1	11	HOMO→L+3	55	
	7	38369	261	0.0026	H-2→LUMO	69	HOMO→L+3	24	H-1→L+1	4	
	8	38808	258	0.0000	HOMO→L+5	98					
	9	40505	247	0.0046	H-4→LUMO	46	H-1→L+2	20	HOMO→L+4	13	
	10	40985	244	0.3004	H-1→L+1	81	H-4→LUMO	9	HOMO→L+3	3	
	11	41533	241	0.0206	H-7→LUMO	10	H-1→L+2	42	HOMO→L+4	28	
	12	42352	236	0.0030	H-3→L+2	94	H-5→LUMO	3			
	13	42443	236	0.0001	H-5→LUMO	91	H-5→L+1	3	H-3→L+2	3	
	14	42771	234	0.0057	H-2→L+1	38	H-1→L+3	21	HOMO→L+3	15	
	15	43559	230	0.1024	H-4→LUMO	17	H-1→L+2	12	HOMO→L+4	48	

Table 7.10 TD-DFT/B3LYP calculated electronic transitions (absorption maxima λ_{\max} in cm^{-1} and nm), oscillator strengths (f) and major MO contributors in percent of Co(III) complexes with *E*-1,3-thiazoles and *E*-1,3-selenazoles in DMF solvent.

Compound	No.	λ_{\max}		f	MO major contributors					
					Transition		%	Transition		%
1-Se	1	15129	661	0.0012	H-1→L+2	54	H-8→L+2	9	H-1→LUMO	9
	2	17165	583	0.0042	H-1→L+1	29	HOMO→LUMO	63		
	3	17406	575	0.0033	H-1→LUMO	36	HOMO→L+1	58		
	4	18368	544	0.0076	H-1→L+1	16	HOMO→L+2	81		
	5	19593	510	0.2780	H-1→L+1	50	HOMO→LUMO	34		
	6	19719	507	0.3441	H-1→LUMO	52	HOMO→L+1	40		
	7	20551	487	0.0152	H-1→L+3	87	H-1→L+1	2		
	8	20775	481	0.0042	HOMO→L+3	90	H-15→L+3	2		
	9	23134	432	0.0116	H-11→L+2	19	H-8→L+2	17	H-1→L+2	36
	10	24167	414	0.0147	H-17→L+2	13	H-16→L+3	24	H-15→L+2	13
	11	24431	409	0.0033	H-17→L+3	13	H-16→L+2	23	H-15→L+3	13
	12	27569	363	0.0377	H-2→L+1	13	HOMO→L+4	70	H-1→L+5	8
	13	27607	362	0.0012	H-2→LUMO	69	H-5→L+1	2	HOMO→L+5	9
	14	27801	360	0.0078	H-3→LUMO	14	H-2→L+1	63	HOMO→L+4	16
	15	27822	359	0.0000	H-1→L+4	65	HOMO→L+5	23	H-2→LUMO	7

Compound	No.	λ_{\max}		f	MO major contributors					
					Transition		%	Transition		%
2-Se	1	15192	658	0.0012	H-8→L+2	10	H-1→L+2	49	H-1→LUMO	8
	2	17029	587	0.0016	H-1→L+1	29	HOMO→LUMO	54	HOMO→L+1	10
	3	17222	581	0.0016	H-1→LUMO	44	HOMO→L+1	47		
	4	18390	544	0.0163	H-1→L+1	14	HOMO→L+2	76	H-1→L+2	5
	5	19354	517	0.2784	H-1→L+1	25	HOMO→LUMO	42	HOMO→L+1	15
	6	19494	513	0.3184	H-1→LUMO	39	H-1→L+1	26	HOMO→L+1	26
	7	20516	487	0.0071	H-1→L+3	78	H-3→L+3	4	HOMO→L+3	9
	8	20855	479	0.0035	HOMO→L+3	80	H-2→L+3	2	H-1→L+3	9
	9	22782	439	0.0093	H-11→L+2	13	H-8→L+2	13	H-1→L+2	34
	10	22972	435	0.0047	H-3→L+1	17	H-2→LUMO	79		
	11	23142	432	0.0034	H-3→LUMO	19	H-2→L+1	66	H-1→L+2	4
	12	24019	416	0.0066	H-17→L+2	16	H-6→L+2	10	H-2→L+2	17
	13	24166	414	0.0027	H-17→L+3	10	H-3→LUMO	33	H-2→L+1	12
	14	24533	408	0.0237	H-3→L+1	80	H-2→LUMO	15		
	15	27437	364	0.0329	HOMO→L+4	79	H-1→L+5	8	HOMO→L+5	7

Table 7.9 Continued

Compound	No.	λ_{\max}		f	MO major contributors					
					Transition	%	Transition	%	Transition	%
3-Se	1	15535	644	0.0001	H-8→L+2	13	H-1→L+2	61	H-11→L+2	8
	2	17372	576	0.0137	H-1→L+1	27	HOMO→LUMO	71		
	3				H-	36		62		
		17473	572	0.0071	1→LUMO		HOMO→L+1			
	4				HOMO→L	93				
		18155	551	0.0056	+2					
	5	19736	507	0.2654	H-1→L+1	65	HOMO→LUMO	22		
	6				H-	58		33		
		19871	503	0.3286	1→LUMO		HOMO→L+1			
	7				HOMO→L	83		5		4
		20726	482	0.0460	+3		H-1→L+1		HOMO→LUMO	
	8	20900	478	0.0051	H-1→L+3	89	H-8→L+3	2	H-7→L+3	2
	9	23723	422	0.0029	H-11→L+2	19	H-8→L+2	23	H-1→L+2	32
	10	24390	410	0.0101	H-17→L+3	26	H-16→L+2	16	H-15→L+2	10
	11	24717	405	0.0059	H-17→L+2	24	H-16→L+3	14	H-15→L+3	9
12	26871	372	0.0016	H-3→L+1	10	H-2→LUMO	57			
13				H-	51		24			
	26971	371	0.0032	3→LUMO		H-3→L+1				
14				HOMO→L	93		4			
	27564	363	0.0569	+4		H-1→L+5				
15	27825	359	0.0056	H-2→L+1	23	H-2→LUMO	20	HOMO→L+5	33	

Compound	No.	λ_{\max}		f	MO major contributors					
					Transition	%	Transition	%	Transition	%
1-S	1	15644	639	0.0002	H-9→L+2	24	H-1→L+2	61		
	2	17660	566	0.0179	H-1→L+1	23	HOMO→LUMO	75		
	3	17811	561	0.0088	H-1→LUMO	34	HOMO→L+1	64		
	4	18235	548	0.0044	HOMO→L+2	91	H-1→LUMO	5		
	5	20016	500	0.1941	H-1→L+1	58	HOMO→LUMO	14	HOMO→L+3	21
	6	20213	495	0.3084	H-1→LUMO	54	HOMO→L+1	32	HOMO→L+2	5
	7	20715	483	0.1014	H-1→L+1	16	HOMO→L+3	69	HOMO→LUMO	9
	8	20867	479	0.0238	H-1→L+3	85	H-9→L+3	4	H-1→LUMO	4
	9	23965	417	0.0031	H-9→L+2	32	H-1→L+2	27	H-11→L+2	8
	10	24481	408	0.0092	H-17→L+3	28	H-16→L+2	15	H-11→L+3	10
	11	24874	402	0.0062	H-17→L+2	21	H-16→L+3	13	H-1→L+2	11
	12	27871	359	0.0605	HOMO→L+4	94	H-1→L+5	3		
	13	28166	355	0.0173	H-1→L+4	14	HOMO→L+5	84		
	14	28593	350	0.0025	H-3→L+1	13	H-2→LUMO	76	H-5→L+1	3
	15	28715	348	0.0044	H-3→LUMO	38	H-2→L+1	53	H-5→LUMO	5

Table 7.9 Continued

Compound	No.	λ_{\max}		f	MO major contributors							
					Transition		%	Transition		%	Transition	
2-S	1	15329	652	0.0013	H-9→L+2	20	H-1→L+2	51	H-1→LUMO	8		
	2	17397	575	0.0020	H-1→L+1	31	HOMO→LUMO	60	HOMO→L+2	5		
	3	17606	568	0.0010	H-1→LUMO	42	HOMO→L+1	49	H-1→L+1	5		
	4	18623	537	0.0123	H-1→L+1	15	HOMO→L+2	79				
	5	19728	507	0.2592	H-1→L+1	41	HOMO→LUMO	36	HOMO→L+2	9		
	6	19841	504	0.3235	H-1→LUMO	48	HOMO→L+1	40	H-1→L+1	4		
	7	20408	490	0.0209	H-1→L+3	80	H-9→L+3	4	H-3→L+3	4		
	8	20771	481	0.0052	HOMO→L+3	86	H-2→L+3	2	H-1→L+3	3		
	9	23057	434	0.0126	H-9→L+2	24	H-1→L+2	35	H-23→L+2	8		
	10	23266	430	0.0034	H-3→L+1	16	H-2→LUMO	80				
	11	23464	426	0.0028	H-3→LUMO	19	H-2→L+1	69	H-1→L+2	3		
	12	24185	413	0.0082	H-17→L+2	17	H-16→L+3	11	H-2→L+2	16		
	13	24341	411	0.0004	H-17→L+3	17	H-3→LUMO	16	H-16→L+2	8		
	14	24861	402	0.0256	H-3→LUMO	57	H-2→L+1	15	H-17→L+3	5		
	15	27750	360	0.0392	HOMO→L+4	78	H-1→L+S	14				

Compound	No.	λ_{\max}		f	MO major contributors							
					Transition		%	Transition		%	Transition	
3-S	1	15659	639	0.0002	H-9→L+2	25	H-1→L+2	61	H-23→L+2	4		
	2	17619	568	0.0174	H-1→L+1	24	HOMO→LUMO	75				
	3	17762	563	0.0089	H-1→LUMO	34	HOMO→L+1	65				
	4	18228	549	0.0046	HOMO→L+2	91	H-1→LUMO	5				
	5	19970	501	0.1954	H-1→L+1	58	HOMO→LUMO	14	HOMO→L+3	21		
	6	20167	496	0.3106	H-1→LUMO	55	HOMO→L+1	32	HOMO→L+2	5		
	7	20651	484	0.0995	H-1→L+1	15	HOMO→L+3	70	HOMO→LUMO	9		
	8	20825	480	0.0193	H-1→L+3	86	H-9→L+3	5	H-1→LUMO	4		
	9	23940	418	0.0027	H-9→L+2	33	H-1→L+2	29	H-11→L+2	8		
	10	24441	409	0.0091	H-17→L+3	28	H-16→L+2	15	H-11→L+3	10		
	11	24794	403	0.0063	H-17→L+2	22	H-16→L+3	13	H-1→L+2	10		
	12	26996	370	0.0005	H-3→L+1	26	H-2→LUMO	66	H-2→L+1	6		
	13	27041	370	0.0020	H-3→LUMO	56	H-2→L+1	38	H-3→L+1	3		
	14	27790	360	0.0527	HOMO→L+4	89	H-2→L+1	5	H-1→L+5	3		
	15	27973	357	0.0066	H-3→L+1	27	H-2→LUMO	16	HOMO→L+5	45		

Table 7.11 Selected highest values of the condensed Fukui functions (f^+ and f^-) for the ligands, considering DFT / DMF / NBO charges according to equations (1 and 2).

Comp. / atom		N ₁	N ₂	N ₃	N ₄	C ₆	C ₈	Se
HLSe¹	f^+	0.063	0.127	0.004	0.046	0.121	0.053	0.084
	f^-	0.023	-0.006	0.100	0.050	0.082	0.123	0.173
HLSe²	f^+	0.064	0.130	0.005	0.047	0.122	0.049	0.081
	f^-	0.018	-0.008	0.069	0.032	0.063	0.127	0.160
HLSe³	f^+	0.064	0.129	0.004	0.047	0.121	0.050	0.082
	f^-	0.085	0.122	0.094	0.090	0.197	0.176	0.253
Comp. / atom		N ₁	N ₂	N ₃	N ₄	C ₆	C ₈	S
HLS¹	f^+	0.064	0.132	0.005	0.047	0.121	0.049	0.073
	f^-	0.025	-0.003	0.106	0.057	0.086	0.139	0.129
HLS²	f^+	0.065	0.134	0.006	0.048	0.122	0.046	0.071
	f^-	0.018	-0.007	0.073	0.036	0.066	0.141	0.120
HLS³	f^+	0.064	0.134	0.006	0.047	0.122	0.047	0.072
	f^-	0.023	-0.004	0.095	0.050	0.080	0.142	0.127

Table 7.12 Calculated absorption maxima (λ^* , nm), oscillator strengths (f) and composition of bands of benzyldene-based (1,3-selenazol-2-yl)hydrazones in DMSO, EtOH and THF obtained by the use of TD/DFT method.

	DMSO			EtOH			THF		
	λ^* (nm)	oscillator strengths (f)	composition of bands	λ^* (nm)	oscillator strengths (f)	composition of bands	λ^* (nm)	oscillator strengths (f)	composition of bands
1	368	0.4753		365	0.4926		369	0.4648	
	287	1.0829	H→L	286	1.0665	H→L	287	1.0928	H→L
	246	0.1120	98%	246	0.1107	98%	246	0.1152	98%
1- OMe	382	0.3162		381	0.3113		390	0.4233	
	309,	0.6381,	H→L	308,	0.6410,	H→L	313,	0.8012,	H→L
	299	0.5974	99%	298	0.5750	99%	304	0.6322	98%
	250	0.1942		250	0.1881		250	0.1876	
1- Me	371	0.4300		372	0.4198		373	0.4191	
	291	1.2247	H→L	292	1.2107	H→L	292	1.2176	H→L
	248	0.1392	98%	248	0.1409	98%	248	0.1475	98%
2	520	0.2038		519	0.2002		519	0.2075	
	364	0.3700	H→L	364	0.3665	H→L	365	0.3707	H→L
	284	0.2790	70%	284	0.2775	70%	287	0.2376	70%
2- OMe	553	0.1469		553	0.1442		554	0.1494	
	382	0.1993	H→L	382	0.1980	H→L	385	0.1960	H→L
	296	0.4174	70%	295	0.4018	70%	295	0.3927	70%
2- Me	530	0.1887		529	0.1852		530	0.1916	
	370	0.3142	H→L	370	0.3128	H→L	372	0.3174	H→L
	290	0.6482	70%	290	0.6138	70%	291	0.5776	70%
3	513	0.3883		511	0.3792		509	0.3796	
	366	0.4766	H→L	365	0.4754	H→L	364	0.4891	H→L
	267	0.3237	71%	266	0.3126	71%	275	0.2553	71%
3- OMe	552	0.2536		550	0.2462		549	0.2438	
	401	0.5407	H→L	400	0.5390	H→L	398	0.5541	H→L
	292	0.3270	71%	292	0.2975	71%	286	0.5542	71%
				286	0.3100				
3- Me	525	0.3474		523	0.3388		521	0.3379	
	377	0.5043	H→L	376	0.5034	H→L	375	0.5179	H→L
	271	0.4224	71%	271	0.4111	71%	280	0.3840	71%
4	/	0.0149		/	0.0148		/	0.0169	
	514	0.4162	H→L	513	0.4039	H→L	509	0.4076	H→L
	378	0.7088	70%	378	0.5929	70%	380	0.8191	70%
	285			290	0.6876		290		
4- OMe	/	0.0112		/	0.0111		/	0.0125	
	544	0.2828	H→L	543	0.2720	H→L	541	0.2282	H→L
	394	0.8309	70%	394	0.8229	70%	396	0.8519	70%
	313			312	0.4535		314	0.4394	
4- Me	/	0.0139		/	0.0138		/	0.0157	
	523	0.3096	H→L	523	0.2997	H→L	520	0.3296	H→L
	384	0.7168	70%	384	0.6712	70%	386	0.6580	70%
	294			293			293		

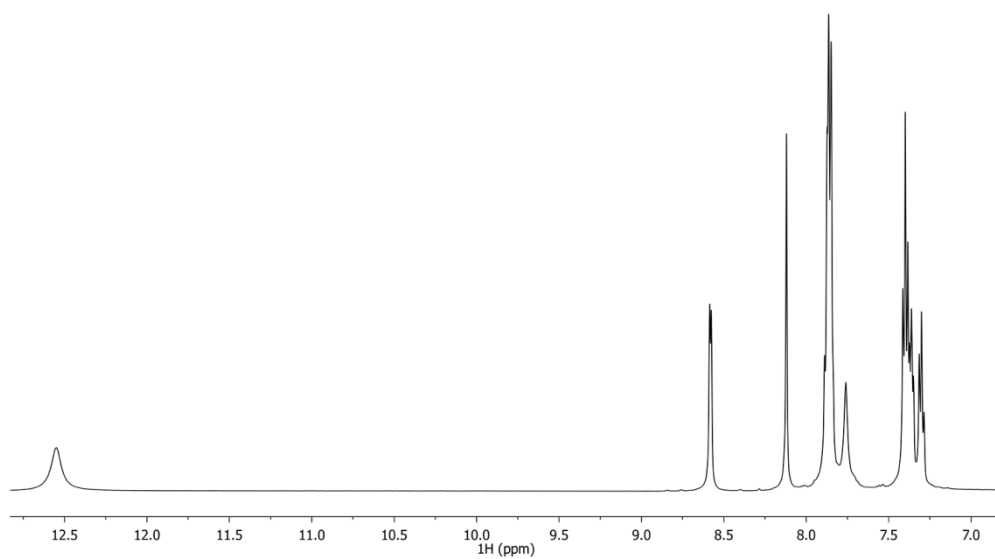


Figure 7.1 ^1H NMR spectrum of HLSe1 in $\text{DMSO-}d_6$

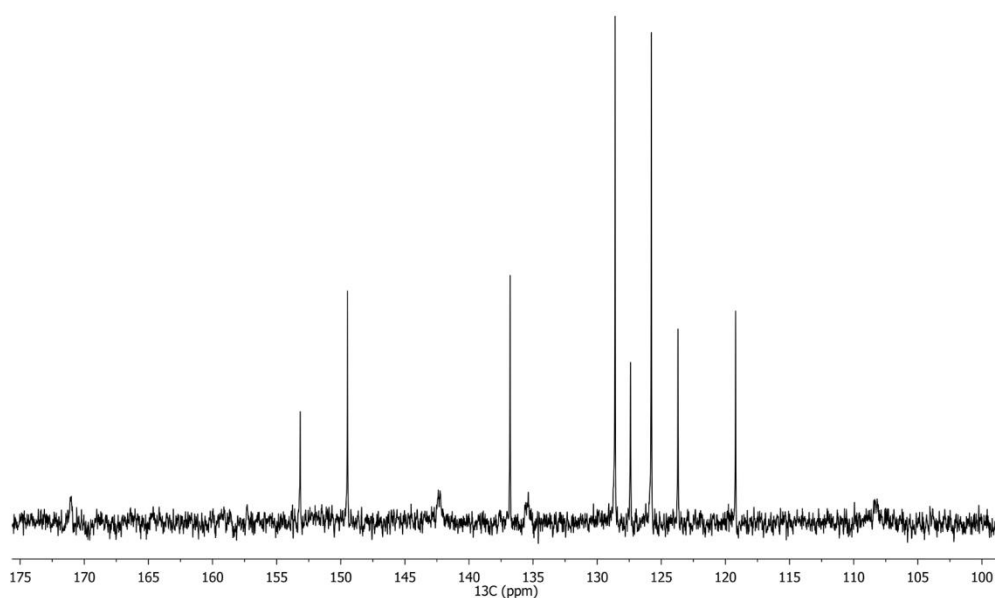


Figure 7.2 ^{13}C NMR spectrum of HLSe1 in $\text{DMSO-}d_6$

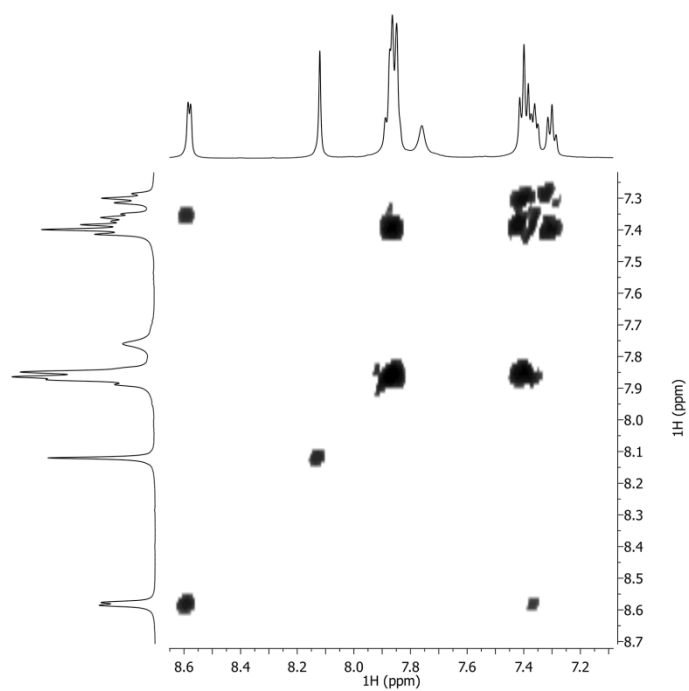


Figure 7.3 2D COSY spectrum of HLSe¹ in DMSO-*d*₆

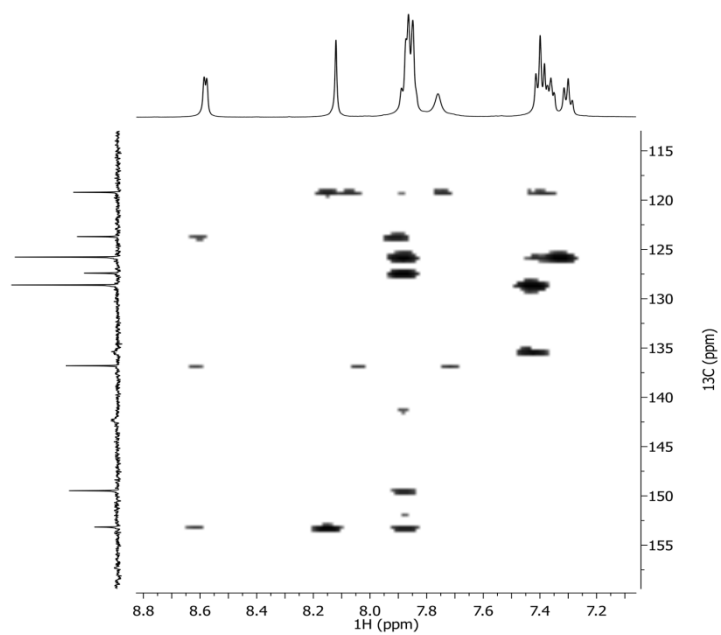


Figure 7.4 2D HMBC spectrum of HLSe¹ in DMSO-*d*₆

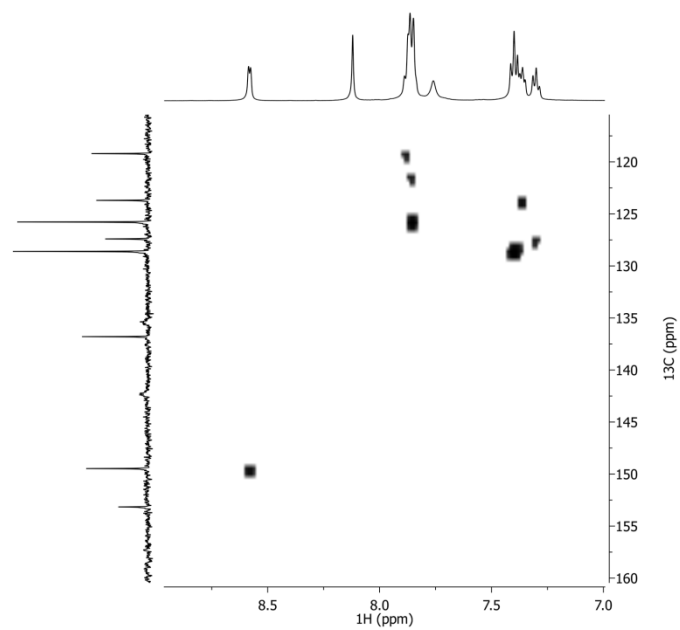


Figure 7.5 2D HSQC spectrum of HLSe¹ in DMSO-*d*₆

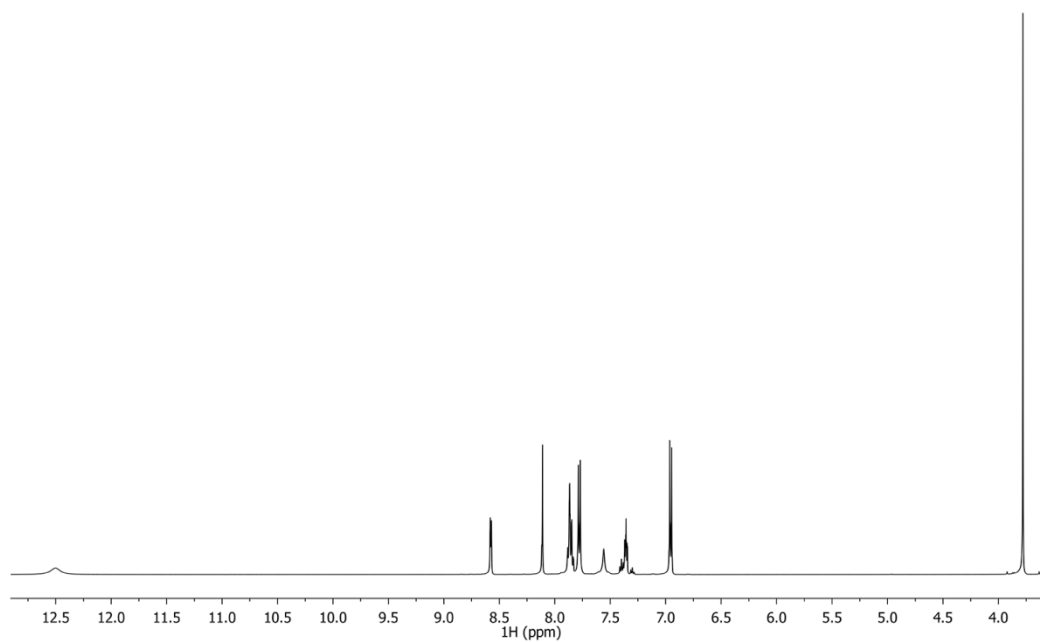


Figure 7.6 ¹H NMR spectrum of HLSe² in DMSO-*d*₆

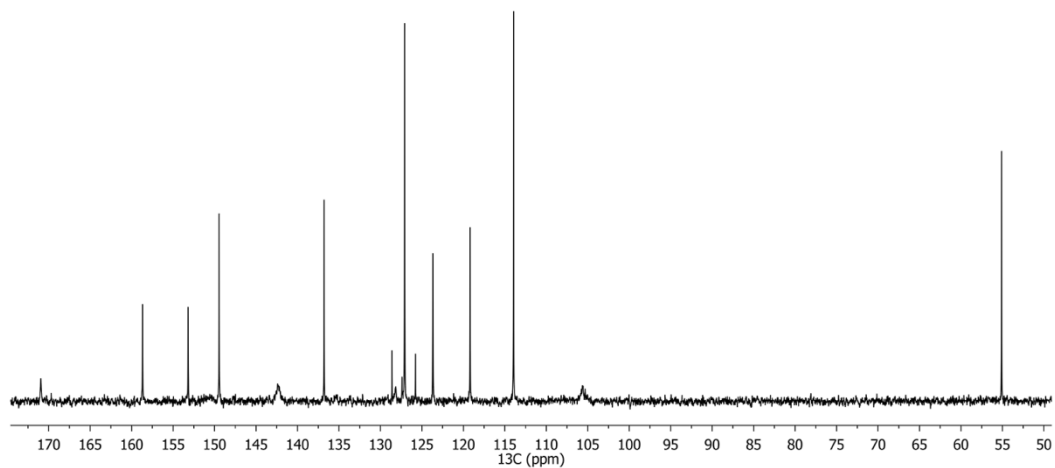


Figure 7.7 ^{13}C NMR spectrum of HLSe^2 in $\text{DMSO-}d_6$

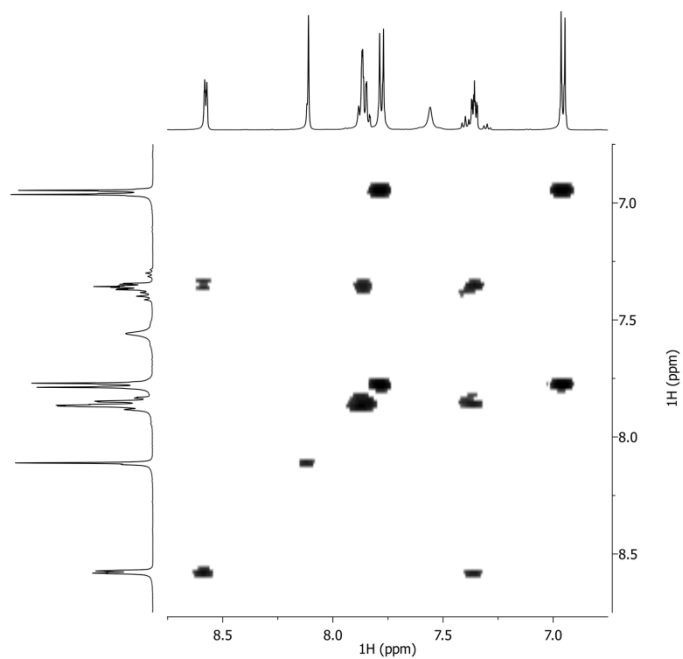


Figure 7.8 2D COSY spectrum of HLSe^2 in $\text{DMSO-}d_6$

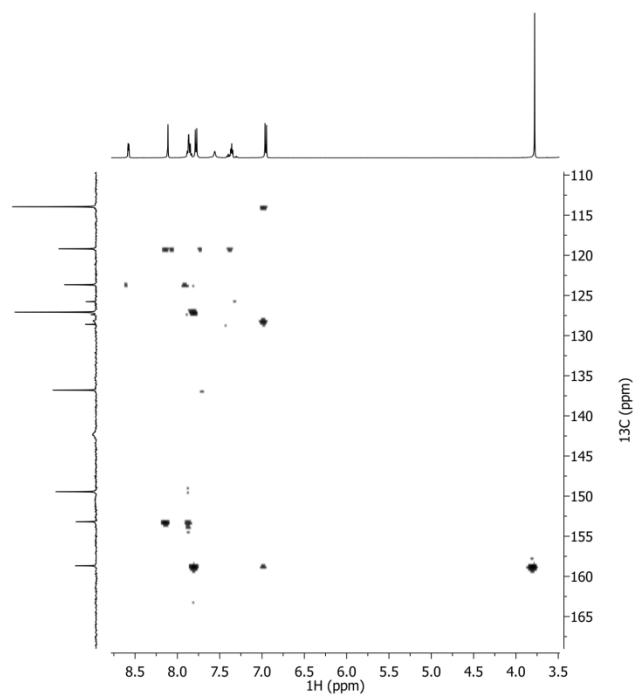


Figure 7.9 2D HMBC spectrum of HLSe^2 in $\text{DMSO-}d_6$

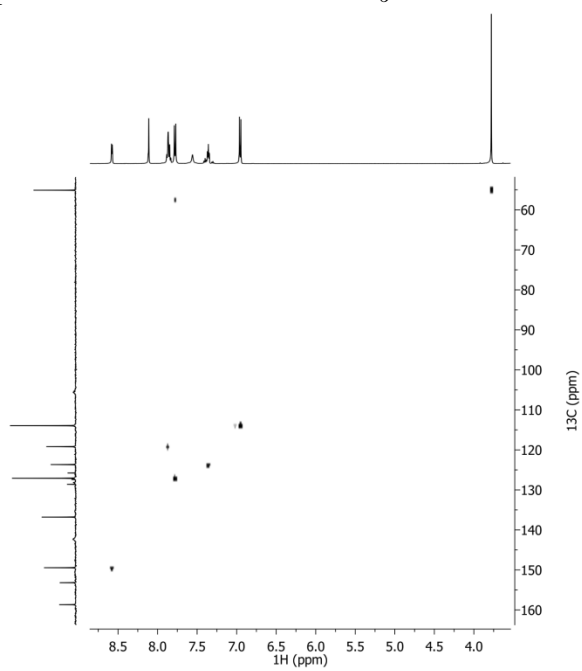


Figure 7.10 2D HSQC spectrum of HLSe^2 in $\text{DMSO-}d_6$

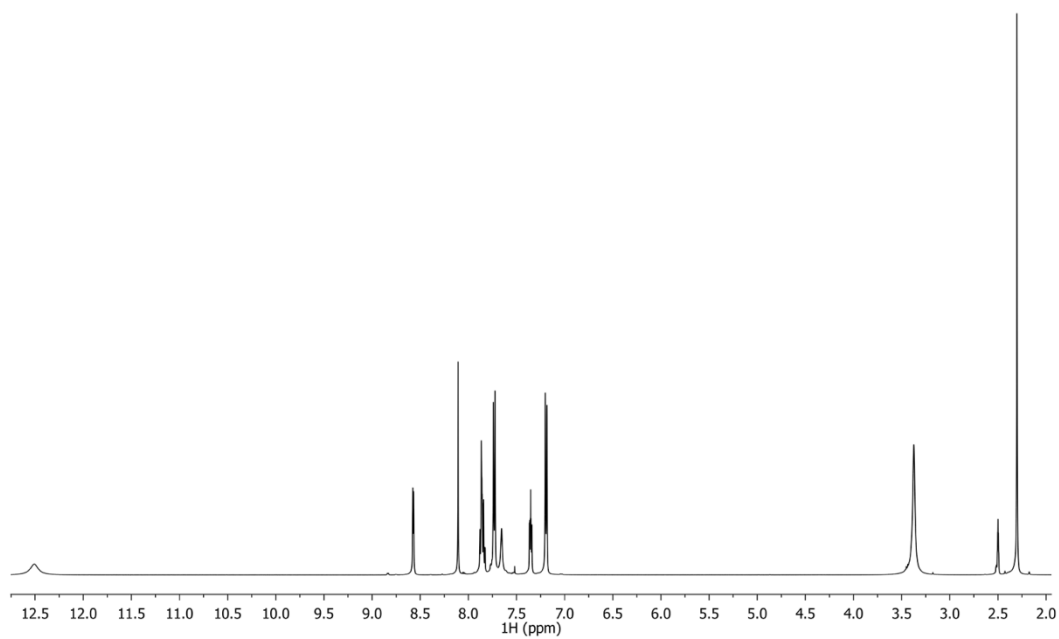


Figure 7.11 ^1H NMR spectrum of HLSe^3 in $\text{DMSO-}d_6$

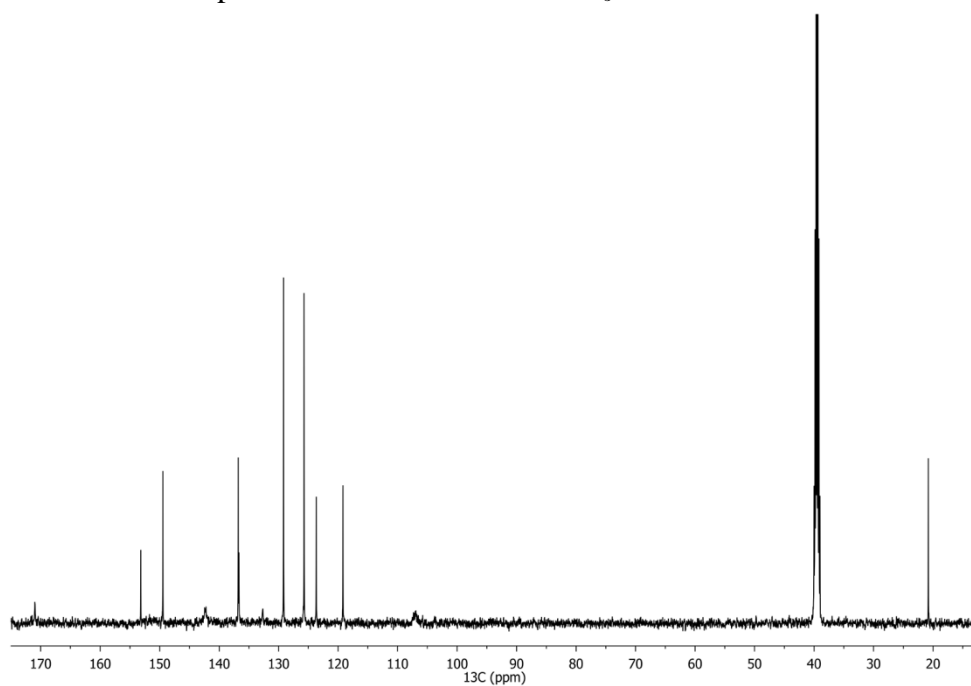


Figure 7.12 ^{13}C NMR spectrum of HLSe^3 in $\text{DMSO-}d_6$

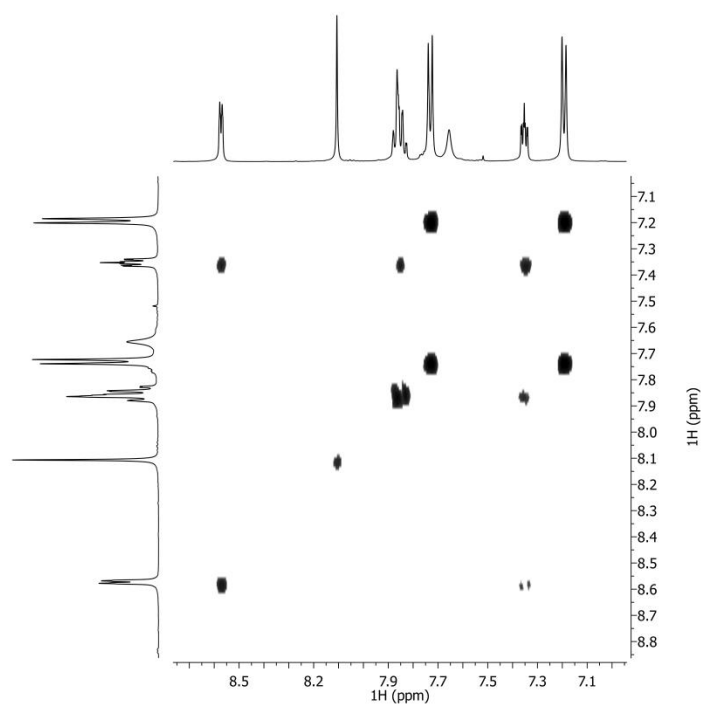


Figure 7.13 2D COSY spectrum of HLSe³ in DMSO-*d*₆

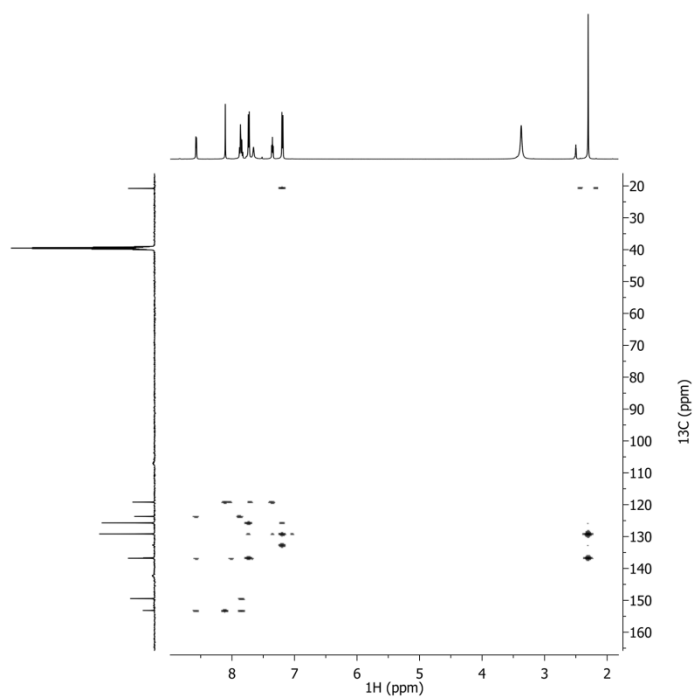


Figure 7.14 2D HMBC spectrum of HLSe³ in DMSO-*d*₆

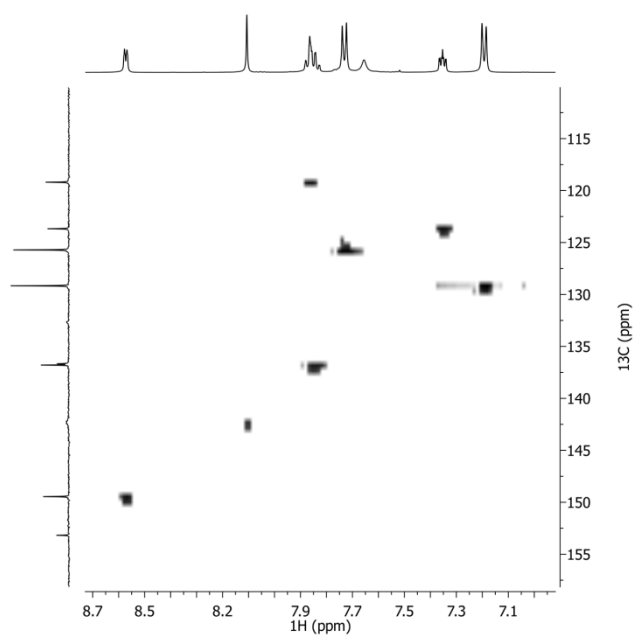


Figure 7.15 2D HSQC spectrum of HLSe³ in DMSO-*d*₆

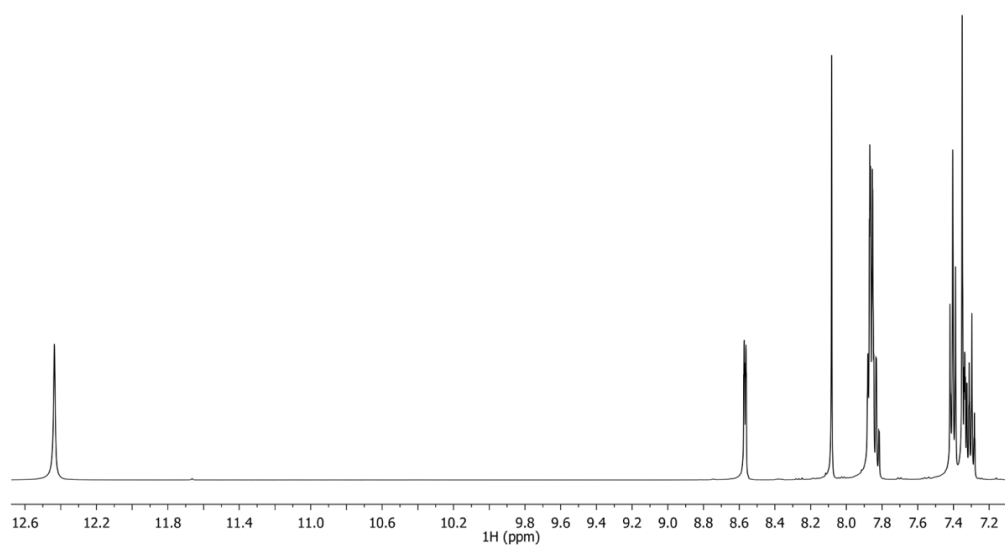


Figure 7.16 ¹H NMR spectrum of HLS¹ in DMSO-*d*₆

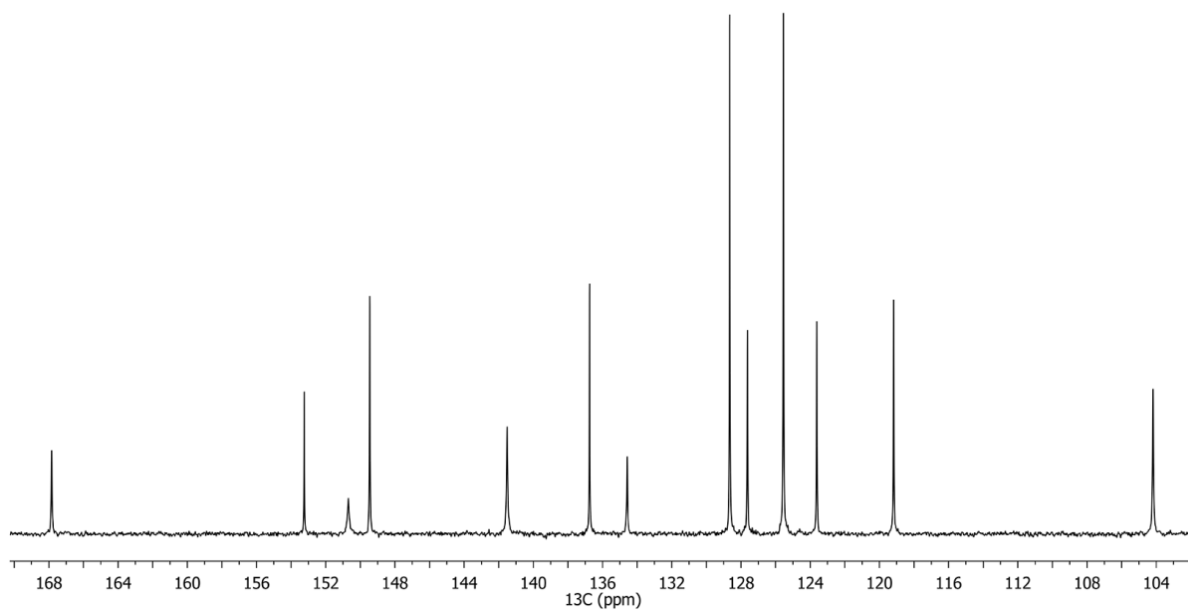


Figure 7.17 ^{13}C NMR spectrum of HLS¹ in DMSO-*d*₆

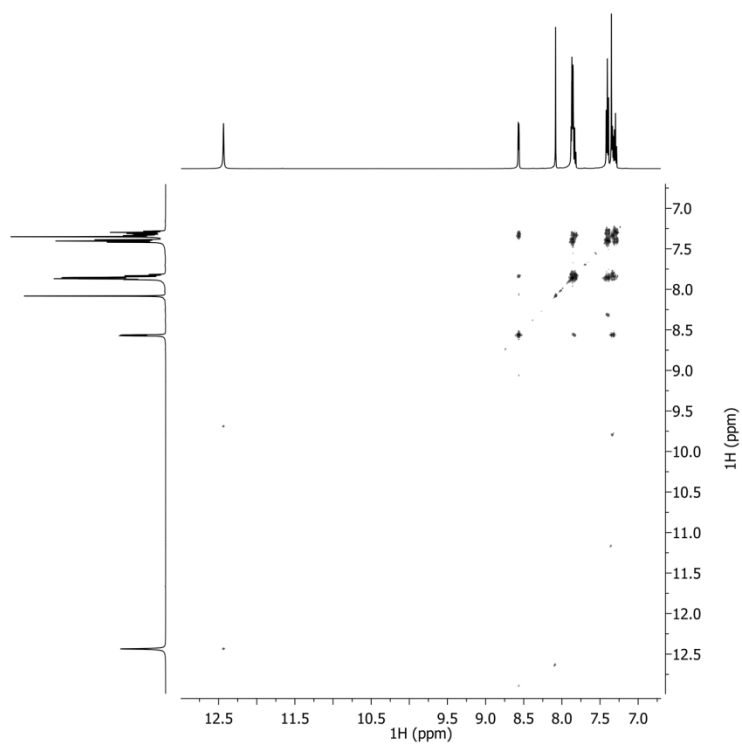


Figure 7.18 2D COSY spectrum of HLS¹ in DMSO-*d*₆

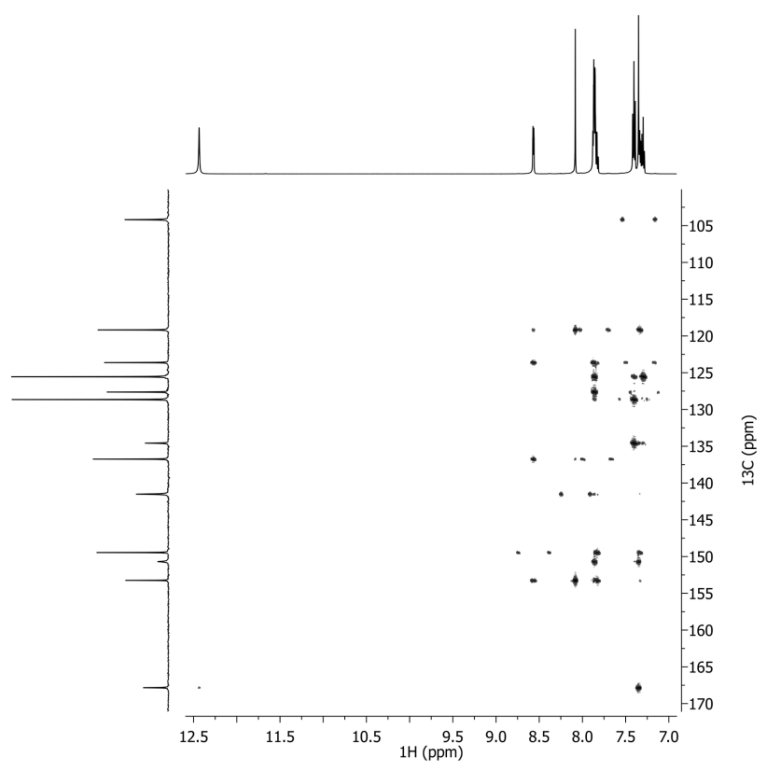


Figure 7.19 2D HMBC spectrum of HLS¹ in DMSO-*d*₆

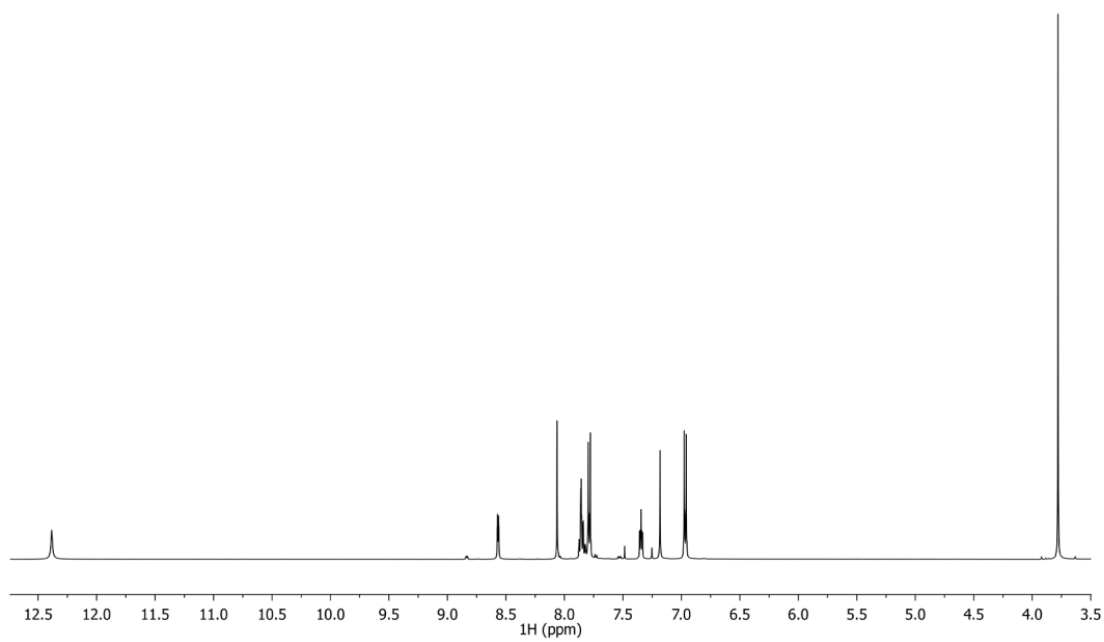


Figure 7.20 ^1H NMR spectrum of HLS² in DMSO-*d*₆

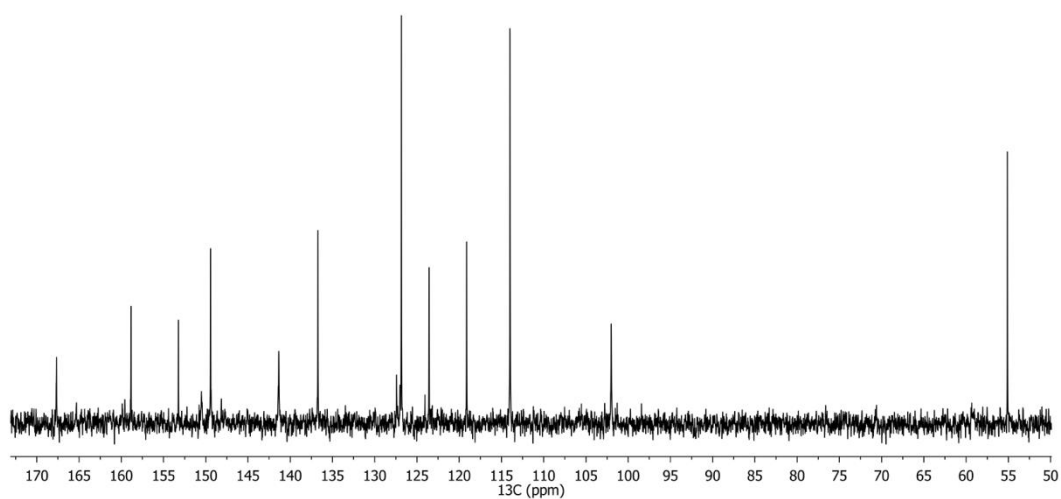


Figure 7.21 ^{13}C NMR spectrum of HLS^2 in $\text{DMSO-}d_6$

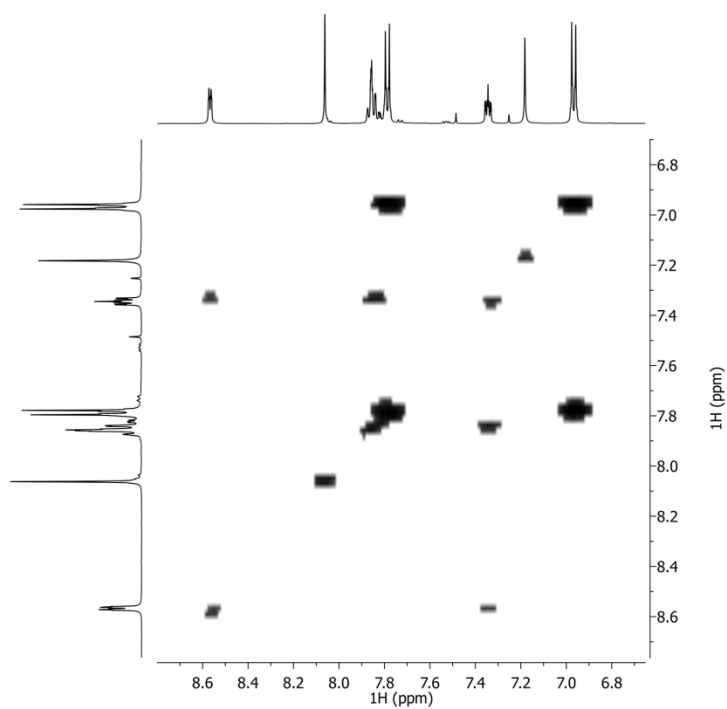


Figure 7.22 2D COSY spectrum of HLS^2 in $\text{DMSO-}d_6$

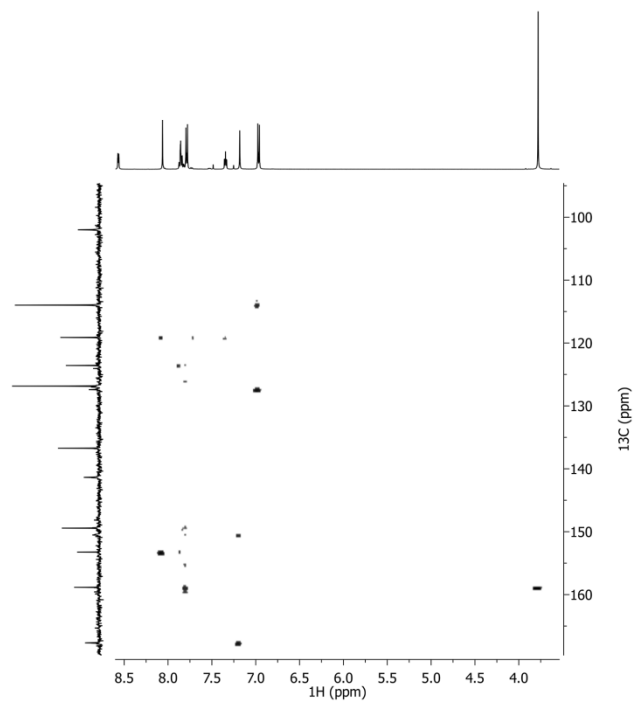


Figure 7.23 2D HMBC spectrum of HLS^2 in $\text{DMSO-}d_6$

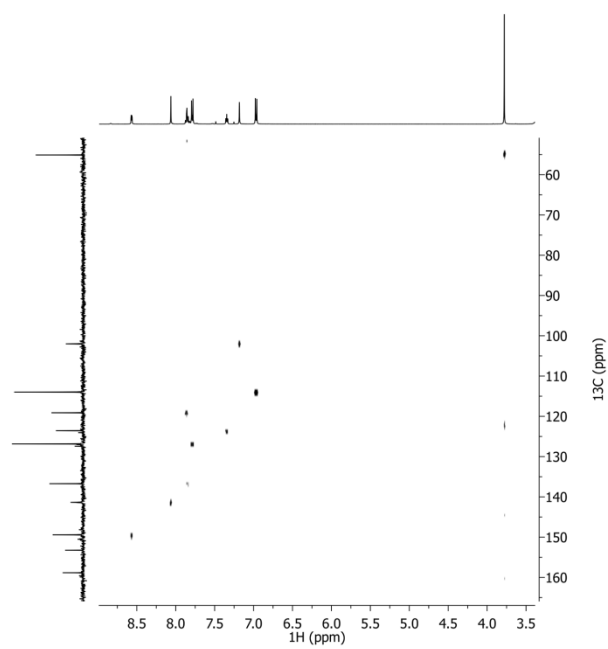


Figure 7.24 2D HSQC spectrum of HLS^2 in $\text{DMSO-}d_6$

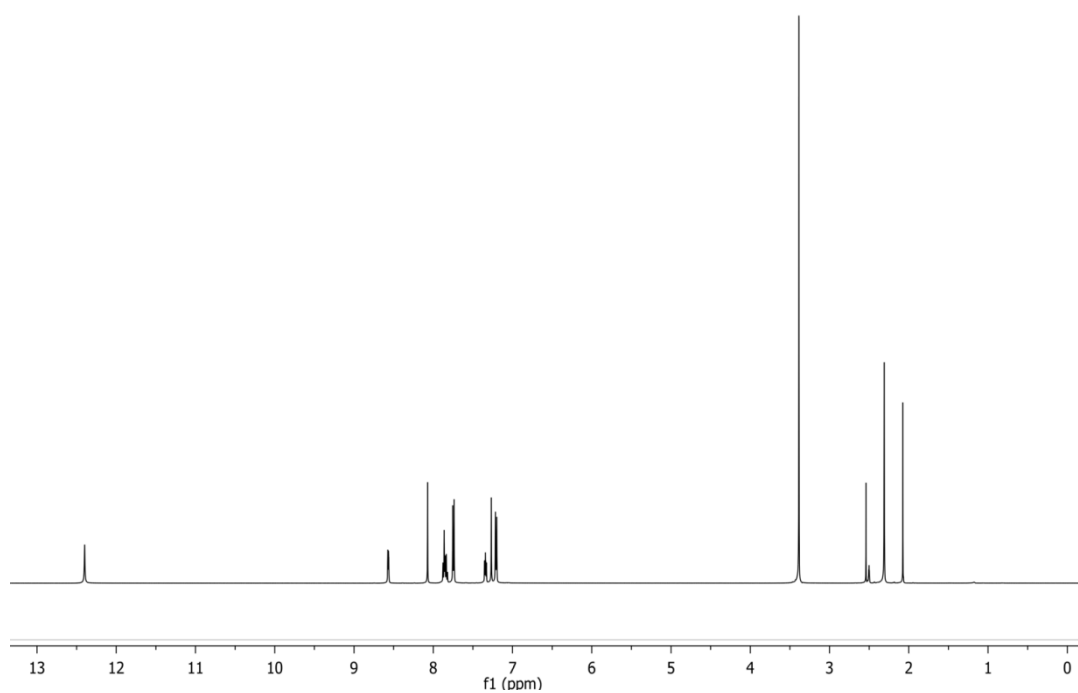


Figure 7.25 ^1H NMR spectrum of HLS^3 in $\text{DMSO-}d_6$

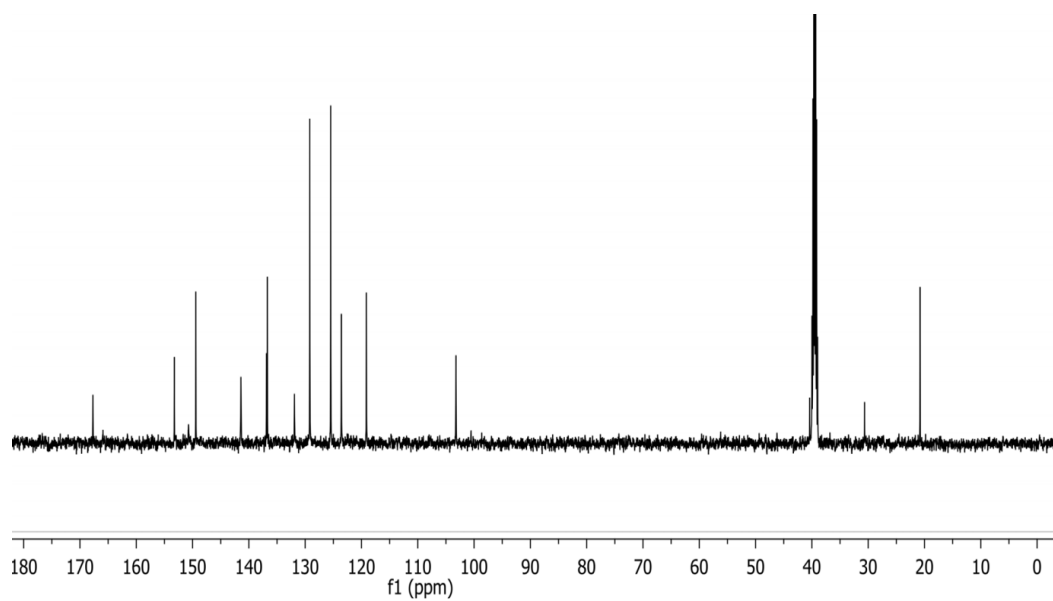


Figure 7.26 ^{13}C NMR spectrum of HLS^2 in $\text{DMSO-}d_6$

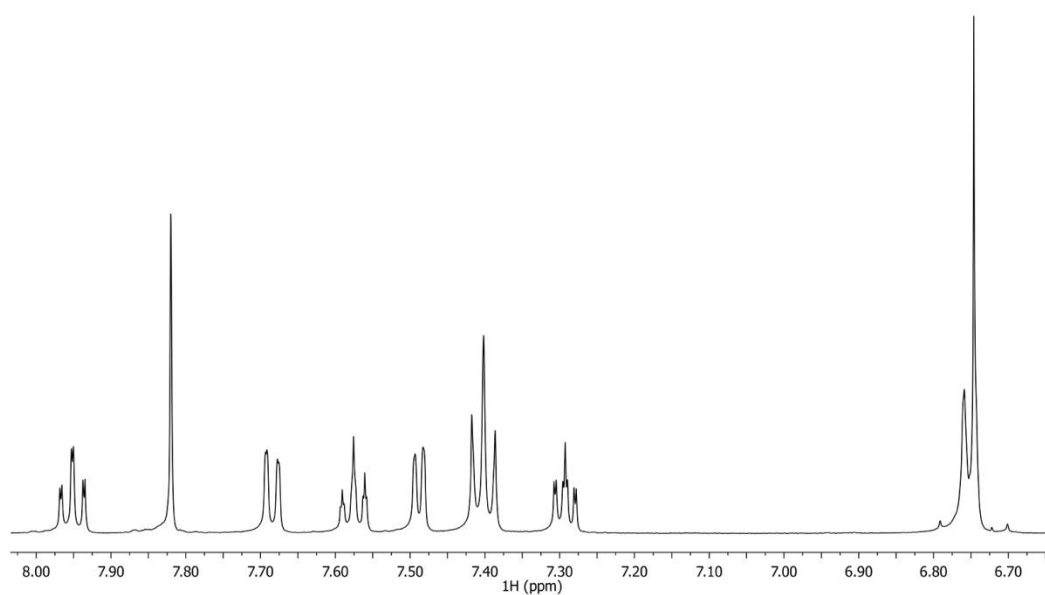


Figure 7.27 ^1H NMR spectrum of 1-Sein $\text{DMSO-}d_6$

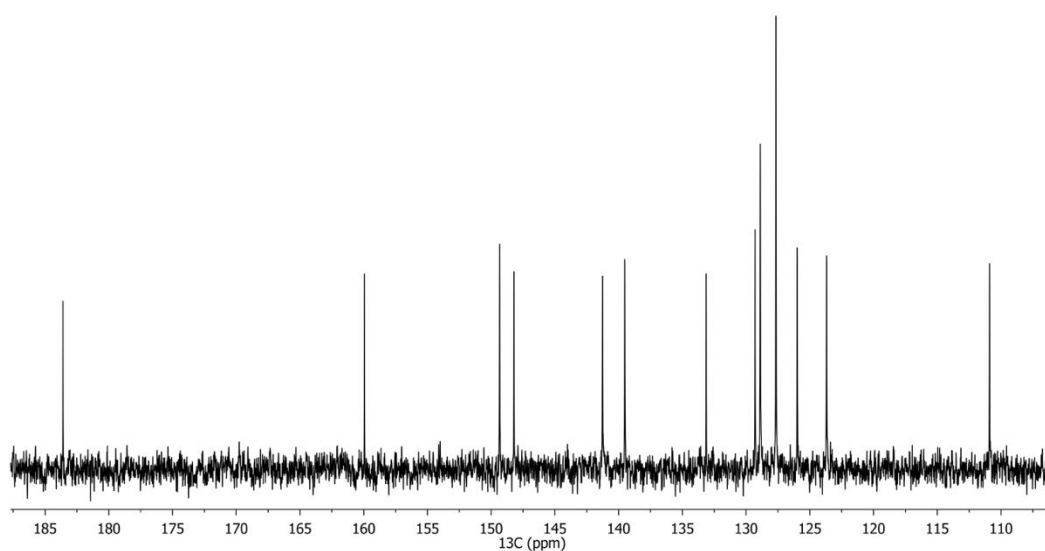


Figure 7.28 ^{13}C NMR spectrum of 1-Se in $\text{DMSO-}d_6$

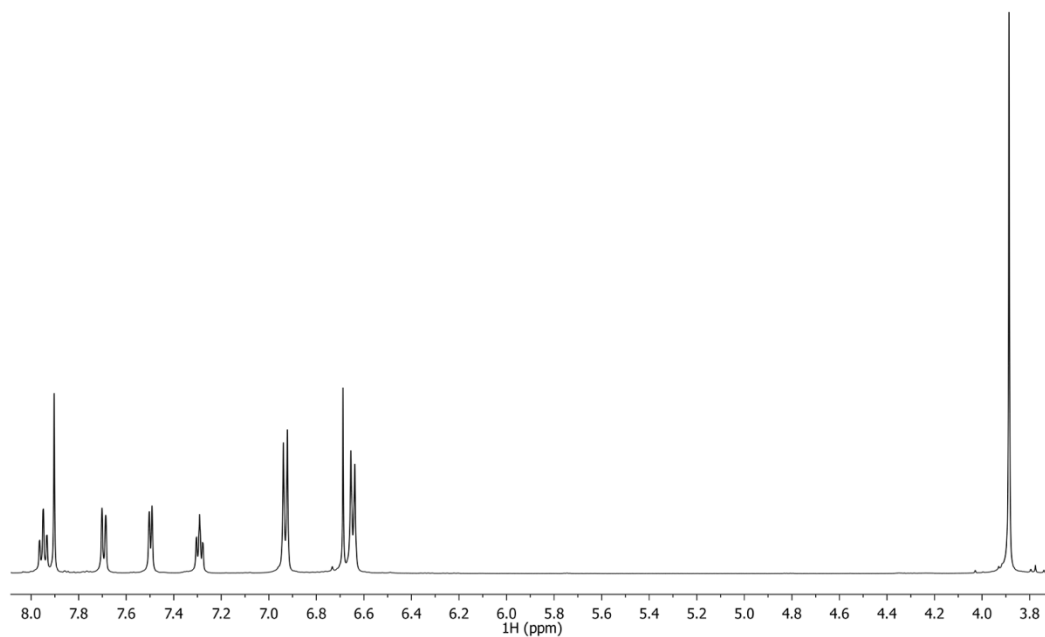


Figure 7.29 ^1H NMR spectrum of 2-Sein $\text{DMSO-}d_6$

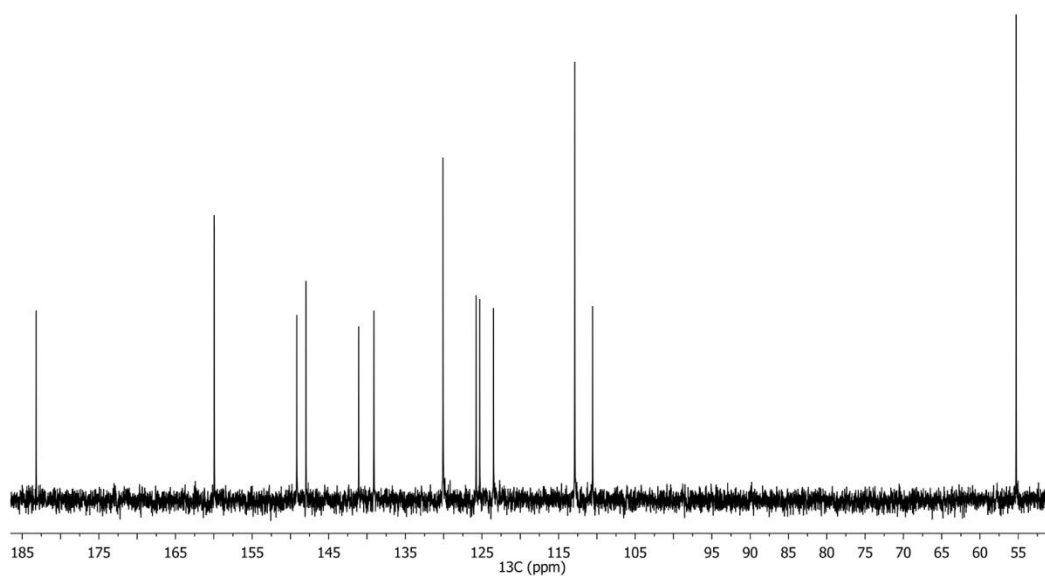


Figure 7.30 ^{13}C NMR spectrum of 2-Sein $\text{DMSO-}d_6$

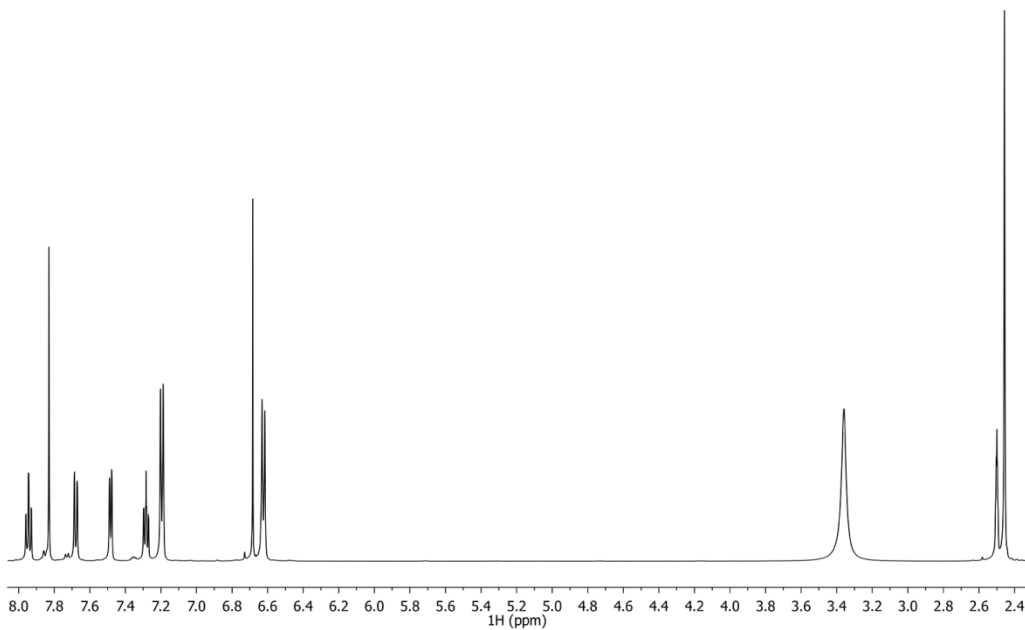


Figure 7.31 ^1H NMR spectrum of 3-Sein $\text{DMSO-}d_6$

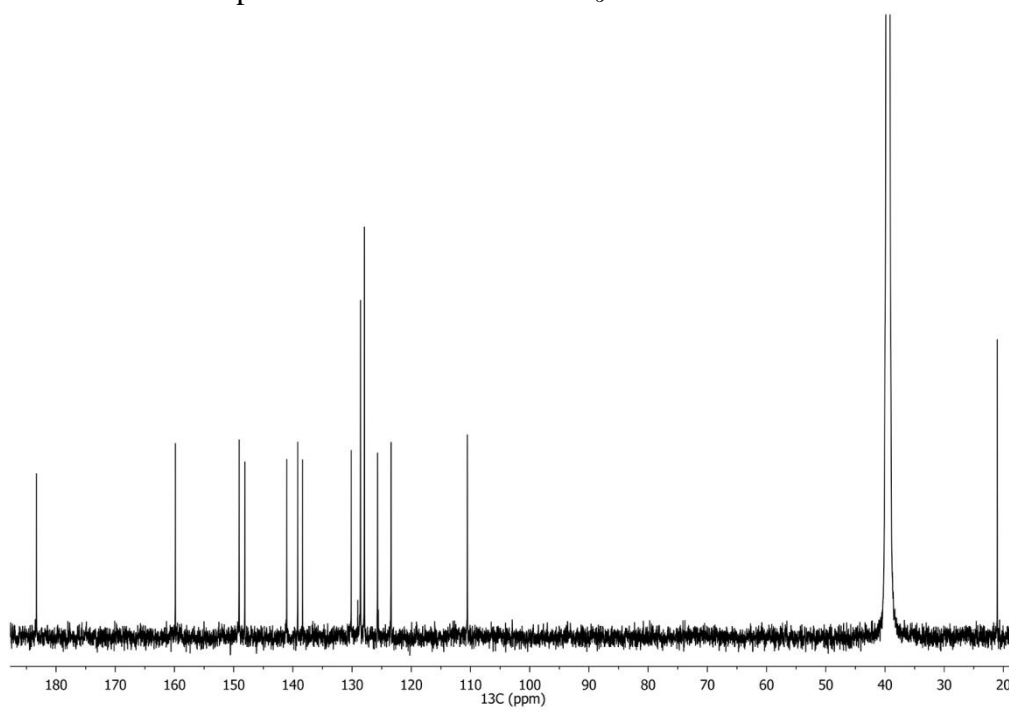


Figure 7.32 ^{13}C NMR spectrum of 3-Sein $\text{DMSO-}d_6$

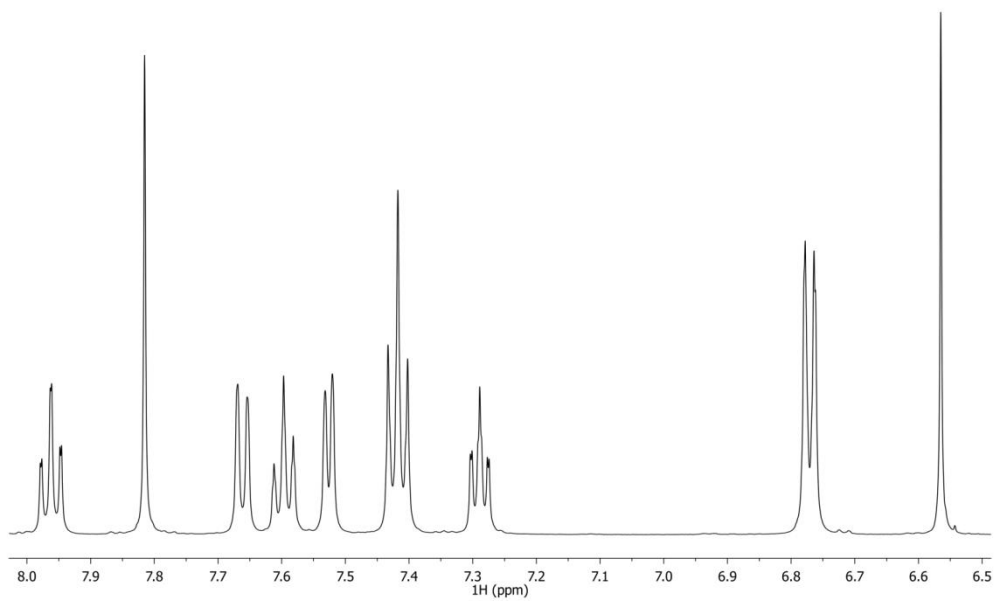


Figure 7.33 ^1H NMR spectrum of 1-Sin $\text{DMSO-}d_6$

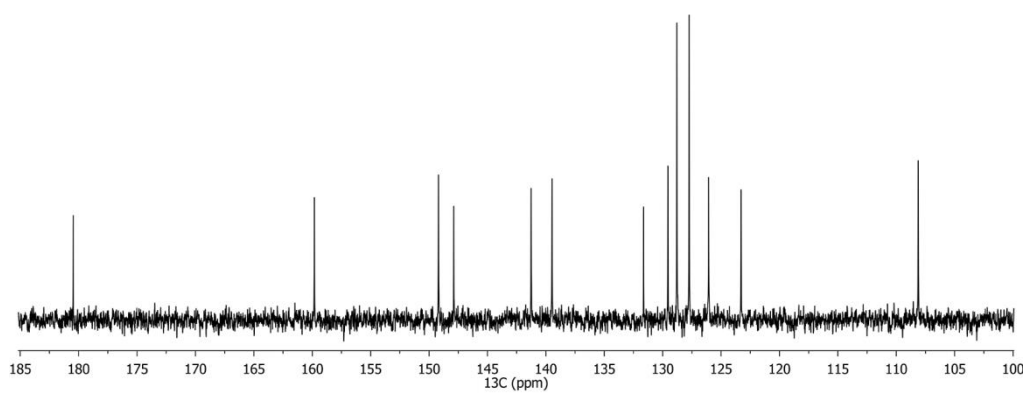


Figure 7.34 ^{13}C NMR spectrum of 1-Sin $\text{DMSO-}d_6$

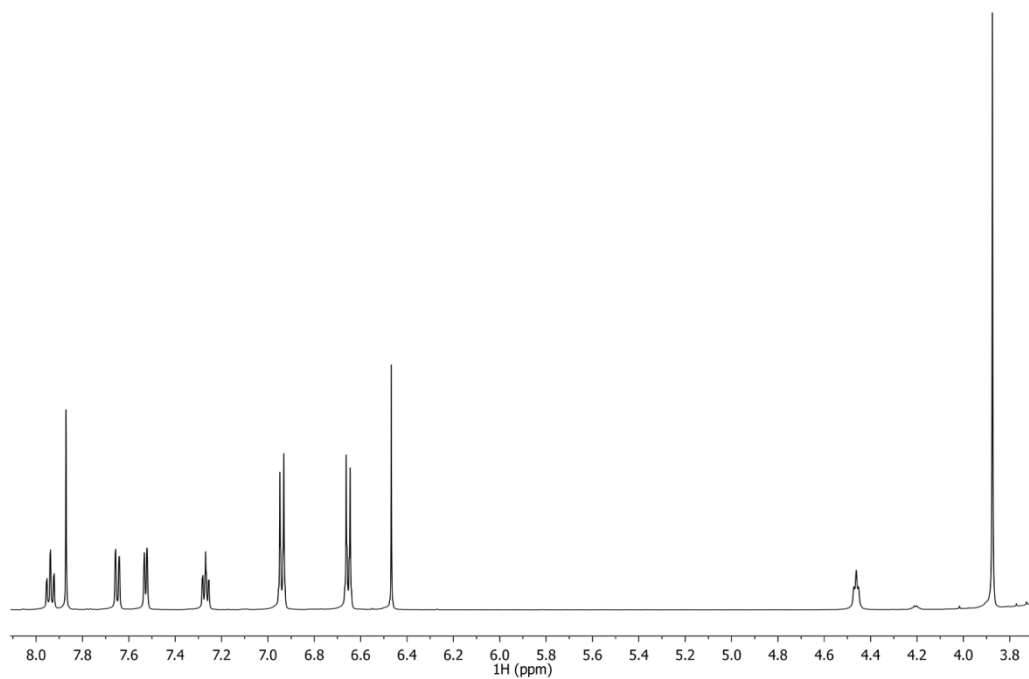


Figure 7.35 ^1H NMR spectrum of 2-Sin $\text{DMSO-}d_6$

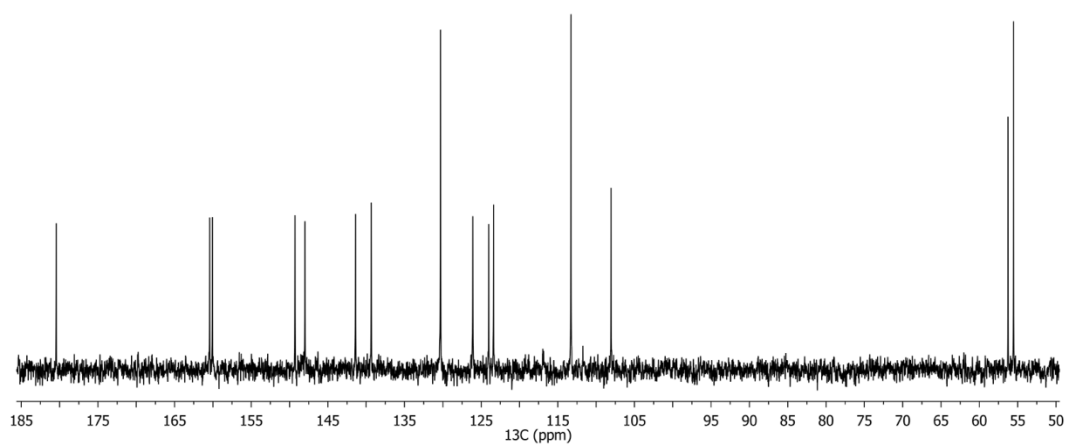


Figure 7.36 ^{13}C NMR spectrum of 2-Sin $\text{DMSO-}d_6$

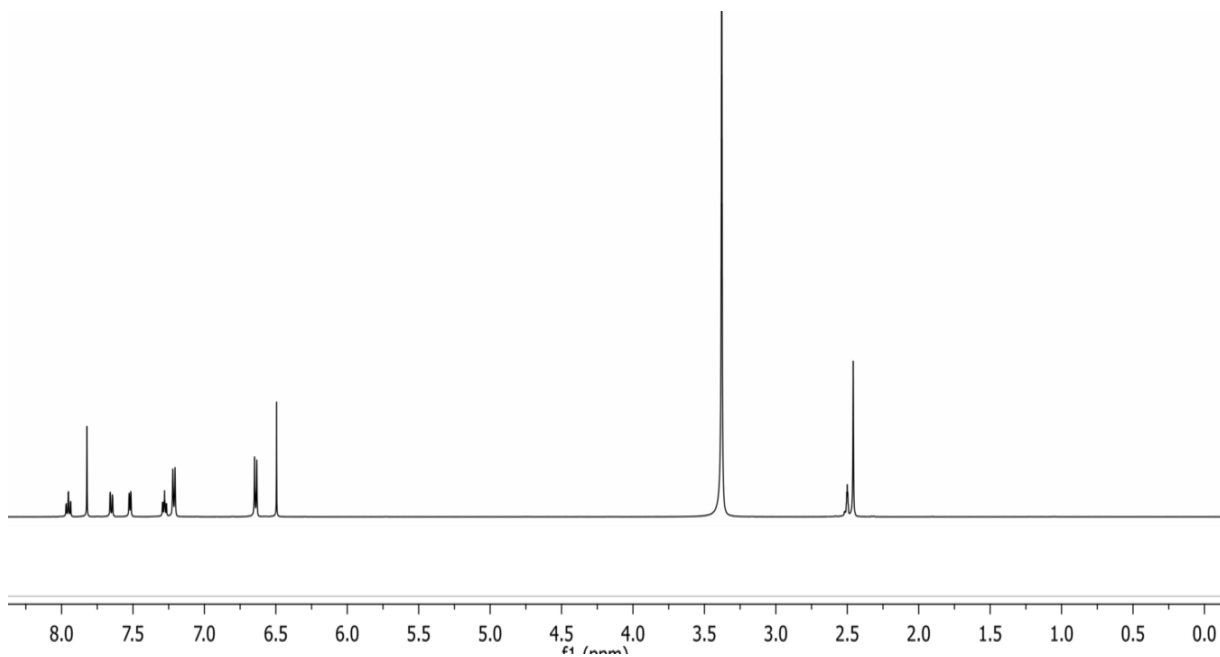


Figure 7.37 ^1H NMR spectrum of 3-Sin $\text{DMSO-}d_6$

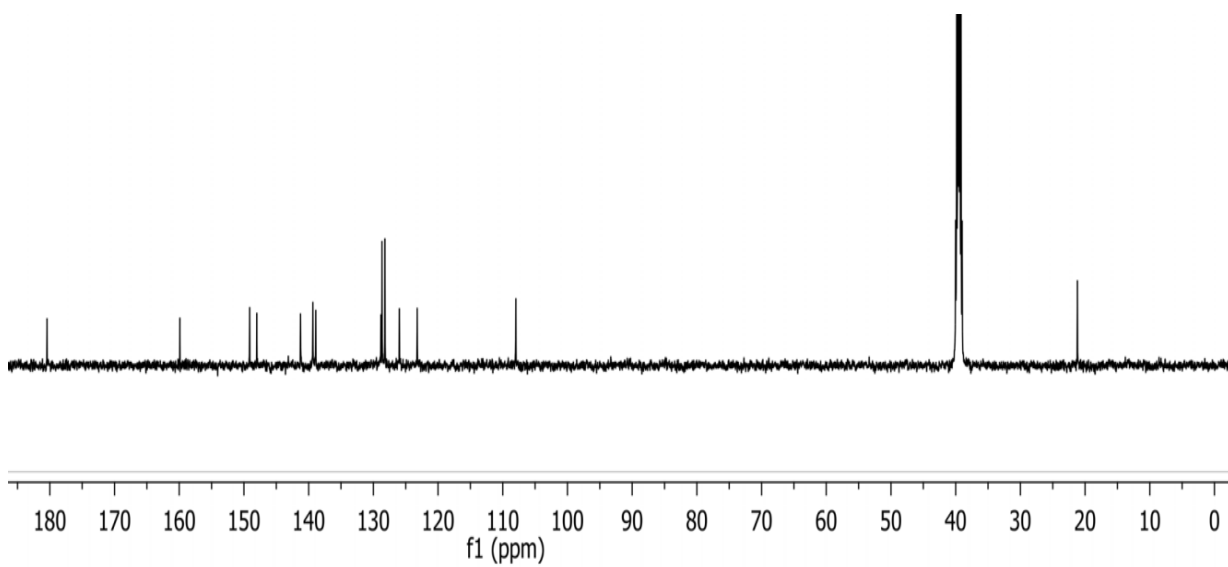


Figure 7.38 ^{13}C NMR spectrum of 3-Sin $\text{DMSO-}d_6$

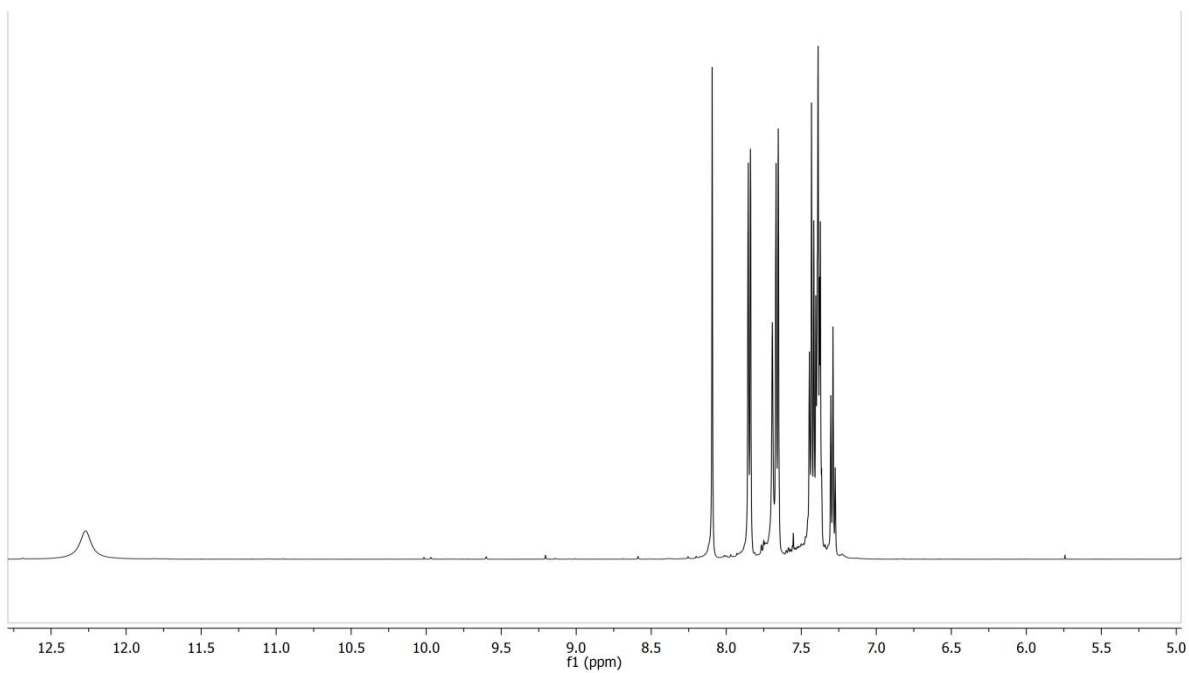


Figure 7.39 ^1H NMR spectrum of 1 in $\text{DMSO-}d_6$.

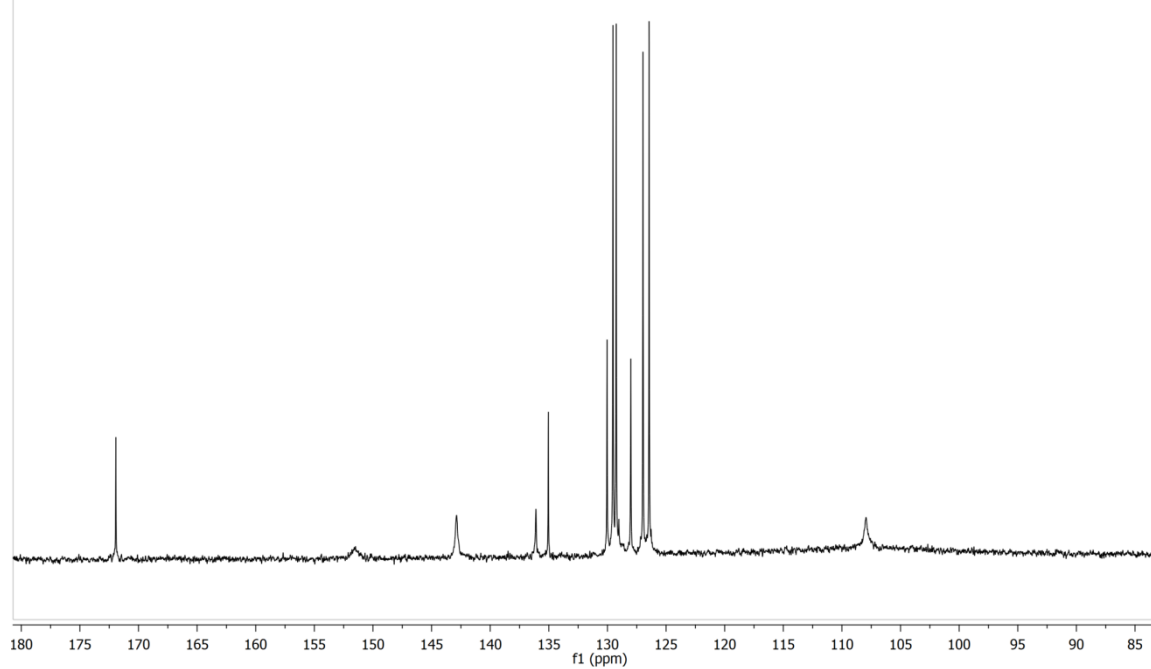


Figure 7.40 ^{13}C NMR spectrum of 1 in $\text{DMSO-}d_6$.

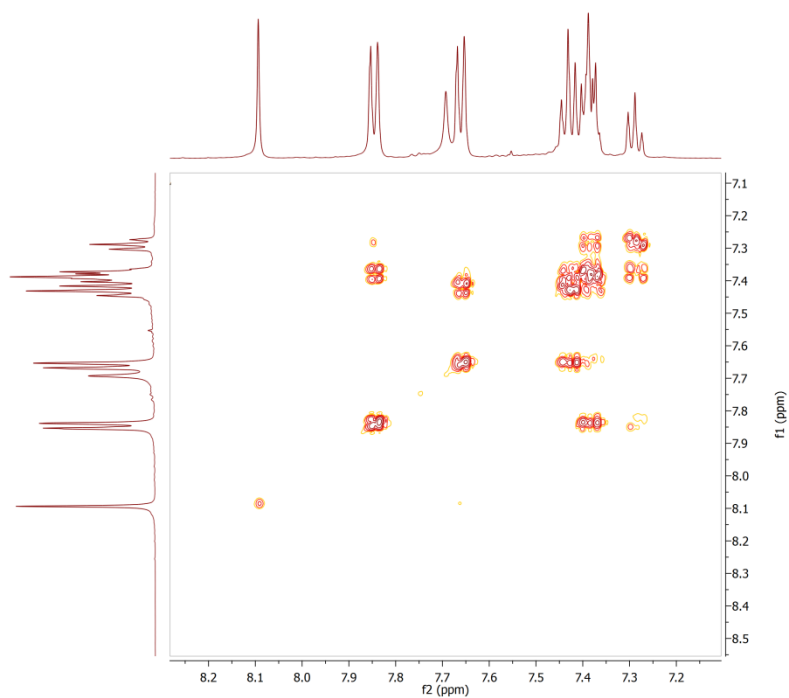


Figure 7.41 COSY spectrum of 1 in DMSO- d_6 .

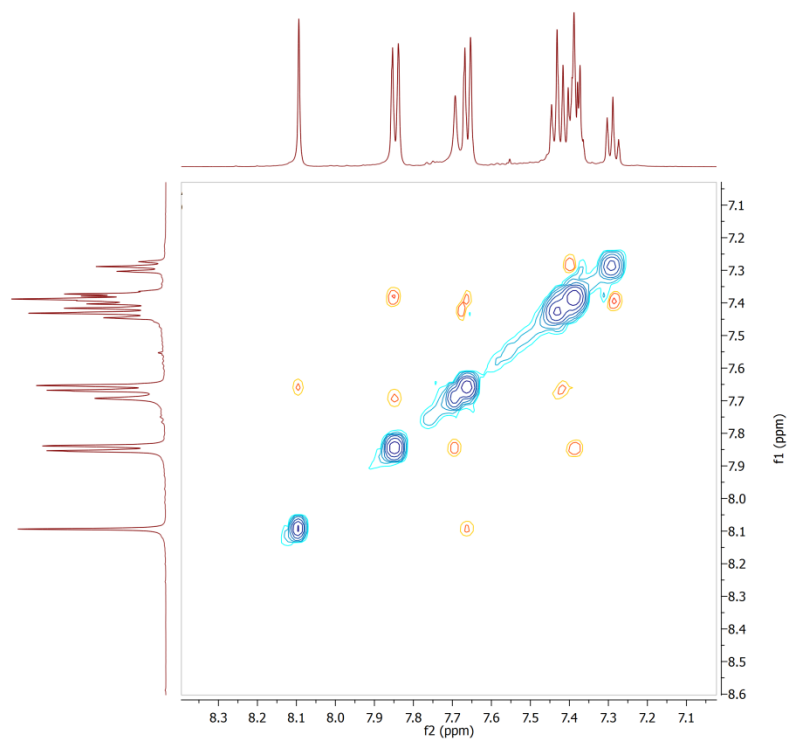


Figure 7.42 NOESY spectrum of 1 in DMSO- d_6 .

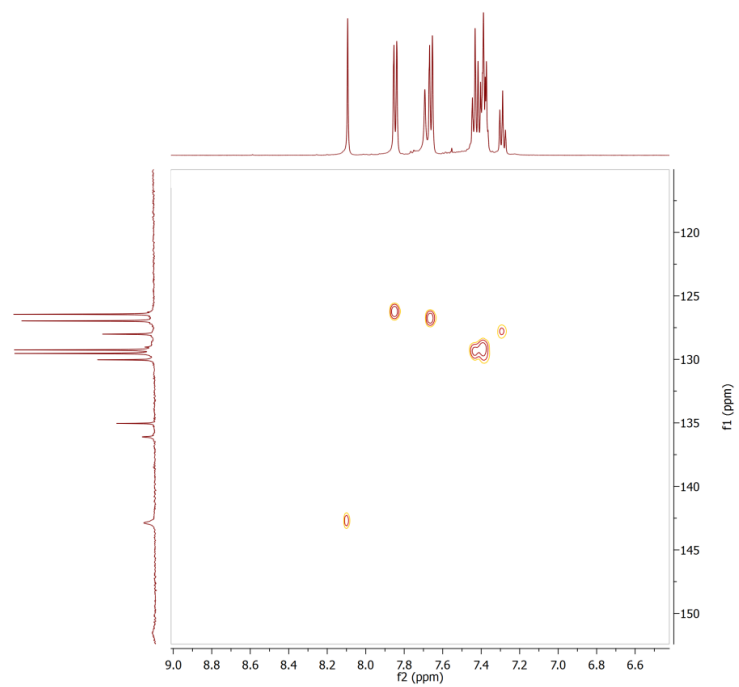


Figure 7.43 ^1H - ^{13}C HSQC NMR spectrum of **1** in $\text{DMSO-}d_6$.

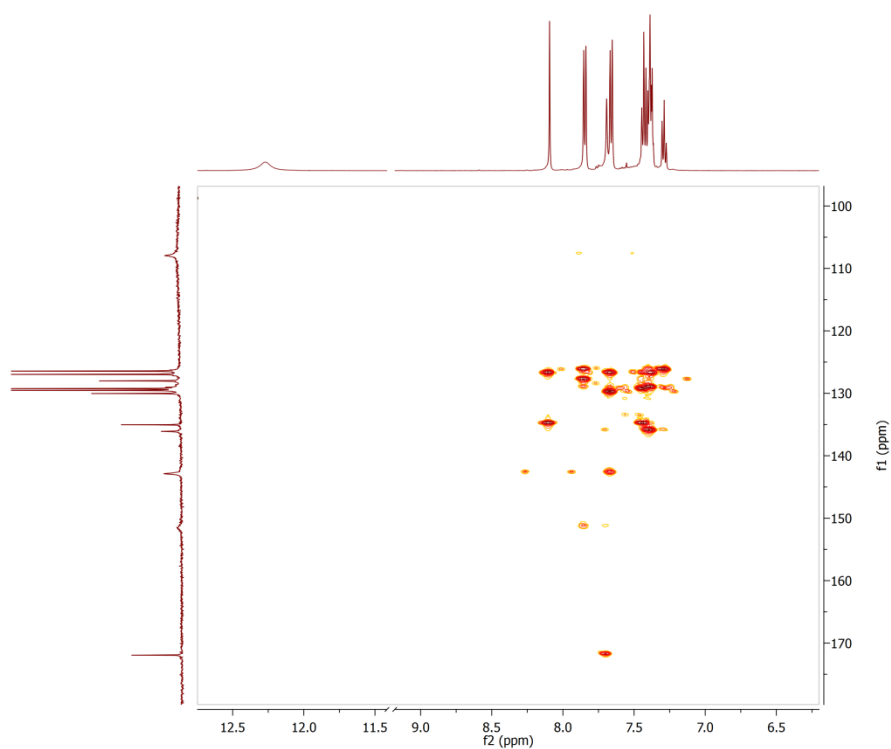


Figure 7.44 ^1H - ^{13}C HMBC NMR spectrum of **1** in $\text{DMSO-}d_6$.

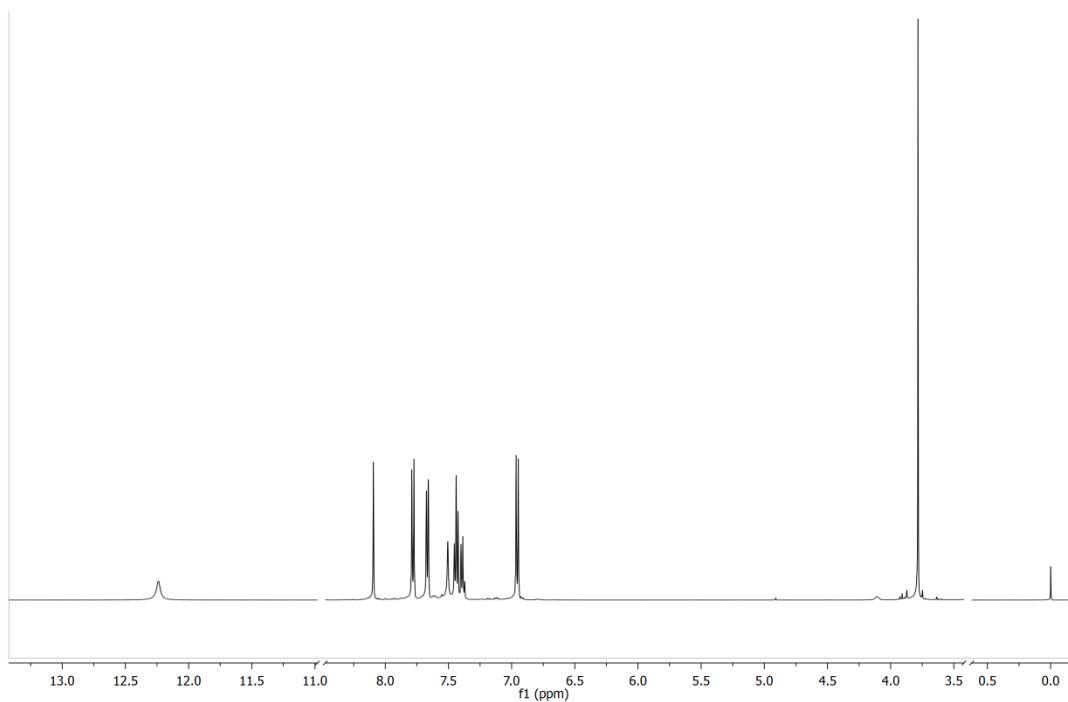


Figure 7.45 ^1H NMR spectrum of 1-OMe in $\text{DMSO-}d_6$.

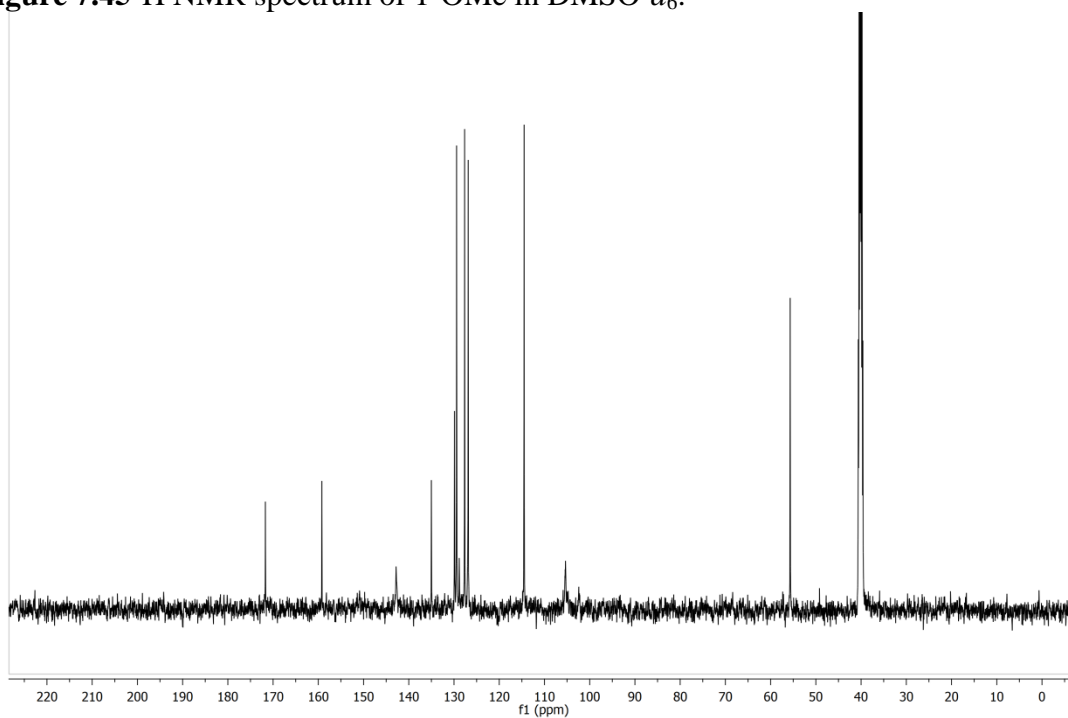


Figure 7.46 ^{13}C NMR spectrum of 1-OMe in $\text{DMSO-}d_6$.

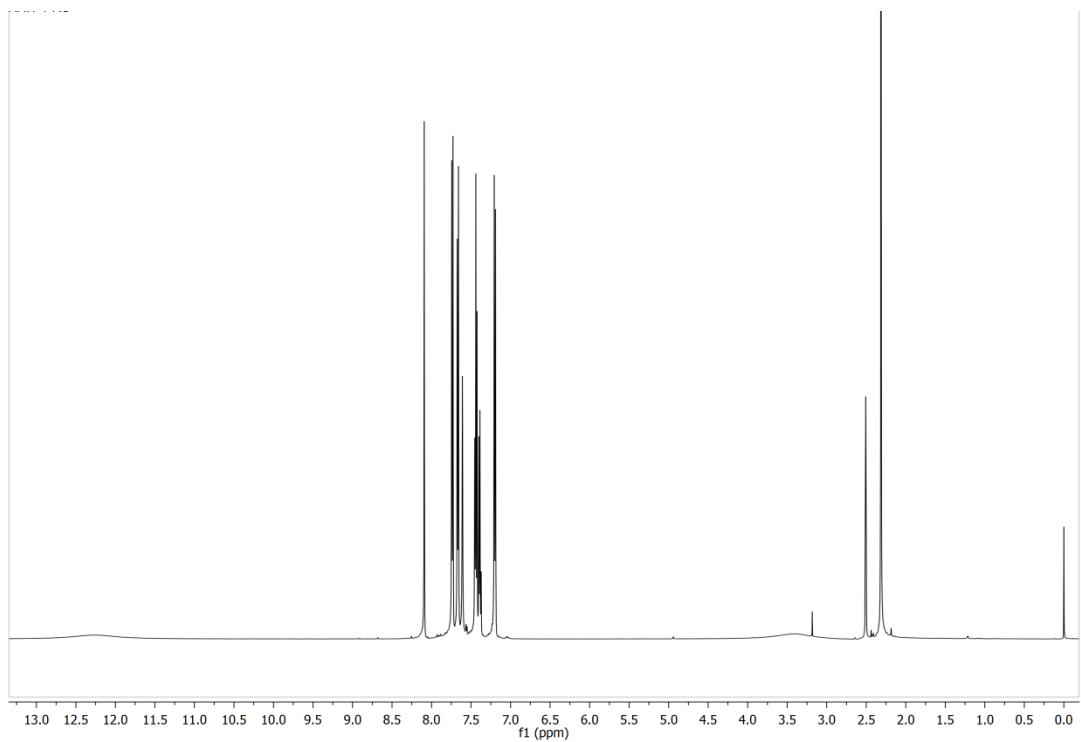


Figure 7.47 ^1H NMR spectrum of 1-Me in $\text{DMSO-}d_6$.

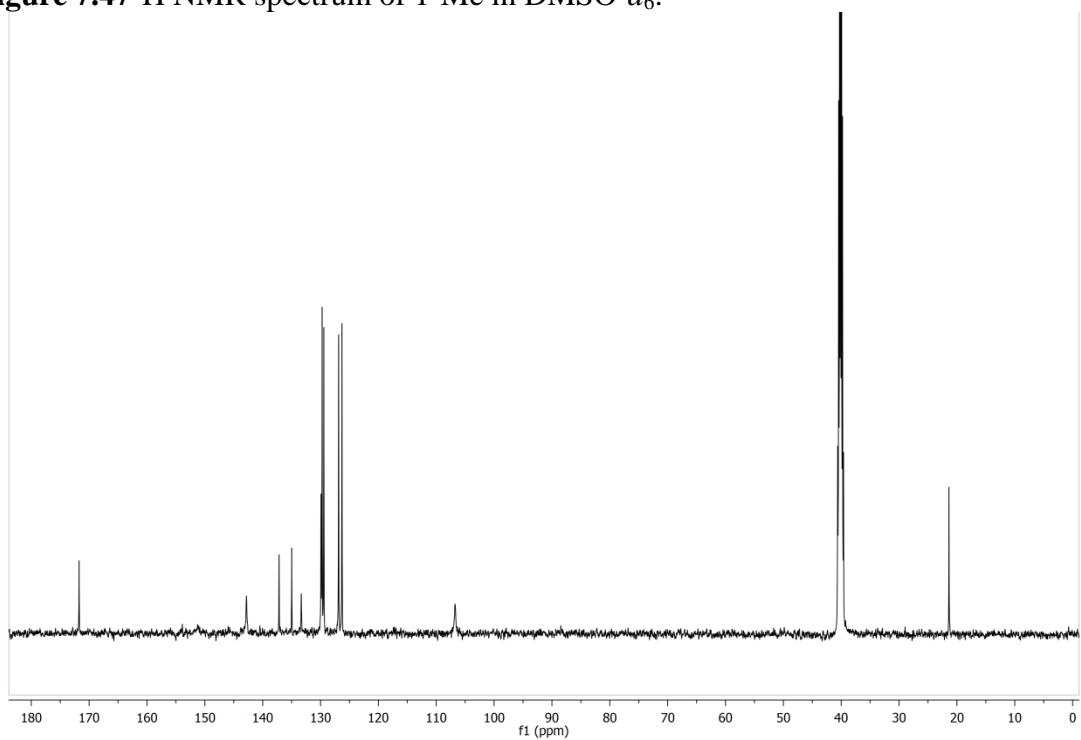


Figure 7.48 ^{13}C NMR spectrum of 1-Me in $\text{DMSO-}d_6$.

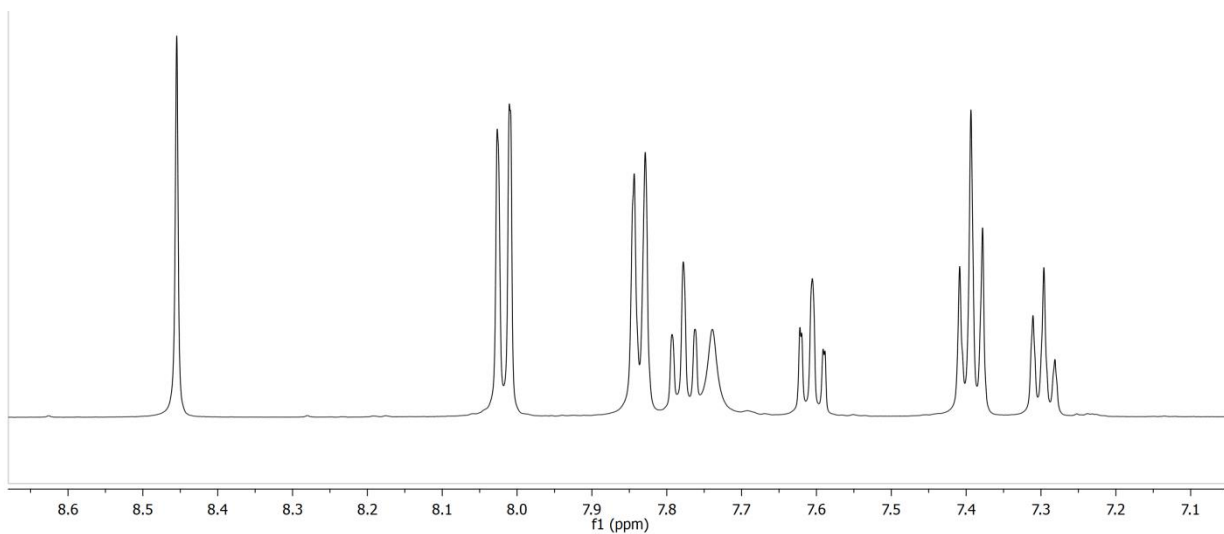


Figure 7.49 ^1H NMR spectrum of 2 in $\text{DMSO-}d_6$.

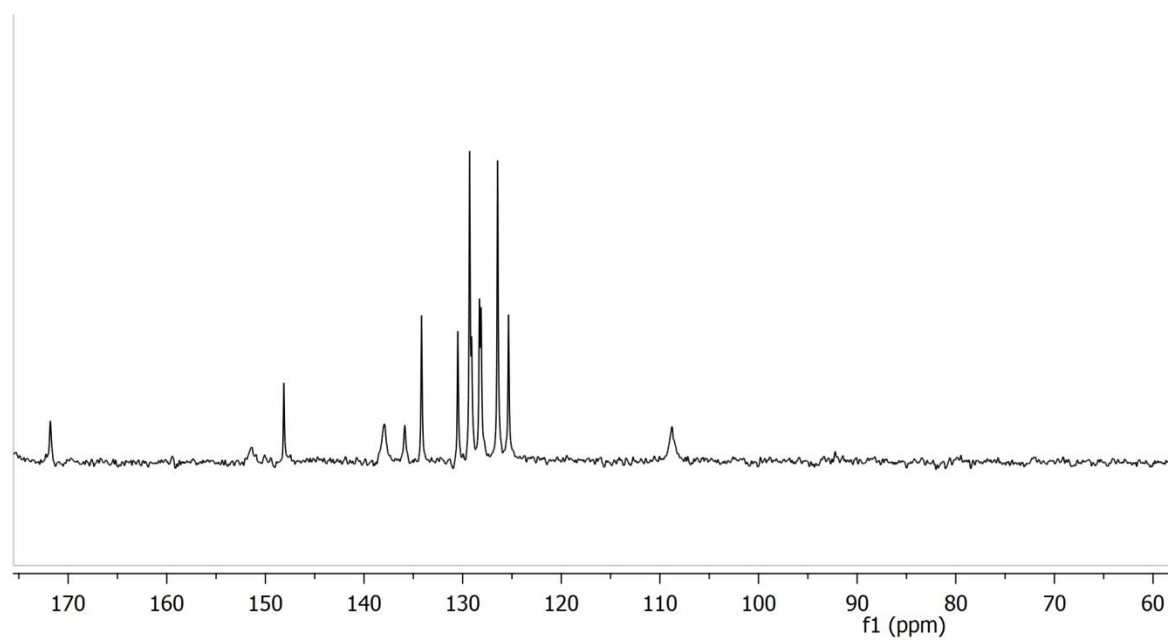


Figure 7.50 ^{13}C NMR spectrum of 2 in $\text{DMSO-}d_6$.

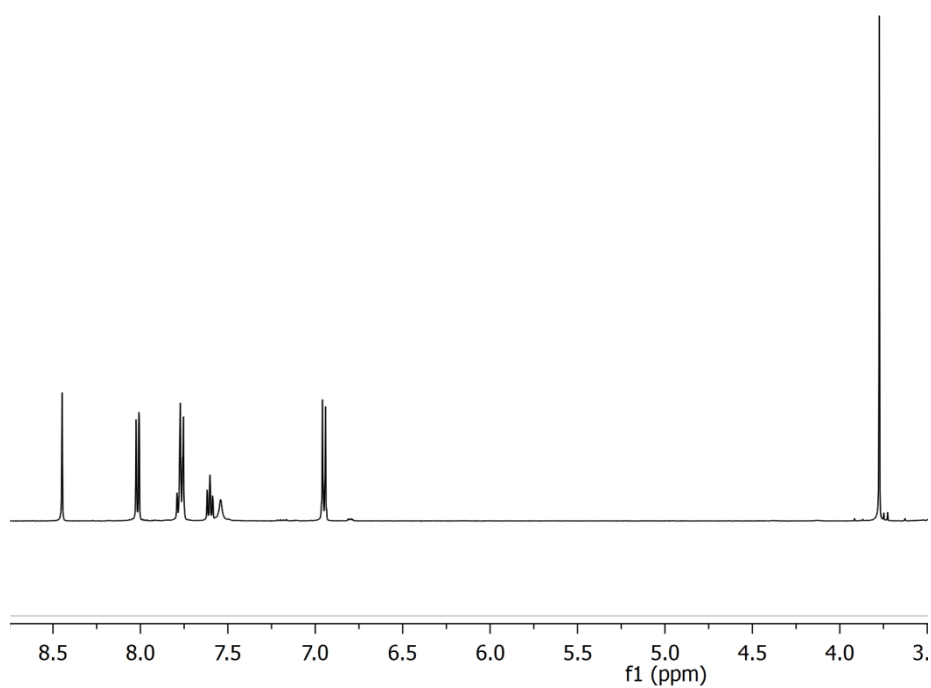


Figure 7.51 ^1H NMR spectrum of 2-OMe in $\text{DMSO-}d_6$.

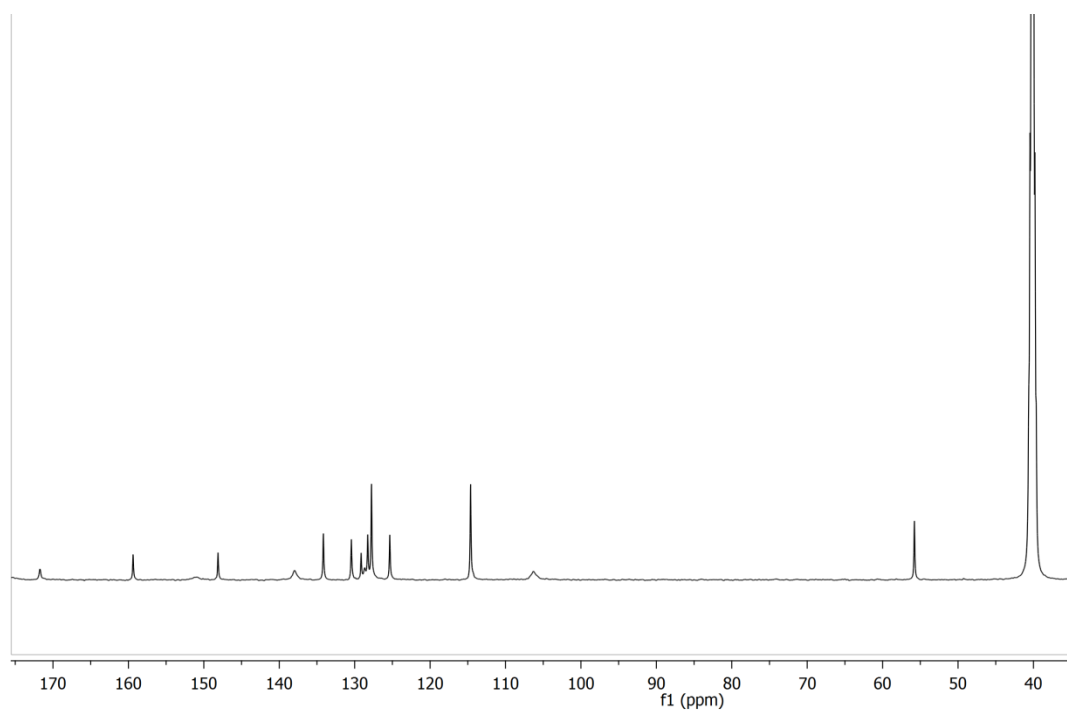


Figure 7.52 ^{13}C NMR spectrum of 2-OMe in $\text{DMSO-}d_6$.

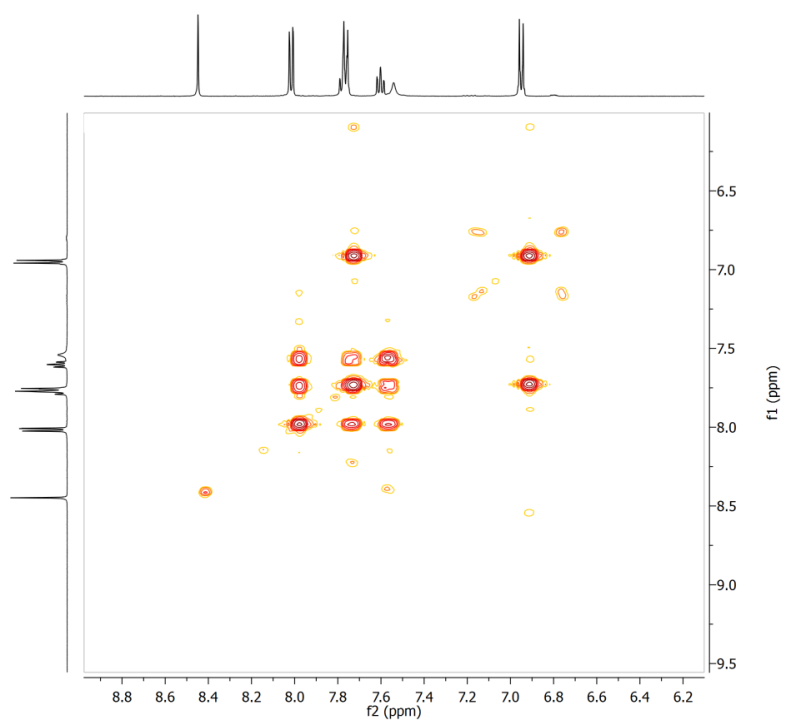


Figure 7.53 COSY spectrum of 2-OMe in DMSO- d_6 .

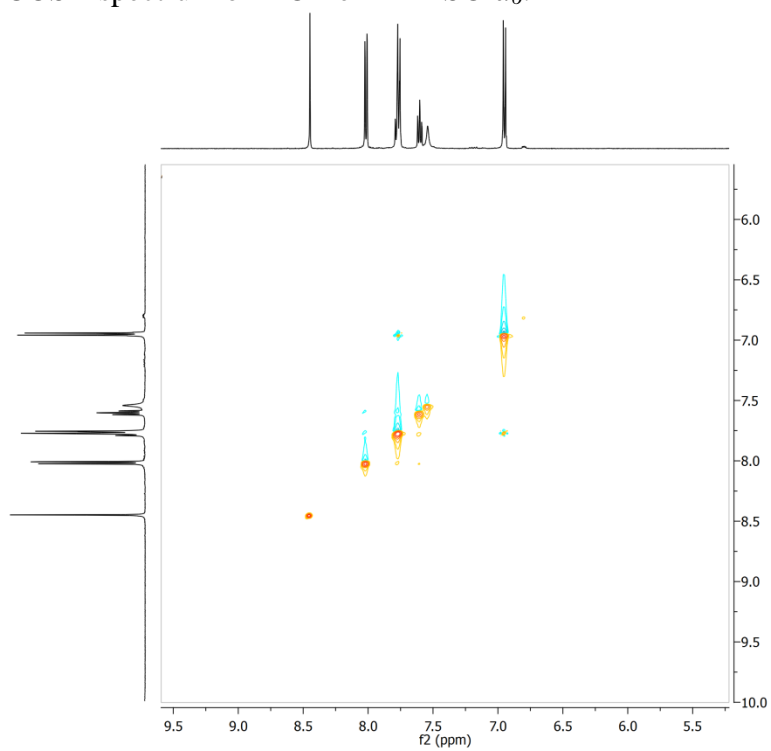


Figure 7.54 NOESY spectrum of 2-OMe in DMSO- d_6 .

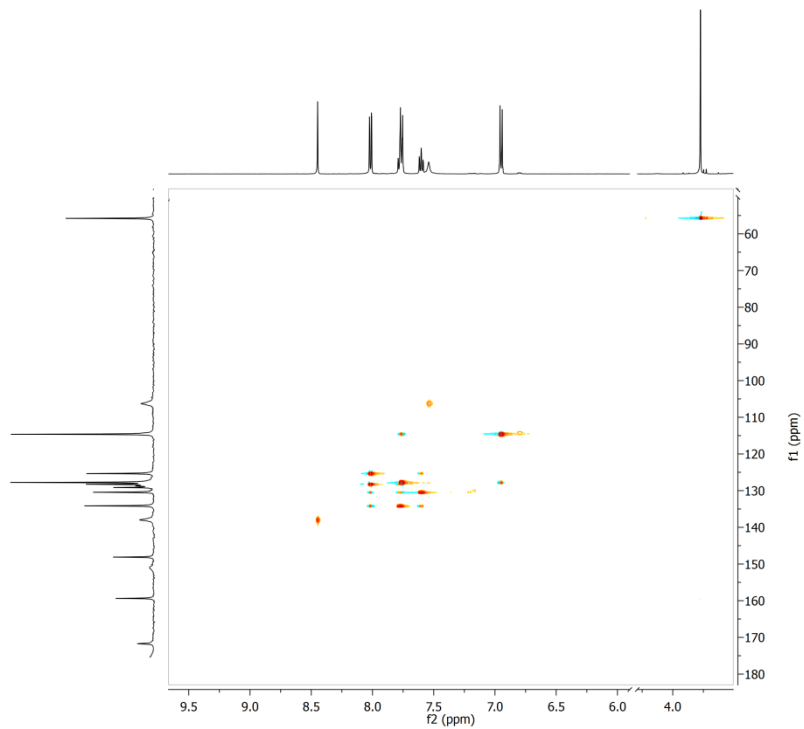


Figure 7.55 ^1H - ^{13}C HSQC NMR spectrum of 2-OMe in $\text{DMSO-}d_6$.

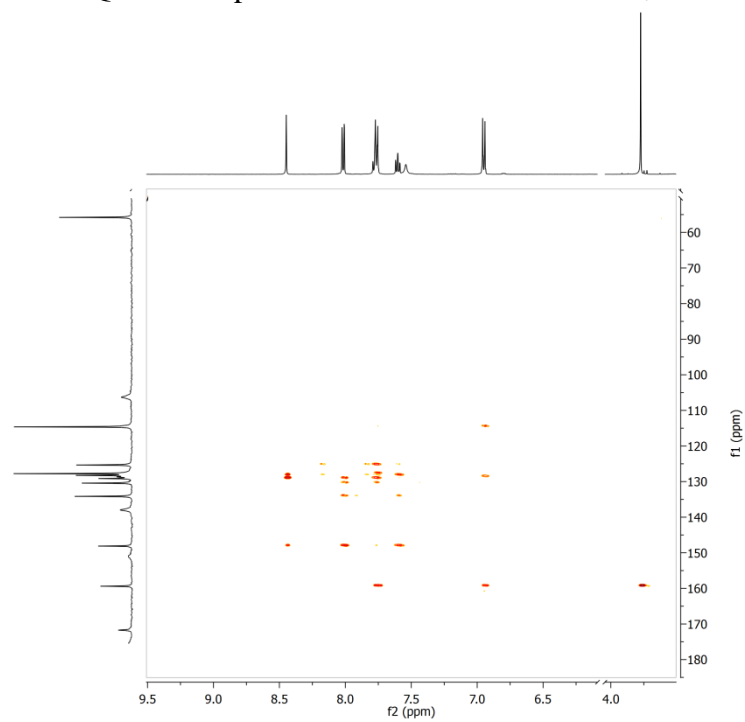


Figure 7.56 ^1H - ^{13}C HMBC NMR spectrum of 2-OMe in $\text{DMSO-}d_6$.

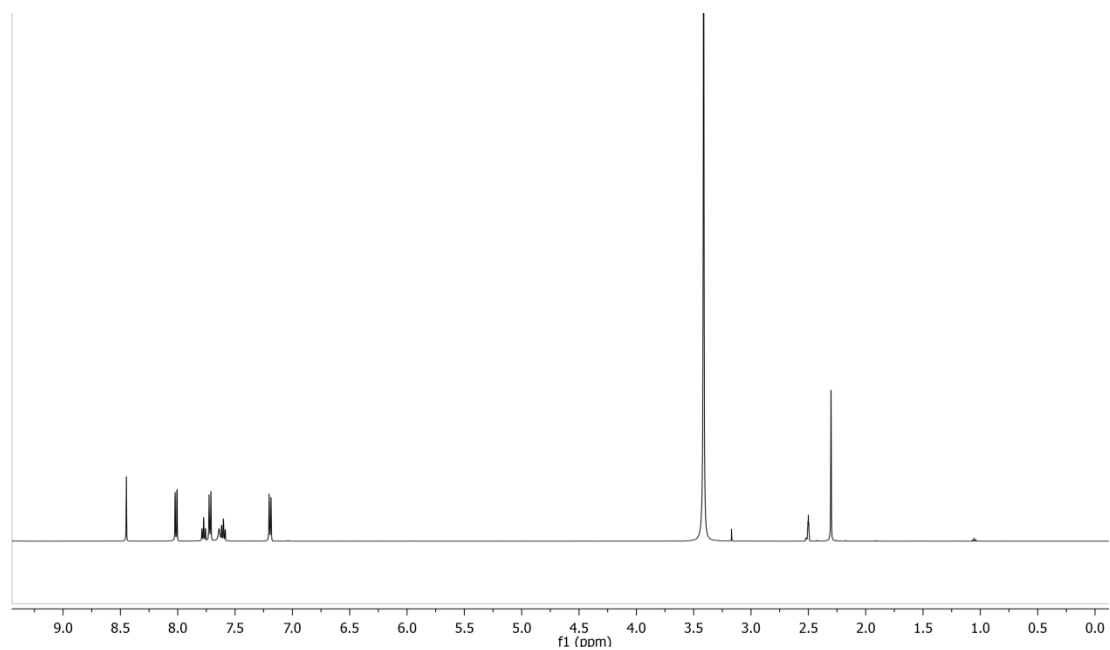


Figure 7.57 ^1H NMR spectrum of 2-Me in $\text{DMSO-}d_6$.

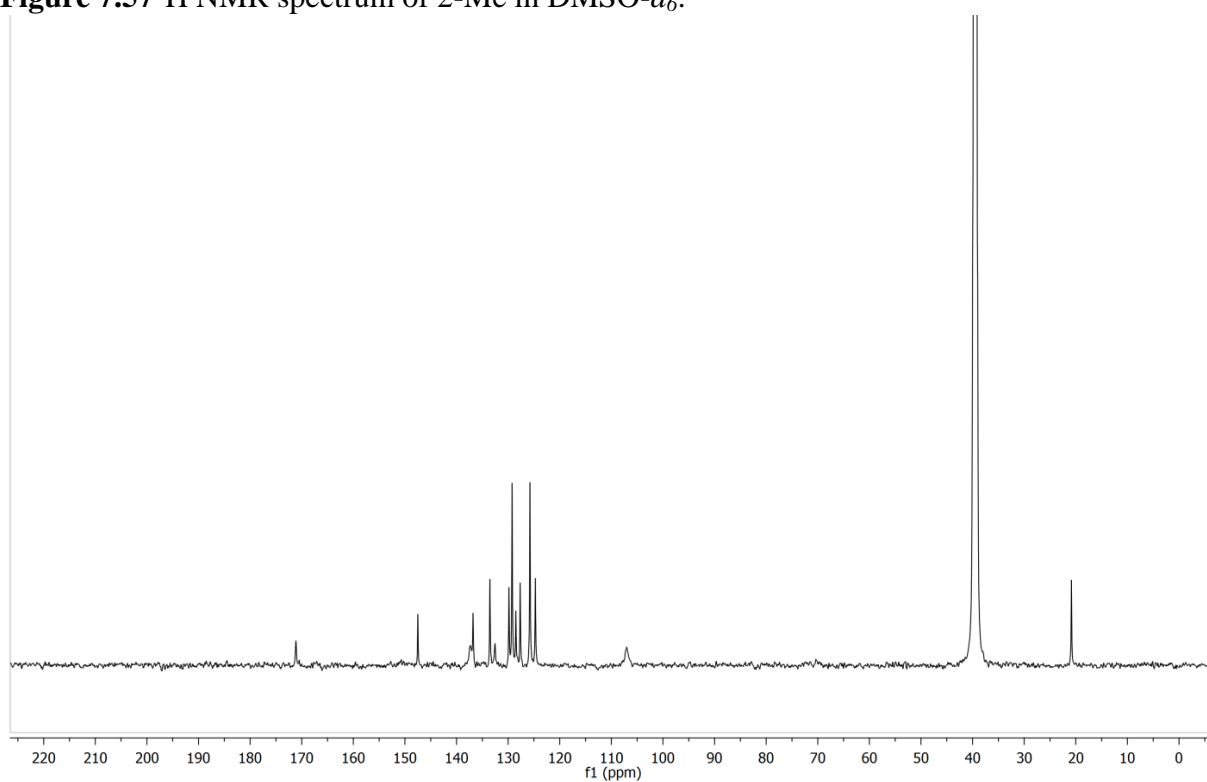


Figure 7.58 ^{13}C NMR spectrum of 2-Me in $\text{DMSO-}d_6$.

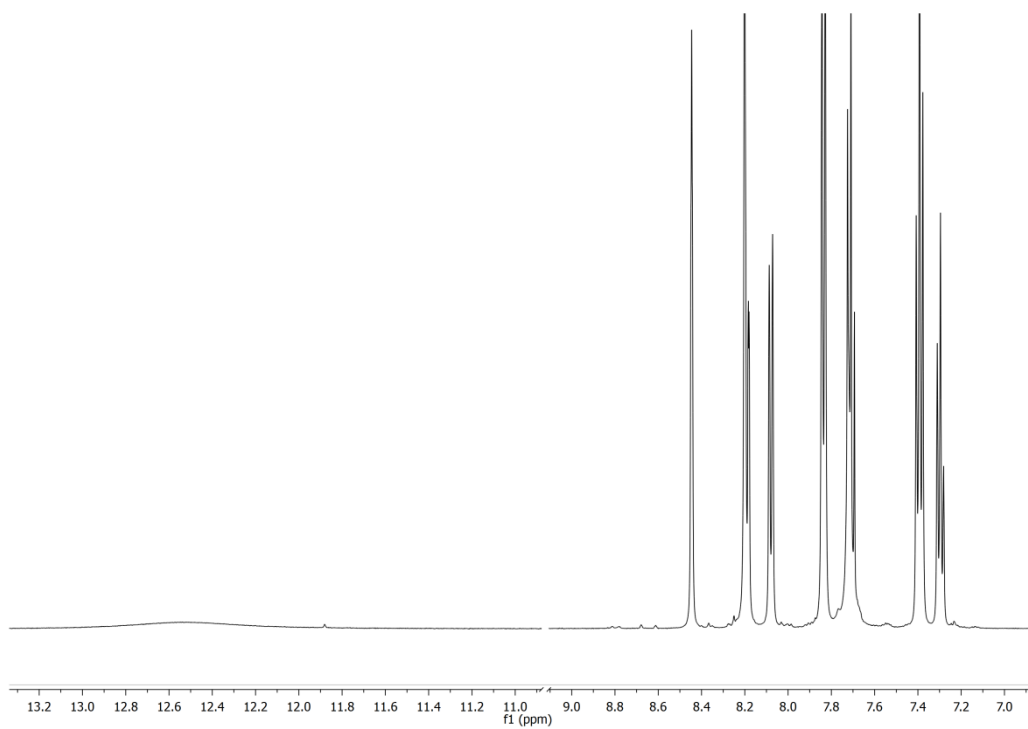


Figure 7.59 ^1H NMR spectrum of 3 in $\text{DMSO-}d_6$.

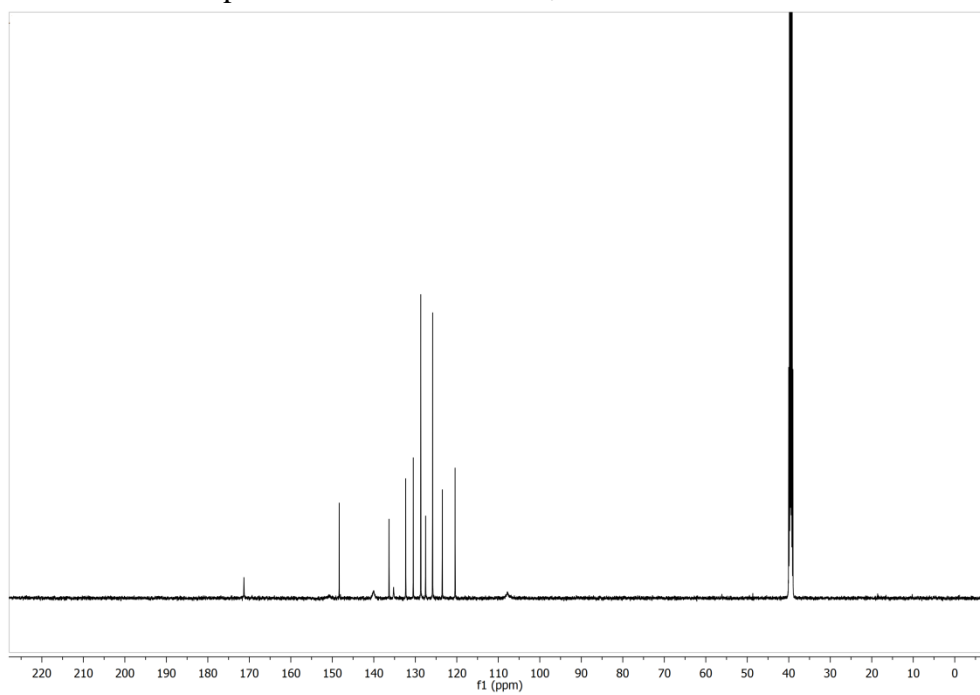


Figure 7.60 ^{13}C NMR spectrum of 3 in $\text{DMSO-}d_6$.

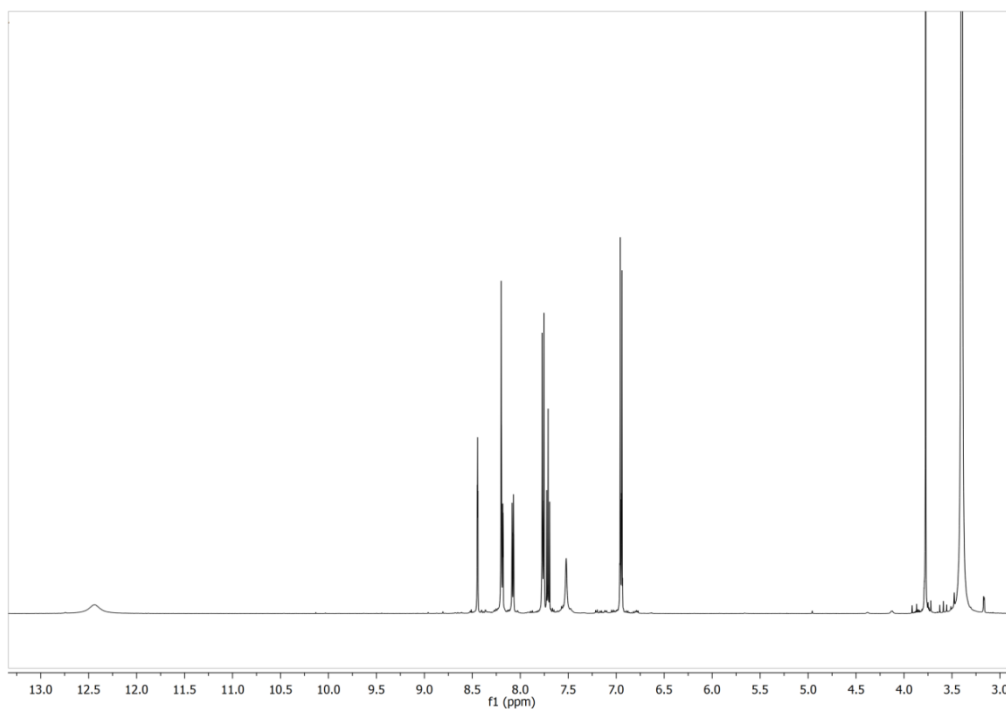


Figure 7.61 ^1H NMR spectrum of 3-OMe in $\text{DMSO-}d_6$.

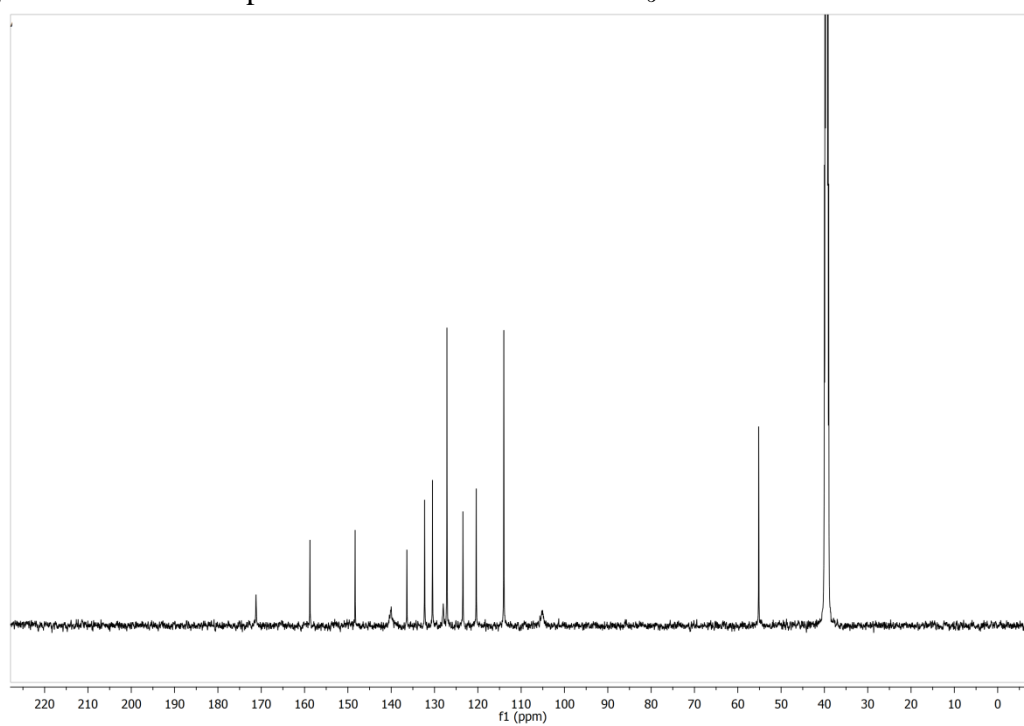


Figure 7.62 ^{13}C NMR spectrum of 3-OMe in $\text{DMSO-}d_6$.

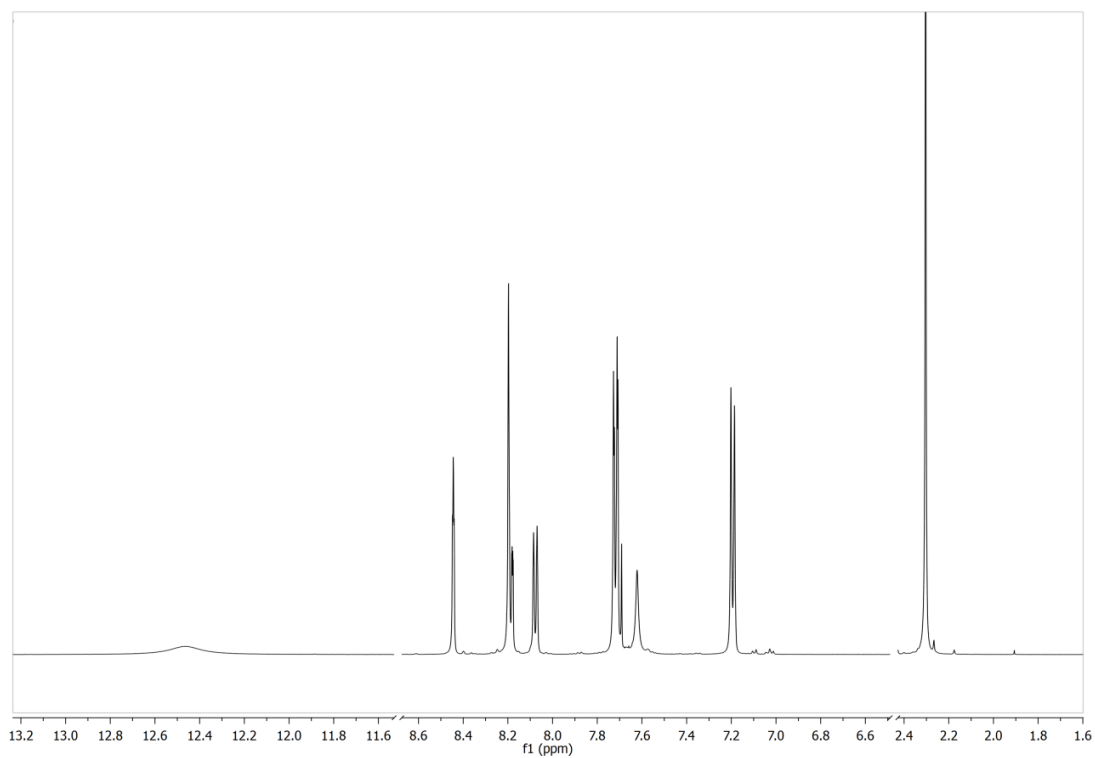


Figure 7.63 ^1H NMR spectrum of 3-Me in $\text{DMSO-}d_6$.

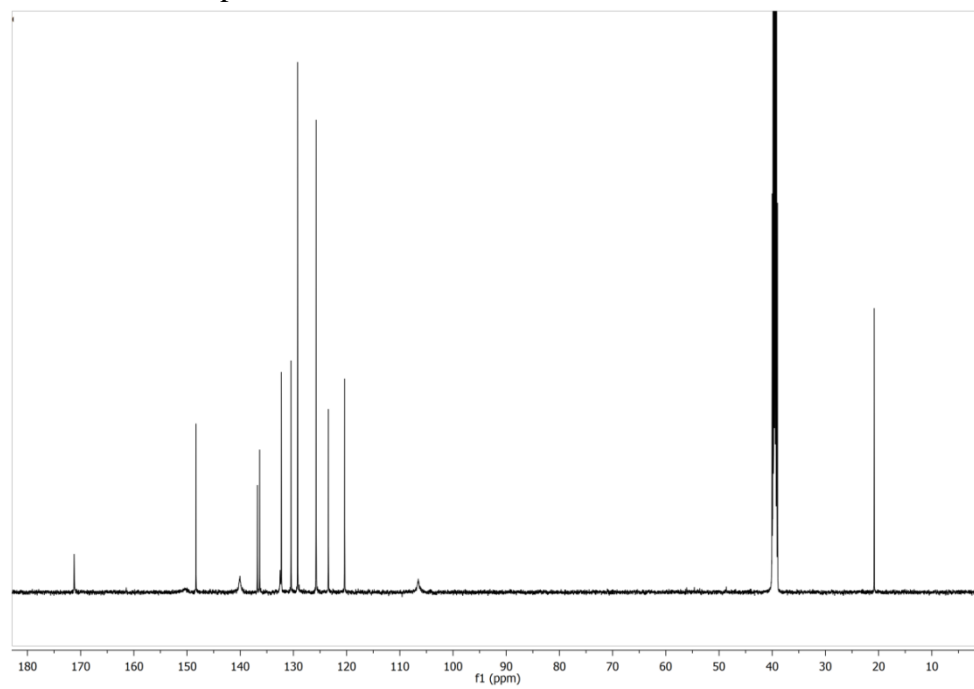


Figure 7.64 ^{13}C NMR spectrum of 3-Me in $\text{DMSO-}d_6$.

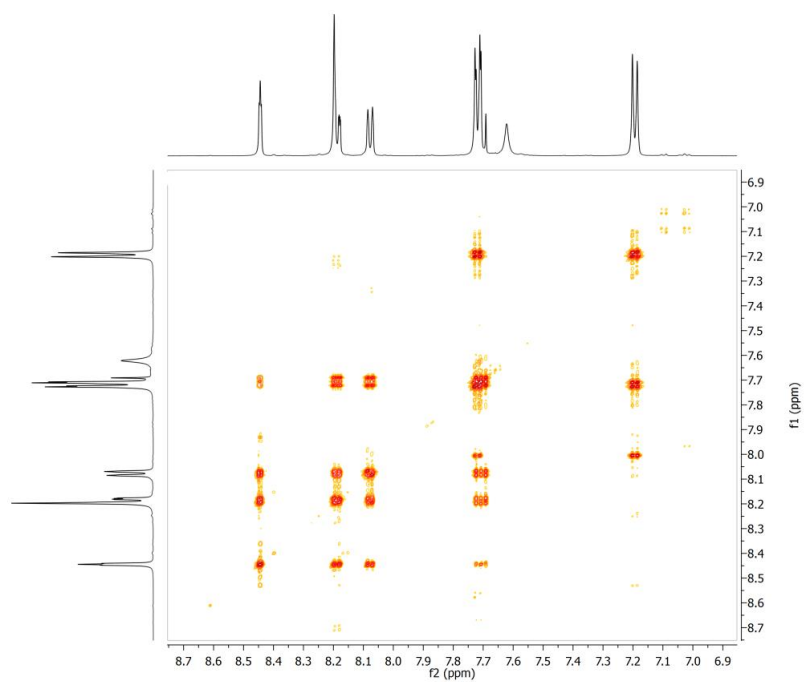


Figure 7.65 COSY spectrum of 3-Me in DMSO- d_6 .

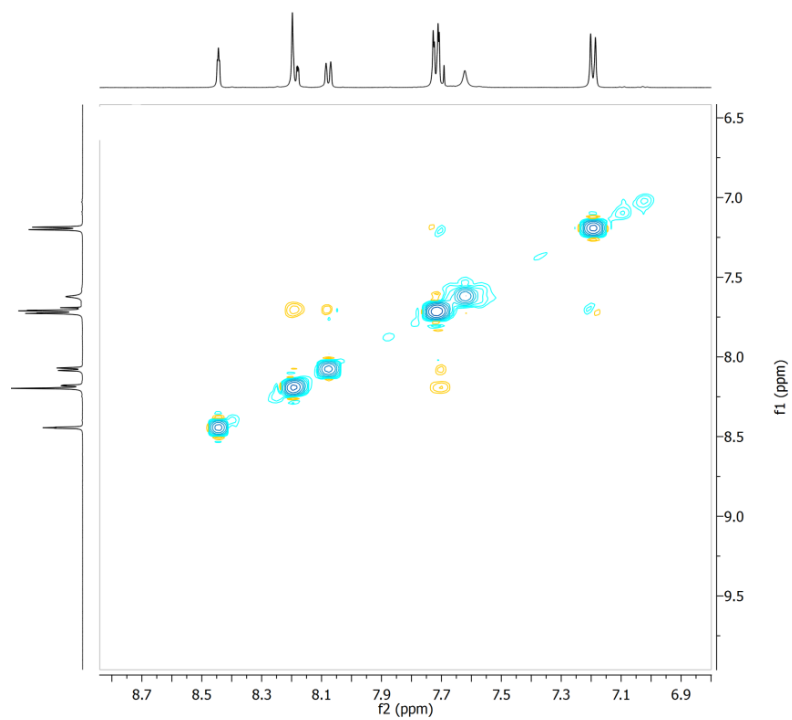


Figure 7.66 NOESY spectrum of 3-Me in DMSO- d_6 .

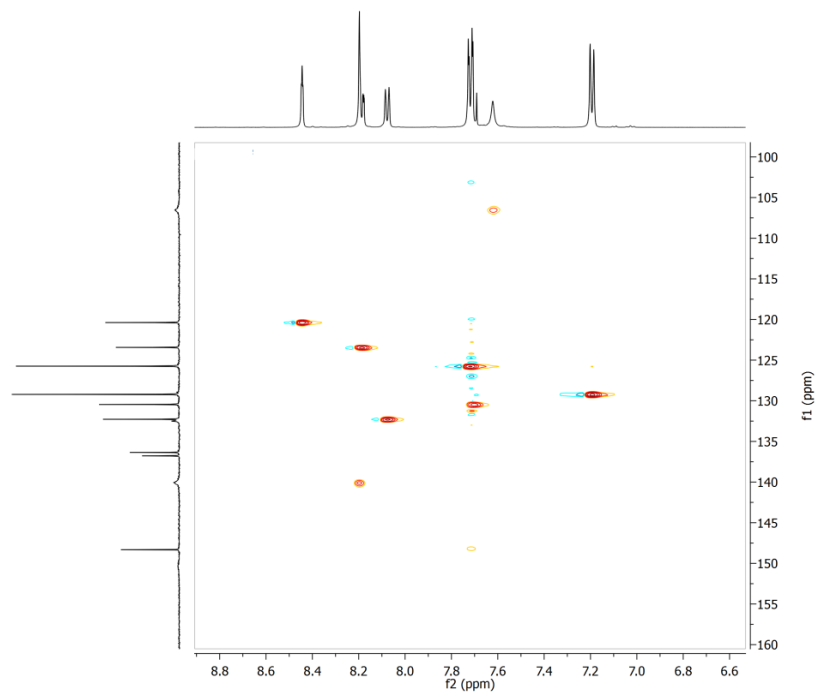


Figure 7.67 ^1H - ^{13}C HSQC NMR spectrum of 3-Me in $\text{DMSO-}d_6$.

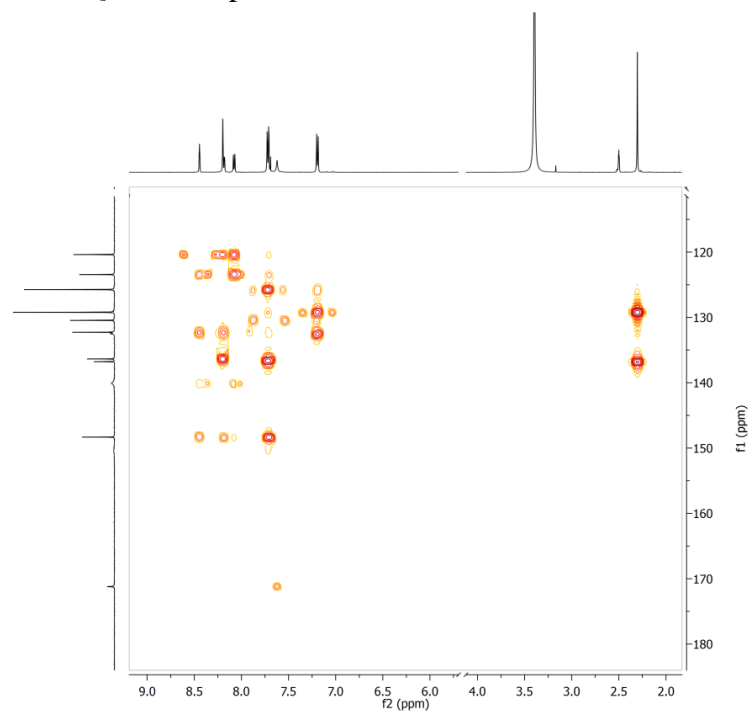


Figure 7.68 ^1H - ^{13}C HMBC NMR spectrum of 3-Me in $\text{DMSO-}d_6$.

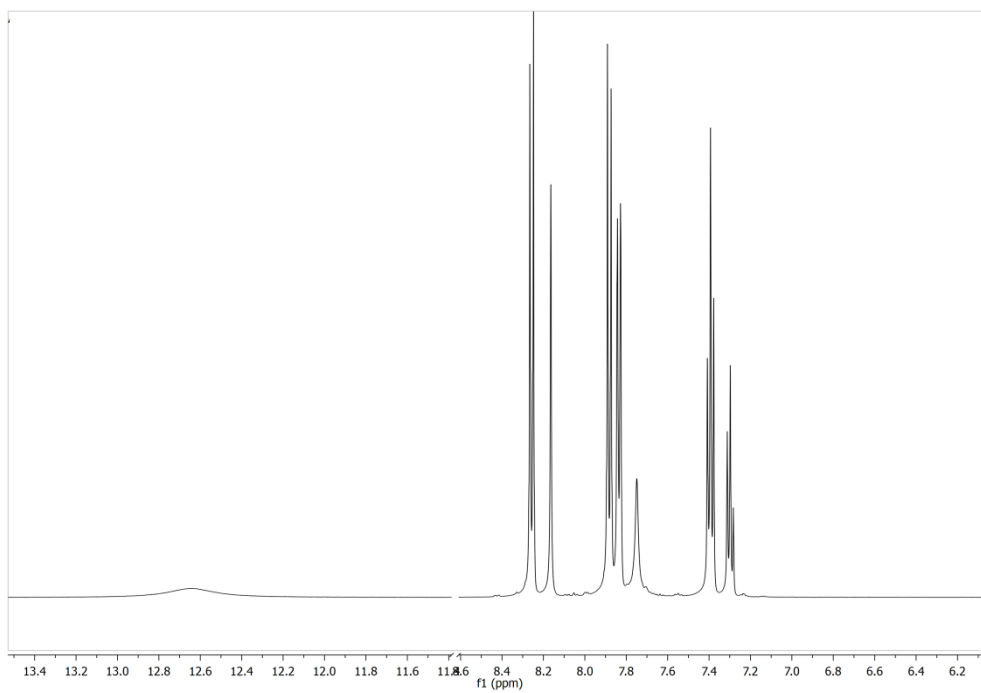


Figure 7.69 ^1H NMR spectrum of 4 in $\text{DMSO-}d_6$.

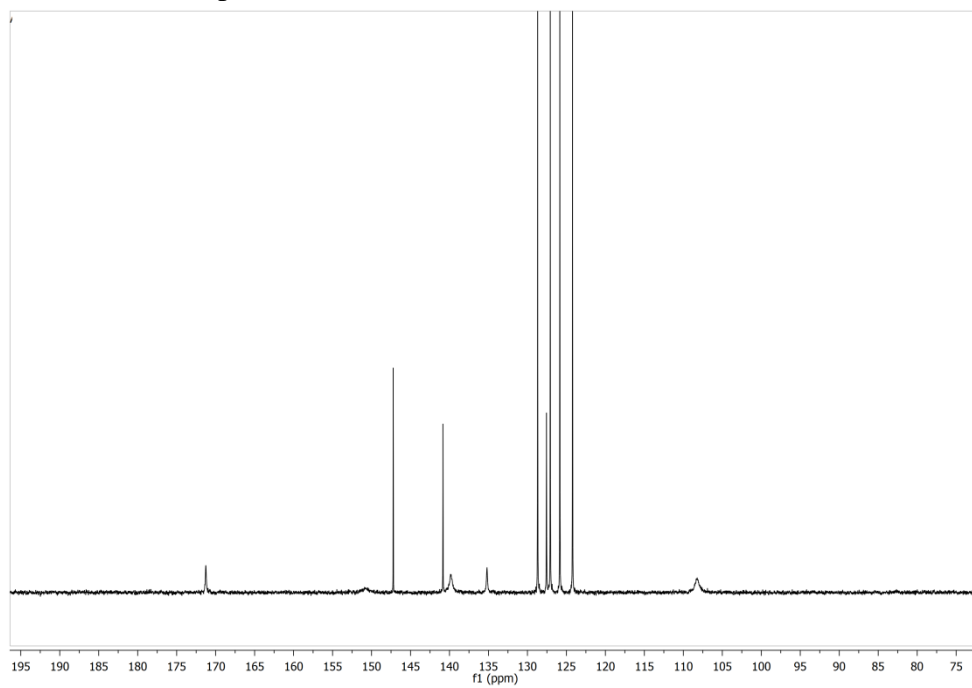


Figure 7.70 ^{13}C NMR spectrum of 4 in $\text{DMSO-}d_6$.

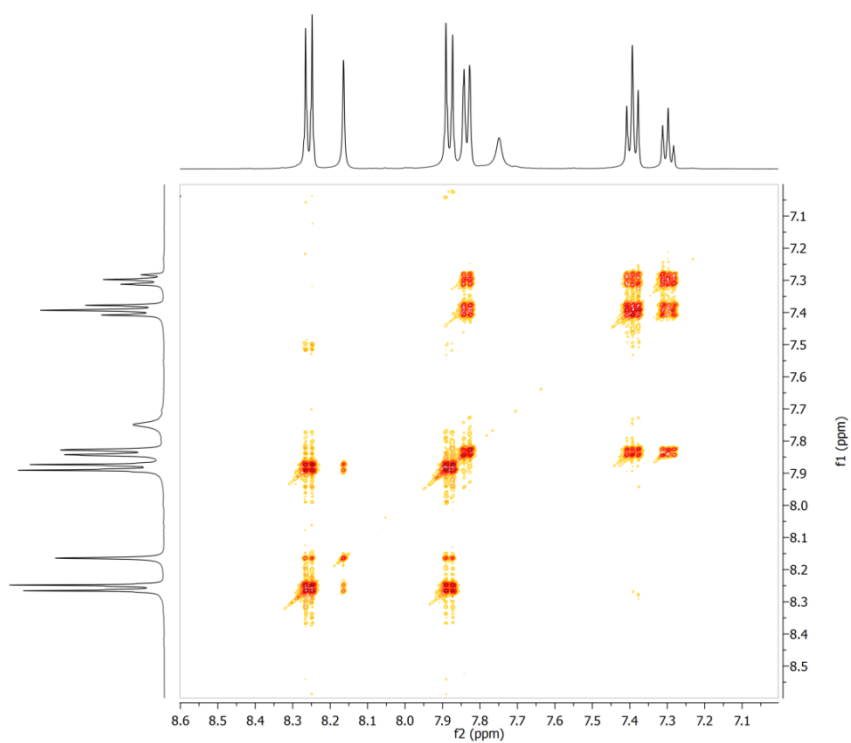


Figure 7.71 COSY spectrum of 4 in DMSO- d_6 .

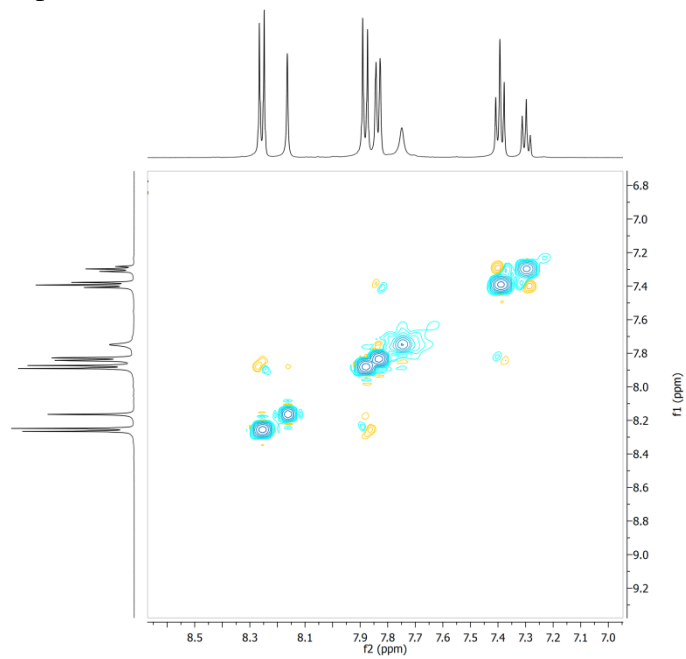


Figure 7.72 NOESY spectrum of 4 in DMSO- d_6 .

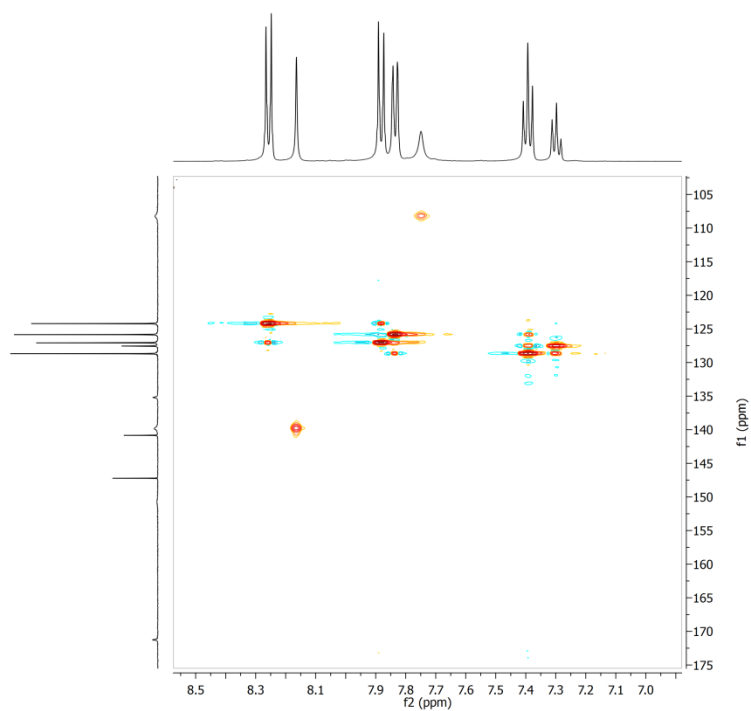


Figure 7.73 ^1H - ^{13}C HSQC NMR spectrum of 4 in $\text{DMSO-}d_6$.

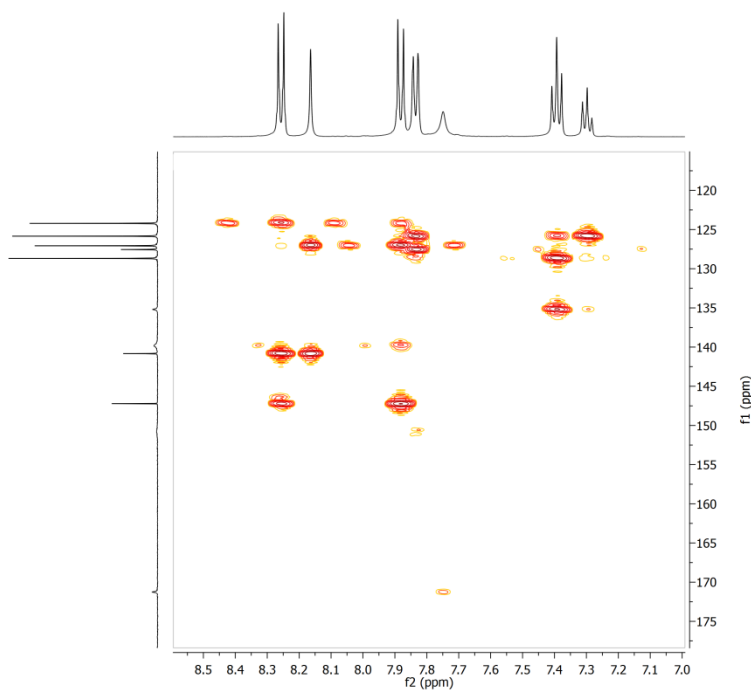


Figure 7.74 ^1H - ^{13}C HMBC NMR spectrum of 4 in $\text{DMSO-}d_6$.

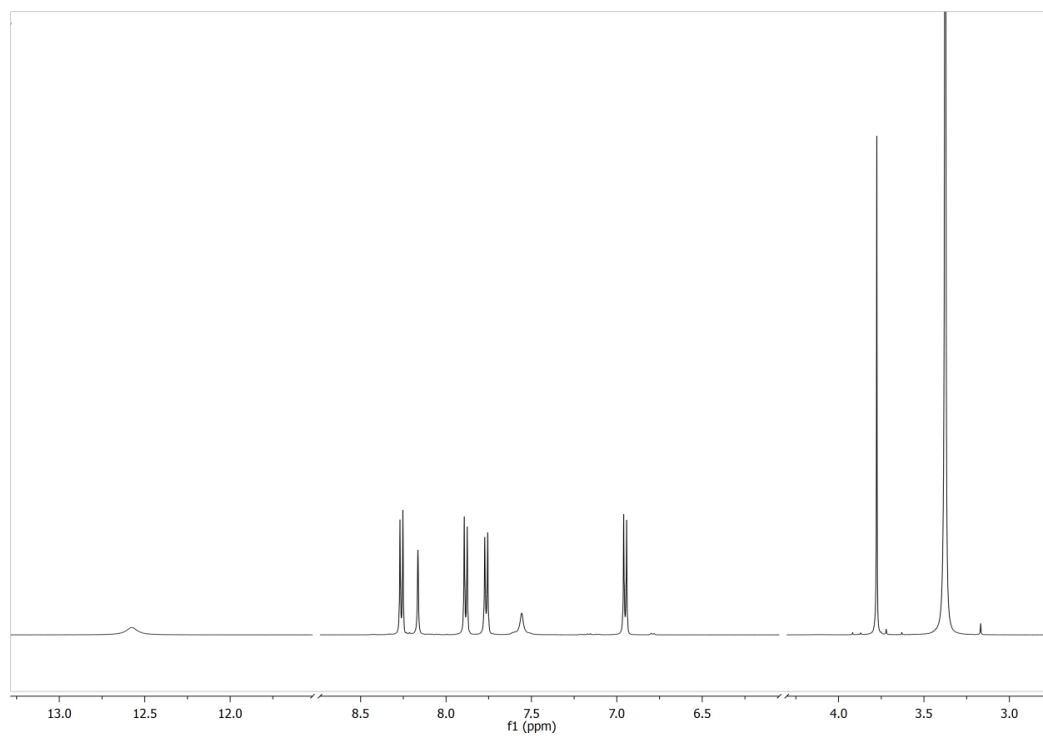


Figure 7.75 ^1H NMR spectrum of 4-OMe in $\text{DMSO-}d_6$.

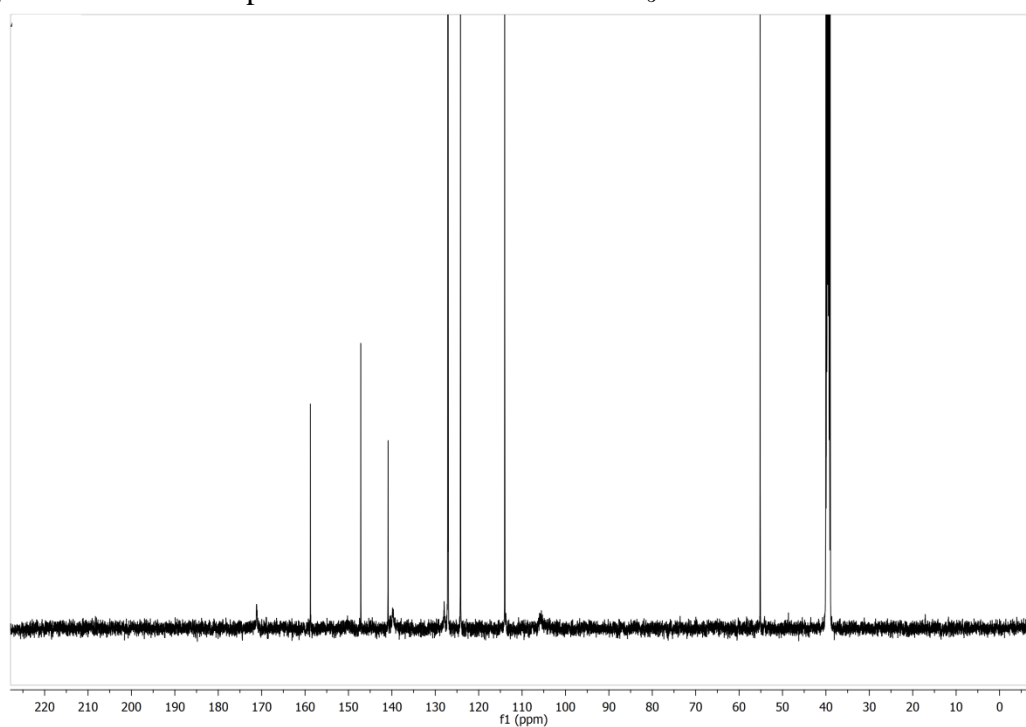


Figure 7.76 ^{13}C NMR spectrum of 4-OMe in $\text{DMSO-}d_6$.

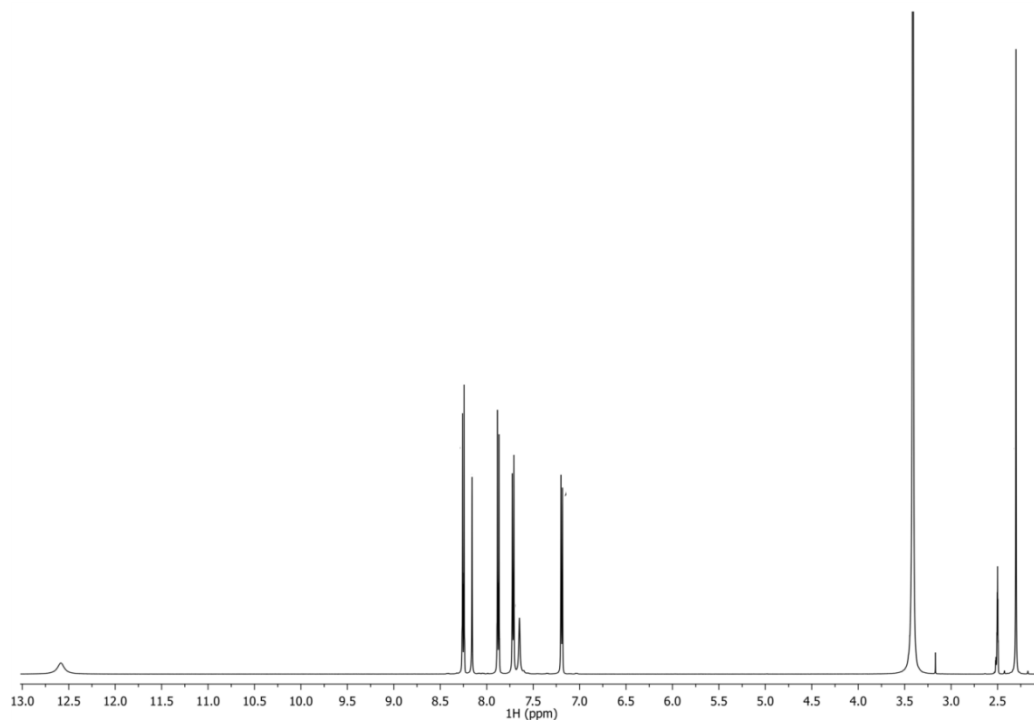


Figure 7.77 ^1H NMR spectrum of 4-Me in $\text{DMSO-}d_6$.

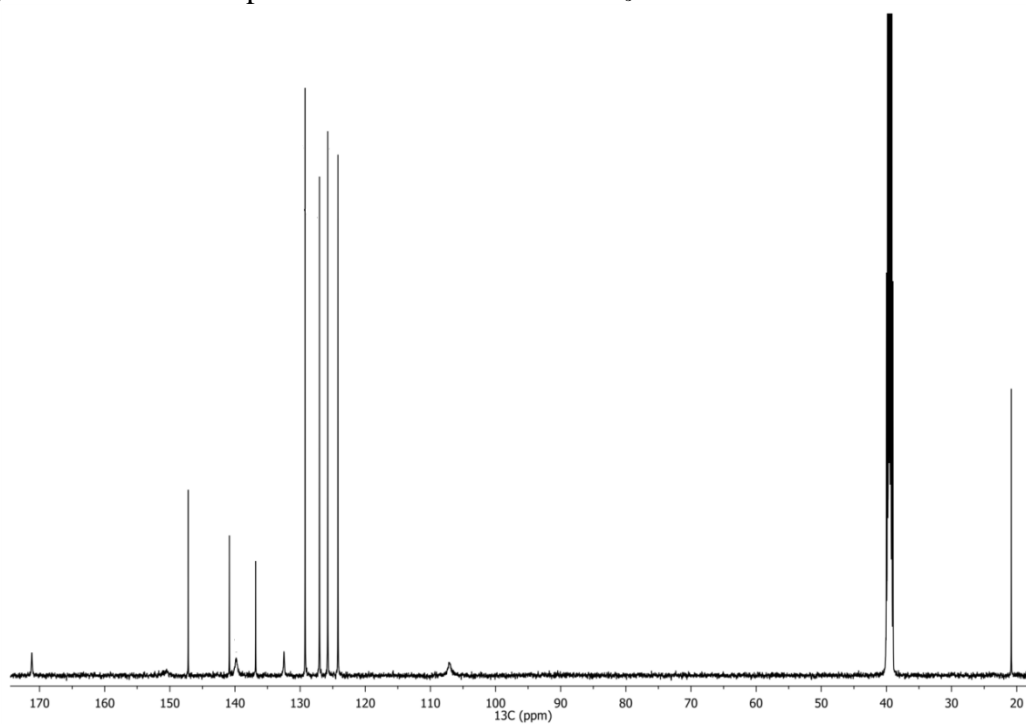


Figure 7.78 ^{13}C NMR spectrum of 4-Me in $\text{DMSO-}d_6$.

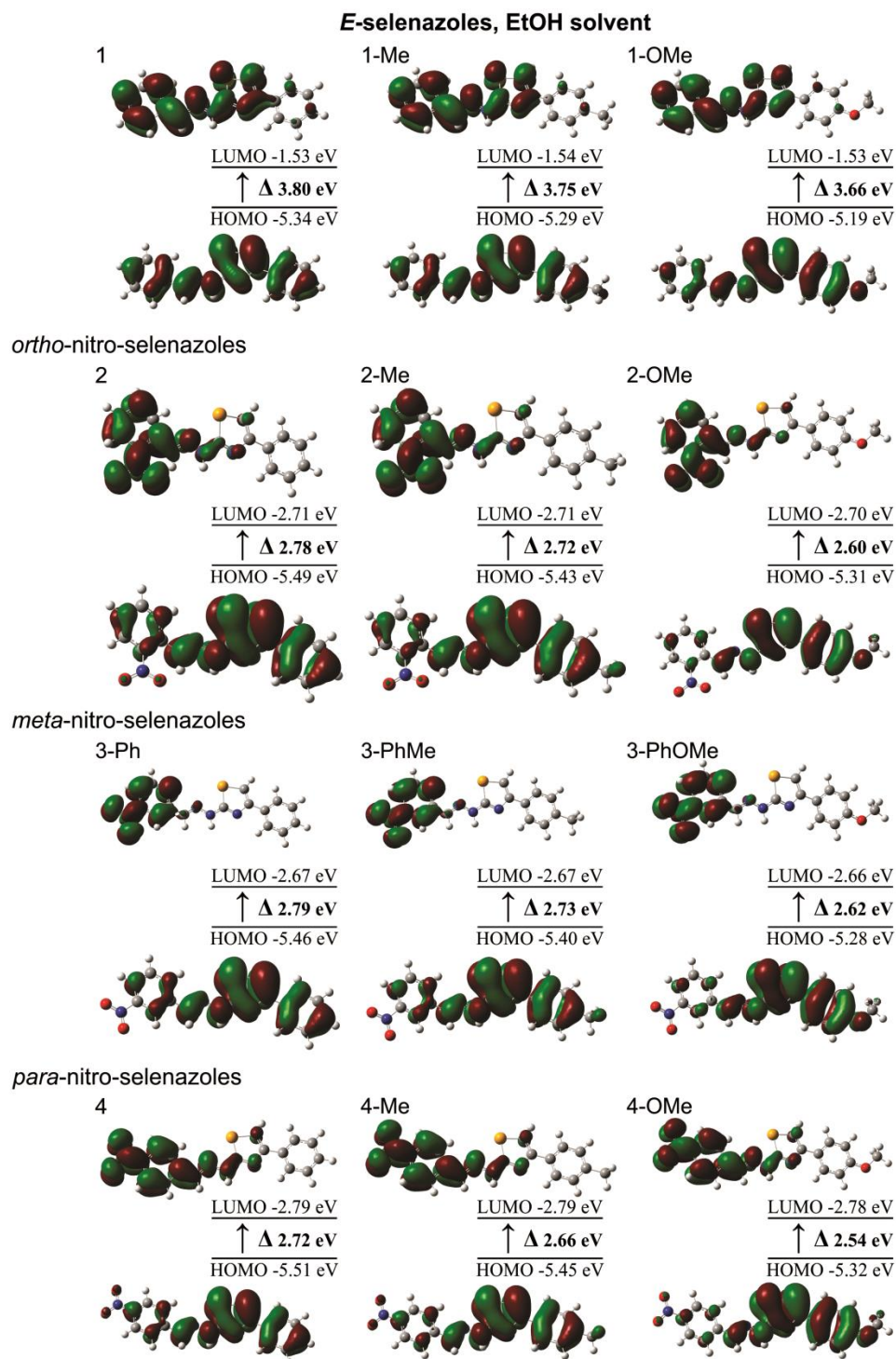


Figure 7.79 Molecular orbital plots and energy levels of the HOMO, the LUMO and HOMO-LUMO transition of the benzyldene-based (1,3-selenazol-2-yl)hydrazones in EtOH.

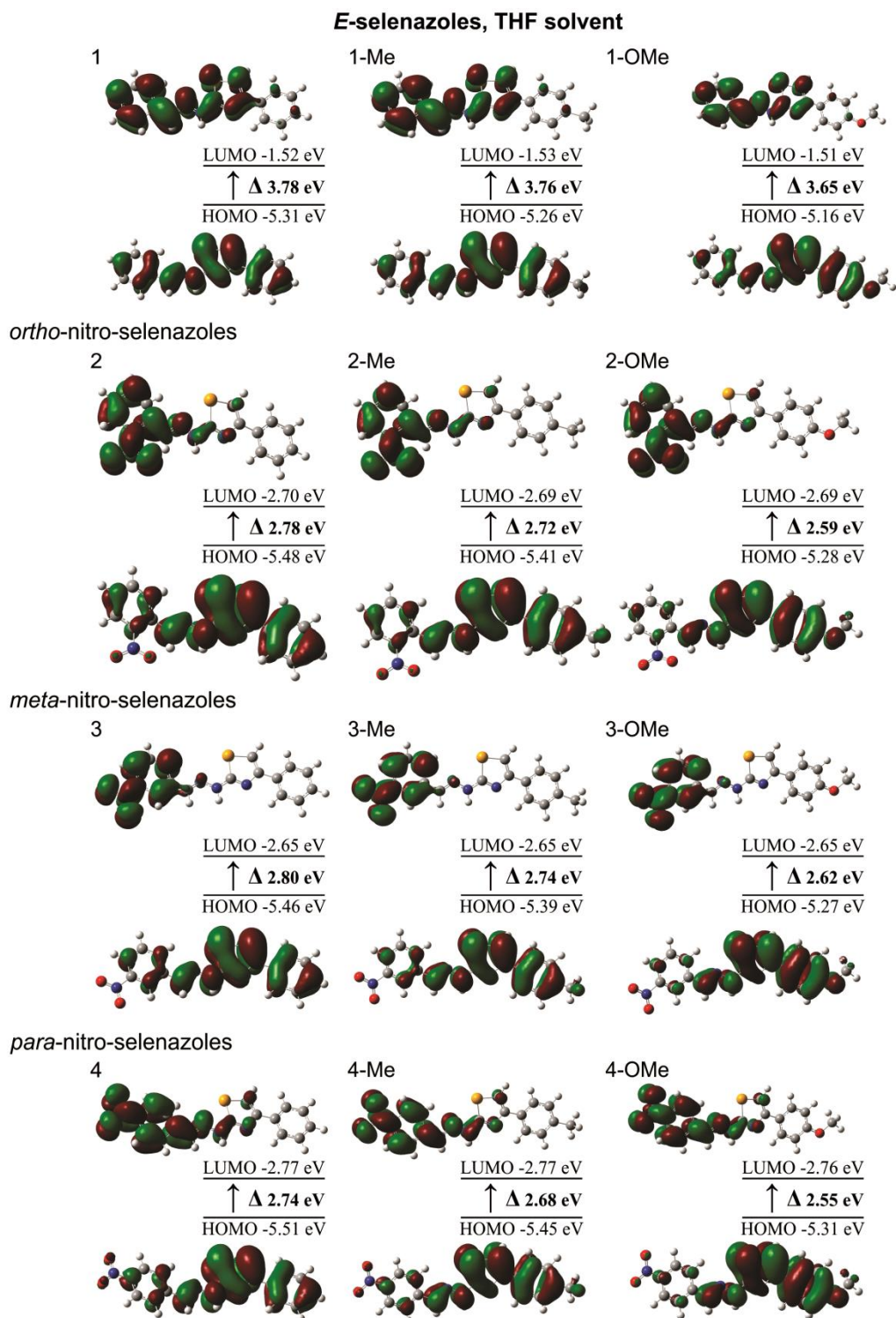


Figure 7.80 Molecular orbital plots and energy levels of the HOMO, the LUMO and HOMO-LUMO transition of the benzyldene-based (1,3-selenazol-2-yl)hydrazones in THF.

BIOGRAPHY

Hana Abdullallah Elshaflu je rođena 19. avgusta 1984. godine u Qasr Alakhyaar-u, Libija, gde je završila osnovno i srednje obrazovanje tokom 1999 - 2002, Elhadi Arafa u Al-Alous sa prosečnom ocenom veoma dobar, 76%.

Osnovne studije na Fakultetu za Umetnost i nauku, Elmergib Univerziteta, Libija, upisala je školske 2001/2002. godine, a završila 2005. godine na Katedri za organsku hemiju sa prosečnom ocenom 68,47%. Tema diplomskog rada pod nazivom "**Synthesis And Characterization Of Schiff Bases From Isatin**" odbranila je 2006. godine na Katedri za hemiju, Elmergib Univerzitet.

Master studije je upisala na Hemijskom fakultetu Univerziteta u Beogradu, i završila školske 2011/2012. godine. Master tezu pod naslovom "**Synthesis And Investigation Of Pseudorotaxanes Containing An Imide Axles And Crown Ethers As Wheels**" odbranila je 2012. godine.

Školske 2012/13.godine upisala je doktorske studije na Tehnološko–metalurškom fakultetu, Univerziteta u Beogradu, studijski program Hemija. Položila je sve ispite predviđene programom doktorskih studija i odbranila završni ispit: "Sinteza, svojstva i primena 1,3-Tiazola i 1,3-Selenazola", 30.06.2015. godine.

Oblast naučnoistraživačkog rada Hane Abdullallah Elshaflu obuhvata sintezu, karakterizaciju i ispitivanje svojstava organskih jedinjenja prirodnog i sintetskog porekla, sa posebnim osvrtom na sintezu i svojstva derivata 1,3-tiazola i 1,3-selenazola i njihovih kompleksa.

Hana Abdullallah Elshaflu govori engleski jezik. Osim toga, odlično poznaje rad na računaru, kao i na instrumentima koji se koriste za karakterizaciju organskih jedinjenja (UV/vis, FTIR i NMR).

Radovi objavljeni u časopisima međunarodnog značaja – M20

Rad u vrhunskom međunarodnom časopisu– (M21)

1. **Elshaflu, Hana**, Tamara R. Todorović, Milan Nikolić, Aleksandar Lolić, Aleksandar Višnjevac, Stefanie Hagenow, José M. Padrón, et al. 2018. “Selenazolyl-Hydrazones as Novel Selective MAO Inhibitors With Antiproliferative and Antioxidant Activities: Experimental and In-Silico Studies.” *Frontiers in Chemistry* 6 (2018). IF (2017) = 4.155; ISSN: 2296-2646; doi:10.3389/fchem.2018.00247.

2. N.R. Filipović, **H. Elshaflu**, S. Grubišić, L.S. Jovanović, M. Rodić, I. Novaković, A. Malešević, I.S. Djordjević, H. Li, N. Šojić, A. Marinković, T.R. Todorović, Co(III) complexes of (1,3-selenazol-2-yl)hydrazones and their sulphur analogues, *Dalt. Trans.* 46 (2017) 2910–2924. IF (2017) = 4.029; ISSN 1477-9226; doi:10.1039/C6DT04785H.

Rad u istaknutom međunarodnom časopisu– (M22)

1. **H. Elshaflu**, S. Bjelogrić, C. D. Muller, T. R. Todorović, M. Rodić, A. Marinković, N. R. Filipović; Co(III) complex with (*E*)-2-(2-(pyridine-2-ylmethylene)hydrazinyl)-4-(4-tolyl)-1,3-thiazole: structure and activity against two- and three-dimensional cancer cell model, *Journal of Coordination Chemistry*, 69(22) (2016) 3354-3366; IF(2015)=1,756; ISSN: 0095-8972; DOI: 10.1080/00958972.2016.1232404

Radovi u međunarodnim časopisima (M23)

1. D. Brkić, A. Božić, A. Marinković, **H. Elshaflu**, J. Nikolić, S. Drmanić; Solvatochromism of isatin based compounds: LSER and LFER study of 3-aryliminoindolin-2-one derivatives, *Journal of the Serbian Chemical Society*, 81(9) (2016) 979–997; IF(2015)=0,970; ISSN 0352-5139; DOI:10.2298/JSC160119049B

Saopštenja sa skupova nacionalnog značaja u izvodu – M64

1. Milica Rančić, Ivana Stojiljković, **Hana Elshaflu**, Miloš Milčić, Aleksandar Marinković Azo-hidrazon tautomerija novih 5-arilazo-6(2)-hidroksi-4-metil-3-cijano-N(1)-fenil-2(6)-okso-piridin-3-karbonitrilnih boja, 53. Savetovanje Srpskog hemijskog društva, Kragujevac, Srbija, Jun 10-11, 2016, Program i kratki izvodi radova, str. 106.

Изјава о истоветности штампане и електронске верзије докторског рада

Име и презиме аутора Хана Елсхафлу (Hana Elshafly)

Број индекса 4061/2012

Студијски програм Хемија

Наслов рада

„Спектроскопска и електрохемијска карактеризација, квантномеханичка студија и биолошка активност 1,3-селеназол-2-ил-хидразона, 1,3-тиазол-2-ил-хидразона и њихових комплекса са кобалтом(III) (Spectroscopic and electrochemical characterization, quantum mechanical study and biological activity of 1,3-selenazol-2-yl-hydrazones, 1,3-thiazole-2-yl-hydrazones and their complexes with cobalt(III))”

Ментори др Александар Маринковић, ванредни професор и др Ненеад Филиповић, ванредни професор

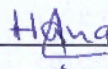
Изјављујем да је штампана верзија мог докторског рада истоветна електронској верзији коју сам предао/ла ради похрањена у **Дигиталном репозиторијуму Универзитета у Београду**.

Дозвољавам да се објаве моји лични подаци везани за добијање академског назива доктора наука, као што су име и презиме, година и место рођења и датум одбране рада.

Ови лични подаци могу се објавити на мрежним страницама дигиталне библиотеке, у електронском каталогу и у публикацијама Универзитета у Београду.

Потпис аутора

У Београду, 21.05.2018. године



Изјава о коришћењу

Овлашћујем Универзитетску библиотеку „Светозар Марковић“ да у Дигитални репозиторијум Универзитета у Београду унесе моју докторску дисертацију под насловом:

„Спектроскопска и електрохемијска карактеризација, квантномеханичка студија и биолошка активност 1,3-селеназол-2-ил-хидразона, 1,3-тиазол-2-ил-хидразона и њихових комплекса са кобалтом(III) (Spectroscopic and electrochemical characterization, quantum mechanical study and biological activity of 1,3-selenazol-2-yl-hydrazones, 1,3-thiazole-2-yl-hydrazones and their complexes with cobalt(III))“

која је моје ауторско дело.

Дисертацију са свим прилозима предао/ла сам у електронском формату погодном за трајно архивирање.

Моју докторску дисертацију похрањену у Дигиталном репозиторијуму Универзитета у Београду и доступну у отвореном приступу могу да користе сви који поштују одредбе садржане у одабраном типу лиценце Креативне заједнице (Creative Commons) за коју сам се одлучио/ла.

1. Ауторство (CC BY)
2. Ауторство – некомерцијално (CC BY-NC)
3. Ауторство – некомерцијално – без прерада (CC BY-NC-ND)
4. Ауторство – некомерцијално – делити под истим условима (CC BY-NC-SA)
5. Ауторство – без прерада (CC BY-ND)
6. Ауторство – делити под истим условима (CC BY-SA)

(Молимо да заокружите само једну од шест понуђених лиценци.
Кратак опис лиценци је саставни део ове изјаве).

Потпис аутора

У Београду, 21.05.2018. године



1. **Ауторство.** Дозвољаваате умножавање, дистрибуцију и јавно саопштавање дела, и прераде, ако се наведе име аутора на начин одређен од стране аутора или даваоца лиценце, чак и у комерцијалне сврхе. Ово је најслободнија од свих лиценци.

2. **Ауторство – некомерцијално.** Дозвољаваате умножавање, дистрибуцију и јавно саопштавање дела, и прераде, ако се наведе име аутора на начин одређен од стране аутора или даваоца лиценце. Ова лиценца не дозвољава комерцијалну употребу дела.

3. **Ауторство – некомерцијално – без прерада.** Дозвољаваате умножавање, дистрибуцију и јавно саопштавање дела, без промена, преобликовања или употребе дела у свом делу, ако се наведе име аутора на начин одређен од стране аутора или даваоца лиценце. Ова лиценца не дозвољава комерцијалну употребу дела. У односу на све остале лиценце, овом лиценцом се ограничава највећи обим права коришћења дела.

4. **Ауторство – некомерцијално – делити под истим условима.** Дозвољаваате умножавање, дистрибуцију и јавно саопштавање дела, и прераде, ако се наведе име аутора на начин одређен од стране аутора или даваоца лиценце и ако се прерада дистрибуира под истом или сличном лиценцом. Ова лиценца не дозвољава комерцијалну употребу дела и прерада.

5. **Ауторство – без прерада.** Дозвољаваате умножавање, дистрибуцију и јавно саопштавање дела, без промена, преобликовања или употребе дела у свом делу, ако се наведе име аутора на начин одређен од стране аутора или даваоца лиценце. Ова лиценца дозвољава комерцијалну употребу дела.

6. **Ауторство – делити под истим условима.** Дозвољаваате умножавање, дистрибуцију и јавно саопштавање дела, и прераде, ако се наведе име аутора на начин одређен од стране аутора или даваоца лиценце и ако се прерада дистрибуира под истом или сличном лиценцом. Ова лиценца дозвољава комерцијалну употребу дела и прерада. Слична је софтверским лиценцама, односно лиценцама отвореног кода.